2D superconductors perturbed by local magnetism: from Yu-Shiba-Rusinov bound states to Majorana quasiparticles

Gerbold C. S Ménard

Thèse

Pour l'obtention du grade de

Docteur de l'université Pierre et Marie Curie

École doctorale Physique en Île de France - ED 564

2D superconductors perturbed by local magnetism: from Yu-Shiba-Rusinov bound states to Majorana quasiparticles

Auteur :
Gerbold Ménard

Sous la direction de :
Pr. Dimitri Roditchev
Dr. Tristan Cren

Thèse défendue le 16 septembre 2016 devant un jury composé de

Pr. Jean-Marc Berroir	Examinateur
Dr. Jean-Pascal Brison	Examinateur
Dr. Laurent Limot	Rapporteur
Dr. Hugues Pothier	Invité
Pr. Vincent Repain	Examinateur
Dr. Peter Wahl	Rapporteur

Two-dimensional superconductors perturbed by local magnetism: from Yu-Shiba-Rusinov bound states to Majorana quasiparticles

Gerbold Ménard

December 5, 2016

Contents

List of Figures

Abstract

2D superconductors perturbed by local magnetism: from Yu-Shiba-Rusinov bound states to Majorana quasiparticles

One of the present days goals of condensed matter physics is to create new systems with topological properties, especially in the field of superconductivity. One of the ways envisioned to create topological superconductors is to locally induce a magnetic interaction in the form of chains of magnetic impurities, vortices or magnetic clusters of ordered magnetic impurities. In this thesis we studied a set of effects from individual impurities to organized clusters interacting with two-dimensional superconductors. Using scanning tunneling microscopy and spectroscopy we considered two systems, monocrystals of 2H-$NbSe_2$ and monolayers of Pb/Si(111). Thanks to the two-dimensional electronic behavior of these two systems we show how the spatial extent of the bound states induced by magnetic impurities is considerably enhanced compared to the case of a three-dimensional superconductor. By combining these magnetic atoms using a self-assembly method we were able to create ferromagnetic clusters that lead to a topological superconductivity in Pb monolayers. In particular we present here measurement of topological edge states at the interface Pb/Si(111) and Pb/Co/Si(111). We also present the measurement of zero bias peaks in the center of larger magnetic clusters that sign the presence of Majorana fermions in these systems. Our results show that an adequate patterning of surfaces could realize topological patches and call for a pursuit of the efforts in the subject in order to be able to control Majorana fermions that could eventually lead to breakthrough in quantum computation.

Keywords

Superconductivity, Yu-Shiba-Rusinov bound states, scanning tunneling spectroscopy, scanning tunneling microscopy, Rashba interaction, triplet superconductivity, spin-orbit coupling, two-dimensionnal superconductivity, 2H-$NbSe_2$, Pb/Si(111) monolayer, local magnetism, topology, edge states, proximity effect.

Résumé

Supraconducteurs 2D perturbés par un magnétisme local: des états de Yu-Shiba-Rusinov aux quasiparticules de Majorana

L'un des buts de la physique de la matière condensée est à l'heure actuelle de fournir de nouveaux systèmes topologiques en particulier dans le domaine de la supraconductivité. L'une des manières envisagée pour générer des supraconducteurs topologiques est d'utiliser une interaction magnétique locale sous la forme de chaînes d'impuretés magnétiques, de vortex ou de clusters d'impuretés magnétiques ordonnées. Dans cette thèse nous avons étudié un ensemble d'effets en partant de l'étude d'impuretés individuelles en allant jusqu'aux clusters organisés en interaction avec un supraconducteur bidimensionnel. En utilisant la microscopie et la spectroscopie tunnel nous avons étudié des monocrystaux de 2H-$NbSe_2$ ainsi que les monocouches de Pb/Si(111). En raison du caractère électronique bi-dimensionnel de ces deux systèmes nous avons pu montrer que l'étendue spatiale des états liés induits par des impuretés magnétiques était considérablement augmentée en comparaison avec les supraconducteurs tridimensionnels. En combinant ces atomes magnétiques par auto-assemblage nous sommes parvenus à réaliser des clusters ferromagnétiques qui génèrent une supraconductivité topologique dans la monocouche de Pb. Nous présentons en particulier ici la mesure d'états de bords topologiques à l'interface entre Pb/Si(111) et Pb/Co/Si(111). Nous présentons également la mesure d'états liés à zéro énergie au centre de clusters magnétiques signant la présence de fermions de Majorana dans ces systèmes. Nos résultats montrent qu'une structuration adéquate des surfaces permet de réaliser des patchs topologiques et appellent à une continuation des efforts de recherche sur ce sujet afin de pouvoir contrôler les fermions de Majorana observés qui sont susceptibles de conduire à des percées futures dans le domaine de l'informatique quantique.

Mots clés

Supraconductivité, états liés de Yu-Shiba-Rusinov, spectroscopie à effet tunnel, microscopie à effet tunnel, interaction Rashba spin-orbite, supraconductivité triplet, couplage spin-orbite, supraconductivité bidimensionnelle, 2H-$NbSe_2$, monocouche de Pb/Si(111), magnétisme local, topologie, états de bords, effet de proximité.

Remerciements

Après ces trois années de thèse, il y a bien des gens que je souhaite remercier qu'ils aient participé à la réussite de cette thèse par leur implication directe dans mon travail, par les discussions informelles, par l'interaction régulière scientifique ou non, au sein du laboratoire ou à l'extérieur.

Tout d'abord je remercie les membres du jury qui ont accepté de juger de la valeur de mon travail et de prendre sur leur précieux temps. Je remercie également la fondation CFM qui a financé ces trois années de travail et m'a permis de participer à de nombreuses conférences à l'étranger via le financement dédié.

Ensuite je souhaiterai remercier les membres de mon équipe à l'INSP Christophe, Tristan et François sans qui les ténèbres du sous-sol m'auraient englouti et avec qui j'ai eu l'impression d'apprendre des choses nouvelles chaque jour. Je remercie Tristan en particulier pour son encadrement, sa disponibilité et les nombreuses discussions scientifiques que nous avons eu tous les deux avant d'aller affronter les théoriciens. Je remercie Dimitri pour l'encadrement plus lointain mais tout aussi enrichissant. Un merci général pour avoir su à la fois me laisser une grande liberté dans mon travail tout en étant toujours disponible en cas de souci. Enfin je remercie les autres membres de l'équipe Stéphane, Sergio, Pascal et Yves avec lesquels j'ai moins eu l'occasion de travailler en collaboration directe ce qui n'a pas empêché de nombreux échanges scientifiques au labo ou à l'extérieur autour d'un verre. Merci à Dominique Demaille pour le temps passé à inspecter nos échantillons au MEB et la patience que cela a demandé.

Merci au service des basses températures qui m'a permis d'utiliser tout cet hélium Richard, David et Florin. Merci à tous les membres du laboratoire que je vous ai vu et discuté avec vous tous les jours ou bien une seule fois.

Merci aux personnes avec lesquelles j'ai collaboré scientifiquement, particulièrement l'équipe théorique du LPS Orsay Sébastien Guissart, Mircea Trif et Pascal Simon. Merci également à l'équipe de l'institut Jean Rouxel, Laurent Cario et Étienne Janod pour avoir fourni les cristaux de $NbSe_2$ sur lesquels un grand nombre des mesures présentes dans cette thèse ont été menées.

Merci aux différents services administratifs du laboratoire qui ont souvent eu à résoudre des problèmes bien plus compliqués que les problèmes physiques auxquels j'ai du m'atteler. Merci à Betty, Natalia, Stéphanie, Lucdivine, Aurélia, Cécile, Myriam et Valérie.

Je souhaite tout particulièrement remercier les thésards de l'INSP qui ont fait en sorte que la bonne humeur et la convivialité règne au laboratoire, en commençant par les représentants successifs des doctorants Diego, Bruno, Céline, Cyril et Suzanne, les anciens thésards de l'équipe Lise et Clémentine et tous les autres Yael, Nathalie, Antoine, Mattia, Lise, Lounès, Danilo, Romain, Louis, Pierre-Yves, Antoine, Vivien, Sophie, Paul, Frédéric, Léonard, Maya, Sébastien et tous ceux que j'aurais oublié ou avec qui j'ai moins interagi.

Merci également aux anciens membres de l'éphémère groupe de musique du laboratoire, Cyrille, Sylvain, Francis, François et Colin. Pour le reste du labo, désolé pour le bruit.

Merci à mes parents et à ma famille de leur soutien et d'avoir accepté d'arrêter de me demander de leur expliquer "simplement" mon sujet de thèse. Désolé d'avoir échoué à cette tâche.

Merci à mes amis. Ceux qui le sont restés malgré la distance Kathleen, Diane, Guillaume, Monika, Antoine, Marie, Valentin, Alexis. Ceux qui le sont devenus au long de ces années d'étude parisiennes Louis, Fabien, Sara, Marine, Marco, Sébastien, Micha. Merci à ceux qui furent mes voisins et sont aujourd'hui

des amis, Marine, Édouard, Céline. Merci aux pouilleux qui m'ont offert un moment de détente plus qu'apprécié après la rédaction du manuscrit Juliette, Pierre, Thibault, Lucile et Indira. Merci à ceux que je n'ai pas cité, je ne vous oublie pas pour autant.

Merci au Finnegan's/Baker Street et au 2 Bis. Merci à l'espace de convivialité du deuxième étage.

Merci enfin à tous ceux que j'ai rencontré au cours de ces trois ans et qui d'une manière ou d'une autre ont contribué à mon envie de continuer dans la recherche ou on simplement fait de ces trois dernières années des années d'exception.

List of abbreviations and notations

ARPES: Angle-Resolved Photoemission Spectroscopy
BCS: Bardeen-Cooper-Schrieffer
BdG: Bogoliubov-de Gennes
DFT: Density Functional Theory
ESPCI: École Supérieure de Physique et Chimie Industrielle
FBZ: First Brillouin Zone
HIC: Hexagonal Incommensurate
INSP: Institut des Nanosciences de Paris
LDOS: Local Density of States
LPN: Laboratoire de Photonique et Nanostructures
LPS: Laboratoire de Physique des Solides
MBE: Molecular Beam Epitaxy
ML: Monolayer
SIC: Stripe Incommensurate
STM: Scanning Tunneling Microscopy
STS: Scanning Tunneling Spectroscopy
TEM: Transmission Electron Microscopy
UHV: Ultra High Vacuum
YSR: Yu-Shiba-Rusinov

$\hat{c}^\dagger_{k\sigma}$: Electron creation operators with wave-vector $\boldsymbol{k}$ and spin σ
$\hat{c}^\dagger_{i\sigma}$: Electron creation operators at site i with spin σ
ξ_k: Free electron dispersion $\frac{\hbar^2 k^2}{2m} - \mu$.
ξ: Superconducting coherence length.
Δ_S: Amplitude of singlet order parameter. When not specified $\Delta = \Delta_S$
Δ_T: Amplitude of triplet order parameter.
$\sigma_{x,y,z}$: Pauli matrices in spin space.
$\tau_{x,y,z}$: Pauli matrices in electron-hole space.
f_n: Fermi-Dirac distribution.
E_S: Eigen energies of YSR bound states.
$\boldsymbol{B}$: Magnetic field expressed in energy units.
ℓ: Mean free path.
T_c: Critical temperature.
θ: In-plane rotation angle. $\theta = 0$ corresponds to the x-axis.
ϕ: Out of plane rotation angle. $\phi = 0$ corresponds to the z-axis.

Introduction

Despite the century long history of superconductivity and the many works in the field, this phenomenon stills raises many fundamental questions, the question of the interaction between superconductors and localized magnetic disorder in particular. Recently, in relation with the emergence of the field of topological insulators, superconductivity was regarded as a potential new and powerful platform in which to create, observe and control topological excitations that could eventually lead to real-life applications in the field of quantum electronics. Due to their build-in electron-hole symmetry, superconductors are expected under certain conditions to enter a topological phase that have been predicted to host zero-bias Majorana bound states.

The question remains to know how to prepare such topological systems and ultimately manipulate the Majorana quasiparticles in braiding operations. The path we follow consists in studying the individual ingredients of topological superconductivity before ultimately combining them and produce robust zero-bias modes. These ingredients are local magnetism, that is controlled by combining magnetic atoms and Rashba spin-orbit interaction that emerges at surfaces. We will thus study both aspects and spend a large part of this thesis discussing individual impurities before presenting results on ferromagnetic clusters.

This thesis aims at answering some of the fundamental questions of topological superconductivity by first understanding the role of systems dimensionality in the coupling between superconductivity and localized magnetic disorder. In order to understand how impurities couple we must first start by studying individual magnetic atoms in a superconducting condensate. We will demonstrate the dramatic expansion of Yu-Shiba-Rusinov (YSR) bound states by dimensionality effects in both 2D-like monocrystals and pure atomically 2D superconductors.

Because Rashba spin-orbit interaction arises at surfaces, the Pb monolayers are ideal systems in which to study topological superconductivity. By assembling local magnetic moments in ferromagnetic clusters we will show that we can obtain topological superconductivity in the helical regime that exhibits two nonequivalent edge states. In particular we will show that the behavior of these states is drastically different from the one of individual impurities as they are not affected by crystalline disorder at the atomic scale. Once we prove that we obtain topological superconductivity we can then study how vortices behave in these structures and induce zero-bias peaks that can be switched on and off using the STM tip.

This thesis is organized in 7 chapters as described below. The first two chapters are general discussion about the theoretical and experimental tools that will be used in the rest of the manuscript. Chapters 3 to 5 present experimental results observed by means of scanning tunneling microscopy and spectroscopy on two different systems which are 2H-$NbSe_2$ and monolayers of Pb/Si(111). The last chapter covers some of the others results that were obtained during this thesis about the Pb/Si(111) monolayer system not related with local magnetism.

Chapter 1: Superconductivity and scanning tunneling microscopy/spectroscopy

In this first chapter we describe the basic ideas of superconductivity that will be needed in the following chapters to understand the concepts discussed. We also present the concept of scanning tunneling microscopy and spectroscopy with which we will probe superconductivity.

We start by presenting a brief history of superconductivity from its discovery in 1911 to its theoretical understanding provided by the BCS theory. We continue by discussing the Bogoliubov-de Gennes approach and the formalism used to interpret our experimental data. We then move to the experimental

technique of scanning tunneling microscopy and spectroscopy with which we probe superconductivity at the atomic scale. In this part we explain the measurements principle and detail particularly the case of a superconducting tip. We end by describing the experimental setup that we used at the INSP and the procedures used for data analysis.

Chapter 2: Magnetic impurities in a superconductor

The theme of this thesis is the interaction between localized magnetic moments and superconductivity. We discuss in this chapter the variety of theoretical approaches that were developed over time to describe this type of interaction.

We start chronologically by discussing the Abrikosov-Gor'kov theory that describes assemblies of randomly distributed classical magnetic moments in a bulk superconductor. We briefly present the theory and its main physical consequences. Before studying in more details the physics of Yu-Shiba-Rusinov bound states. In this part we go in depth inside the theory as we explain the role of dimensionality on the spatial extension of the wave function associated to individual localized magnetic moments. This part will be used in Chapter 3 and 4 to interpret our experimental results. We pursue this part on Yu-Shiba-Rusinov bound states by presenting a review of the literature on the STM measurement of these states. Finally we briefly mention the quantum limit of the Kondo physics as well as the spectroscopic signatures of the Fano lineshapes.

Chapter 3: Magnetic and non-magnetic impurities in 2H-$NbSe_2$ monocrystals

The third chapter presents the experimental results obtained on monocrystals of 2H-$NbSe_2$ in which were inserted magnetic impurities of Fe, Cr and Mn. We show in this chapter that the 2D-like electronic structure of this material leads to an increase by a factor 10 of the spatial extension of the Yu-Shiba-Rusinov bound states compared to bulk systems. We present tight binding calculations done by S. Guissart and P. Simon supporting our experimental data as well as joint-DOS calculation that helps us understand the contribution of the different parts of the Fermi surface to the electronic scattering. We discuss the relation between the positive and negative bias states and the phase of the associated wave function in the framework of the Rusinov theory and compare different types of impurities. We also present the results obtained when trying to deposit Co impurities on the crystal surface and the characteristic signature of non-magnetic Ta impurities in relation with the two gaps structure of 2H-$NbSe_2$.

Chapter 4: Magnetic and non-magnetic impurities in Pb/Si(111) monolayers

This chapter presents the summary of our study of individual and disordered clusters of magnetic impurities in monolayers of Pb/Si(111). We discuss the effects of the atomic structure of the monolayers on the spatial structure of the Yu-Shiba-Rusinov bound states. We show that the link between the system dimension and the spatial extent of the states confirms the results obtained in the case of 2H-$NbSe_2$. For the specific case of the $\sqrt{7} \times \sqrt{3}$ reconstruction we discuss the periodicity of the oscillations of the wave-function of the Yu-Shiba-Rusinov bound states in relation with the structure of the Fermi surface measured by ARPES. In the last part of the chapter we present the case of randomly distributed magnetic impurities in clusters. We show that the combined effect of individual Yu-Shiba-Rusinov bound states leads to a gap reduction over the clusters as well as a gap filling. These results are well reproduced by a simple calculation that uses the analytical formula derived for magnetic impurities in 2D systems.

Chapter 5: Magnetic clusters and topological systems

This chapter is dedicated to the study of topological superconductivity. We first discuss the effects of different ingredients needed to obtain topological superconductivity: Rashba spin-orbit interaction, triplet superconductivity and magnetism. We then present the results obtained by growing ferromagnetic Co clusters embedded in a Si substrate covered by a Pb monolayer and measured by using a superconducting tip. We show that we obtain edge states expected in the case of a topological superconductor put in close contact with a trivial superconductor. We detail the energy and spatial dispersion of those edge states and present the theoretical analysis performed in order to explain our results. We conclude the chapter by showing how the inclusion of vortices in topological domains leads to the emergence of Majorana

bound states that can be controlled by switching of the magnetization of the Co clusters. The theoretical calculation presented in this chapter were also done in collaboration with S. Guissart, M. Triff and P. Simon who developed the necessary theory.

Chapter 6: The Pb/Si(111) monolayer: A playground for 2D physics

In this chapter we gather the results obtained for the Pb/Si(111) monolayer without magnetic perturbation. This chapter first presents results covering the different phases existing in the Pb/Si(111) monolayer (3×3, $\sqrt{3} \times \sqrt{3}$, SIC, HIC, $\sqrt{7} \times \sqrt{3}$) and the measurement of their electronic structure by scanning tunneling spectroscopy beyond the characteristic superconducting gap energy. The second half of the chapter is devoted to proximity effect. There we present the measurement of the proximity effect between a superconductor and a quasi-Mott system.

Chapter 7: Superconducting proximity effect

In this last chapter we discuss the superconducting proximity effect between monolayers of Pb/Si(111) and bulk-like Pb islands. We present measurement of superconducting correlations from the islands to the monolayer below and above the critical temperature of the HIC phase. We compare those results with calculations performed by J. C. Cuevas using the Usadel equations describing a superconductor in the diffusive limit. We show how the theory accounts well for our experimental results when calculating the superconducting order parameter self-consistently.

The conclusion summarizes the results obtained and presented in this thesis and give an outlook to the things yet to come in the domain of topological superconductivity and 2D superconductors and the possibilities offered by the results presented here.

A short summary (15 pages) of the thesis, written in French is included after the bibliography.

Chapter 1

Superconductivity and scanning tunneling microscopy

1.1 Introduction

In this chapter we will present the main concepts and tools that will be used in the following of the manuscript. We will first briefly present an history of superconductivity before discussing the Bardeen-Cooper-Schrieffer (BCS) theory in more details. Building on the BCS theory of superconductivity we will present the Bogoliubov de Gennes approach and introduce the mathematical spinor formalism that was used for numerical calculations in this thesis. In the second part of the chapter we will discuss the experimental techniques of scanning tunneling microscopy and spectroscopy which will be used for the experimental probing of the local properties of superconductivity. We present as well the basic principles of the data analysis and sample preparation.

1.2 Superconductivity

1.2.1 Historical overview of superconductivity

Superconductivity is a phenomenon discovered in 1911 by Heike Kamerlingh Onnes in Leiden [1]. In his laboratory he measured the resistivity of Hg as a function of temperature and observed a sudden drop of resistivity under 4.2 K. While the first response to this observation was disbelief he was able to prove that is was not caused by any error in the measurement process and that the zero resistivity measurement was real. The same experiment was repeated with many other elements and it was shown that superconductivity was more the rule than the exception in nature as only a few elements, such as Cu, Ag or Fe for instance, didn't experience this transition. Onnes received the Nobel Prize in 1913, not for the discovery of superconductivity but [2]

> *For his investigations on the properties of matter at low temperatures which led, inter alia, to the production of liquid helium.*

Another important aspect of superconductivity was discovered by Walther Meissner et Robert Ochsenfeld in 1933 [3]. Meissner and Ochsenfeld discovered that a superconductor would expel any applied magnetic field and is therefore a perfect diamagnet. The most impressive consequence of this diamagnetism is the possibility to levitate a superconductor in a magnetic field strong enough. These two properties (zero electric resistance and perfect diamagnetism) are the two basic requirements for a material to be a superconductor.

The first piece of understanding in the field of superconductivity was provided by the brothers Fritz and Heinz London in 1935 [4]. In their work they proposed the following relation between the current

density and the vector potential in the London gauge ($\boldsymbol{\nabla} \cdot \boldsymbol{A} = 0$)

$$\boldsymbol{j}_s(\boldsymbol{r}) = -\frac{n_s e^2}{m}\boldsymbol{A}(\boldsymbol{r}), \tag{1.1}$$

where e is the elementary electric charge[1], m the mass of the electron and n_s is the density of electrons taking part to the superconductivity. This equations allows for the determination of the magnetic field inside a superconductor and leads to the introduction of the penetration length λ_L defined as

$$\lambda_L = \frac{c}{e}\sqrt{\frac{m\varepsilon_0}{n_s}}. \tag{1.2}$$

This length describes the characteristic size over which an external magnetic field penetrates a superconductor and therefore the London theory serves as a theoretical framework to explain the Meissner effect. However the quantity n_S introduced in the London equation is a phenomenological one and does not provide any deep understanding of the underlying phenomena. This theory nevertheless has the merit to envision superconductivity as a macroscopic manifestation of quantum mechanics.

London theory is still unsatisfactory as the equation describing this macroscopic effect is local in nature. In 1953, Pippard [5] built upon the previous theory by analogy with the non-local generalization of Ohm's law $\boldsymbol{J}(\boldsymbol{r}) = \sigma\boldsymbol{E}(\boldsymbol{r})$ written in a metal [6]

$$\boldsymbol{J}(\boldsymbol{r}) = \frac{3\sigma}{4\pi l}\int \frac{\boldsymbol{R}(\boldsymbol{R}\cdot\boldsymbol{E}(\boldsymbol{r}'))}{R^4}e^{-R/l}\mathrm{d}\boldsymbol{r}' \tag{1.3}$$

with $\boldsymbol{R} = \boldsymbol{r} - \boldsymbol{r}'$. The length l is related to the range over which an electric field $\boldsymbol{E}(\boldsymbol{r}')$ affects the current at a point $\boldsymbol{r}$.

Pippard's theory leads to the definition of another characteristic length scale in superconductivity namely the coherence length ξ. This length is obtained by taking advantage of the Heisenberg uncertainty principle. Pippard considers that the electrons with an energy of the order of $k_B T_c$ play the main role in superconductivity. These electrons thus have have a momentum in the range $\Delta p \simeq k_B T_c / v_F$ with v_F the Fermi velocity. From the Heisenberg relation $\Delta x \Delta p \geq \hbar$ (we forget the 1/2 term as we only look for orders of magnitude here) we can obtain

$$\Delta x \simeq \frac{\hbar v_F}{kT_c}. \tag{1.4}$$

We thus obtained a characteristic length and we define

$$\xi_0 = a\frac{\hbar v_F}{kT_c} \tag{1.5}$$

with a a dimensionless constant of the order of unity. This length scale can be interpreted as the smallest scale on which superconductivity can appear and the coherence of electrons is maintained. This constant plays more or less the same role in superconductivity in reaction to a vector potential as the mean free path in normal metals in reaction to an electric field. Pippard then proposes the following generalized form for the current density in a superconductor

$$\boldsymbol{J}_s(\boldsymbol{r}) = \frac{3n_s e^2}{4\pi m\xi_0}\int \frac{\boldsymbol{R}(\boldsymbol{R}\cdot\boldsymbol{A}(\boldsymbol{r}'))}{R^4}e^{-R/\xi}\mathrm{d}\boldsymbol{r}' \tag{1.6}$$

where ξ is called the coherence length and in presence of scattering is defined by a combination of ξ_0 and l as

$$\frac{1}{\xi} = \frac{1}{\xi_0} + \frac{1}{l}. \tag{1.7}$$

[1] $e > 0$ and equal to $1{,}6.10^{-19}$ C in the following.

This expression is only true for $l \simeq \xi$ while in all generality and one should write the correct form

$$\xi = \sqrt{\xi_0 l}. \tag{1.8}$$

Writing eq. 1.6 in this form allows (for a slowly varying $\boldsymbol{A}(\boldsymbol{r}')$) to find once again the London equation (eq. 1.1).

Superconductivity is now equipped with a set of two characteristic length-scales, the penetration length λ_L and the coherence length ξ. Depending on a relation between these two lengths we thus expect differences in the behavior of superconductors.

The next theory of superconductivity was proposed by Ginzburg and Landau in 1950 [7]. This theory is based on the previous work of Landau on phase transitions. The idea is here to find a free energy describing the state of the system as a function of temperature and magnetic field. Ginzburg and Landau proposed the following form for the free energy difference between the superconducting (F_s) and normal (F_n) state

$$F_s(T,B) - F_n(T,B=0) = \int d^3r \left[\alpha |\Delta(\boldsymbol{r})|^2 + \frac{\beta}{2}|\Delta(\boldsymbol{r})|^4 + \frac{\hbar^2}{4m}\left| \left(\frac{\boldsymbol{\nabla}}{i} - \frac{2e}{\hbar}\boldsymbol{A}(\boldsymbol{r}) \right) \Delta(\boldsymbol{r}) \right|^2 + \frac{|\boldsymbol{B}(\boldsymbol{r}) - \mu_0 \boldsymbol{H}_0|^2}{2\mu_0} \right]. \tag{1.9}$$

In this equation the parameters α and β are such that $\alpha(T) = \alpha_0(T - T_c)$ with $\alpha_0 < 0$ and $\beta > 0$. The form of the free energy is only valid close to the transition which justifies the form of $\alpha(T)$. $\Delta(\boldsymbol{r})$ is the order parameter of the theory that will be different from 0 in the superconducting phase and equal to 0 in the normal phase. This term will play the same role as the superconducting gap when interpreted in the framework of the BCS theory. The mass term $1/4m$ multiplies a kinetic energy term which was originally postulated by Landau as an analog to the Schrödinger equation. Originally the form of this mass term was $1/2m^*$ with m^* the reduced mass of the electrons which is exactly equal to $2m$ due to the underlying electronic pairing. In the same way, the original writing of the charge term $4e/\hbar$ was $2e^*/\hbar$ where once again the pairing of electrons in the form of Cooper pairs leads to an effective charge equal to twice the electron charge. By minimizing the free energy of the system, Ginzburg and Landau found two equations

$$\frac{\hbar^2}{4m}\left(\frac{\boldsymbol{\nabla}}{i} - \frac{2e}{\hbar}\boldsymbol{A}(\boldsymbol{r}) \right)^2 \Delta(\boldsymbol{r}) + \alpha \Delta(\boldsymbol{r}) + \beta |\Delta(\boldsymbol{r})|^2 \Delta(\boldsymbol{r}) = 0 \tag{1.10}$$

$$\boldsymbol{j}_s(\boldsymbol{r}) = \frac{2e}{\hbar}\frac{\hbar^2}{4m}\left[\frac{1}{2}(\Delta^*(\boldsymbol{r})\boldsymbol{\nabla}\Delta(\boldsymbol{r}) - \Delta(\boldsymbol{r})\boldsymbol{\nabla}\Delta^*(\boldsymbol{r})) - \frac{2e}{\hbar}\boldsymbol{A}(\boldsymbol{r})|\Delta(\boldsymbol{r})|^2 \right]. \tag{1.11}$$

The first equation describes the spatial evolution of the order parameter while the second one gives the current density in a superconductor. The superconducting coherence length is obtained in the framework of the Ginzburg-Landau theory as

$$\xi = \sqrt{\frac{\hbar^2}{2m|\alpha|}}. \tag{1.12}$$

Interestingly enough, equation 1.10 served as an inspiration to the Gross-Pitaevskii equation describing the dynamic of an ultra-cold bosonic gas [8, 9]. The proximity between these two equations helps to understand the bosonic behavior in superconductivity, in accordance with the BCS theory. The Ginzburg-Landau theory was successful in the prediction of vortex lattices by Abrikosov in 1957 [10] and is still very much used in the calculation of vortex configurations [11]. These equations also give a good understanding of the difference between superconductors of type I and II *via* the introduction of the quantity $\kappa = \lambda/\xi$.

- For $\kappa > 1/\sqrt{2}$ superconductors will be called type I superconductors and will follow the Pippard equation.
- For $\kappa < 1/\sqrt{2}$ superconductors will be called type II superconductors and will follow the London equation. This type of superconductors will present a magnetic field transition called the vortex phase.

1.2.2 BCS theory

In 1957 John Bardeen, Leon Neil Cooper and John Robert Schrieffer published their work [12] in which they propose their microscopic scenario for superconductivity. Their theory stems from the electron phonon interaction described by Frölich [13] and suggested by the isotope effect [14, 15]. A first step was provided by Cooper [16] who studied the problem of adding two electrons to the Fermi sea with a small attracting interaction between those electrons. He showed that the Fermi surface is unstable under such perturbation which tends to diminish the energy of the system.

Based on the Cooper problem that shows that the minimum of energy is obtained in the center of frame of two electrons, Bardeen, Cooper and Schrieffer considered the following reduced Hamiltonian

$$\hat{H}_{BCS} = \sum_{k,\alpha} \varepsilon_k \hat{c}^\dagger_{k\alpha} \hat{c}_{k\alpha} - V \sum_{k,k'} \hat{c}^\dagger_{k'\uparrow} \hat{c}^\dagger_{-k'\downarrow} \hat{c}_{-k\downarrow} \hat{c}_{k\uparrow}. \tag{1.13}$$

An energy cut-off is imposed on V such that it is non zero only for $-\omega_D < E_k < \omega_D$ (with ω_D the Debye energy).

A few things can be said about this equation. First we place ourselves in the center of mass frame. This assumption is justified by the Cooper problem. The second thing that can be said is that the spin is conserved during the interaction and that the concerned spins come with opposite directions. This form comes from the assumption made that the fundamental interaction is of the form $V\delta(\boldsymbol{r})$ which only authorizes electrons of angular momentum $l = 0$ as the Fourier transform of the contact interaction leaves only the s-wave channel to be non-zero while other channels p, d and f give no contribution. This imposes, due to the Pauli principle, that the final state is globally antisymmetric. In all generality for an interaction that conserves the spin we could consider the following Hamiltonian

$$\hat{H} = \sum_{k,\alpha} \varepsilon_k \hat{c}^\dagger_{k,\alpha} \hat{c}_{k,\alpha} - \sum_{k_1,k_2,k_3,k_4,\alpha,\beta} V_{k_1,k_2,k_3,k_4} \hat{c}^\dagger_{k_1\alpha} \hat{c}^\dagger_{k_2\beta} \hat{c}_{k_3\beta} \hat{c}_{k_4\alpha}. \tag{1.14}$$

This more general form is the one that should be used in the case of p-wave superconductivity as can be obtained when spin-orbit interaction is present in the problem. Here again a cut off at the Debye frequency has to be introduced in the precise form of the interaction V_{k_1,k_2,k_3,k_4}.

Starting from the less general Hamiltonian 1.13 and following the idea that the ground state of the system must be written in the form of a coherent state, Bardeen, Cooper and Schrieffer finally found the following wave function

$$|\psi_{BCS}\rangle = \prod_k \left(u_k + v_k \hat{c}^\dagger_{k\uparrow} \hat{c}^\dagger_{-k\downarrow} \right) |0\rangle , \tag{1.15}$$

to which is added the normalization condition

$$|u_k|^2 + |v_k|^2 = 1. \tag{1.16}$$

The form of the wave function 1.15 allows for a physical interpretation of the BCS ground state. It is possible to see this ground state as a superposition of combinations of the Fermi sea ($|0\rangle$) and Cooper pairs ($\hat{c}^\dagger_{k\uparrow} \hat{c}^\dagger_{-k\downarrow} |0\rangle$). A given state $|k\uparrow\rangle$ (or its time reversed $|-k\downarrow\rangle$) is filled with a probability $|v_k|^2$ and empty with a probability u_k^2.

In order to obtain the expression of the terms u_k and v_k, it is necessary to perform a variational calculation to minimize the mean value of the energy of the ground state.

$$E = \langle \psi_{BCS} | \hat{H}_{BCS} | \psi_{BCS} \rangle . \tag{1.17}$$

This approach leads to the introduction of the quantity Δ defined as

$$\Delta = V \sum_k^{\omega_D} u_k v_k. \tag{1.18}$$

The final result for the terms u_k and v_k is the following

$$u_k = \sqrt{\frac{1}{2}\left(1+\frac{\xi_k}{E_k}\right)},$$
$$v_k = \sqrt{\frac{1}{2}\left(1-\frac{\xi_k}{E_k}\right)},$$

where $E_k = \sqrt{\xi_k^2+\Delta^2}$, $\xi_k = \varepsilon_k - \mu$ and $\varepsilon_k = \frac{\hbar^2 k^2}{2m}$.

The quasiparticle states of this system are then obtained by performing a Bogoliubov transformation introducing the fermionic excitation operators $\hat{\gamma}_k$ defined as a linear combination of the electronic operators $\hat{c}$ and $\hat{c}^\dagger$ such as

$$\hat{c}_{k\downarrow} = u_k\hat{\gamma}_k - v_k^*\hat{\gamma}_{-k}^\dagger, \tag{1.19}$$
$$\hat{c}_{-k\uparrow}^\dagger = v_k\hat{\gamma}_k + u_k^*\hat{\gamma}_{-k}^\dagger. \tag{1.20}$$

The $\hat{\gamma}$ and $\hat{\gamma}^\dagger$ operators will then diagonalize the BCS Hamiltonian with energies $\pm E_k$.

The final result is that the density of states of a superconductor is given by

$$\rho(E) = \nu_0 \frac{|E|}{\sqrt{E^2-\Delta^2}}. \tag{1.21}$$

This density of states is represented on Fig. 1.1.b. The term Δ is an energy gap in the excitation spectrum of the superconductor and can be interpreted as the quantity of energy one has to provide in order to break a Cooper pair. Rigorously speaking excitations are always of positive energy, however in the semiconductor model, adding an electron to the system will be written as a positive energy excitations while adding a hole (or removing an electron) will be written as a negative energy excitation.

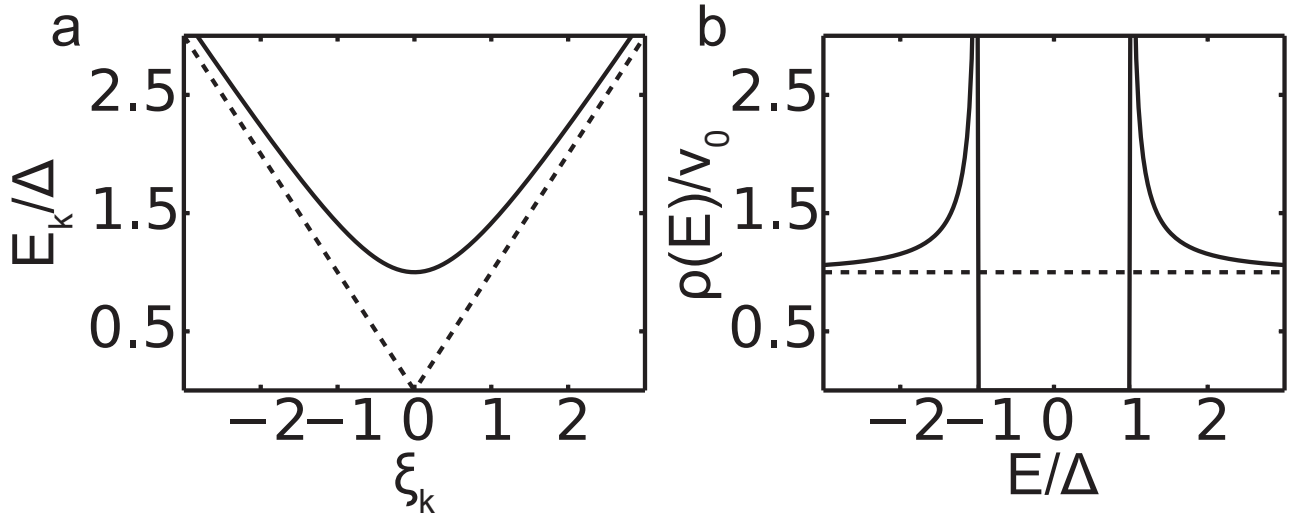

Figure 1.1: **BCS density of states:** a. Relation between E_k and ξ_k. b. BCS quasiparticle excitations density of states as a function of the energy normalized to the value of ν_0, density of states of the normal metal at the Fermi energy. In both figures the dashed lines refer to the case of a normal metal that is effectively recovered in a superconductor for $E \gg \Delta$.

Within the BCS framework the gap temperature dependence can be calculated and in particular we can find the following equation for the self-consistent calculation of the superconducting gap [6]

$$\Delta_k = -\sum_l V_{kl}\frac{\Delta_l}{2E_l}\tanh\frac{\beta E_l}{2}. \tag{1.22}$$

with V_{kl} the strength of the contact interaction defined in eq.1.13.

1.2.3 Bogoliubov-de Gennes approach

A mean field approach of superconductivity is provided by the Bogoliubov-de Gennes approach [17] that was first introduced in order to describe the effect of inhomogeneities in superconductors. The principle is to consider the following Hamiltonian

$$\hat{H}_{BdG} = \sum_{k,\sigma} \varepsilon_k \hat{c}^\dagger_{k,\sigma} \hat{c}_{k,\sigma} + \Delta \sum_k \hat{c}^\dagger_{k\uparrow} \hat{c}^\dagger_{-k\downarrow} + h.c. \tag{1.23}$$

where ε_k is defined for a chemical potential $\mu = 0$. This Hamiltonian is the Hartree-Fock development of the full BCS Hamiltonian. By applying a Fourier transform to the Hamiltonian 1.23 and introducing the following Bogoliubov transformation

$$\hat{\psi}_{\mathbf{r}\uparrow} = \sum_n \left(\hat{\gamma}_{n\uparrow} u_n(\mathbf{r}) - \hat{\gamma}^\dagger_{n\downarrow} v^*_n(\mathbf{r}) \right) \tag{1.24}$$

$$\hat{\psi}_{\mathbf{r}\downarrow} = \sum_n \left(\hat{\gamma}_{n\downarrow} u_n(\mathbf{r}) + \hat{\gamma}^\dagger_{n\uparrow} v^*_n(\mathbf{r}) \right) \tag{1.25}$$

we obtain (see appendix .4) a set of equations for the terms u_n and v_n in real space

$$u_n \varepsilon_n = H_e u_n + \Delta v_n, \tag{1.26}$$

$$v_n \varepsilon_n = -H_e v_n + \Delta^* u_n, \tag{1.27}$$

With H_e the free electronic Hamiltonian.

Another interesting quantity one can compute within the Bogoliubov-de Gennes framework is the value of the gap in an auto-coherent manner. When looking at the problem of an inhomogeneous superconducting gap that can therefore be written $\Delta(\boldsymbol{r})$, one can show [17] that it obeys the following equation derived from eq. 1.22

$$\Delta(\boldsymbol{r}) = V \sum_n v^*_n(r) u_n(r)(1 - 2f_n), \tag{1.28}$$

whith V the contact interaction and f_n the Fermi-Dirac distribution at energy E_n.

The main advantage of writing the Hamiltonian in the form of eq. 1.23 is the possibility to introduce the spinors $\Psi^\dagger(k) = \begin{pmatrix} \hat{c}^\dagger_{k,\uparrow} & \hat{c}_{-k,\downarrow} \end{pmatrix}$ that result in a representation called the Nambu representation [18]. Using these spinors we can rewrite the Hamiltonian 1.23 as (see appendix .4)

$$\hat{H}_{BdG} = \Psi^\dagger(k) H \Psi(k), \tag{1.29}$$

with H a matrix written as (for $\mu = 0$)

$$H = \begin{pmatrix} \varepsilon_k & \Delta \\ \Delta^* & -\varepsilon_k \end{pmatrix}. \tag{1.30}$$

Diagonalizing the Hamiltonian is now only a matter of diagonalizing the matrix H, a task that can be easily performed analytically or numerically. The advantage of this method that we will use later is that when we start to include interactions such as spin-orbit or magnetism and a spatial dependence, the numerical diagonalization can still be easily implemented. Using Fourier transformation it is easily shown that the BCS term in the Bogoliubov-de Gennes Hamiltonian can be rewritten in real space as

$$H_{BdG-BCS} = \Delta \sum_i \hat{c}^\dagger_{i\uparrow} \hat{c}^\dagger_{i\downarrow} + h.c. \tag{1.31}$$

while the kinetic part is written using hopping terms t_{ij} as

$$H_{kin} = \sum_{\langle i,j \rangle} t_{ij} c_i^\dagger c_j. \tag{1.32}$$

It is then still possible to define a Nambu spinor to diagonalize the Hamiltonian in real space. It is worth noting that such formalism introduces a degeneracy of the eigenvalues of the Hamiltonian due to the electron-hole symmetry introduced in the equations.

Another remark can be made when studying a case with Rashba spin-orbit interaction. Because this interaction couples terms of different spins but same $\boldsymbol{k}$ vectors we need to expand our Nambu formalism to a Nambu-Gorkov basis that can be for instance written in the form of the spinors $\Psi_k^\dagger = \begin{pmatrix} \hat{c}_{k\uparrow}^\dagger & \hat{c}_{k\downarrow}^\dagger & \hat{c}_{-k\downarrow} & \hat{c}_{-k\uparrow} \end{pmatrix}$ [19].

In chapter 4 we will make use of Rashba interaction to explain and study topological superconductivity. This interaction is written in its first quantization form as

$$\hat{H}_{Rashba} = \alpha(\boldsymbol{k} \times \boldsymbol{S}) \cdot \boldsymbol{u}_n, \tag{1.33}$$

where S refers to the electronic spin and u_n the axis of the Rashba field that describes the direction along which the spatial inversion symmetry is broken. In the following we will take $\mathbf{u}_n = \mathbf{u}_z$. Let us then consider the same term in its second quantization form

$$\hat{H}_{Rashba} = \alpha \sum_{k,\mu,\nu} \hat{c}_{k,\nu}^\dagger \boldsymbol{k} \times \boldsymbol{\sigma}_\mu^\nu \cdot \boldsymbol{u}_n \hat{c}_k^\mu = \alpha \sum_{k,\mu,\nu} \hat{c}_{k,\nu}^\dagger (k_x \sigma_{y,\mu}^\nu - k_y \sigma_{x,\mu}^\nu) \hat{c}_k^\mu, \tag{1.34}$$

with α the strength of the interaction and σ the 2×2 Pauli matrices. The index μ and ν refer to the spin degree of freedom and in the matrix form of this equation to the row and column of the σ Pauli matrices. Using the Nambu-Gorkov spinors, a Hamiltonian resulting from the addition of a BCS Hamiltonian and a Rashba interaction will be written in its matrix form as

$$H_{Rashba} = \begin{pmatrix} \xi_k & -i\alpha|k|e^{i\theta} & \Delta & 0 \\ i\alpha|k|e^{-i\theta} & \xi_k & 0 & -\Delta \\ \Delta^* & 0 & -\xi_k & -i\alpha|k|e^{i\theta} \\ 0 & -\Delta^* & i\alpha|k|e^{-i\theta} & -\xi_k \end{pmatrix}. \tag{1.35}$$

In this matrix, the angle θ describes the orientation of the vector $\boldsymbol{k}$ such that $k_x + ik_y = |\boldsymbol{k}|e^{i\theta}$.

From this matrix one can directly obtain the eigenvalues of the system in the form of the dispersion relation

$$E_{k,\lambda,\mu} = \lambda \sqrt{\Delta^2 + \mu(\xi_k + k\alpha)^2}, \tag{1.36}$$

where λ and μ are equal to ± 1. This gives 4 different branches : two for the electrons and two for the conjugated solutions of opposite energy (that in both cases will be a mixture of electrons and holes one would consider in the simple semiconductor view).

It is useful to make some remarks concerning the construction of the matrices in the Nambu and Nambu-Gorkov formalism. First, due to the structure of the Hamiltonian and the necessity for it to be hermitian, the matrix describing the Hamiltonian must also be hermitian. When implementing this Hamiltonian numerically, this hermiticity is an easy thing to check by looking at the symmetry of the real and imaginary part of the resulting Hamiltonian (see Fig. 1.2.a and b.). The real part of the H matrix should be symmetric along the diagonal while the imaginary part should be antisymmetric along the same axis.

Secondly the anti-commutation relations of the electronic operators adds another symmetry on the superconductivity terms. Because we have $\hat{c}_{k\uparrow}^\dagger \hat{c}_{-k\downarrow}^\dagger = -\hat{c}_{-k\downarrow}^\dagger \hat{c}_{k\uparrow}^\dagger$ the adjacent terms associated to superconductivity (in orange and blue on fig. 1.2.a) must change signs and we recover the same symmetry as

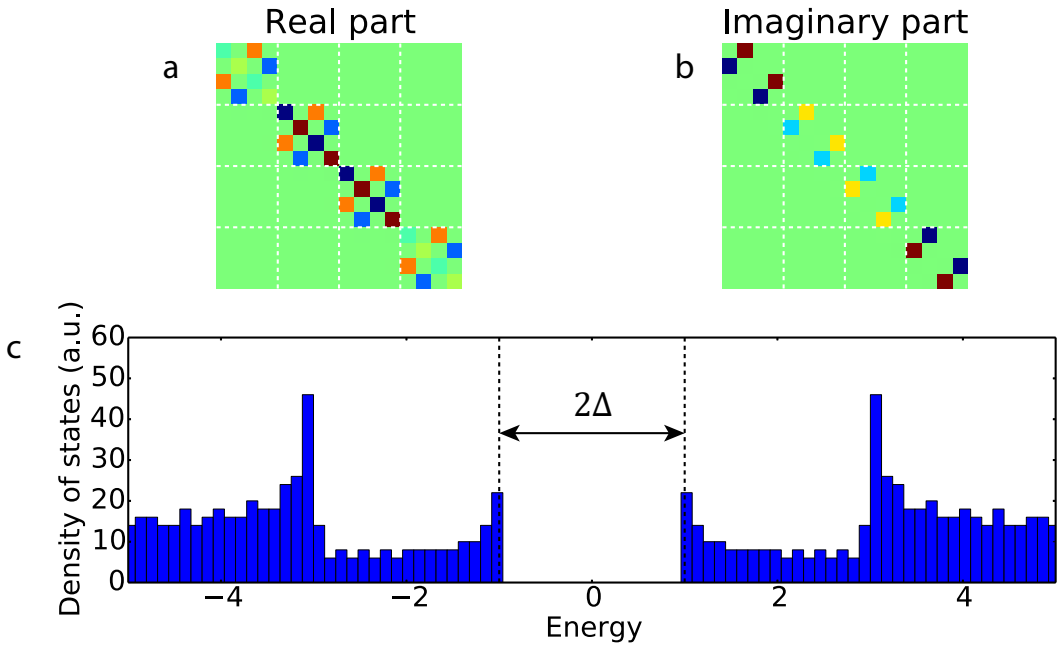

Figure 1.2: **Bogoliubov de Gennes Hamiltonian:** Representation of the real (a) and imaginary (b) part of a Bogoliubov-de Gennes Hamiltonian in the Nambu-Gorkov formalism. Visualizing the Hamiltonian is such forms allows to check its Hermiticity. The color code refers to the numerical value of each term. (In this case we took a real value for the order parameter Δ). c. Density of states obtained by taking a 2D lattice containing 25×25 sites. The dashed lines refers to the value of the superconducting gap Δ.

for the diagonal terms. In this context the real part of the Hamiltonian is therefore fully anti-symmetrical inside each 4×4 blocs along the anti-diagonal direction.

The message is that the commutation rules of the operators describing the system are fully encoded inside the matrix form of the Bogoliubov-de Gennes Hamiltonian. It is therefore often a good idea to start every calculation by checking that those symmetries are present before engaging in any more complex calculation.

On Fig. 1.2.c we show the density of states obtained from an s-wave superconductor in a two dimensionnal Rashba ground state. This figure is actually an histogram of the eigenvalues obtained from the diagonalization of the matrices written in the Nambu Gorkov representation. The two dashed lines on this figure represent the value of the energy gap Δ. Such implementation of superconductivity in a Rashba system is not correct. This is simply due to the fact that in the case of Rashba interaction, we witness the appearance of p-wave superconductivity. This p-wave superconductivity emerges from a modification of the ground state of the system for a phonon mediated electronic interaction in presence of Rashba spin-orbit. The correct term to include inside the Hamiltonian must possess a phase factor dependent on the orientation of the $\boldsymbol{k}$ vector [20]. We will discuss this point more in detail in Chapter 4.

1.3 Scanning tunneling microscopy and spectroscopy

The question we now have to ask is now how we will be able to experimentally probe the superconducting properties of the systems we are interested in. The experimental technique used throughout this thesis is scanning tunneling microscopy (STM) and spectroscopy (STS). This technique was invented in 1986 by Gerd Binnig and Heinrich Rohrer [21] and is based on the tunnel effect. The main idea behind STM is

to consider a fixed sample and a tip moving over the sample without touching it. In this configuration a bias voltage is applied between the tip and the sample that induces a shift between the Fermi levels of the tip and the sample. The conduction electrons from the tip can then tunnel to the sample or the conduction electrons from the sample can tunnel to the tip, depending on the sign of the bias. The tip is controlled in the three spatial directions by different piezoelectrics that allow for a fine control of the position (see Fig. 1.3.a).

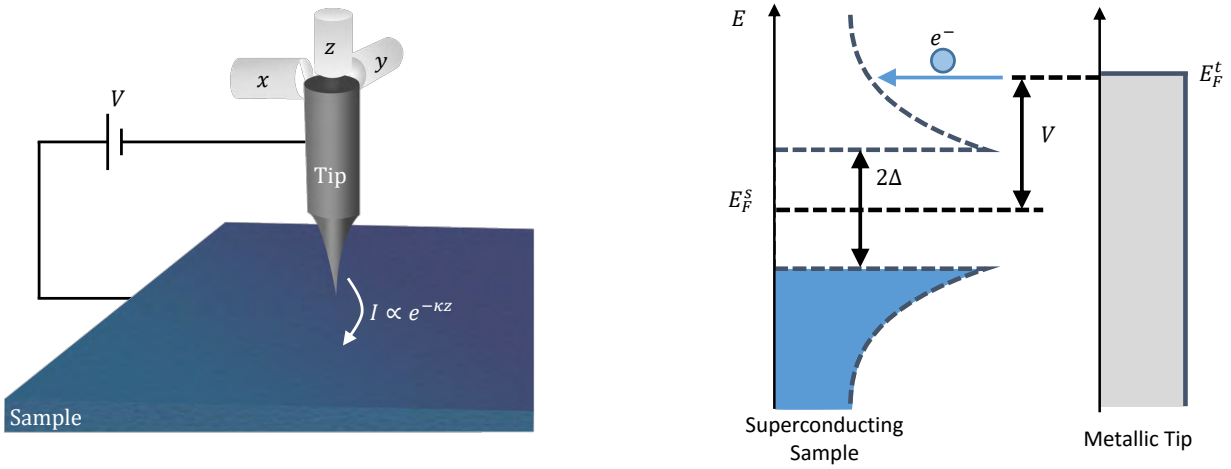

a b

Figure 1.3: **Principle of scanning tunneling:** a. In microscopy mode we measure the electronic current between the sample and the tip from which the distance between these two elements can be obtained. b. In spectroscopy mode, the electrons from the side with the higher chemical potential travel to the other side with a probability linked to the number of states available at the same energy. This mode is called elastic tunneling.

Because the tunneling rate will be dependent on the density of states of both the sample and the tip, STS will be able to probe the electronic properties of the system under study. As we will discuss later, for superconductors the spectroscopy mode will provide information on the local electronic structure of the samples as it was done by Hess et al. [22] for the vortices in $NbSe_2$. The basic principle is to obtain conductance maps color-coded with the intensity of the derivative of the tunneling current (see fig. 1.4). Because the derivative of the tunneling current is directly related to the local density of states, the contrast of the conductance maps provides information on the local electronic structure and in particular is used to image the states (vortex cores, gap fluctuations, bound states...) that might exist inside the superconducting gap.

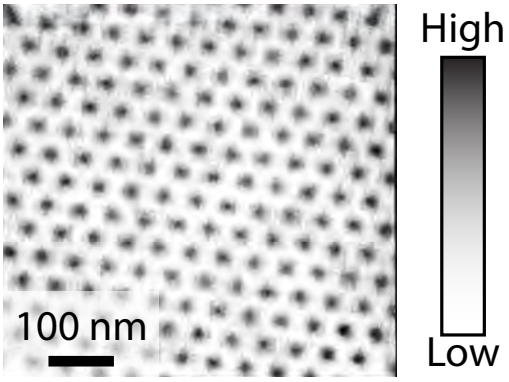

Figure 1.4: **Vortex lattice in 2H-$NbSe_2$:** Abrikosov lattice at 1 T in 2H-$NbSe_2$. Original figure from [22]. The conductance is color-coded in grey scale from low conductance in white (for the superconducting gap) to high conductance in black (for the normal vortex cores).

1.3.1 Topographic measurements

The first and most commonly used mode of scanning tunneling is the microscopy mode. In this mode there

are two possibilities when scanning the surface. The first possibility is to position the tip at constant current using a feedback loop. By measuring continuously the tunneling current the electronic behind the system regulates the extension of the z piezoelectrics in order to recover the current setpoint. The electronic current being exponentially dependent on the distance between the two electrodes, in first approximation the tip stays at a constant height of the surface. When simultaneously measuring the extension $z(x, y)$ of the piezoelectric we obtain the topography of the sample. This mode is called constant current mode microscopy which is the one we will use all along this thesis.

The second mode is called the constant height mode in which the tip stays at the same position along z and is then moved laterally while recording the current. The inconvenient of this technique is that the absence of feedback in the z direction leaves the tip vulnerable to potential obstacles on the surface such as steps or any other types of defects. It is thus only used for flat small areas.

1.3.2 Spectroscopy

Normal tip

The microscopy mode can be combined with a spectroscopy mode that allows to obtain the dependence of the tunneling current as a function of the voltage bias between the tip and the sample. By making the assumption that the density of states of the tip is constant one can show that the derivative of the current with respect to the bias can be written as [23]

$$\frac{dI}{dV} \propto -\int_{-\infty}^{\infty} \mathrm{d}E\rho(x,E)\frac{\partial f_{FD}(E-eV)}{\partial E}. \tag{1.37}$$

with $f_{FD}(E)$ the Fermi-Dirac distribution and $\rho(x, E)$ the local density of states of the sample at the point x in real space. From this expression we observe that at absolute zero the derivative of the current is directly proportional to the density of states (DOS) and does not include any thermal broadening. A direct consequence of this fact is that we will try to work as much as possible at the lowest temperature accessible in order to avoid the broadening of the spectral features in the system we want to probe. Obviously we cannot work at absolute zero and for the case of our STM, working at 300 mK limits the spectral resolution to approximately 100 μeV ($\simeq 3.5k_BT$).

The term $\rho(x, E)$ in equation 1.37 contains matrix elements that tend to privilege certain tunneling channels between the two electrodes. In particular these matrix elements induce a selectivity for k close to 0 that corresponds to slowly decreasing wave-functions in the vacuum.

It was shown by J. R. Schrieffer [24, 25] that in the case of tunneling between a superconductor with a gap Δ and a normal metal one would obtain at zero temperature the following conductance

$$dI_S/dV \propto \left|\mathrm{Re}\left(\frac{V}{\sqrt{V^2-\Delta^2}}\right)\right|, \tag{1.38}$$

namely the BCS density of states. At 0 K the derivative of the Fermi-Dirac distribution is simply a distribution $\delta(E)$ and thus only leaves in eq. 1.37 the density of states.

Superconducting tip

Another possibility for scanning tunneling spectroscopy is to use a superconducting tip. In this case, the tip S_1 possesses a gap Δ_1 and in the case that we will study later, this gap is larger than the gap Δ_2 of the sample[2]. This configuration is presented on fig. 1.5.a. In order for electrons to tunnel from one electrode to the other, the Fermi level from one electrode has to be shifted at the minimum by the sum

[2]We will present STS measurements using a superconducting tip on a Pb monolayer. In this configuration the tip will have almost the same gap as bulk Pb ($\simeq$ 1.3 meV) while the monolayer only has a gap of a few tenth of meV. At 300 mK, no electron can be promoted to positive energy states by thermal activation and thus we will not observe zero bias conductance at this temperature.

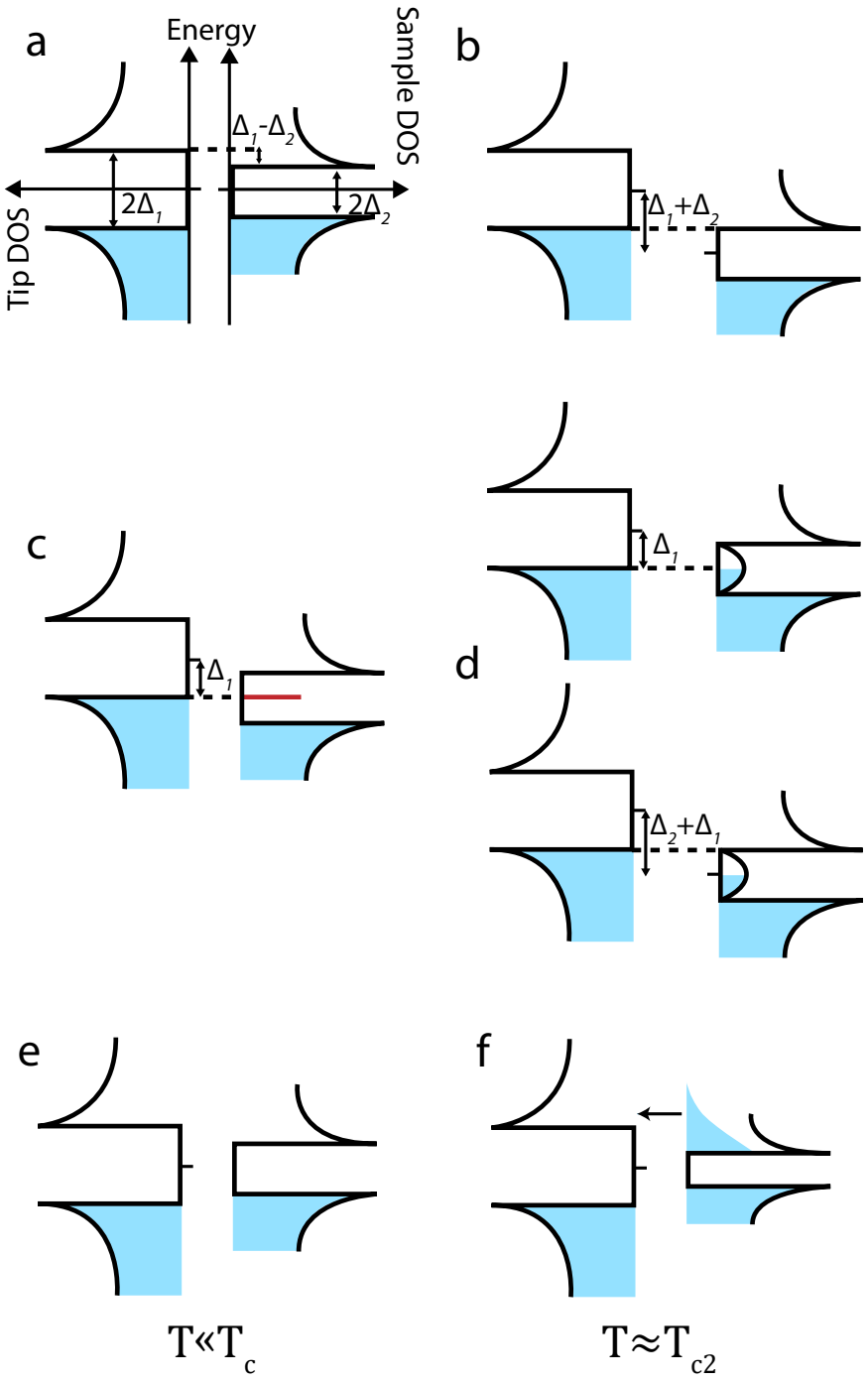

Figure 1.5: **Scanning tunneling spectroscopy using a superconducting tip at $T = 0$:** a. We consider a superconducting tip with a gap Δ_1 and a superconducting sample with a gap $\Delta_2 < \Delta_1$. b. In the absence of in-gap states the tunneling is only possible for $E_{\text{bias}} = \Delta_1 + \Delta_2$. c. For an in-gap state at $E = 0$ the tunneling is allowed at $E_{\text{bias}} = \Delta_1$. d. For a continuum of states around the Fermi level, for a given bias sign, the electrons can only tunnel to half of the continuum for $E_{\text{bias}} \in [\Delta_1, \Delta_1 + \Delta_2]$. e. At temperatures small compared to the critical temperature of the sample no electronic current can occur at 0 bias. f. However for T smaller and of the order of T_c the thermal broadening caused by the Fermi-Dirac distribution leads to the occupation of states on the other side of the superconducting gap and thus to the possibility for electrons to tunnel from sample to tip even at 0 bias.

of both gaps $\Delta_1 + \Delta_2$ (fig. 1.5.b). At this point electrons will tunnel from the quasiparticle peak energy of one electrode to the quasiparticle peak energy of the other electrode.

At sufficiently low temperature, the Fermi-Dirac distribution does not leak from negative energies to positive energies an thus the resolution of the spectroscopic measurements is not limited by the thermal broadening and is even enhanced by the sharp decrease at the coherence peaks of the superconducting gaps. As shown on fig. 1.5.f, for $T \approx T_{c_2}$ but still below T_{c2}, thermal broadening fills states at positive energy above the gap. In this case the convolution of the density of states of the two electrodes produces states at zero bias.

If we now consider a zero-bias in-gap state in our sample (like expected for a Majorana bound state for instance), as shown on fig. 1.5.c, the minimal bias at which electrons will be able to tunnel for S_1 to S_2 will correspond to the gap of the tip Δ_1. If this state is perfectly isolated we will obtain a sharp peak in the DOS at exactly Δ_1 with a width relative to the intrinsic width of the tip quasiparticle peaks at $T = 0$ K. However if we are looking at a continuum of states or a dispersion of in-gap states (fig. 1.5.d) things are slightly different. The lowest energy at which the electrons will be able to tunnel will also be Δ_1 due to the fact that states at lowest energy are filled and electrons cannot tunnel into them. However for any larger bias electrons will freely tunnel. In the case of an in-gap distribution of states (see fig. 1.5.d) a superconducting tip will thus allow to visualize half the states (below the Fermi level) at positive bias and half the states (above the Fermi level) at negative bias. The states of the continuum will be observed in the intervals $[\Delta_1, \Delta_1 + \Delta_2]$ and $[-(\Delta_1 + \Delta_2), -\Delta_1]$. This is only valid at $T = 0$ K as temperature effects would affect the electronic distribution around the Fermi level and allow a partial filling of the states leading to a spectroscopic signal in between these two intervals.

Let us be more precise and consider the general expression for the tunneling current between the tip (T) and the sample (S)

$$I(V) \propto \int dE \left[f(E - eV) - f(E)\right] N_T(r_0, E - eV) N_S(r_0, E) T(r_0, eV). \tag{1.39}$$

In this equation, the function $f(E)$ refers to the Fermi-Dirac distribution, $N_{S,T}$ to the density of states of the sample and tip respectively and T to the matrix elements. We consider a tip with a superconducting gap Δ_T and a sample with a gap Δ_S as presented on fig. 1.6.a. The development of this expression shows that (if ignoring the tunneling matrix elements) one can rewrite this expression in the form of the difference of two convolution products.

$$I(V) \propto (fN_T \otimes N_S)(eV) - (N_T \otimes fN_S)(-eV). \tag{1.40}$$

In fig. 1.6 we present the results of such calculation for a tip with a gap Δ_T such that the gap of the sample $\Delta_S < \Delta_T$. On figs. 1.6.a and b. we first treat the case of tunneling at two different temperatures (respectively 25% and 50% of the superconducting gap of the sample). The first effect that one witnesses is the appearance of peaks in the conductance inside the gap at energies equal to $\pm(\Delta_T - \Delta_S)$. The presence of these peaks is explained by a temperature effect and they are absent when the temperature is low enough. Because of the Fermi-Dirac distribution, at finite temperature there exists some occupied states at $E > \Delta_S$ from which electrons are able to tunnel to the empty states of the tip for a bias that would bring the quasiparticle peaks of the sample to the level of the quasiparticles peaks of the tip, thus exactly $\Delta_T - \Delta_S$. The same thing appears at negative bias when the situation is reversed. The main gap originates from the case discussed in fig. 1.6.b where, without taking into account any thermal effect, the empty states of the tip are brought in front of the filled state of the sample for a bias $eV = \Delta_S + \Delta_T$. This case corresponds to the one described schematically on fig. 1.5.b. It is interesting to notice that unlike what was observed in the case of a normal tip, temperature does not have any effect on the sharpness of these peaks but only on the temperature. This fact is illustrated on figs. 1.7 where we have computed the conductance at 5% and 50% of the sample gap (respectively figs. a. and b.) for both a superconducting tip (in blue) and a normal one (in green). The thermally induced broadening of the conductance does not

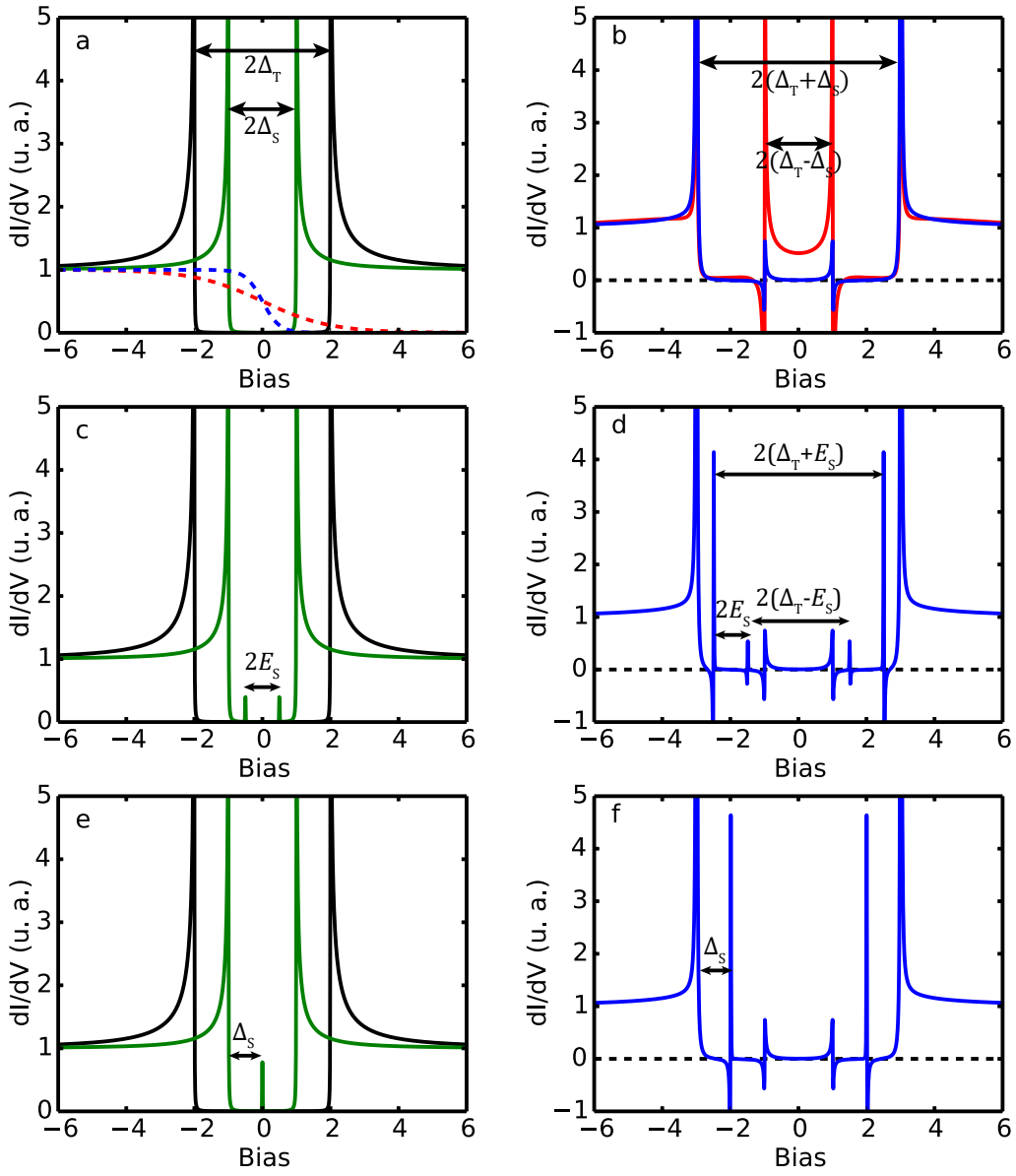

Figure 1.6: **In-gap states and temperature effects on a superconducting tip:** a. We consider a tip with a BCS DOS and a gap Δ_T and a sample with a BCS DOS and a gap Δ_S whose spectra are represented respectively in black and green. The red and blue dashed lines corresponds to two thermal configurations for the Fermi-Dirac distribution. b. Spectra resulting from the tunneling between a tip and a sample in the configuration presented in a. where the blue and red colors refer to the colors of the Fermi-Dirac distributions. c. Case of two in-gap states at energies $\pm E_S$. d. Resulting conductance spectra at low temperature (blue Fermi-Dirac distribution from a.). e. Case of one in-gap state at the Fermi-level. d. corresponding spectra at low temperature (blue Fermi-Dirac distribution from a.).

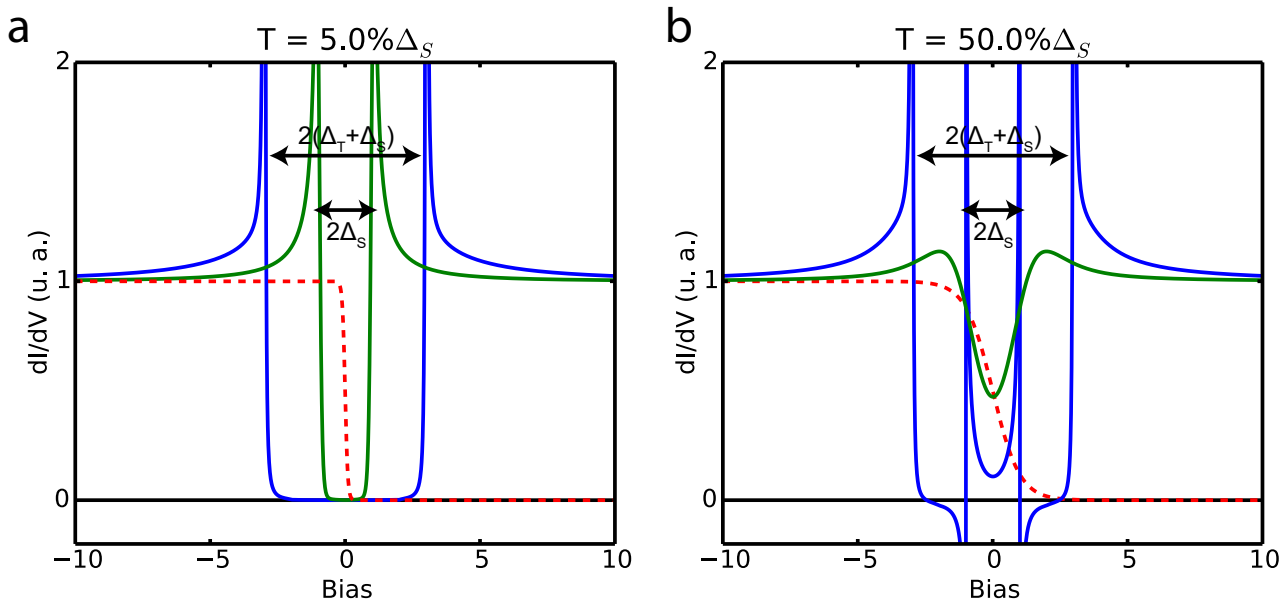

Figure 1.7: **Temperature dependence for SIS and SIN configurations:** a. Comparison of the conductance obtained by tunneling from a superconducting tip (blue) or a normal one (green) for a temperature $T = 5\%\Delta_S$. Same for $T = 50\%\Delta_S$. The gap values Δ_S and Δ_T used in this calculation are the same as the one used for fig. 1.6

exist when using a superconducting tip as the only width a peak might possess arises from the intrinsic width of the quasiparticle peaks of the tip.

As we will discuss in-gap states in the next chapter, we computed on fig. 1.6.d the expected conductance at a temperature equivalent to 25% of the sample gap, of a sample possessing a pair of in-gap states at energies $\pm E_S$. The in-gap thermal peaks discussed in the previous paragraph are still present and on top of these we observe two pairs of peaks at energies $\pm(\Delta_T + E_S)$. The larger peaks at $\pm(\Delta_T + E_S)$ correspond to a configuration in which the bias is adjusted in order to make coincide the filled (emptied) in-gap state with the empty (filled) quasiparticle peak of the tip. Due to thermal effects the empty (occupied) states at zero temperature get occupied accordingly to the Fermi-Dirac distribution and are themselves able to create a current that produces peaks in the conductance at energies $\pm(\Delta_T - E_S)$. The amplitude of these secondary peaks is much smaller than the principal ones as their filling is only ensured by the tail of the Fermi-Dirac distribution. One should note that unlike what is to expect with a normal tip, in this configuration in-gap states are seen in the conductance curve in the form of peaks coming hand in hand with a dip of negative conductance. This negative conductance comes from the divergence in the BCS density of states at the energy of quasiparticle peaks from which electrons will tunnel to in-gap states. Tunneling between in-gap states and quasiparticle peaks does indeed lead to a current larger than the one obtained by tunneling from in-gap states to the continuum of the tip for $|V| > \Delta_T$. At one point a decrease in the tunneling current is thus to be expected. This decrease will translate as a negative conductance in the dI/dV curves.

Finally, on fig. 1.6. e. and f. we present the case of an in-gap state at zero-energy (such as a Majorana peak for instance). In this last configuration, the two pairs of peaks discussed in the previous paragraph merge together and only leave a single pair of states at energies Δ_T. This case corresponds to the one schematically described in fig. 1.6.c.

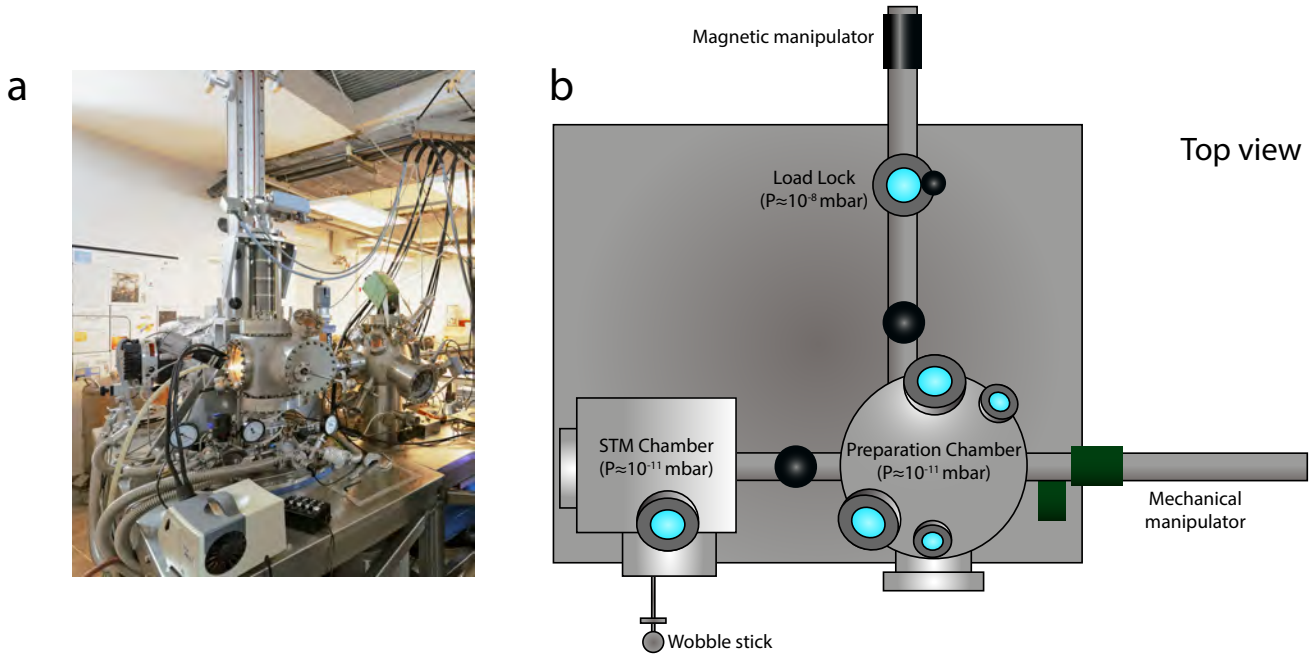

Figure 1.8: **The M3 microscope on which were performed all the STM and STS measurement presented in this thesis:** a. Picture of the experimental setup. b. Top-view scheme of the setup.

1.3.3 M3 microscope

All the measurements presented in this thesis were performed on the M3 STM at the INSP (Fig. 1.8). This STM is a home-built STM working at a minimum temperature of 300 mK at a base pressure of 10^{-11} mbar with the possibility to apply a magnetic field up to 7 T.

The system is constituted of two main parts: the STM chamber and the preparation chamber. The sample is introduced *via* a load lock at a minimal pressure of around 2.10^{-8} mbar. The Pb monolayers used in this thesis were prepared into the preparation chamber under high vacuum by means of molecular beam epitaxy (MBE). The evaporator possesses three cells and in addition to Pb we can also deposit Co and Cr. The quantity of material deposited by MBE is calibrated using a quartz microbalance (see fig. 1.9).

The samples are then directly transferred into the STM chamber for measurement without encountering a pressure over 10^{-10} mbar. The Si samples used for the preparation of the Pb monolayers were also prepared prior to the Pb deposition inside the preparation chamber by direct current heating as we will describe more precisely in chap. 4. This possibility to prepare our samples in such conditions allows for a very small contamination of the surface and therefore very clean samples.

The cryogenic part of the microscope is accessed from the STM chamber by lowering the STM inside the cryostat. The temperature of 300 mK is then obtained by means of ^{3}He condensation. The condensation process is limited in time by the quantity of ^{3}He available. The characteristic time one can expect from this apparatus is around 40 hours. As a consequence the maximum experimental time possible for one measurement without thermal variation is of the order of 37 hours when taking into account the time needed to stabilize the tip and to check the scan area beforehand.

For all the STM/STS experiments presented here we used tips made from Pt/Ir wire soldered into tip-holders before being mechanically sheared by hand. The tips were then placed inside the preparation chamber in order to be outgassed at 300°C before using them.

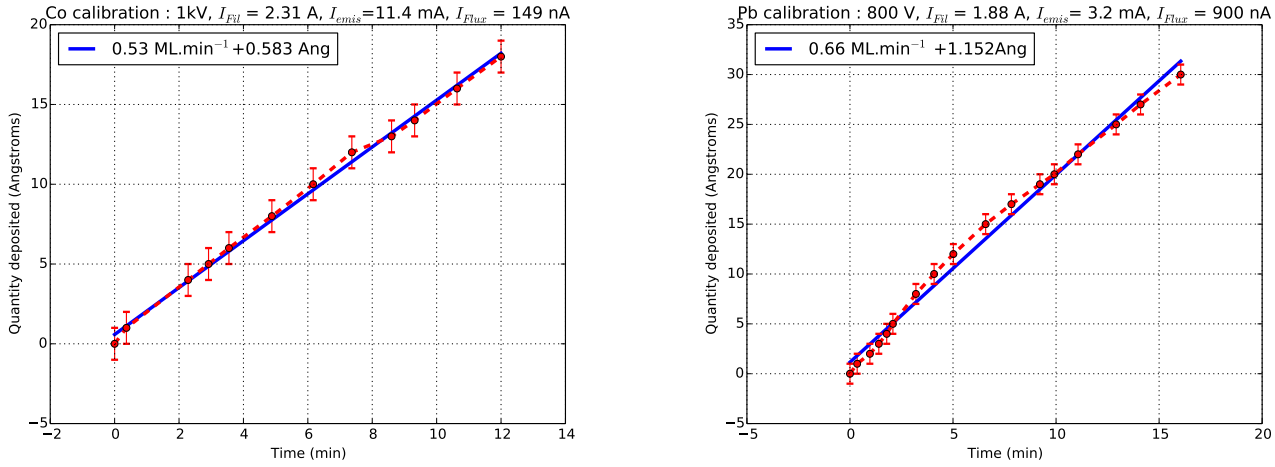

a b

Figure 1.9: **Calibration of sources for evaporation:** a. Calibration curve of the Co source showing the stability in time of the flux. b. Same curve for the Pb evaporator.

The scanning area on the sample is controlled by two sets of piezoelectric tubes controlling the rough and fine motion of the tip respectively. The rough motion allows for a XY movement around the whole surface of the sample and a Z movement allowing for a rough approach of the surface by eye. The fine motion is then able to scan a maximum size of around 6 μm in X and Y direction and 1 μm in the Z direction at room temperature. The approach of the tip to the surface is controlled by using both rough and fine movement along the Z direction.

Temperature modifies the response of piezoelectric tubes to an applied electrical potential. The X, Y and Z calibration of the STM must therefore be modified with the temperature. The consequence of this is a reduction of the available measurement area. For instance, when scanning at 300 mK the correction factor compared to room temperature is of 0.415 that limits the area accessible by the tip to 1200×1200 nm^2. The whole system is controlled by the Matrix electronic from Omicron which allows for a simultaneous topographic and spectroscopic acquisition. The measurement is performed by alternatively measuring a topographic point and a spectrum. The two sets of data are obtained with different voltages and current setpoints. This difference in parameters introduces an additional measurement time needed to guarantee a good stabilization of the tip after the different voltage ramps.

The topographic measurements performed here were all obtained in constant current mode with a typical voltage gap of 50 mV and a current setpoint of 40 pA. The spectroscopic measurements were performed with a typical voltage gap of 5 mV and a current setpoint of 120 pA.

1.3.4 Data analysis

The data obtained on the M3 microscope are processed *via* a simple program I wrote using the Python language.

Topographic data

The raw topographic data often comes with a slope that has to be corrected in order to correctly interpret our results. The slope is subtracted on every topographic line by means of a linear fit.

Some artifacts can appear from such procedure. For instance a defect in the surface of an ill-placed step can give rise to discontinuity along the y-axis but these effects can be suppressed easily by either

restricting ourselves to some part of the image for a reference slope or calculating the global slope of the scanned area in 2D.

Spectroscopic data

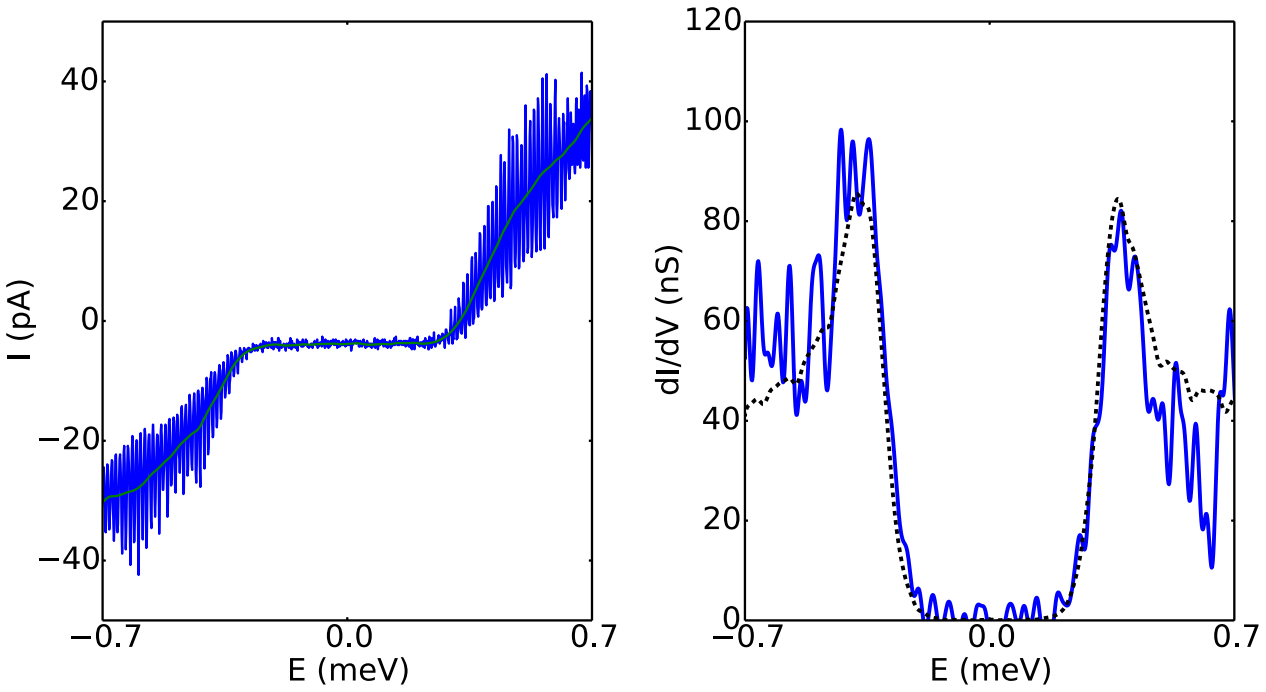

Figure 1.10: **Smoothing and derivation procedure:** On the left panel we present the superposition of a single raw spectrum (blue) with a spectrum smoothed using the Savitzky-Golay procedure (green). These spectra contain 1200 points and were obtained at 300 mK. On the right panel we present the derivative of the same spectrum using once again the Savitzky-Golay procedure. The dashed spectrum corresponds to the spectrum averaged over 500 spectra.

The main kind of spectroscopic data we acquire in our experiments is the signal $I(V)$. By taking the derivative of this signal we can obtain the local density of states (**LDOS**). The procedure by which we obtain the derivative $dI(V)/dV$ must be carried out in a clean way due to presence of noise in the raw signal. The presence of noise is due to the experimental constraint of the ^{3}He condensation time. Because we have 37 hours for a measurement, we must divide this time between the topography measurement and the spectroscopy measurement. A topography lasts typically between 3 and 8 hours, depending on the size of scanning area. This leaves about 30 hours of spectroscopy measurement. For a well spatially resolved map of 256× 256 points we are only allowed to a spectrum every 1 or 2 seconds. This would leave an irreducible noise even with a very stable tip.

We proceed by first smoothing the data using a Savitzky-Golay filter [26]. The principle of this procedure is to perform the derivation by using a convolution of our data with a list of well known coefficients. This type of derivation has the effect of averaging over the noise by acting as a quadratic or cubic polynomial filter. The only parameter of this type of procedure is the size of the list used for the convolution that corresponds to an effective convolution over a discrete number of points in the spectra equal to this list size. This size depends on the noise present on the data and we typically use a size that stays smaller than the thermal broadening of the density of states of $3.5k_BT$. We give an example

of a single spectrum mesured in 1.3 s before and after performing the smoothing procedure on Fig. 1.10 with 1000 points between -0.7 and 0.7 mV. In order to correctly normalize the set of spectra we measure in a conductance map we need to be able to have an energy window large enough in order to include not only the superconducting gap but also the side part of the spectra on which the density of states is approximately constant. This allows us to compare the spectra between themselves and correctly evaluate the density of states without being bothered by the local features induced by superconductivity.

While one individual spectrum may stay quite noisy, by averaging over a few spectra the non-coherent noise can be easily suppressed and we thus obtain clean spectra (i.e. representative of the probed area).

The origin of the noise can be diverse. The most common origin is the environment and the mechanical vibrations from talking in the room, loudly closing the doors in the corridor, the different construction works on the campus or the nearby subterranean train. The second type of noise we have on our signal comes from electromagnetic perturbations. The main frequency we have in our system is a frequency around 38 Hz induced by the 1K pot.

Once the derivative of the data has been collected into a single object we can play with it and perform different operations depending on what we want to show. For instance our program allows us to perform cuts through the data in order to extract a position and energy dependent LDOS map. It is also possible to average the spectra over a chosen area of our data set. Combining these tools and the different image processing methods (such as gaussian or median filters) allows for a large variety of possibilities and ways to represent the relevant information extracted from our measurements.

Chapter 2

Magnetic impurities in a superconductor

2.1 Introduction

As we have seen in the introductory chapter, the BCS theory describes superconductivity by means of couples of electrons forming Cooper pairs. The nature of the electrons forming these pairs is highly dependent on the considered system but the simplest and best understood case one can obtain is an s-wave superconductor in which the electrons forming the Cooper pairs possess opposite spins $(\uparrow, \downarrow)$. The Anderson theorem [27, 28] states that in the case of such s-wave superconductor, only time reversal symmetry breaking interactions can induce in-gap states. Thus non magnetic impurities will not give any spectroscopic signature within the superconducting gap while magnetic ones will. Because the electrons inside a Cooper pair are of opposite spins, the interaction they experience leads to a Zeeman effect that tends to destroy the pair.

In this chapter we will discuss the theoretical aspects of the interaction of superconductors with magnetism. First we will look at how a random assembly of magnetic impurities affects the superconducting condensates in the framework of the Abrikosov Gor'kov theory [29]. After that we will study in details the Yu-Shiba-Rusinov (YSR) states [30, 31, 32] which are created by localized single impurities in a superconductor. We will review the different assumptions of the model and solve exactly the eigen-energy equation and study the form of the associated wave-function depending on the dimensionality of the system. Finally in the last part of this chapter we will briefly discuss the so-called 'impurity problem' in a normal metal in relation to the Kondo effect [33]. From this we will extract the necessary information to understand the difference between a classical and a quantum impurity. A review of the effect of impurities in superconductors can be found in [34].

2.2 Abrikosov Gor'kov theory of dilute magnetic impurities in a superconductor

The study of the interaction of magnetic impurities with superconductors was first introduced in the seminal work of Abrikosov and Gor'kov in 1961 [29] and later continued in many other papers both theoretically [35, 36, 37, 38, 39] and experimentally [40, 41, 42, 43]. The goal of this research is to study the mean effect of a given density of impurities over the density of states of the materials in which they are embedded. The Hamiltonian to add to the BCS Hamiltonian can be written as

$$H_{imp} = \sum_i \{v_1(\boldsymbol{r} - \boldsymbol{R}_i) + v_2(\boldsymbol{r} - \boldsymbol{R}_i)\boldsymbol{S}_i \cdot \hat{\boldsymbol{s}}\}, \tag{2.1}$$

where the sum is performed over all impurities with spin $\hat{\mathbf{S}}_i$ in the system. The first term is a simple non magnetic diffusion potential with no effect on the spin of electrons and simply depends on the distance from the impurity i. This terms diffuses spins $\uparrow$ and spins $\downarrow$ in the same way. The second term is

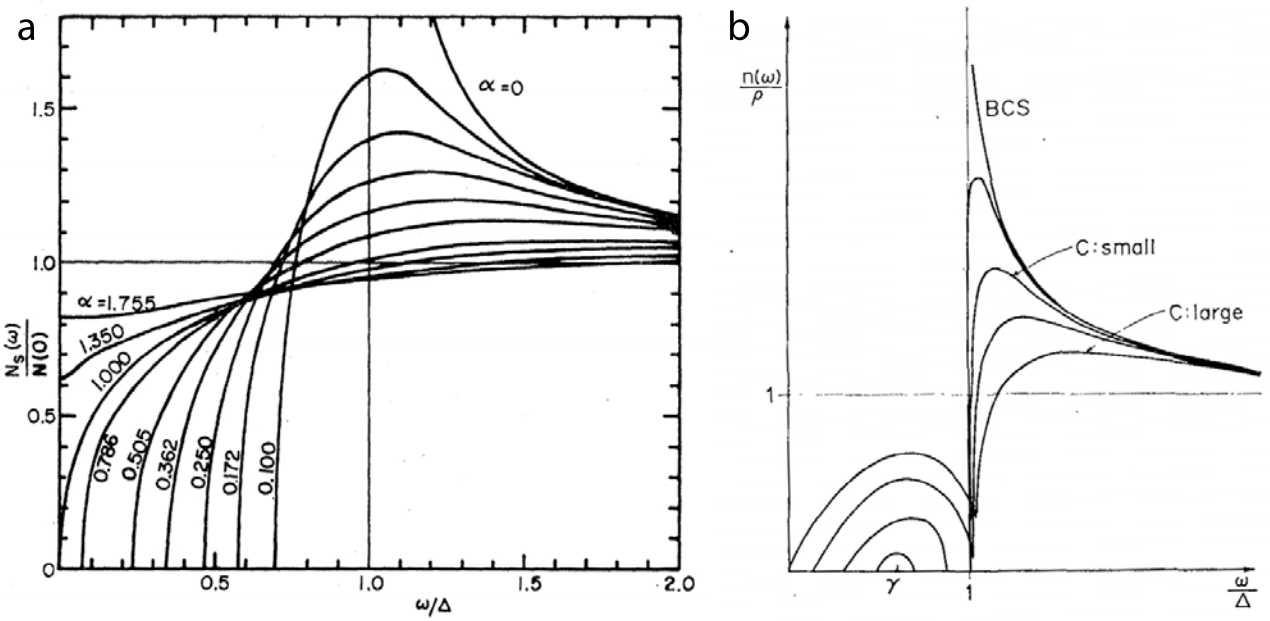

Figure 2.1: **Density of states in the Abrikosov-Gor'kov theory:** a. Density of states of a superconductor with a finite density of random magnetic impurities as the function of energy. The parameter α controls the density and strength of the magnetic impurities (original figure from [44]) b. Qualitative density of states of a superconductor with random magnetic impurities showing the growth of an in-gap impurity band (original figure from [30])

the spin diffusion term and in all generality the spin of the impurities $\mathbf{S}_i$ must be considered in its operator form. However in the case of a large spin we can use the classical spin approximation in which the impurity moment can be considered fixed with no internal degrees of freedom. This term causes a Zeeman splitting of the paired electrons. The main assumptions of the Abrikosov-Gor'kov theory are the absence of correlation between the impurities and the classical nature of their spins. This can be translated mathematically as $\langle S \rangle = 0$ (covering the random orientation of the spins of the impurities) and $\langle S_i S_k \rangle = \frac{1}{3} S(S+1)\delta_{ik}$ (covering the absence of correlation between two impurities i and k).

The second approximation of this theory consists to place the calculation in the framework of the lower order Born approximation. This approximation means that the impurity density is small enough to avoid coherent diffusion of electrons by multiple impurities. In this approximation, the self-energy can be written for the diffusive part as

$$\Sigma = n^i \int \frac{d^3k}{(2\pi)^3} v_1(\boldsymbol{k}, \boldsymbol{k}') \tau_3 \mathcal{G}(k') \tau_3 v_1(\boldsymbol{k}, \boldsymbol{k}'),$$

with n^i the impurities density and $\mathcal{G}(k')$ the Green's function of the system. The magnetic part is similar to the diffusive part except for the term $\boldsymbol{S} \cdot \hat{\boldsymbol{s}}$ that should be taken into account.

From this self-energy it becomes possible to compute the density of states as well as the superconducting order parameter. The result obtained by Abrikosov and Gorkov is that the critical temperature of the superconductor evolves with the concentration of magnetic impurities. For a low concentration of impurities, they obtain a linear evolution of the critical temperature

$$T_c = T_{c0} - \frac{\pi}{4\tau_s}, \tag{2.2}$$

while at higher concentration, they obtain the following expression

$$T_c^2 = \frac{1}{\pi\tau_s^2} \ln \frac{\pi T_{c0}\tau_s}{2\gamma}. \tag{2.3}$$

In these expressions, τ_s is the characteristic diffusion time which is inversely proportional to the concentration of impurities and is directly related to the characteristic non magnetic and magnetic diffusion times (resp. τ_1 and τ_2). From these asymptotic behaviors one can deduce a critical concentration ρ_{cr} for which the critical temperature of the material is 0 and therefore when superconductivity is destroyed (see appendix 7.5).

Before completely closing the gap at the critical concentration, the density of states of an Abrikosov-Gorkov system is strongly modified, as shown on fig. 2.1.a. For low concentration of impurities, the first effect of magnetic disorder is to weaken the quasiparticle peaks. This diminution of the amplitude of quasiparticle peaks reveals the loss of coherence of the macroscopic superconducting wave function due to the random scattering and pair-breaking induced by the magnetic disorder. The second effect induced by magnetic disorder is a gap filling effect that will ultimately lead to gapless superconductivity (at which the gap in the excitation energy spectrum zero despite maintaining pair correlations and non zero transition temperature) before reaching the critical concentration described above. The qualitative growth of the impurity band inside the gap is shown on fig. 2.1.b.

In the case of magnetic impurities coupled between themselves with a variable magnetic strength ($1/\tau_s \neq$ Cte), the Abrikosov Gor'kov is slightly modified [36]. In this case an impurity band appears inside the gap at the energy corresponding to the magnetic coupling between electrons and impurities. The spectral weight associated to this band grows in intensity with the strength of the interaction as shown on fig. 2.1.b. This case is the limiting case of a distribution of Shiba bound states that will be discussed in the next section.

2.3 Yu-Shiba-Rusinov states

2.3.1 Assumptions

Instead of an assembly of randomly dispersed magnetic impurities we now go and look at an isolated impurity. In the Abrikosov-Gorkov configuration, an ensemble of individual and non correlated spins lead to the destruction of superconductivity after a critical concentration (Fig 2.2 top). We will now look at the case where impurities are sufficiently spatially separated to avoid the superposition of the perturbations they are associated to (Fig 2.2 bottom).

We still consider a classical spin for the impurity and in addition to the magnetic coupling J, we allow the possibility to include a non magnetic interaction of strength K. The interaction Hamiltonian H_{Imp} can therefore be written as

$$\hat{H}_{Imp} = -\frac{JS}{2}(\hat{c}_{0\uparrow}^\dagger \hat{c}_{0\uparrow} - \hat{c}_{0\downarrow}^\dagger \hat{c}_{0\downarrow}) + K(\hat{c}_{0\uparrow}^\dagger \hat{c}_{0\uparrow} + \hat{c}_{0\downarrow}^\dagger \hat{c}_{0\downarrow}) \tag{2.4}$$

Because we will consider that the interaction with the impurity is mostly localized at the impurity center, the diffusion potential $V(r)$ is approximated as $\delta(r)$ and this leads to the use of the electronic operators $\hat{c}_0$ and $\hat{c}_0^\dagger$ where the index 0 refers to the site of the impurity. This interaction is superimposed to the mean-field BCS Hamiltonian written as

$$\hat{H}_{BCS} = \sum_k \left\{ \xi_k(\hat{c}_{k\uparrow}^\dagger \hat{c}_{k\uparrow} + \hat{c}_{k\downarrow}^\dagger \hat{c}_{k\downarrow}) + \Delta \hat{c}_{k\uparrow}\hat{c}_{-k\downarrow} + \Delta^* \hat{c}_{-k\downarrow}^\dagger \hat{c}_{k\uparrow}^\dagger \right\}. \tag{2.5}$$

A discrepancy appears when it comes to the spaces in which we treat the problem. The magnetic and diffusive potentials are indeed better expressed in real space while the BCS Hamiltonian is more naturally written in reciprocal space. As we will later use a tight binding calculation to compute the density of

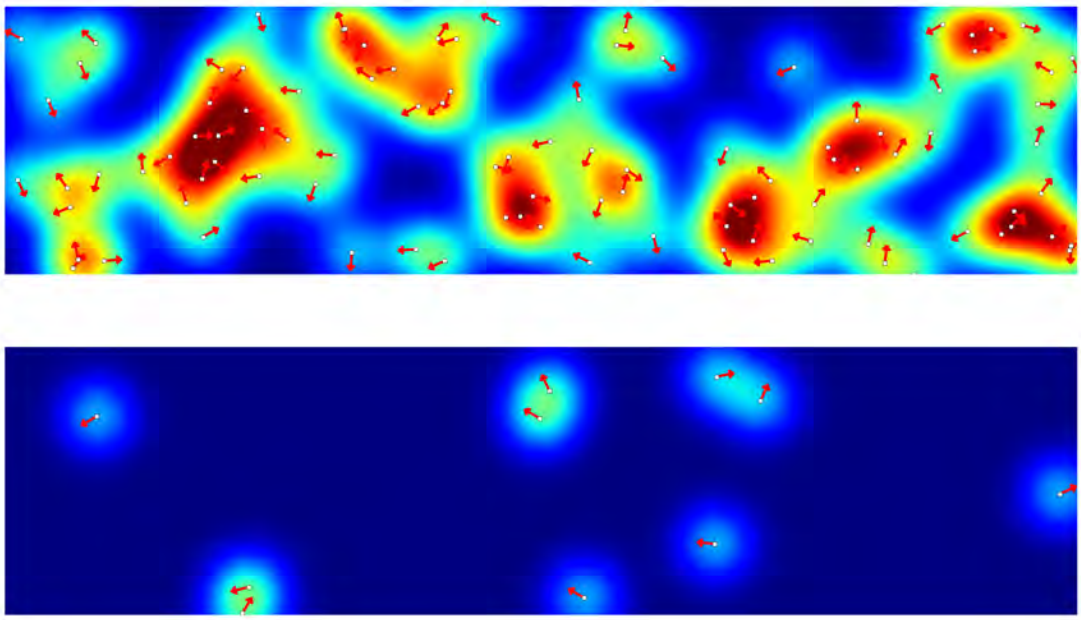

Figure 2.2: **Abrikosov Gorkov to Shiba :** Conceptual view of the transition between the Abrikosov-Gorkov (top) and Shiba (bottom) limits.

states associated to the magnetic atoms in 2H-$NbSe_2$ we will homogenize the spaces in which we are working and transform the BCS Hamiltonian in the r representation. The first part of the Hamiltonian will be obtained in the form of a tight binding Hamiltonian where the $t_{i,j}$ coefficients will be derived from *ab-initio* DFT calculations fitting the ARPES data. The BCS interaction will be simply rewritten by noting that the Fourier transform of $c_{k\downarrow}c_{-k\uparrow}$ is simply $c_{i\downarrow}c_{i\uparrow}$ and finally we can write for the full Hamiltonian containing both superconductivity and magnetic and non-magnetic interaction

$$H_{BCS} = \sum_{i,j} t_{ij}\hat{c}_i^\dagger \hat{c}_j + \sum_i \left(\Delta \hat{c}_{i\uparrow}^\dagger \hat{c}_{i\downarrow}^\dagger + \Delta^* \hat{c}_{i\downarrow}\hat{c}_{i\uparrow}\right) - \frac{JS}{2}(\hat{c}_{0\uparrow}^\dagger \hat{c}_{0\uparrow} - \hat{c}_{0\downarrow}^\dagger \hat{c}_{0\downarrow}) + K(\hat{c}_{0\uparrow}^\dagger \hat{c}_{0\uparrow} + \hat{c}_{0\downarrow}^\dagger \hat{c}_{0\downarrow}). \tag{2.6}$$

In order to simplify this expression Δ will often be chosen real.

2.3.2 Eigenstates

The energies of the YSR states are found using a Bogoliubov transformation (see Appendix .4). The principle of this transformation is to find a diagonalization of the full Hamiltonian in the form

$$H = E_g + \sum_{n,\sigma} \varepsilon_n \hat{\gamma}_{n\sigma}^\dagger \hat{\gamma}_{n\sigma}, \tag{2.7}$$

where the operators $\hat{\gamma}$ are defined as follows

$$\hat{\psi}_{\boldsymbol{r},\uparrow} = \sum_n \left(\hat{\gamma}_{n,\uparrow} u_n(\boldsymbol{r}) - \hat{\gamma}_{n,\downarrow}^\dagger v_n^*(\boldsymbol{r})\right), \tag{2.8}$$

$$\hat{\psi}_{\boldsymbol{r},\downarrow} = \sum_n \left(\hat{\gamma}_{n,\downarrow} u_n(\boldsymbol{r}) + \hat{\gamma}_{n,\uparrow}^\dagger v_n^*(\boldsymbol{r})\right). \tag{2.9}$$

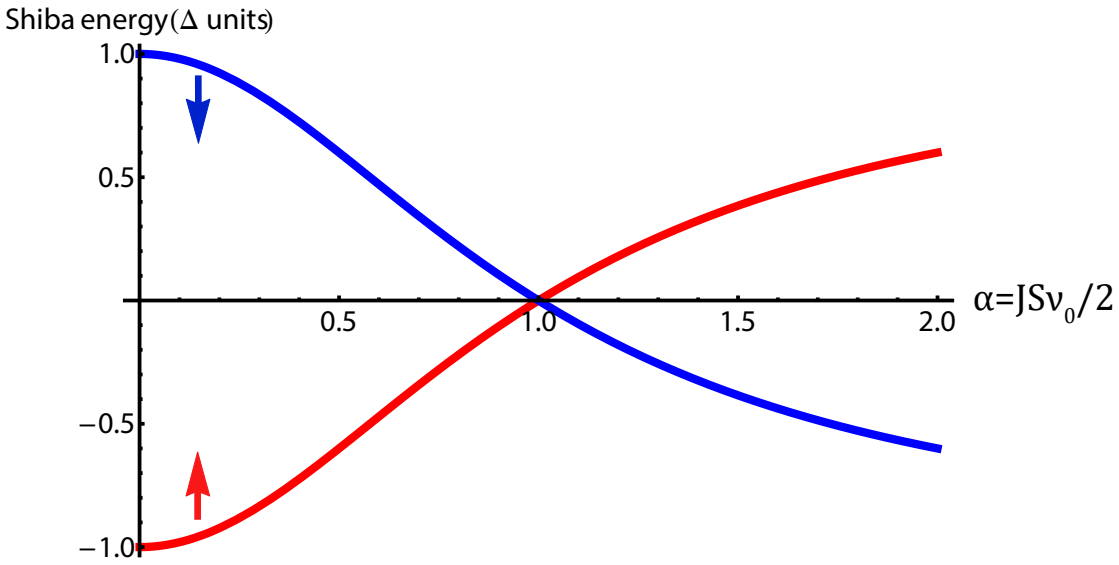

Figure 2.3: Energy of the electron-like (blue) and hole-like Shiba bound states as a function of the magnetic coupling strength J for $K = 0$.

The operators $\hat{\psi}$ are themselves the Fourier transform of the $\hat{c}$ operators in reciprocal space

$$\hat{\psi}_{\boldsymbol{r},\sigma} = \sum_k e^{ikr} \hat{c}_{\boldsymbol{k},\sigma}. \tag{2.10}$$

Starting from the impurity interaction including both the magnetic and non magnetic potentials, we can write the following equations for the Bogoliubov coefficients $u_\alpha(r)$ and $v_\alpha(r)$ [31]

$$\omega u_\alpha(r) = \xi(k)u_\alpha(r) + H^{imp}_{\alpha\beta}u_\beta(r) + i\Delta(r)\sigma^y_{\alpha\beta}v_\beta(r) \tag{2.11}$$

$$\omega v_\alpha(r) = -\xi(k)v_\alpha(r) - H^{imp}_{\alpha\beta}v_\beta(r) - i\Delta(r)\sigma^y_{\alpha\beta}u_\beta(r) \tag{2.12}$$

where we have explicitly written the indexes of the spinors v and u as well as those of the matrices H and σ. These equations are simply the Bogoliubov-de Gennes equations derived in the previous chapter to which were added the impurity terms.

This system can be separated between the solutions for $(u_\uparrow, v_\downarrow)$ and $(u_\downarrow, v_\uparrow)$. The solutions of each system of equation can be obtained from the other by simply changing the sign of J. Writing the previous set of equations in the restricted space $(u_{k\uparrow}, v_{k\downarrow})$ we now obtain the system

$$u_{k\uparrow} = \nu_0 \frac{(K + \frac{JS}{2})(\omega + \xi_k)u_{k\uparrow} - \Delta(K - \frac{JS}{2})v_{k\downarrow}}{\omega^2 - \Delta^2 - \xi_k^2} \tag{2.13}$$

$$v_{k\downarrow} = \nu_0 \frac{-(K - \frac{JS}{2})(\omega + \xi_k)v_{k\downarrow} + \Delta(K - \frac{JS}{2})u_{k\uparrow}}{\omega^2 - \Delta^2 - \xi_k^2}, \tag{2.14}$$

where ν_0 is the density of states at the Fermi energy. The solutions of this linear system of equations give us the energy of the Shiba bound states as a function of the magnetic and non magnetic diffusion potential. For convenience we introduce the parameters $\alpha = \pi\nu_0 JS/2$ and $\beta = \pi\nu_0 K$ and write the Shiba energies as

$$E_{Shiba} = \pm\Delta \frac{1 - \alpha^2 + \beta^2}{\sqrt{4\alpha^2 + (1 - \alpha^2 + \beta^2)^2}}. \tag{2.15}$$

The $\pm$ values correspond to the electron and hole-like states. These energies are located inside the superconducting gap and are not dependent on the sign of J. The expression of the Shiba energies can

be substantially simplified by the introduction of a scattering phase $\delta^{\pm}$ defined as $\tan\delta^{\pm} = K\nu_0 \pm \frac{JS}{2}\nu_0$. We then have

$$E_{Shiba} = \pm\Delta\cos(\delta^{+} - \delta^{-}). \tag{2.16}$$

We plot the evolution of the Shiba energy as a function of the magnetic coupling (and for $K = 0$) in Fig. 2.3

For $J \to 0$ we tend to a limit where the impurity has a minimal effect on the condensate. Therefore the YSR bound states will be located at $E_S = \pm\Delta$. By increasing the coupling the states will then find their energy moving toward the Fermi level.

From fig. 2.3 we can observe that at one value of the magnetic coupling the energy of the Shiba bound state is exactly at zero. The point where this happens corresponds to the point where the energy associated to the coupling J becomes comparable to the strength of the superconducting interaction. This transition also corresponds to a different ground state for the system where it goes from a singlet spin state to a doublet spin state. The classical interpretation of this second ground state is that the electrons from the Cooper pairs get separated and one of the two stays linked to the impurity while the other one is left to evolve unpaired. The doublet ground state is similar to what is expected from a quantum impurity forming a Kondo doublet [45]. After this point the classical spin approximation starts to fall apart and the ground state is different and calculations should be handled with care [46].

The YSR bound states are fully spin-polarized. This polarization arises from the fact that equations 2.11 and 2.12 are unchanged if one performs the exchange $(u_\uparrow, v_\downarrow) \to (v_\uparrow, u_\downarrow)$.

By analyzing the crossover point for the Shiba energies as a function of the non magnetic coupling we obtain the relation $\pi\nu_0\frac{JS}{2} = \sqrt{1 + (\pi\nu_0 K)^2}$ (see Fig. 2.4). This can be interpreted as follows: when increasing the non magnetic coupling, the diffusion of the electrons by the magnetic potential gets weaker in proportion. Therefore the bonding of the pair is less affected in the limit of large non magnetic potentials and the strength of the magnetic coupling needed to enter the Kondo singlet regime, and completely break the Cooper pairs, increases.

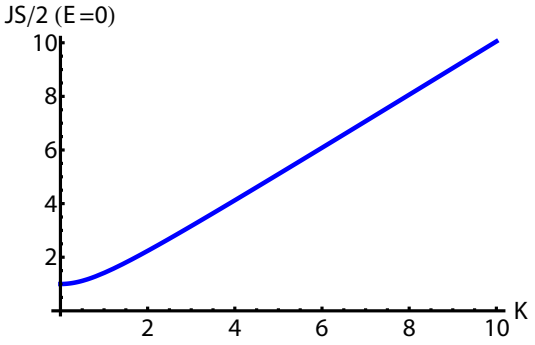

Figure 2.4: Value of the magnetic coupling $JS/2$ for which $E_{Shiba} = 0$ as a function of the non magnetic coupling K

2.3.3 Writing the wave function of YSR states

We have explained above how a local magnetic interaction induces states inside the superconducting gap and discussed the physical interpretation of such states. Let us now compute the associated wave-function and study the effect of dimensionality on their spatial extent.

Formalism

We define the spinor in momentum space as:

$$\Psi(k_{nm}) = \frac{1}{NM}\sum_{jl} e^{2i\pi jn/M + 2i\pi lm/N}\psi(r_{jl}), \tag{2.17}$$

where the k_{nm} are the allowed values for the $\boldsymbol{k}$ vector. N and M denote the number of atomic sites of lattice in $\boldsymbol{a}$ and $\boldsymbol{b}$ directions. If we apply the Hamiltonian to this spinor, we find:

$$[E - \xi_{nm}\tau_z - \Delta_0\tau_x]\psi_{nm} = \frac{1}{NM}(-\frac{JS}{2} + K\tau_z)\psi(r_{imp}). \tag{2.18}$$

We can then infer this equation :

$$\psi(r_{jl}) = \sum_{nm} \frac{1}{NM} \frac{e^{i2\pi(nj/N+ml/M)}[E_0 + \xi_{nm}\tau_z + \Delta\tau_x]}{E_0^2 - \xi_{nm}^2 - \Delta^2}(-\frac{JS}{2} + K\tau_z)\psi(r_{imp}). \tag{2.19}$$

From this equation by taking $r_{jl} = r_{imp}$, we can compute the amplitude of the wave function at the impurity site, and then the full spatial dependence of the Shiba wave function. The only two adjustable parameters are $JS/2$ and K when considering a given band structure.

2D vs. 3D

We can show easily with the relation $\frac{\psi_+(0)}{\psi_-(0)}\frac{\cos(\delta^-)}{\cos(\delta^+)} = 1$ that the asymptotic forms (for $r \gg \lambda_F = 2\pi/k_F$)of the eigenstates are given for a 3D system (as found by Rusinov [31])

$$\psi_\pm(r) = \frac{1}{\sqrt{N}} \frac{\sin(k_F r + \delta^\pm)}{k_F r} e^{-\Delta \sin(\delta^+ - \delta^-) r/\hbar v_F}, \tag{2.20}$$

and for a 2D system [47] (see appendix .2):

$$\psi_\pm(r) = \frac{1}{\sqrt{N\pi}} \frac{\sin(k_F r - \frac{\pi}{4} + \delta^\pm)}{\sqrt{k_F r}} e^{-\Delta \sin(\delta^+ - \delta^-) r/\hbar v_F}. \tag{2.21}$$

N is a normalization factor defined in dimension n by $1 = \int \frac{d^n k}{(2\pi)^n} \left(|\psi_+(k)|^2 + |\psi_-(k)|^2\right)$. The comparison between the 2D case and 3D case is presented on Figs. 2.5

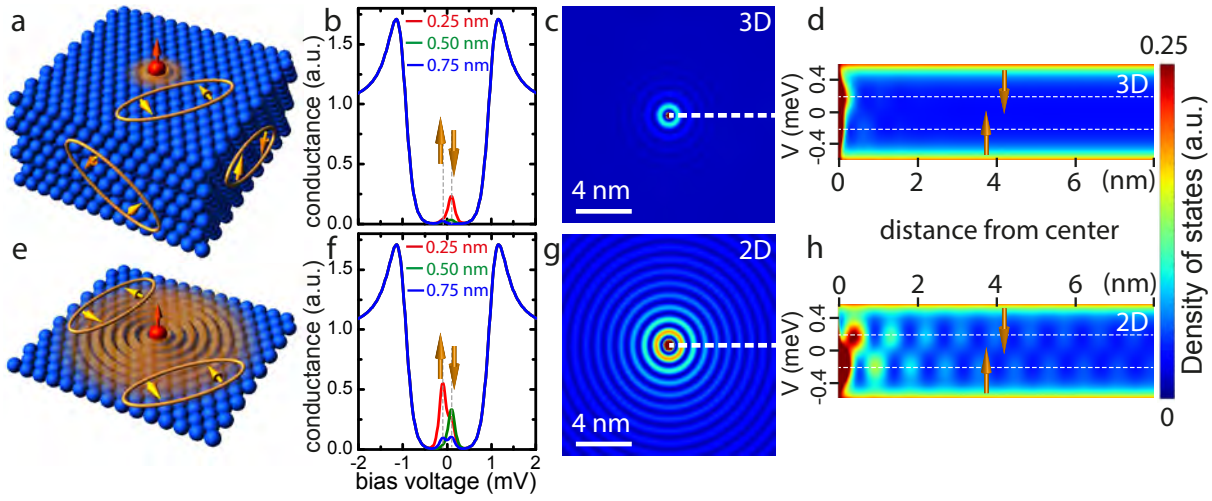

Figure 2.5: **Comparison between 3D and 2D for the spatial extent of Yu-Shiba-Rusinov states** a to d (e to h) Calculated behavior of a Yu-Shiba-Rusinov bound state in an isotropic s-wave superconductor with three-dimensional (two-dimensional) electronic band structure. a and e are schematic views of the interaction of Cooper pairs with a classical magnetic impurity. b and f are calculated scanning tunneling spectra at various distances from the impurity showing the fully polarized YSR states inside the superconducting gap. c and g are simulated conductance maps around the impurity showing the spatial extent of one peak of the YSR state presented in Figs. b. and f. respectively. d and h are simulated conductance between -0.6 and 0.6 mV along the dotted line out of the impurity in Figs. c and g respectively. A cut-off has been applied in order to get rid of the divergence at $r = 0$.

Decay of the wave function

The main difference between the 3D and 2D cases concerns the decrease behavior of the wave function. While in both cases we obtain a combined power law and exponential decay, the power law is different. Due to what can be simply be seen as a Jacobian constrain in the calculations or a weaker screening, the 2D case behaves as $1/\sqrt{r}$ therefore decaying much slower than in the 3D case.

From an experimental point of view this power law is the key ingredient when it comes to probing the fine structure of the wave function. In the case of a small amplitude YSR state the $1/r$ decay from the 3D case would dominate the LDOS and make more difficult to measure the oscillatory behavior at larger scales. The coupling of impurity by means of YSR bound states is also much more complicated in this case. However in 2D, for a same amplitude of the state on top of the magnetic impurity one can hope to extract more information from a spatially resolved STS experiment.

Phase of the wave function

The parametrization of the wave function by the terms $\delta^{\pm}$ shows us that these terms only depend on the energy of the in-gap states as $E_S = \pm\Delta\cos(\delta^+ - \delta^-)$. The spatially oscillating wave function is also solely determined by this energy. Because STS measures the density of states which is actually the proportional to $|\psi(r)|^2$, the oscillatory behavior one is expected to observe on the conductance maps is related to twice the phase difference of the wave function between the electron and hole like parts.

2.3.4 State of the art experiments on YSR states

The first experimental probing of YSR states is due to Bauriedl et al. [48] in 1981 where the authors measured impurity bands of Mn atoms in Pb. The first STM measurement however can be found in the work of Yazdani et al. [49] dating back to 1997. This experiment was concomitant with new theoretical works such as [50, 51, 52] focused on the precise spatial behavior of the wave function. In the work of Yazdani et al. (see fig. 2.6.A and B.) the authors studied Mn and Gd atoms on a Nb crystal in order to reveal the in-gap states associated to the magnetic impurities interaction with the superconducting condensate. One of their important result was that the signal associated to the YSR states was almost non retrievable at distances of the order of 1 nm. This limited spatial extent did not allow for a precise measurement of the inner structure of the wave function close to the impurity. However they were able to show the existence of an asymmetry of the electron and hole-like peaks in the DOS over the magnetic atoms.

Yazdani work was done at 3.8 K, intrinsically limiting the resolution of the measurement. The first measurements at 300 mK are due to Shuai et al. in 2008 [53]. In this case the system used was a Pb thin film on Si(111) covered with impurities of Mn and Cr. Using a superconducting tip the authors were able to have a much more precise look into the structure of the in-gap states (see fig. 2.6.a to f.). What they observed was the existence of more than one Shiba peak as predicted for impurities with a larger range of the magnetic interaction. In this work the authors also studied the structure of Mn dimers spaced out by a few Å in order to probe the bonding and anti-bonding states expected to appear between two magnetic impurities. Just like Yazdani the spatial extent of the YSR bound state was limited to a distance of the order of the nanometer. The consequence of this fact was the extreme difficulty to draw any definitive conclusion concerning the spatial evolution of the wave function associated to the YSR bound states as it would be hidden by its power law decay.

A lot of work was later put into the understanding of the interplay between Shiba and Kondo physics especially using phtalocyanines molecules [54, 45].

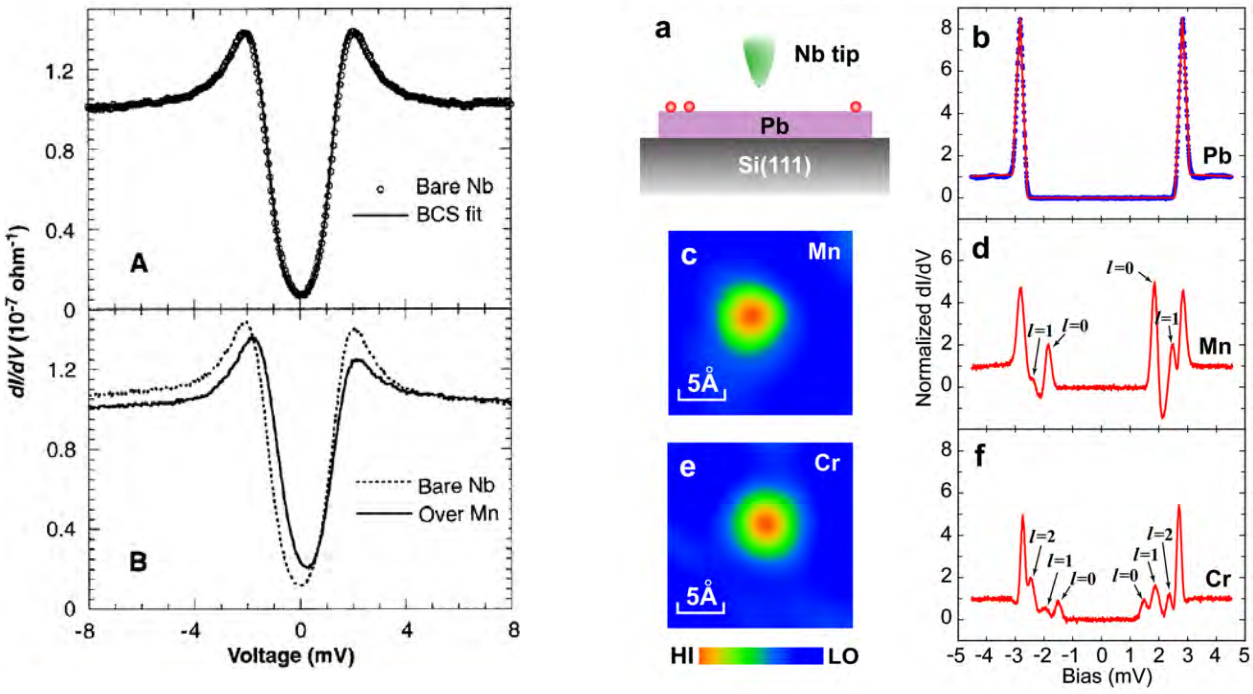

Figure 2.6: **State of the art of YSR bound states:** Left, dI/dV curves obtained by STM for Mn atoms on Nb. Fig. b. shows the difference between the bare Nb spectra (dashed line) and the Shiba bound state measured on top of a magnetic atom (full line). Original figure from [49]. Right, STS of Mn and Cr atoms on Pb thin films using a superconducting Nb tip. Figs. c. and d. show the conductance map and spectra obtained over a Mn atom while figs. e. and f. are obtained over a Cr atom. Original figure from [53].

2.4 The impurity problem (Kondo physics)

The YSR bound states and the Abrikosov-Gorkov theory are only a minor part of a larger problem in physics known as the impurity problem and more specifically the Kondo physics. The Kondo effect [33] refers to an anomaly in the resistivity of metals containing magnetic impurities. Kondo showed that this effect arises from the quantum nature of magnetic defect which leads to a logarithmic divergence in the perturbative development of the resistivity. Experimentally this is materialized by a minimum in the resistivity at a temperature T_K called the Kondo temperature. The Hamiltonian Kondo studied was very close to the Abrikosov-Gorkov Hamiltonian (eq. 2.1) with the difference that the impurity spins were treated as quantum spins. The Hamiltonian associated to such interaction reads as

$$\hat{H}_{\text{Kondo}} = \sum_{k,\sigma} \varepsilon_k \hat{c}^\dagger_{k,\sigma} \hat{c}_{k,\sigma} + \sum_i J \hat{\boldsymbol{S}}_i \cdot \hat{c}^\dagger_k \hat{\boldsymbol{\sigma}} \hat{c}_k, \tag{2.22}$$

with i the index of a given impurity in a random position in the system. In Kondo's calculation, impurities are treated not as a constant magnetic field with no degrees of freedom but as a multilevels quantum spin.

It was later shown that the Kondo effect can be linked to the Anderson problem *via* a canonical transformation called the Schrieffer-Wolff transformation [55]. Essentially this transformation states that the case considered in the Kondo problem is equivalent to the coupling of an isolated quantum level with an energy continuum. This energy level posses an on-site electron-electron repulsive interaction. The

Anderson impurity Hamiltonian is written

$$\hat{H} = \varepsilon_d \hat{c}_d^\dagger \hat{c}_d + \sum_k \xi_k \hat{c}_k^\dagger \hat{c}_k + \sum_k V_{kd} \hat{c}_{kd}^\dagger \hat{c}_d + h.c. + U \hat{n}_{d\uparrow} \hat{n}_{d\downarrow}, \tag{2.23}$$

where the operators $\hat{c}_k$ destroy an electron in state $|k\rangle$ and operators $\hat{c}_d$ destroy an electron in state $|d\rangle$. $\hat{n}_{d\sigma}$ is the number operator giving the number of electrons on the level $|d\rangle$ and the corresponding term in the Hamiltonian describes an on-site repulsion. This type of Hamiltonian leads to a resonance in the density of states called Abrikosov Suhl resonance around the Fermi level.

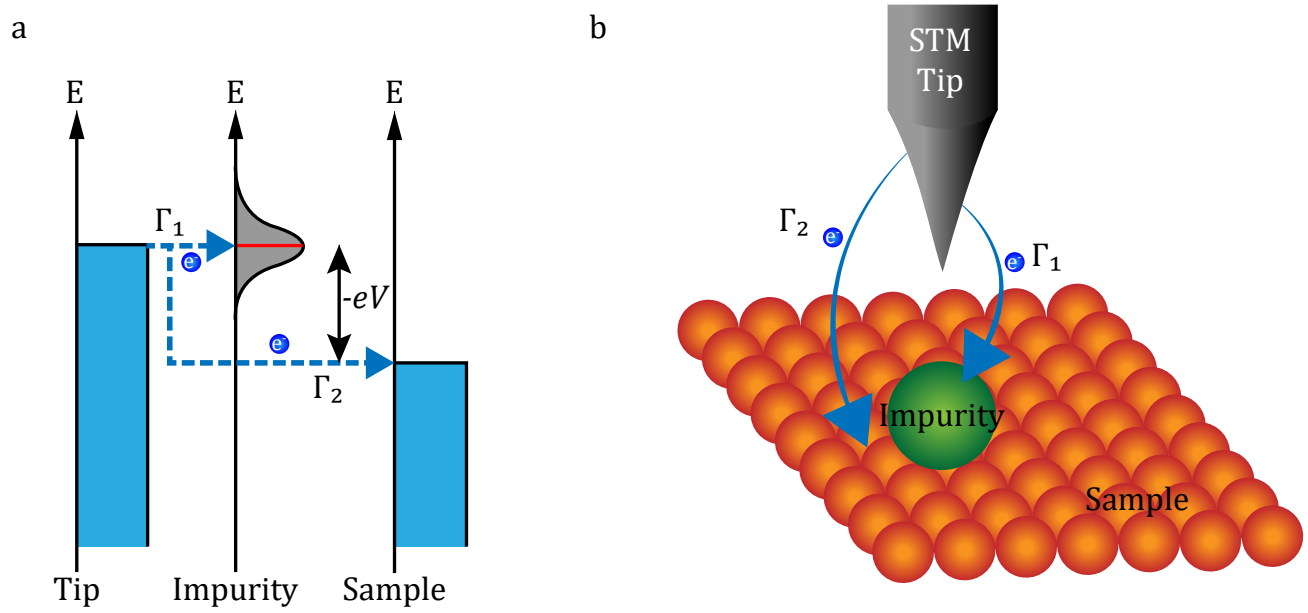

Figure 2.7: **Process by which to obtain a Fano form:** An electron from the tip is interfering with itself due to the possibility to tunnel either through the states on the impurity (with an hybridization factor Γ_1) or directly into the Fermi sea of the substrate (with an hybridization factor Γ_2). a. Energy diagram representation. b. Real space representation.

Due to the proximity of the interaction with the Shiba case many work is put into the understanding of the interplay between the Kondo effect and superconductivity [56, 57, 54, 58]. Because a Kondo resonance can be mapped to a discrete energy level one could intuitively expect it to manifest as a sharp resonance in an STS spectrum. However in the framework of the Anderson model this state is hybridized with the energy continuum of the substrate. This hybridization gives a Lorentzian line shape for the resonance.

There is actually a second effect that must be taken into account. When performing STM measurements there can exist an interference of the path of electrons during tunneling (see appendix .4 and fig. 2.7) giving rise to a Fano resonance [59, 60]. This interference occurs between a direct tunneling of electrons to the surface and an indirect one through the impurity. For a discrete level of energy ε_d if we define $x = \frac{eV - \varepsilon_d}{\Gamma}$, the expected density of states is given by the following formula for the Fano line shape [61]

$$G(x) = \rho_0 \frac{(q+x)^2}{x^2+1} \tag{2.24}$$

where q is the ratio of the real and imaginary part of the free Green function of the continuum that can physically be interpreted as the ratio of resonant scattering to the direct scattering amplitude. The form of this line shape is represented on Fig. 2.8 for different values of the factor q.

A key difference between the YSR bound states and Kondo effect is that the later does not need a superconductor to be present. This difference gives us a way to know in which case we are. By destroying

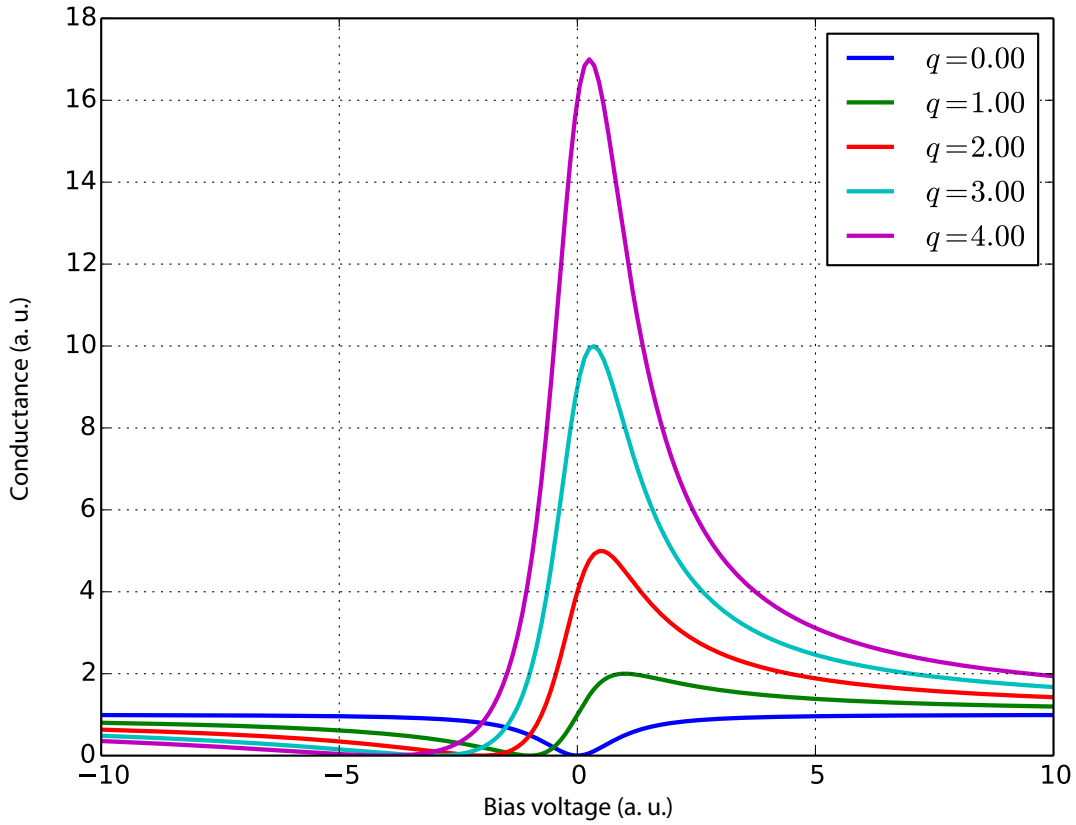

Figure 2.8: Fano line shapes for different values of the parameter q

superconductivity, the YSR bound states must disappear in the normal state while a Kondo resonance will remain and split by Zeeman effect [62]. As destroying superconductivity with temperature is detrimental to the spectroscopic precision of the STS measurements we will prefer to destroy superconductivity by applying an external magnetic field. Doing so, in the case of a Kondo impurity we should be able to observe some signal while in the case of a classical impurity there should not have any trace of bound states in the normal regime.

2.5 Conclusion

In this chapter we have discussed the different phenomena associated to the presence of local magnetism in superconductors starting from the Abrikosov-Gor'kov theory finishing by the Kondo effect. We mostly focused on the YSR bound states for which we expect to observe pairs of peaks inside the superconducting gap around magnetic impurities. These induced states originate from the time reversal breaking interaction that tend to break the Cooper pairs made of electrons of opposite spins. We discussed the role of the dimensionality on the YSR wave function and showed how 2D superconductors were better systems to study the YSR bound states compared to 3D systems due to a different power law dependence.

We also discussed the way states at positive and negative bias are expected to be spatially dephased in relation with their energy positions inside the superconducting gap.

In the next chapter we will use this information to discuss the in-gap states measured by STM in 2H-$NbSe_2$.

Chapter 3

Impurities in $2H - NbSe_2$ monocrystals

3.1 Introduction

As we mentioned in the previous chapter, the spatial extent of YSR bound states in previous STM experiment was limited to a few angströms. Here we will show that by choosing a material with two dimensional properties, the YSR bound states will present spatial extents order of magnitudes larger. Finding such systems with long-range YSR bound states will allow for a measurement of finer effects such as oscillations of the LDOS at the scale of the Fermi wave-length and dephasing between the electron and hole component.

The discussion taking place in this chapter mostly covers the contents of our article [47] about the experimental study of single magnetic impurities in a monocrystal of 2H-$NbSe_2$. The case of 2H-$NbSe_2$ is particularly interesting as its band structure is two-dimensionnal while from the point of view of superconductivity it is an anisotropic three dimensional material whose coherence length along c exceeds the periodicity along the c-axis. We will show that the large spatial extent of the YSR bound states in this system is due to the fact that we are in presence of a quasi-2D Fermi surface.

We will end this chapter by briefly discussing the effect of non magnetic impurities.

3.2 Crystallographic and band structure of the material

2H-$NbSe_2$ is a three dimensional bulk system. It is constituted of Se prisms surrounding Nb atoms (see Fig. 3.2.a). The Se prisms are turned by 30° in each alternating slabs giving to the system a global hexagonal symmetry. This structure creates a Fermi surface in the normal state constituted of two sheets as shown on figs. 3.1.a and b. The sheets originate from the Nb d_{z^2} and $d_{xy}/d_{x^2-y^2}$ orbitals and form close contours in the a-b plan but do not close along the c-axis. In this aspect, the band structure of the system is two-dimensional. It then becomes possible to model the Fermi surface of the system as presented on fig. 3.1.d: the surfaces associated to band 1 and 2 obtained by DFT are in good agreement with ARPES data. It should be noted that the full three dimensional system exhibits a small pocket surrounding the Γ point. This pocket is associated to a hole band originating from the Se atoms taking part to the inter-plan coupling (not represented on Fig. 3.1).

A topographic STM measurement at 320 mK of the surface of 2H-$NbSe_2$ cleaved under UHV is presented on Fig. 3.2.b. On this image we can witness a 3×3 nearly commensurate charge density wave characteristic of this system [64] that appears under the temperature of 33.5 K [65].

$NbSe_2$ undergoes a superconducting transition at a critical temperature of 7 K. One of the specificity of this system is that it is a two bands superconductors in the sense that it has two distinct gapped band at the Fermi level [66, 63]. This two-band originated superconductivity has been described in the framework of the modified BCS theory [67, 68] or an anisotropic superconductor [69]. Independently of the precise nature of the BCS interaction, the final result is a coupling of the same nature as for

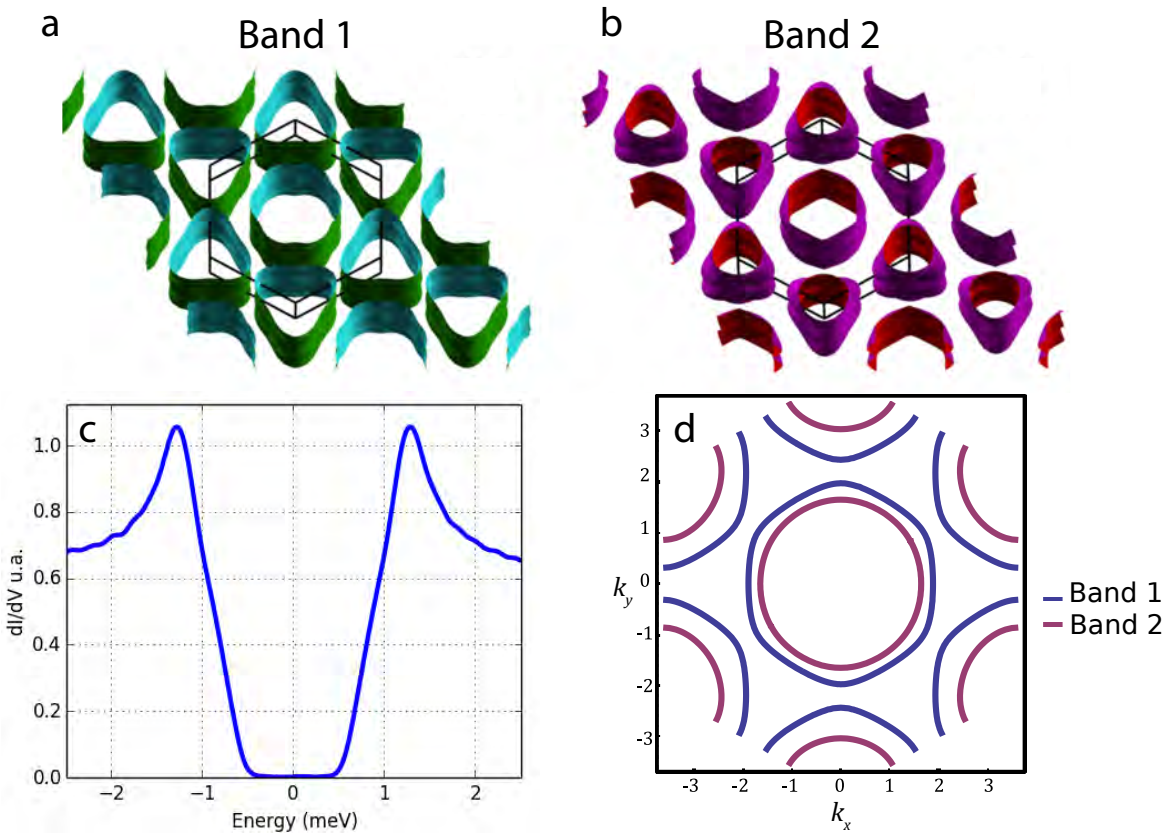

Figure 3.1: **Electrons in 2H-$NbSe_2$:** a.-b. Structure of the Fermi surface for the two bands in the reciprocal space (original figures from [63]). c. Superconducting spectrum of a 2H-NbSe2 sample at 300 mK obtained using a Pt/Ir tip. b. Fermi surfaces of band 1 and band 2 of 2H-$NbSe_2$ in a two-dimensional double layer model in which was only considered one unit cell along the c axis.

usual BCS superconductors in which the electrons are paired in a singlet state. $NbSe_2$ being an s-wave superconductor, as stated by the Anderson theorem only magnetic impurities induce in-gap states. Thus any observed in-gap signatures will be associated to time-reversal symmetry breaking interaction, i.e. vortices or YSR bound states.

When applying a magnetic field to the system vortices appear and order in the form of an Abrikosov lattice with hexagonal symmetry. These vortices are seen in the form of characteristic six pointed stars (see Fig. 3.2.c) and present Caroli-Matricon-de Gennes states at the vortex core. We will see in the following that the same six-fold symmetries is also observed around individual magnetic impurities and arises from the structure of the Fermi surface.

3.3 Sample preparation

3.3.1 Sample growth

The 2H-$NbSe_2$ crystals used in our experiments were grown at the Institut Jean Rouxel in Nantes by E. Janod and L. Cario, using an iodine vapor transport technique. Stoichiometric amounts of the elements (Nb 99.8% Alfa Aesar, Se 99.99 % Aldrich) were sealed under vacuum in a silica tube with a small amount of Iodine (4 mg/cm^3, 99.9985% Puratronic). The tube was then heated up for a period of 170 h in a gradient furnace. The mixture was located in the high temperature zone of the furnace at 700°C while the cold end part of the tube was around 660°C (gradient 3°C/cm).

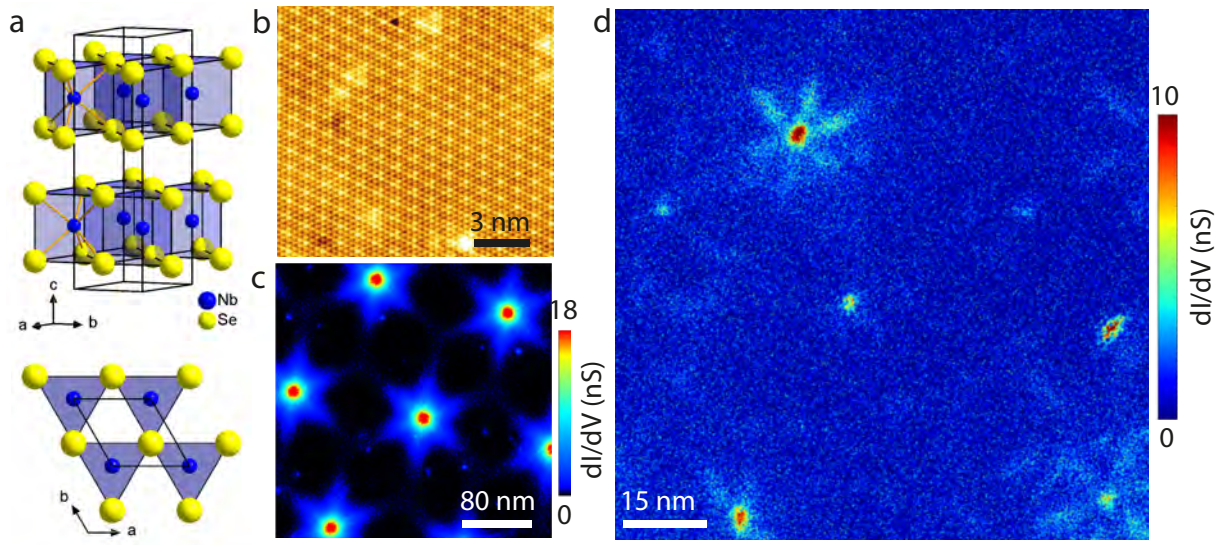

Figure 3.2: **Structural and superconducting properties of 2H-$NbSe_2$** a. Atomic structure of a 2H-$NbSe_2$ crystal. b 19×17 nm^2 topographic image of a 2H-$NbSe_2$ sample with the atomic lattice modulated by a charge density wave. The image is taken at V=-200 meV and I=80 pA. c. Abrikosov lattice in 2H-$NbSe_2$ showing the star shaped structure of vortices in a magnetic field of 0.1 T. d. Conductance map taken at V=-0.05 meV integrated over ± 0.02 meV showing a few star-shaped structures created by localized magnetic impurities at zero magnetic field. Measurements were performed at 320 mK.

This synthesis yielded large shiny black layered crystals (of a few mm in size) along with some black powder. X-Ray diffraction pattern of the powder ascertained that it is composed of a majority of the 2H-$NbSe_2$ phase (90%). Five single crystals were then tested for crystallographic quality using a four circles FR 590 Nonius CAD-4F Kappa-CCD diffractometer at 300 K. All of them revealed an hexagonal cell with parameters a = b $\simeq$ 3.44 Åand c $\simeq$ 12.56 Å, in very good agreement with parameters reported for the 2H-$NbSe_2$ phase [70]. Finally the composition of several crystals was tested by Energy Dispersive X-ray Spectroscopy using an electronic microscope JEOL JSM 5800LV. A ratio Nb/Se close to 1:2 was measured in agreement with the stoichiometry. No impurity traces could be detected using this technique as the threshold of detection is larger than 1000 ppm. However the certificate of analysis delivered by the company Alfa Aesar for the Niobium powder used as precursor (Lot number K08Q025) revealed as main magnetic impurity 175 ppm of Fe, 54 ppm of Cr and 22 ppm of Mn. This synthesis yielded therefore to 2H-$NbSe_2$ crystals unintentionally doped by a few hundreds of ppm of magnetic species with a dominance of Fe impurities that as we will see in the following give the dominant spectroscopic signal (see Tab. 3.1).

Element	Ta	Cr	W	Ni	Al	C	N
Concentration (ppm)	970	54	<5	14	30	47	555
Element	Fe	Si	Mo	Mn	Ti	H	O
Concentration (ppm)	175	41	3	22	30	14	4000

Table 3.1: Chemical characterization of the Nb powder used for growing the 2H-$NbSe_2$ crystals

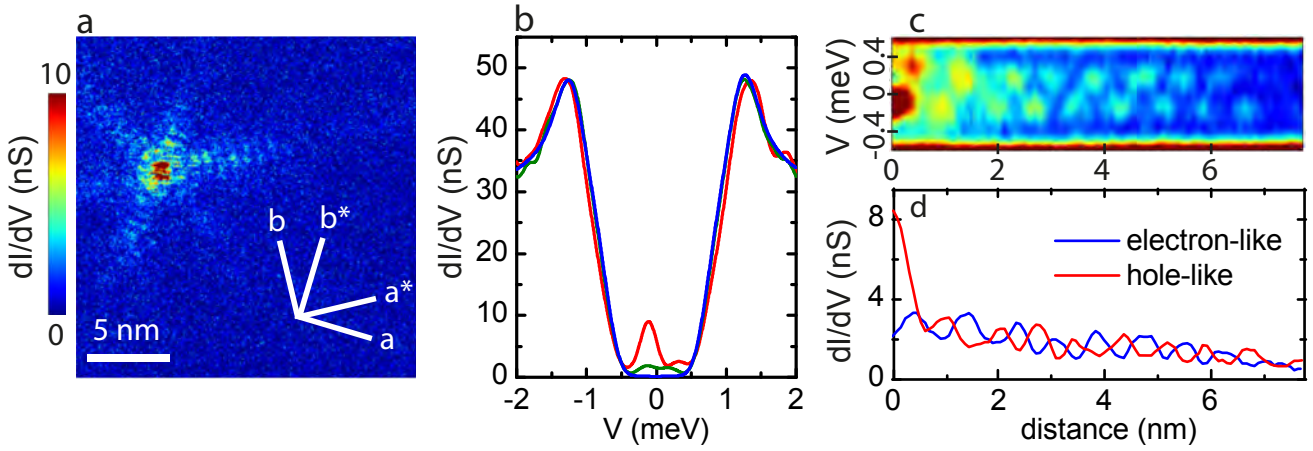

Figure 3.3: **Spectral and spatial properties of an extended Yu-Shiba-Rusinov bound state in 2H-$NbSe_2$** a. Experimental conductance map measured at -0.13 meV. The two a and b lines indicate the crystallographic axes of 2H-$NbSe_2$ while the a* and b* indicate the directions in the reciprocal space. b. Characteristic experimental spectra taken on top of the impurity (red), on the right branch, 4 nm from the center of the impurity (green) and far from the impurity (blue). c. Spatial and energy evolution of the experimental tunneling conductance spectra, $dI/dV(x,V)$ along one branch of the star. The left side of the figure corresponds to the center of the star and the right side to the top-right corner of the scanning area. The color conductance scale is the same as the one used in a. d. Conductance profiles of the electron and hole like YSR states as a function of the distance to the impurity along the same line as for c.

3.3.2 Preparation for STM Measurement

The samples were glued on molybdenum sample holders using epoxy glue. These samples were cleaved under ultra high vacuum (10^{-11} mbar) in order to get the cleanest surface possible. Large scale topographic measurements performed on the samples (see Fig. 3.2) revealed a relatively small concentration of defects.

3.4 Observation of single magnetic impurities

3.4.1 Increase of the spatial extent by dimensionality

Simple topographic measurement on the surface of 2H-$NbSe_2$ show different types of defects appearing either bright or dark on fig. 3.2.b. The issue is that topography is not sufficient to determine whether the defects we see are associated to magnetic or non magnetic impurities. Only spectroscopy can distinguish between the two kinds thanks to the presence or absence of YSR bound states. Moreover we observed that the YSR spectroscopic signatures do not necessary come along with topographic defects as the magnetic atoms are present from the beginning of the synthesis of the crystal and are completely embedded inside the crystal. Finding impurities thus needs to be accomplished by scanning large areas of the sample and performing dense $I(V)$ grids centered around the superconducting gap in order to distinguish spatially localized in-gap bound states. This constraint adds to the complexity of the task and to the characteristic time scale of the experiment. Being limited by the quantity of ^{3}He at our disposal (a maximum condensation time of 40 hours) we looked for signatures of the YSR in areas of 300×300 nm^2 with a resolution of approximately one spectrum per nanometer. Then we are able to witness about a dozen of impurities in each image and consequently we can choose from these the one to look more closely at.

By performing STS experiments at the temperature of 320 mK we observed YSR bound states around

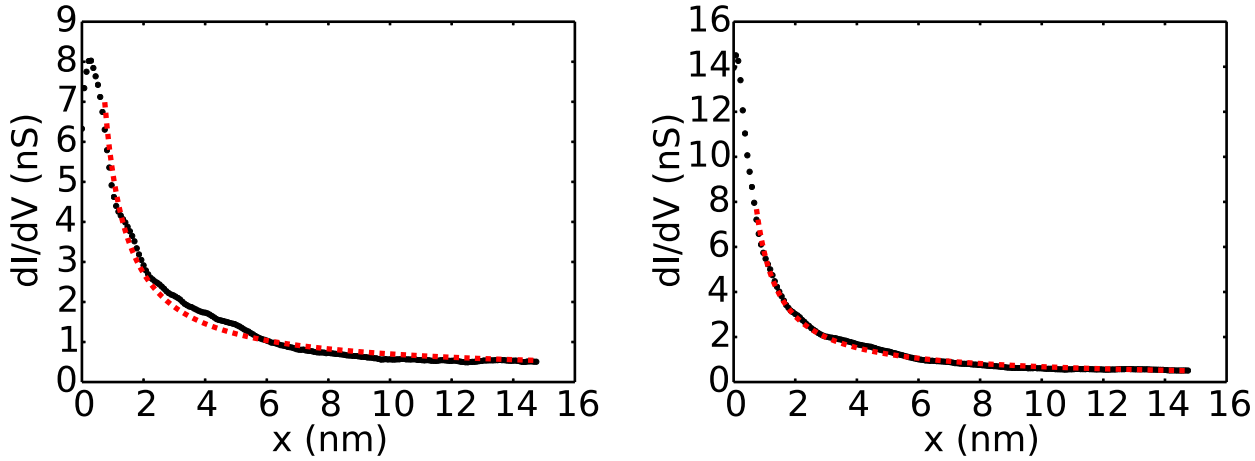

Figure 3.4: a. Hole like states spatial dependance angularly integrated. b. Same for electron like states. The black dots are the experimental points and the red dashed lines are the power law fits calculated ignoring the first points directly on top of the magnetic impurities in order to match the asymptotic assumption made in the calculation.

Fe impurities randomly dispersed as presented on Fig. 3.2.d. These states do not present themselves as circular waves localized around the magnetic defects as they would in the case of an isotropic material. Due to the hexagonal structure of the atomic lattice, the YSR bound states are characterized by a six-pointed star shaped electronic signature in 2H-$NbSe_2$. The scale on which these states can be observed extends as far as 10 nm from their origin. When compared to previously observed YSR bound states [49, 53, 54], this corresponds to an increase of the spatial extent by a factor 10. As we explained previously, the dimensionality of the electron gas plays a decisive role on the power law decay (as $1/\sqrt{r}$) of the wave function associated to the YSR bound states. In the case of 2H-$NbSe_2$ inter-plan Van der Waals interaction is such that the electronic structure presents 2D characteristics with a Fermi surface that almost does not experience any dispersion along the z direction. Another aspect that could possibly play a role on the difference with other experiments is the fact that here the impurities are embedded in the atomic lattice while in previous experiments, the YSR bound states were due to adatoms on the surface. The electronic coupling experienced by the impurities to the superconducting condensate may be increased in our case.

Because the star shaped structure of the YSR states originates from the symmetries of the 2H-$NbSe_2$ hexagonal lattice, it is of interest to compare the orientation of the branches of the stars with the crystallographic axes. We observed that the direct lattice vectors and the arms of the stars were angularly shifted by an angle of 30° (Fig. 3.2.a). This direction for the arms of the stars corresponds to the direction of the reciprocal lattice vectors ($\mathbf{a}^*$ and $\mathbf{b}^*$). Such an angular shift is also found in the vortex lattice of 2H-$NbSe_2$ in which the vortices also exhibit a six-pointed star shape (Fig. 3.2.c). This similarity calls for a common origin of the six-fold symmetry that would reflect the anisotropy of the Fermi surface [71], as supported by our simulations.

As expected theoretically [32, 30, 31], the tunneling spectra acquired over a given Fe impurity (see spectroscopic map in Fig. 3.3.a) show two peaks inside the superconducting gap (red curve in Fig. 3.3.b), one at positive bias and one at negative bias with symmetric positions with respect to the Fermi level ($E_{Shiba} \simeq \pm\ 0.2\ \Delta$). The peak at negative bias is much stronger than the one at positive bias. This difference highlights a very strong local particle-hole asymmetry as can be seen in Fig.2.5.h. Having a single pair of YSR conductance peaks in the gap is interpreted as the possibility to only access the s-wave diffusion channel (for which the angular momentum is $l = 0$ [1]) for the electronic diffusion by the

[1]The maximum value for the quantized angular momentum is constrained by the extent of the diffusion potential as

impurity. The authorized values of the angular momentum do indeed depend on the extent and form of the diffusion potential and observing solely the $l = 0$ channel suggest that one can consider the iron impurities as punctual defects. The same kind of behavior was observed in the case of Gd/Nb, Mn/Nb [49] or Mn-Phtalocyanine on Pb [54] where the $l = 0$ diffusion channel was the only one to be activated. On the contrary in [53] where the authors observed Mn atoms on Pb, the YSR states were observed for momenta $l = 0$ and $l = 1$ while for Cr impurities they observed angular momenta up to $l = 2$. In all these studies the spectroscopic signatures were strongly localized over the magnetic atoms and they disappeared a few Å from their center. A long range effect of magnetic defects on the density of states is thus totally decoupled from the local nature of the interaction from which they arise.

We also present on Fig. 3.4 the fit with the 2D power law of the radial dependance of the YSR bound state. On this figure the slight spatial phase shift between the different branches completely mask the oscillatory behavior and only leaves the power law decay of the YSR wave function. This result highlights the dimensionality dependence as the decay of the local density of states goes as $1/r$ in 2D and $1/r^2$ in 3D.

3.4.2 Interference effects and phase conditions for YSR bound states

Witnessing long range effects of the magnetic impurities on the density of states allows a finer analysis of the inner structure of the wave function associated to YSR states. On Fig. 3.3.a we present the LDOS taken at the energy of the strongest YSR peak -0.13 mV. The center of the star corresponds to a very strong peak in the tunneling spectra (red curve on Fig. 3.3.b) localized on the impurity [72]. The green conductance curve on Fig. 3.3.b was acquired 4 nm from the impurity site. The decrease of the LDOS between these two points both localized on one branch of the star is oscillatory with a periodicity of 0.8 nm as evidenced by the interference fringes clearly visible on the conductance map. Fig. 3.3.c shows the evolution of the LDOS as a function of the voltage bias as well as a function of the distance from the center of the impurity. On this figure we can see that the interference fringes for the electron-like and hole-like excitations are in almost perfect spatial antiphase. Let us go back to the expression of the YSR wave function 2.21

$$\psi_{\pm}(r) = \frac{1}{\sqrt{N\pi}} \frac{\sin\left(k_F r - \frac{\pi}{4} + \delta^{\pm}\right)}{\sqrt{k_F r}} e^{-\Delta \sin(\delta^+ - \delta^-) r/\hbar v_F}.$$

From this equation we observe that the dephasing between positive and negative energy wave-functions will be determined by the quantity $\delta^+ - \delta^-$. Because we experimentally probe the DOS which corresponds to $|\psi_{pm}(r)|^2$, the dephasing that will be observed in our conductance maps will be $2(\delta^+ - \delta^-)$.

As discussed in section 2.16, the phase difference between the positive and negative bias YSR states is determined by the ratio $E_s/\Delta = \cos(\delta^+ - \delta^-)$. In the case of 2H-$NbSe_2$ the value E_s/Δ is difficult to obtain precisely due to the two band gap with different values for Δ. However by comparing qualitatively the mean gap value and the energy of the YSR state ($E_S \ll \Delta$) they fall into the domain in which the phase difference of the wave function is close to $\pi/2$ and thus the phase difference observed in the DOS is close to π.

Because all the physical quantities that characterize YSR bound states are defined from the values of the magnetic and non-magnetic diffusion potentials J and K, a different type of impurity will lead to a different spectroscopic signature.

As mentioned previously, Fe is not the only contaminant of the Nb used for the crystal synthesis. There is no direct way to unequivocally determine the nature of an atom by STM. The claim that the impurities observed in the previous section were Fe atoms is solely based on the number of signatures of a given type we can observe compared to the known concentration of said atomic species from the chemical analysis of the Nb (see for instance the case of large scale conductance maps as in 3.2.d). This chemical analysis reveals that Co and Mn are the two other main magnetic contaminants of our Nb. While the

$k_F R \lesssim l_{\max}$.

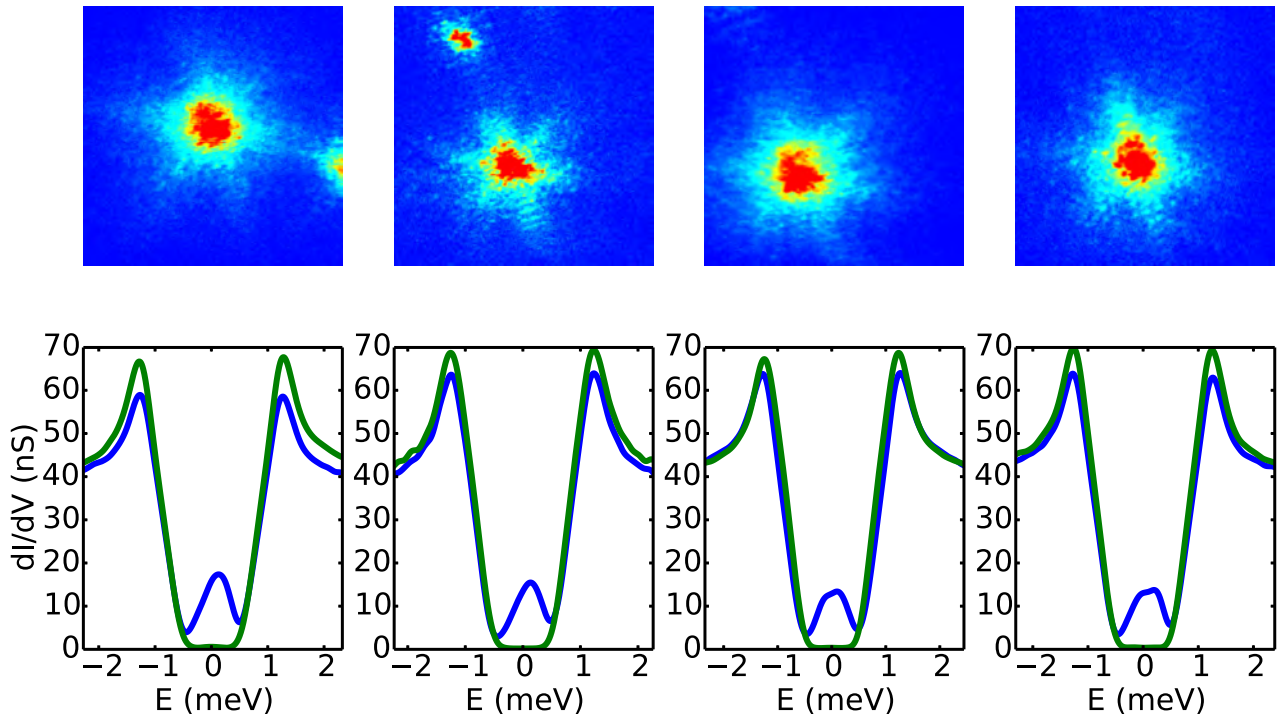

Figure 3.5: Spectroscopic maps integrated over the width of the overlapping Shiba peaks. The respective lateral size of the spectroscopic pictures are 17 nm, 21 nm, 14 nm and 17 nm. In the lowest row, the green spectra refer to the superconducting spectra of $NbSe_2$ taken far from the impurity and the blue ones to the spectra taken on top of the magnetic impurities. In each case the impurity and reference spectra are taken from the same data set.

precise magnetic moment of these elements is not really known in the context of them being embedded in 2H-$NbSe_2$ one can safely argue that they can keep their magnetic properties.

We have observed signatures of magnetic impurities that present different shapes and characteristic energies from the one presented in the previous section (Fig. 3.3). A sample of them are presented on Fig. 3.5. While the global six-branch star shape is preserved in each and every case as well as the orientation of this pattern, the precise details of the spectroscopy can vary quite a lot. This is no surprise as the band structure is responsible for the star shape while the nature of impurity will have an effect on the magnetic and non-magnetic diffusion potentials J and K and thus on the energy of the bound states E_S.

In Fig. 3.6 we show the case of an impurity whose YSR bound states are located at an energy of ± 0.8 meV. The first observation that can be made on these data is that no matter the energy of the YSR bound states, the spatial extent is conserved as we still have a clear spectroscopic signal 7 nm from the center of the impurity.

A second observation one can make is that contrary to what was observed on fig. 3.3.c the phase difference between the positive and negative energy states is in this case almost equal to 0. If we go back to the expression of the dephasing $\delta^+ - \delta^-$ (eq. 2.16) we see that we obtain $\delta^+ - \delta^- \simeq 0$ for $E_{Shiba} \simeq \Delta$. Therefore we expect no phase difference between the positive and negative bias states for energies close to the value of the superconducting gap. The observation of this difference between the case of fig. 3.3.c and fig. 3.6 confirms the link between the phase shift $\delta^+ - \delta^-$ and the energy of the YSR bound states.

Because the energy of the YSR bound states in fig. 3.6 corresponds to the limits of the gap edge, the

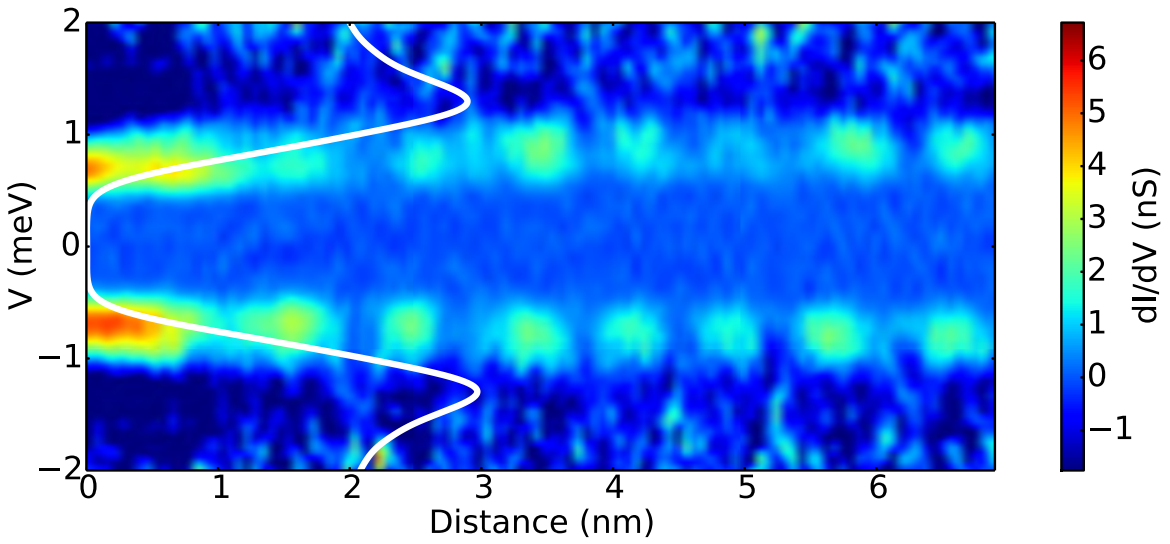

Figure 3.6: **Gap edge YSR bound states:** Spatial evolution of the Shiba bound states for an impurity with Shiba energy close to the gap edges. The white spectra represents the bare $NbSe_2$ that has been subtracted to the radial cut in order to increase the contrast on the YSR states.

contrast one can hope for in a cut of the conductance map is not optimal. Therefore we subtracted to fig. 3.6 the mean superconducting spectrum taken in the same scanning area and we represent it in white in order to help locate the bound states in the full DOS landscape.

We now take a closer look to what really happens in the center of the observed stars. In Fig. 3.7 we present a conductance map obtained over a 5.5×5.5 nm^2 area centered around the origin of one of the stars presented in Fig. 3.5. What we observe in this figure is that what could from a distance look like a single impurity is actually a cluster of 3 magnetic atoms giving rise to their own YSR bound states. On the spectra of Fig. 3.7.d we observe that the YSR bound states do come by pair but that we have 3 different characteristic energies in this case : 0 meV (green curve), ±0.1 meV (red curve) and ±0.3 meV (blue curve). An interesting feature of these spectra is that one impurity does not seem to have any real effect on its neighbor as the spectra look as if they are simply a superposition of different YSR bound states. This is best seen on the blue spectra in Fig. 3.7.d.

3.5 Theoretical modeling

The results we presented before were well understood in the framework of the Rusinov theory for what concerns the spatial extent, the oscillations and the phase shift of YSR bound states. However, this model can be analytically solved only for a parabolic dispersion. The band structure and symmetry of 2H-$NbSe_2$ thus is not included and cannot be reproduced. We present here the tight binding model we used to take into account the specific electronic dispersion of 2H-$NbSe_2$. The work performed in this section (as well as in appendix .2), both on the analytical and numerical side in the BdG formalism, was performed by S. Guissart and P. Simon.

3.5.1 Tight binding parameters and model

In order to perform the numerical calculation, we project our tight binding model on a triangular lattice. We have considered hopping terms up to the fifth nearest neighbour. The hopping amplitudes have been chosen in order to reproduce the band structure obtained from DFT and in good agreement with ARPES

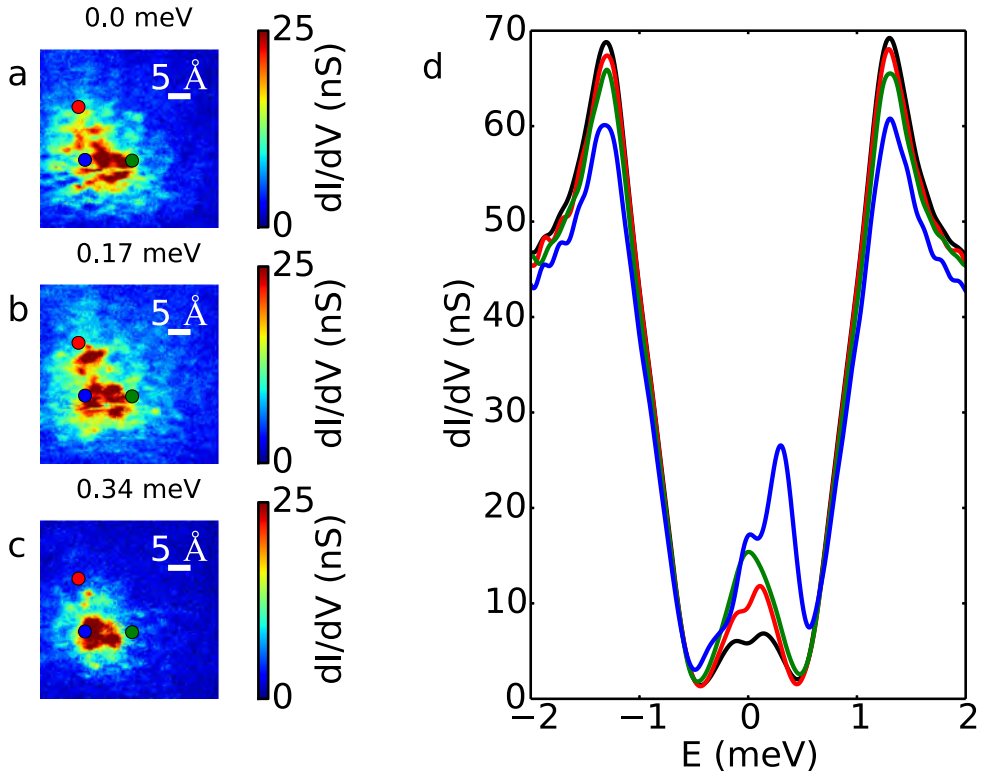

Figure 3.7: **Cluster of impurities in 2H-$NbSe_2$:** Zoom over a 5.5×5.5 nm^2 area corresponding to a cluster of 3 magnetic impurities. The three conductance maps (a to c) show the center of these impurities and the spectra (d) correspond to the conductance curves obtained over each impurity. The colors refer to the colors of the dots on the conductance maps while the black spectrum is the averaged spectrum over the whole area.

measurements. We refer to Refs [73, 74, 75, 76, 77] for the $NbSe_2$ band structure. The diagonalization of the tight-binding model results in the following 2-band dispersion relation (See Fig. 3.1):

$$\begin{aligned}\xi(k) = \xi_0 + t_1(2\cos\xi\cos\eta + \cos 2\xi) + t_2(2\cos 3\xi\cos\eta + \cos 2\eta) + t_3(2\cos 2\xi\cos 2\eta + \cos 4\xi) \\ + t_4(\cos\xi\cos 3\eta + \cos 5\xi\cos\eta + \cos 4\xi\cos 2\eta) + t_5(2\cos 3\eta\cos 3\xi + \cos 6\xi),\end{aligned} \tag{3.1}$$

with $\xi = \frac{1}{2}k_x a$ and $\eta = \frac{\sqrt{3}}{2}k_y a$ and a is the lattice spacing. The hopping parameters take the values presented in Tab. 3.2 (in meV):

	ξ_0	t_1	t_2	t_3	t_4	t_5
band 1	10.9	86.8	139.9	29.6	3.5	3.3
band 2	203.0	46.0	257.5	4.4	-15.0	6.0

Table 3.2: Parameters for the 2 bands of 2H-$NbSe_2$ obtained by *ab initio* calculations. The numerical values are given in meV.

To describe the 2H-$NbSe_2$ monocrystal in presence of one magnetic impurity, we assume the impurity spin to behave classically and use for the superconducting part the following Bogoliubov de Gennes

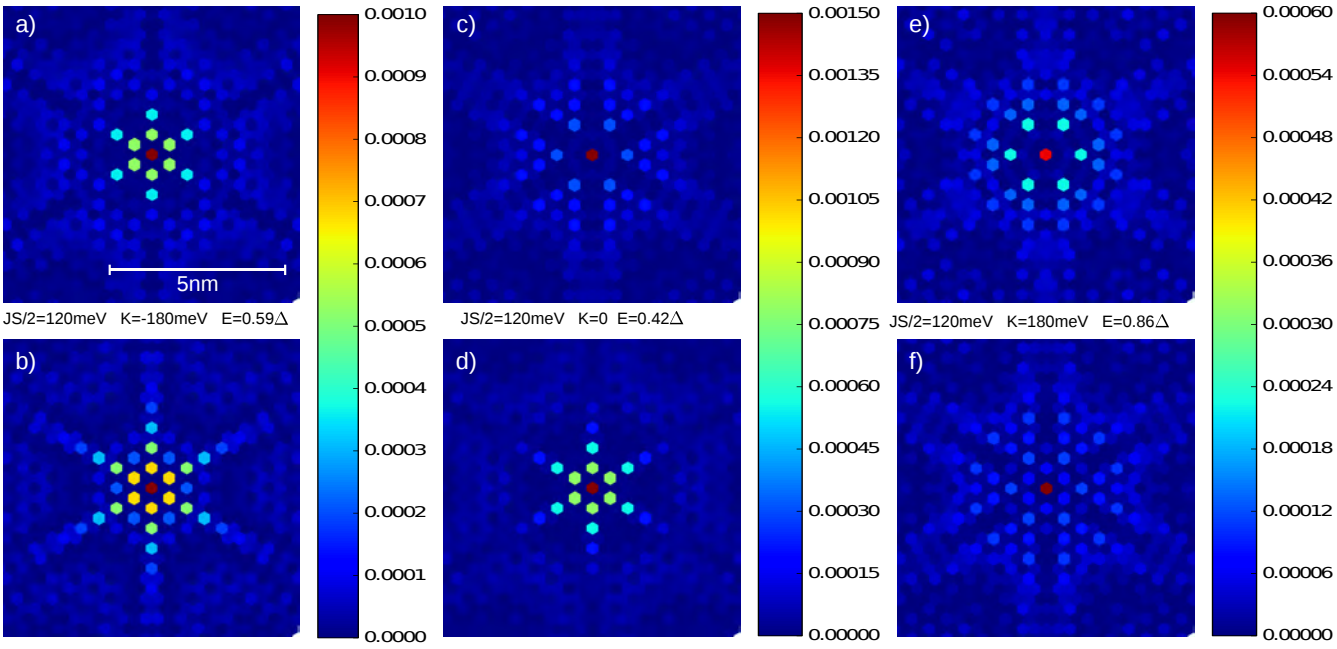

Figure 3.8: LDOS computed by solving exactly the Shiba equation. Figs **a** and **b** are the Shiba states with energy $E = 0.59$ meV and $E = -0.59$ meV respectively. Figs **c** and **d** are the Shiba states with energy $E = 0.42$ meV and $E = -0.42$ meV respectively and finally Figs **e** and **f)** are the Shiba states with energy $E = 0.86$ meV and $E = -0.86$ meV respectively. Colorbars give the density of states on each sites $\psi(r_{jl})\psi^*(r_{jl})$ normalised at $\sum_{jl} |\psi_+(r_{jl})|^2 + |\psi_-(r_{jl})|^2$=1. These theroretical calculations should be compared to the experimental data from fig. 3.3 and figs. 3.5.

Hamiltonian

$$H_{BdG} = \sum_{i,j}(c^\dagger_{i\uparrow}c_{j\uparrow} + c^\dagger_{i\downarrow}c_{j\downarrow}) + \sum_i \Delta(c^\dagger_{i\uparrow}c^\dagger_{i\downarrow} + c_{i\downarrow}c_{i\uparrow}), \tag{3.2}$$

where $c^\dagger_{i\sigma}$ and $c_{i\sigma}$ denote the creation and annihilation operators of electron at site i with spin σ.

The hexagonal symmetry observed experimentally in Figs. 3.2.d and 3.3.a is well reproduced in the framework of the Bogoliubov-de Gennes formalism [50]. This is done by numerically solving the Schrödinger equation with the almost exact tight-binding description of the band structure of 2H-$NbSe_2$. As we only observe $l = 0$ states we assume a strictly on-site interaction while we treat the magnetic impurity classically, *i.e.* assuming a large spin number S treated as a constant scalar. The interaction potential contains both a magnetic and non-magnetic part and reads

$$H_{Imp} = -\frac{JS}{2}(c^\dagger_{0\uparrow}c_{0\uparrow} - c^\dagger_{0\downarrow}c_{0\downarrow}) + K(c^\dagger_{0\uparrow}c_{0\uparrow} + c^\dagger_{0\downarrow}c_{0\downarrow}), \tag{3.3}$$

where the c_0 and $c^\dagger_0$ operators are respectively the annihilation and creation operators for electrons with spin σ on the magnetic atom site. The first term corresponds to the Zeeman splitting between spin up and spin down electrons for a coupling strength $J/2$ between the superconducting electrons and the individual atom. The second term is the non-magnetic diffusion potential of amplitude K. Using this approach, we calculate the LDOS for both the electron-like and hole-like YSR state. Since our experimental data are obtained in the large tip-sample distance regime, according to [72] the measured current is carried by single-electron tunneling rather than by Andreev processes. Therefore we can directly compare the calculated LDOS with the experimental data and we recover the typical star shaped structure as presented on Figs. 3.8 aligned along the reciprocal lattice vectors.

Because of the BdG part we can solve the Hamiltonian in the Nambu space using spinors of the form $\psi(r_{jl}) = (\phi_\uparrow(r_{jl}), \phi^\dagger_\downarrow(r_{jl}))$ where $r_{jl} = ja\overrightarrow{e_x} + la(\frac{\sqrt{3}}{2}\overrightarrow{e_y} + \frac{1}{2}\overrightarrow{e_x})$ denote site position in space with

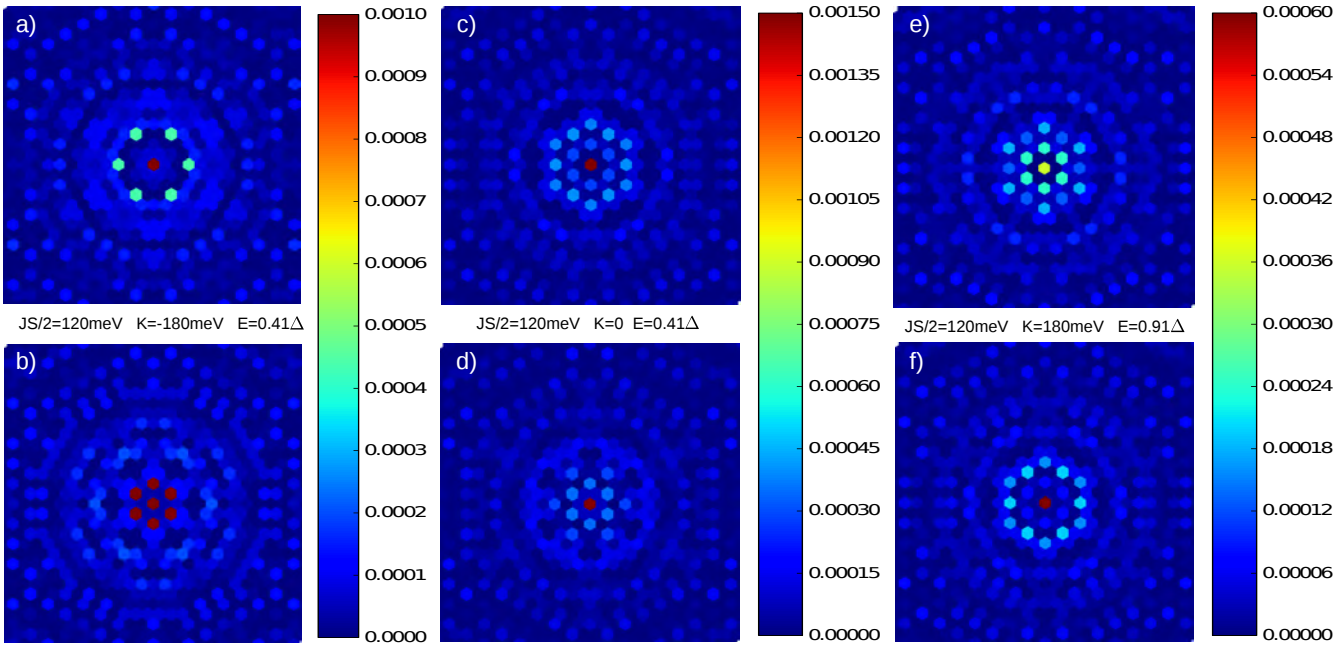

Figure 3.9: Same calculation as in Fig. 3.8, performed using band 2 instead of band 1.

$a = 3.444$Å the inter site distance. We also consider periodic boundary conditions and Fourier transform the Hamiltonian.

3.5.2 Numerical calculation

A magnetic impurity embedded in $NbSe_2$ hybridizes with the two bands and can potentially give rise to two Shiba in-gap states. Let us consider both bands separately. For most values of parameters characterizing the magnetic impurity, we find that band 2 gives a more isotropic Shiba state with a much smaller spatial extension. This is due to the fact that the two bands do not have the same anisotropy. Band 1 has a deeper saddle point than band 2 and is therefore more isotropic. Therefore, band 1 will provide more states near saddle point to the Shiba wave function. These states will be responsible of the longer spatial extension of the Shiba state associated with band 1 and also of its spatial anisotropy.

Since we are interested in long-ranged Shiba states to reproduce the experimental data, we thus focus on band 1. Fig. 3.8 presents the results obtained on a lattice of size $N \times M = 500 \times 500$ with a superconducting gap $\Delta = 1meV$ for different values of $JS/2$ and K using band 1. Fig. 3.9 shows the same calculation but using band 2. We see on these two figures that the best fit of our experimental data is obtained with band 1 that clearly shows a well defined 6 fold symmetry that is hard to see for band 2. We also observe that when varying the non magnetic diffusion parameter K the fine structure of the LDOS is modified but keeps the same symmetry and orientation. This is in accordance with the variation observed experimentally in the spatial pattern surrounding impurities of different types and thus different typical YSR eigen-energies.

3.5.3 Joint-DOS approach

The observed oscillations being of the order of the Fermi wave-length, they cannot be captured by a discrete tight binding model such as the one shown on figs. 3.8 and 3.9.

It is of interest to study what parts of the Fermi surface can give rise to the observed effects of magnetic impurities in 2H-$NbSe_2$. To do so we start by taking the tight binding parametrization of the band structure of 2H-$NbSe_2$ (using the coefficients defined in Tab. 3.2) for band 1. We do not include

here the case of band 2 as the tight binding calculation clearly shows that this band does not contribute much to the star shape of the YSR bound states.

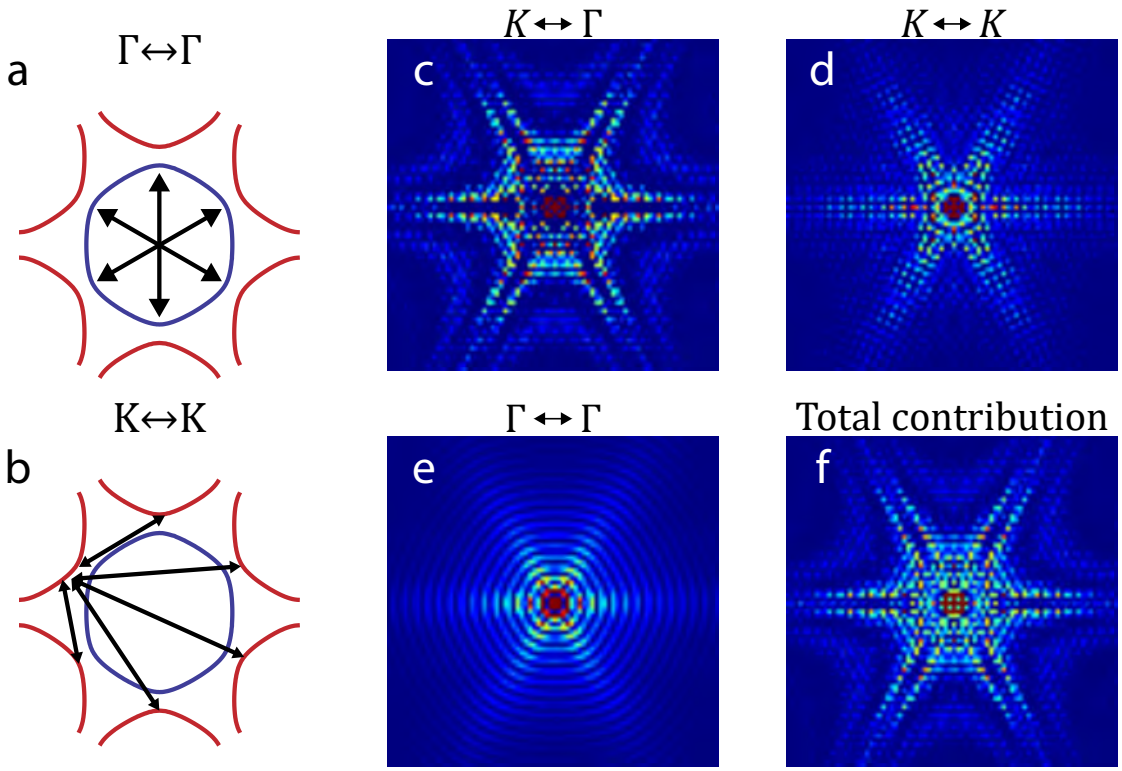

Figure 3.10: **Joint DOS calculation on the Fermi surface of 2H-$NbSe_2$:** a. and b. Principle in reciprocal space of the calculation. The two different sheets of the Fermi surface are represented in two different colors. On a. we represent the transition authorized in order to simulate electronic scattering from the inner Γ pocket (blue) onto itself while on b.we do the same for the K pockets (red). c. to d. 4 different calculations in real space obtained by calculating the auto-convolution of the Fermi surface by selecting some part of the Fermi surface of the band 1 (see Fig. 3.1). $K \leftrightarrow \Gamma$ refers to the convolution of the outer pockets with the inner pocket. $\Gamma \leftrightarrow \Gamma$ refers to the convolution of the inner pocket with itself. $K \leftrightarrow K$ refers to the convolution of the outer pocket with itself. "Total contribution" refers to the auto-convolution of the full Fermi-surface.

We then performed a joint-DOS calculation on the Fermi surface of 2H-$NbSe_2$. The principle of this method, widely used in cuprates [78, 79], is to couple parts of the Fermi surface weighted by the Fermi velocity $v_F(\boldsymbol{k})$ in order to reproduce the interference pattern around impurities or defects. Formally the joint DOS at the Fermi level is written simply as a convolution product[2]

$$j(\boldsymbol{k}) = \int_{FS} d^2k' \delta(\boldsymbol{k} - \boldsymbol{k'}) v_F(\boldsymbol{k} - \boldsymbol{k'}) \times \delta(\boldsymbol{k'}) v_F(\boldsymbol{k'}). \tag{3.4}$$

We are interested in the real space wave function associated to magnetic impurities and therefore to the Fourier transform of $j(\boldsymbol{k})$. As the Fourier transform of a convolution product is the product of the Fourier transforms of each term taken separately we have for the local density of states

$$\rho(\boldsymbol{r}) = |FT(j(\boldsymbol{k}))|^2 = |FT(\delta(k) v_F(k)) \times FT(\delta(k) v_F(k))|^2 = |FT(\delta(k) v_F(k)|^4, \tag{3.5}$$

[2] As the tight binding calculation is obtained for a 2D lattice we ignore the k_z direction. This omission is also justified by the 2D power law decrease of the YSR bound states measured experimentally.

when considering the full Fermi surface.

Now one has to consider what happens in the case of tunnel selectivity and selective electron diffusion. A natural separation of the Fermi surface in the case of 2H-$NbSe_2$ is between the surface around Γ (referred to as FS_Γ in the following and shown in blue on figs. 3.10.a and b.) and the surfaces surrounding the K points (referred to as FS_K in the following and shown in red on figs. 3.10.a and b.). When considering a tunnel selectivity that would favor the center of the Brillouin zone (as represented on fig. 3.10.a) we would write

$$\rho_\Gamma(\boldsymbol{r}) = |FT(\delta_\Gamma(k)v_F(k))|^4 \tag{3.6}$$

while a tunnel selectivity favoring the outside of the Brillouin zone (as represented on fig. 3.10.b) would be written as

$$\rho_K(\boldsymbol{r}) = |FT(\delta_K(k)v_F(k))|^4. \tag{3.7}$$

We can also include a selectivity of electrons undergoing a scattering from the Γ pocket to the K pockets and we would have in that case

$$\rho_{\Gamma\leftrightarrow K}(\boldsymbol{r}) = |FT(\delta_\Gamma(k)v_F(k)) \times FT(\delta_K(k)v_F(k))|^2. \tag{3.8}$$

These different configurations are represented on Figs. 3.10.c. to e.

On this figure we observe that the pattern most compatible with the experimentally observed interference fringes arise from the auto-convolution of the central part of the Fermi-surface (3.10.e). We also observe that the fine branches observed experimentally on the stars on the conductance maps fit better with this same configuration. The conclusions one can draw from this is that either our STM measurements are highly sensible to what happens in the center of the Brillouin zone or that there exists a real physical effects that would tend to privilege a scattering of the Cooper pairs and its constituting electrons inside the central pocket of the Fermi surface.

A major issue with STM is the problem of correctly taking into account the matrix element for the tunneling current [80] as it has been shown in the specific case of 2H-$NbSe_2$ [63]. These matrix elements can lead to an important selectivity over the Fermi surface and can help explain the difference between the joint-DOS results and the experimental measurement. These types of calculations do not claim to reproduce the fine characteristic of the YSR bound states as they do not include superconductivity at all. However they allow us to get a better intuition in relation to the mechanisms underlying the scattering of electrons in this specific context.

3.6 Deposited magnetic and non magnetic impurities

3.6.1 Magnetic Co impurities

We also performed experiments by depositing Co impurities over the 2H-$NbSe_2$ crystals. The main difference with the case of embedded impurities is that Co atoms are only present at the surface. On Fig. 3.11.a we show a topography of such sample with 10^{-3} ML of Co. We observe different types of configurations: single atoms and trimers. Like in the case of embedded impurities we observe a large variety of in-gap states (see Fig. 3.11.b).

Scanning over deposited Co impurities is much more difficult as they have a strong interaction with the STM tip that moves the atoms during spectroscopy measurements. This interaction causes the discontinuities in the conductance maps in figs 3.11.d-f at some impurity sites. We do not observe the same kind of long range effects of the magnetic atoms and this is detrimental to the observation of the spatial oscillations of the YSR bound states. On fig. 3.11.c we show a cut (from which was subtracted the bare $NbSe_2$ spectrum) in the conductance map following the white arrow drawn on fig. 3.11.a. As this cut passes through different magnetic atoms we observe different peaks at various energies inside the gap.

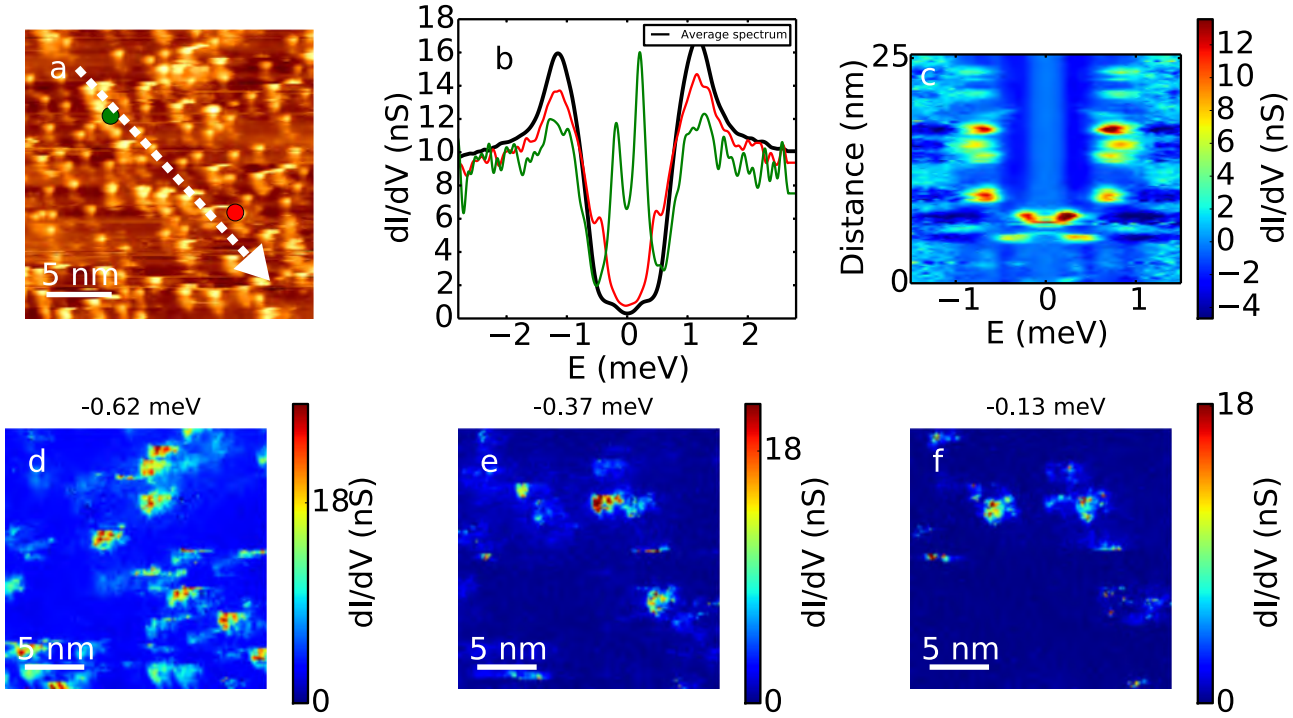

Figure 3.11: **Effect of adsorbed Co adatoms on 2H-$NbSe_2$:** a. Topography of a 20×20 nm^2 area of a 2H-$NbSe_2$ sample on which were deposited a total amount of 10^{-3} ML of Co. b. Selection of spectra over the area presented in a where the colors of the spectra refer to the colors of the markers on the topography. c. Diagonal cut in the spectroscopy from the top-left corner (0 nm) to the bottom right corner (25 nm). The color code corresponds to the obtained dI/dV from which was subtracted the bare $NbSe_2$ spectrum. d.-f. Conductance maps at 3 different energies inside the superconducting gap showing the typical spatial extent of the spectroscopic signatures of Co adatoms on 2H-$NbSe_2$.

There is also a difference in the amplitude of the measured peaks with embedded impurities. For instance the green spectrum in fig. 3.11 reaches to a value of 16 nS at its maximum that is higher than the background value of 10 nS. An hypothesis we have is that indeed, there could be some hydrogen atoms attached to the tip or to Co atoms enhancing the response in STS [81]. This effect was observed for a 2H-$NbSe_2$ sample that was kept for a long time in UHV at $T < 4K$ (about a month) before performing the Co evaporation. Because H is the first contaminant of UHV it is therefore the most probable contaminant one could think of. In comparison for a fresh new sample on which we deposited Co before directly transferring it to low temperature this effect was not observed as much.

To support the claim that H is responsible for the increased spectroscopic response one should perform controlled experiments in which a small hydrogen flux is send on the sample after the Co deposition. From such samples by performing a statistical analysis on the amplitude of the in-gap states observed it should be possible to establish a correlation between the quantity of H and the mean value of the amplitude of the in-gap states. Due to time constrains we were not able to perform this kind of experiment but we did observe a qualitative increase of the number of high amplitude in-gap states after moving the sample from the cryostat to the preparation chamber for a long time and back to the cryostat. Such manipulation usually results in an increase of the pressure in the STM chamber and a pollution of the sample. Hydrogen is also known to modify the magnetic properties of Co [82].

We also observe on some impurities several in-gap states. This behavior is close to what was observed by Shuai et al. [53] in the case of bulk Pb and can be explained by a larger value of the magnetic potential

associated to such defects.

Non magnetic impurities signature

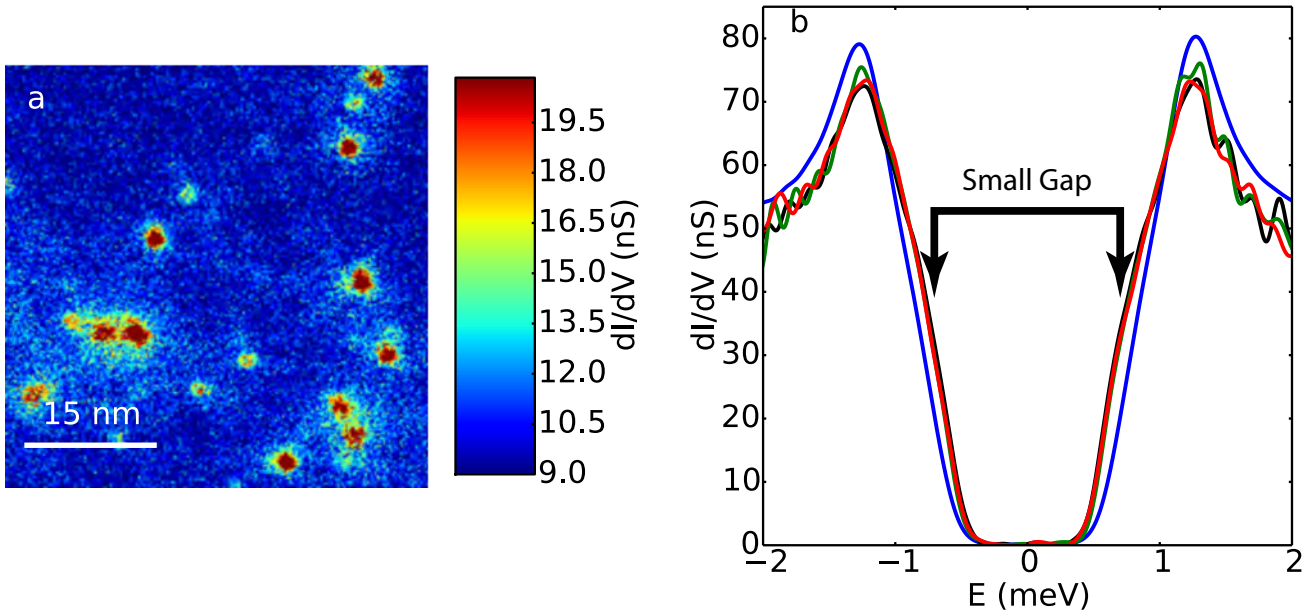

Figure 3.12: **Effect of non magnetic impurities in 2H-NbSe2:** a. Conductance map measured at the gap edge (0.61 meV) showing the signatures of non magnetic Ta impurities in 2H-$NbSe_2$. b. Spectra taken over individual defects (black, green and red curves) compared with the bare spectra of 2H-$NbSe_2$ (blue curve). The black arrows indicate the position of the small gap of 2H-$NbSe_2$.

The shape of the dI/dV spectra obtained on 2H-$NbSe_2$ is strongly dependent on the orbitals involved in the tunneling of electrons. For instance the spectra obtained when tunneling in the ab plane of 2H-$NbSe_2$ significantly differs from what can be observed along the c-axis as the weight of the large gap dominates in the first case and the small gap weight dominates in the second [63]. We will discuss in this section the effect of non magnetic impurities that locally modify the tunneling conditions and reveal a spatial dependence of the respective weight of the large and small gap. We will show that the difference observed on the fine structure of the gap edge manifests in spectroscopic signatures of the defects present in the system.

On Fig. 3.12.a we present a spectroscopic map over area of 50×50 nm^2 on 2H-$NbSe_2$. This map was taken at 0.61 meV on the gap edge. On this figure we observe approximately 15 defects appearing in red corresponding to a high conductance value. The spectra associated to these defects are all exactly the same and three of them are displayed on Fig 3.12.b. Unlike the magnetic impurities discussed before or the vortex lattice we do not see appearing any star-shaped pattern in the LDOS. The star shape we observed in the magnetic case was attributed to a coupling of the defect to the superconducting electrons and was shown to directly arise from the shape of the Fermi surface. The absence of such characteristic shape in Fig. 3.12 indicates that the spectroscopic signatures does not arise from a coupling of the defects to the superconducting electrons but rather to a matrix elements effects highlighting, in the two-gap pictures of 2H-$NbSe_2$, the contribution of one part of the gap rather than the other.

STM experiments on 2H-$NbSe_2$ [63] have shown that spectroscopy with the tip perpendicular to the xy plane was more sensitive to the large gap of 2H-$NbSe_2$ while tunneling with the tip parallel to the xy

plan was more sensitive to the smaller gap. The only case where the matrix element effect is suppressed is in the point contact regime. Because local defects break the translational invariance of the system, they modify the tunnel selectivity and because this selectivity is directly linked to the relative amplitude of the small and large gap probed in a dI/dV spectrum, non-magnetic impurities can modify the relative weight between the large and small gap. We observe here that it leads to the appearance of a contrast in the conductance maps at the energy of the small-gap.

Another aspect to mention is the density of impurities compared to what we observed in Fig. 3.2.d. Inside roughly the same area we were able to observe 5 impurities giving rise to a star-shaped pattern while in fig. 3.12 there are about 17 of them. The 1/3-4 ratio between magnetic and non magnetic impurities roughly corresponds to the ratio between Ta and Fe presented in table 3.2. Therefore we tend to attribute the defects appearing in Fig. 3.12 to the most present impurities i.e. tantalum. Ta is isoelectronic with Nb and thus do not modify the electronic structure and act as a weak scatterer in the crystals.

3.7 Conclusion

In this chapter we discussed the effect of various impurities embedded and absorbed on 2H-$NbSe_2$. We showed in the case of embedded magnetic impurities how the induced YSR states couple to the 2D Nb band in order to present a long range bound state in agreement with the theoretical calculations. Our measurements revealed that we were able to measure YSR bound states over distances ten time larger than for three dimensional systems. This long range behavior of the YSR bound states enabled us to probe the fine structure of the LDOS and to link the phase of the measured oscillations to the energy of the in-gap states. We discussed how the different parts of the Fermi surface influence the diffraction pattern and showed that the saddle points between the Γ pocket and the K pockets strongly increases the anisotropy of the system leading to six-fold symmetry states.

We then briefly discussed the case of embedded clusters of impurities and showed that we did not measure any sign of an additional in-gap state that would have signed a coupling between impurities.

In a third step we presented the results obtained when depositing Co atoms on top of 2H-$NbSe_2$ samples. We did not observe any long range effect of the YSR bound states in this configuration and interpret this as a weak coupling to bands 1 and 2 that completely suppresses the long range effect observed for embedded impurities.

Finally we briefly showed that due to the multi-gap structure of 2H-$NbSe_2$, non-magnetic impurities also produce spectroscopic signatures at the gap edge because of tunnel selectivity effects.

In the next chapter we will start from these results and compare them with what happens for Pb/Si(111) monolayers that are pure two-dimensional superconductors. We will first study individual impurities before moving to disordered magnetic clusters .

Chapter 4

Impurities in Pb/Si(111) monolayers

4.1 Introduction

The study of superconducting monolayers is a rich yet rather new field that started with the work of Zhang et al. [83] that proved that superconductivity could occur in the systems Pb/Si(111) and In/Si(111). Because such systems are made of a purely two-dimensional layer of Pb or In, they are the ultimate limitation in the reduction of the dimensionality from 3D to 2D. Numerical calculations seem to point toward a localization of the superconducting electrons between the Pb atoms (>90%) and the 3 first Si atomic layers [84, 85]. In these calculations superconductivity is attributed to phonon mediated interaction modified by the mismatch between the Si and Pb lattice parameter which leads to a softening of the phonon modes [86, 84].

In this chapter we will study how such superconducting 2D electron gases react to the presence of localized magnetic disorder. We will focus on two phases of the system Pb/Si(111) namely the $\sqrt{7} \times \sqrt{3}$ and the stripped incommensurate (SIC) phases. After a brief presentation of the system under study, we will present the results obtained on single magnetic impurities before moving to cluster of magnetic atoms.

4.2 Structural properties of Pb/Si(111) monolayers

The Pb/Si(111) system is extremely rich in monolayer structures as the phase diagram of this systems contains more than 4 well distinct phases and 15 intermediate phases for Pb coverages ranging from 1/3 monlayer (ML) to 4/3 monolayers [87, 88, 89].

The most studied phase is the $\sqrt{7} \times \sqrt{3}$ phase where the $\sqrt{7}$ and $\sqrt{3}$ values refer to the lattice parameters of the 1×1 surface of the Si(111) (see fig. 4.1.a). This phase appears below 270 K [89] and corresponds to a nominal coverage of 1.2 ML. This phase exhibits a strong 1D behavior and is seen on STM images as thin lines composed of a dense arrangement of Pb atoms (see Fig. 4.1). As the 1×1 substrate possesses a threefold symmetry, we will find on the same sample three different orientations of the $\sqrt{7} \times \sqrt{3}$ phase turned by 120° between each other.

A second phase of the Pb/Si(111) system is the hexagonal incommensurate phase (HIC) (see fig. 4.1.b). This phase is formed by combinations of triangular domains in two different orientations [90].

A third phase we will talk about in the next chapter is the 3×3 phase (see fig. 4.1.c). This phase and the $\sqrt{3} \times \sqrt{3}$ (see fig. 4.1.c) possess the same coverage and the transition from one the $\sqrt{3} \times \sqrt{3}$ to the 3×3 structure is obtained under the structural critical temperature of 86 K [91].

We also mention the existence of the SIC phase (see fig. 4.1.d) which is close to the HIC structure but with meandering walls not hexagonaly ordered and appears for higher coverages (of the order of 1.30 ML). In this phase, due to the high density of Pb on the surface we will often obtain a coexistence of the Pb monolayer with small islands with a maximum height of a few atomic layers.

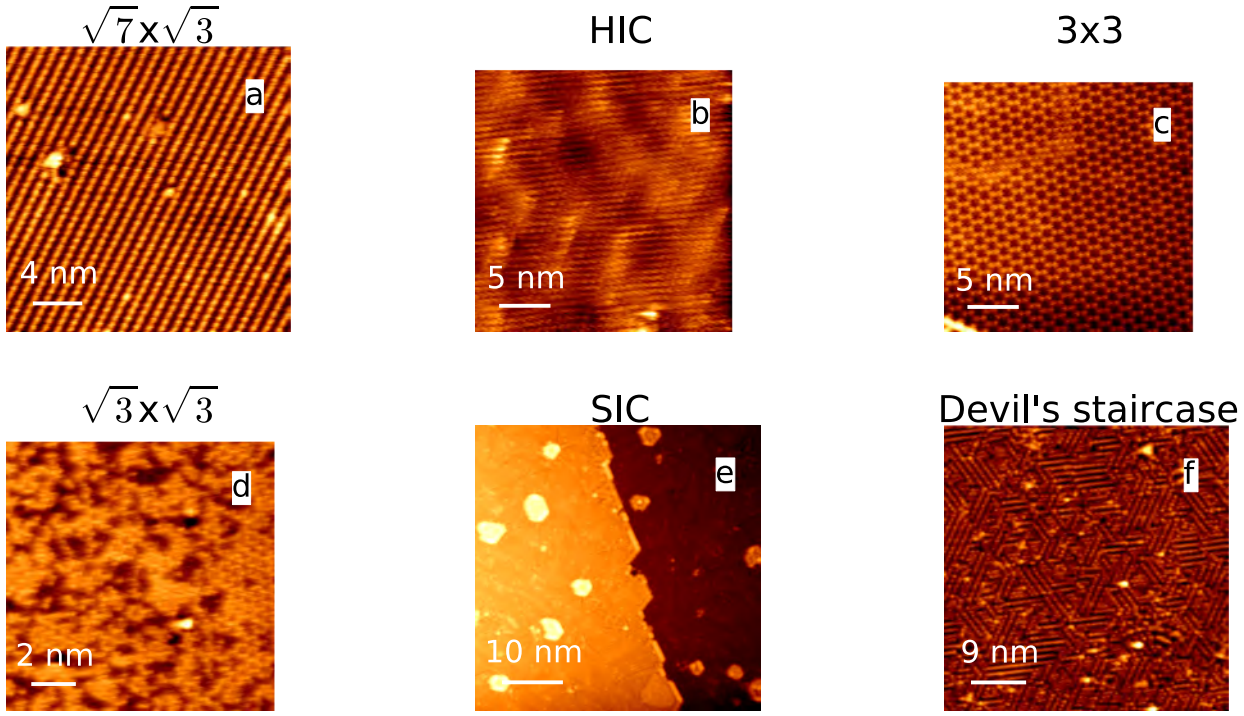

Figure 4.1: **Phases of the Pb/Si(111) system:** The name of each phase is indicated over each picture.

Finally there exists a pseudo-phase called "devil's staircase". This pseudo-phase contains many phases with different reconstructions borrowing periodicity from the $\sqrt{7} \times \sqrt{3}$ or $\sqrt{3} \times \sqrt{3}$ phases (see fig. 4.1.f for an example). We call it a pseudo-phase as its atomic structure can highly vary depending on which extremity of the coverage spectrum we are. We will see later that it is possible in this configuration to obtain a 1D-like phase (the $2\sqrt{7} \times \sqrt{3}$ close to the $\sqrt{7} \times \sqrt{3}$ phase) appearing as an alternation of two close rows of Pb atoms and one isolated row. There has been about 15 phases reported so far in the devil staircase regime [92, 88].

4.3 Superconductivity in monolayers

Superconductivity in Pb and In monolayers was first discovered in 2010 by Zhang et al [83]. In this paper they studied three different systems, two of Pb/Si(111) and one of In/Si(111). The two phases of Pb they studied are the SIC and $\sqrt{7} \times \sqrt{3}$ phases. They showed that these phases open a gap that disappears around 1.8 K and 1.6 K respectively. The temperature dependance of these gaps follows nicely the BCS theory and they were also able to measure the LDOS associated to vortices at different fields in the SIC phase.

On fig. 4.2 we present how vortices appear on a Pb/Si(111) sample in the SIC phase. This structure was obtained for a coverage of 1.4 ML instead of the nominal 1.3 ML for the perfect structure. The Pb in excess forms 1 ML high Pb nano-islands. These nano-island do not play any significant role in the behavior of superconductivity in the system and only slightly increase the disorder thus leading to a slightly smaller gap compared to the case of Zhang et al. [83]. Fig. 4.2.a shows the topography of a 690×690 nm^2 area that we studied at different magnetic fields.

Figs. 4.2.d.-g. show the zero bias conductance of the same area with applied magnetic fields between 0 and 40 mT. For $B \neq 0$ the conductance maps clearly show the appearance of vortices and the increase of their density with the amplitude of the magnetic field.

By studying the dependence of the LDOS around an individual vortex we can obtain the value of the coherence length of the superconductor through the heuristic formula[93, 94, 95]

$$\rho(x,0) = \nu_0 + (1-\nu_0)\left(1 - \tanh\frac{x}{2\xi}\right). \tag{4.1}$$

We thus take a cut through the isolated vortex of fig. 4.2.e and fit the obtained LDOS with the above formula. We obtain from this fit a coherence length equal to 55 nm in accordance with previous determinations using the critical field H_{c_2} and its relation to the coherence length $H_{c2}(T) = \Phi_0/2\pi\xi^2$ [83, 96].

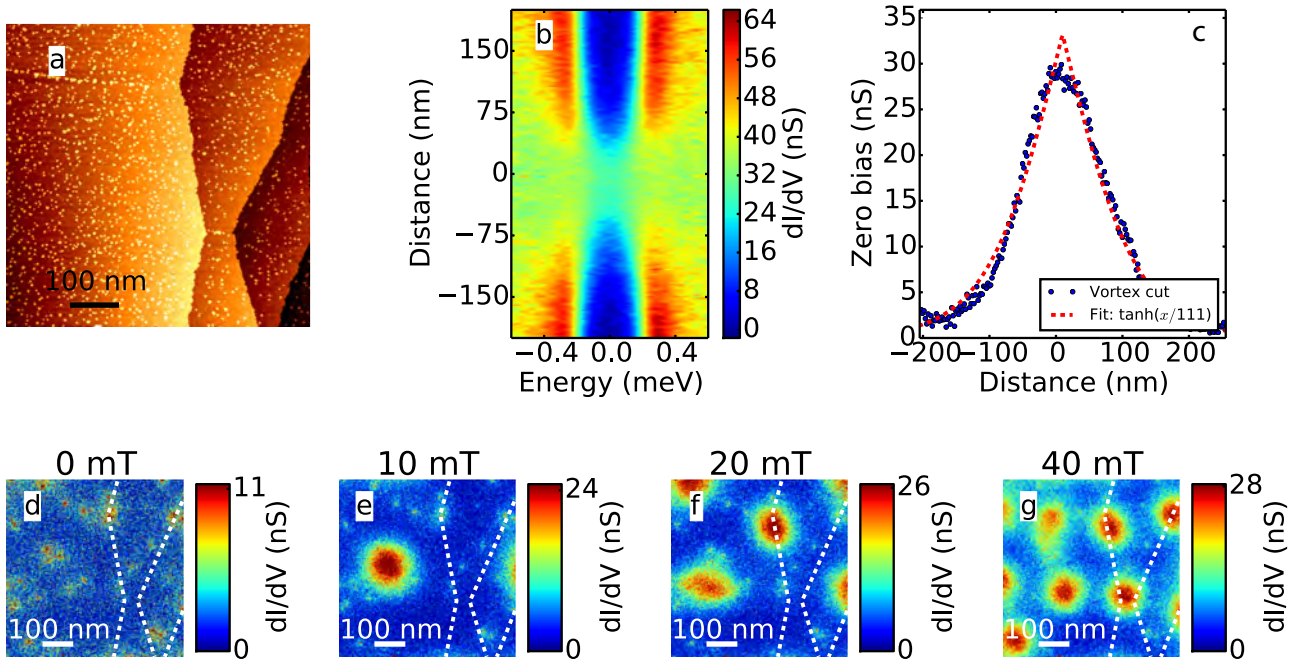

Figure 4.2: **Vortices in SIC phase of Pb/Si(111):** a. Topography of a 690×690 nm^2 area of a Pb/Si(111) sample in the SIC phase. b. Energy and space dependence of the LDOS measured through a vortex core. c. Fit of the zero bias conductance using eq. 4.1 leading to a coherence length $\xi = 55$ nm. d.-g. Conductance maps at zero bias for 4 different magnetic fields (0 mT, 10 mT, 20 mT and 40 mT). The white dashed lines represent the single atomic steps present on the sample visible in the topography a.

The first observation that can be made on the behavior of vortices in this system is the fact that vortices are rather round and do not seem to "see" the atomic steps. We see that by increasing the magnetic field vortices appear without any pinning effect. This suggest that superconductivity is very homogeneous contrary to what has been observed for the $\sqrt{7}\times\sqrt{3}$ that tends to form Josephson junctions on the step edges [96].

For monolayer systems we are in the diffusive limit for superconductivity[1]. As a consequence, the vortex cores do not exhibit Caroli-Matricon-de Gennes states and we simply observed a normal state as shown by the constant conductance in fig. 4.2.b for $d = 0$ nm.

Because the superconducting properties of the Pb/Si(111) system originate from the interaction over 3 atomic layers with the Si substrate, the structural differences of the surface Pb layer do not modify

[1]The coherence length $\xi \propto \sqrt{\xi_0 l}$ is much larger than the mean free path ℓ

unduly the coherence length, critical temperature and superconducting gap. This can be verified on the coherence length for the $\sqrt{7} \times \sqrt{3}$ ($T_c = 1.52\ K$) and SIC ($T_C = 1.83\ K$) phases for instance. Starting from the $\sqrt{7} \times \sqrt{3}$ phase, every other phase with a higher Pb coverage (SIC, HIC, devil's staircase) will present a superconducting transition at temperatures low enough (see tab. 4.1). While the coverage of these phases can have some overlap, the main difference to obtain one phase rather than the other comes from the preparation conditions. By modifying the deposition temperature and time as well as the annealing temperature we will go through the different phases and obtaining the right phase in an homogeneous way can be very difficult.

Coverage	$\sqrt{7} \times \sqrt{3}$	SIC	HIC	Devil's staircase
Critical temperature (SC)	1.52 K	1.83 K		
Coverage	<1.2 ML	>1.3 ML	1.22 ML - 1.3 ML	1.2 ML - 1.33 ML

Table 4.1: Phases of Pb/Si(111) and their superconducting (SC) critical temperatures and Pb coverages

4.4 Individual impurities

4.4.1 Case of the $\sqrt{7} \times \sqrt{3}$ phase

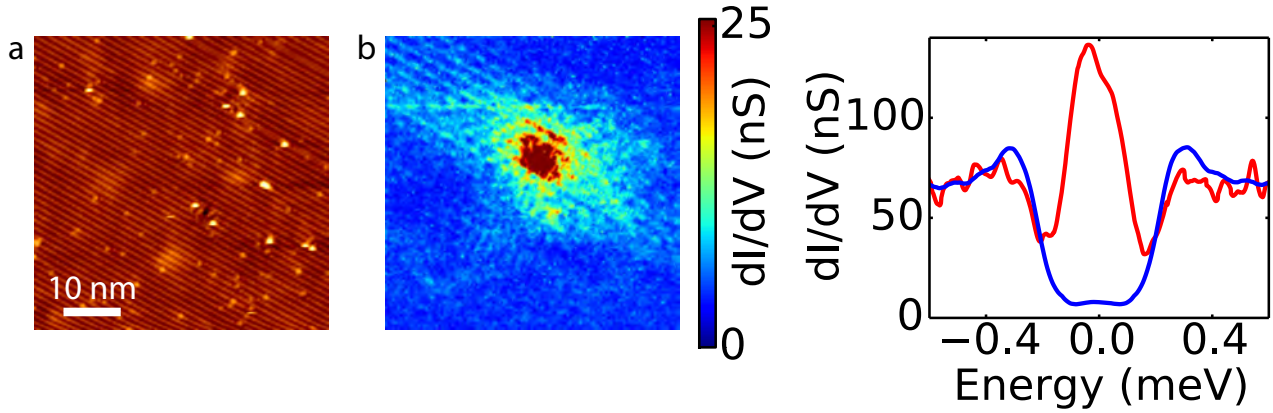

Figure 4.3: **Shiba states in $\sqrt{7} \times \sqrt{3}$ structure:** a. Topography of a 51×51 nm^2 area with atomic resolution. b. Spectroscopy of the same area around the Fermi level averaged over 20 energy pixels (0.15 meV). c. Selected spectra at the maximum intensity site (red), and 15 nm (blue) away from the impurity center.

We will start our discussion of magnetic impurities in Pb/Si(111) monolayers by focusing on the well ordered $\sqrt{7} \times \sqrt{3}$. The impurities we will discuss are not chemically identified as they are natural contaminants of our Pb source and are evaporated conjointly. On fig. 4.3 we present the results obtained for an isolated impurity embedded in the Pb layer in the $\sqrt{7} \times \sqrt{3}$ phase. In this figure the considered magnetic atom is located in a single domain and we do not have any domain wall close to it. The spatial extension of the impurity is even larger than it was in 2H-$NbSe_2$ as we obtain a spectroscopy signal through the whole scanning area of a 51 nm width. This extent can be explained by the large coherence length of the $\sqrt{7} \times \sqrt{3}$ phase that is around 50 nm [96]. It can also be explained by the extremely strong amplitude of the two peaks at $\pm 0.058 \pm 0.002\ meV$ (see fig. 4.3.c) that go as high as 130 nS for the

negative bias one in the same fashion as in the case of the disordered HIC phase discussed previously. In the perpendicular direction the extent of the YSR bound states is much smaller and most of the signal has vanished 10 nm away from the impurity center.

Due to the close proximity in energy and the limitations imposed by the thermal broadening of the peaks at 300 mK we cannot distinguish clearly the positive bias states from the negative ones. It is thus not possible to study in this specific case the phase of the YSR states as we did for 2H-$NbSe_2$.

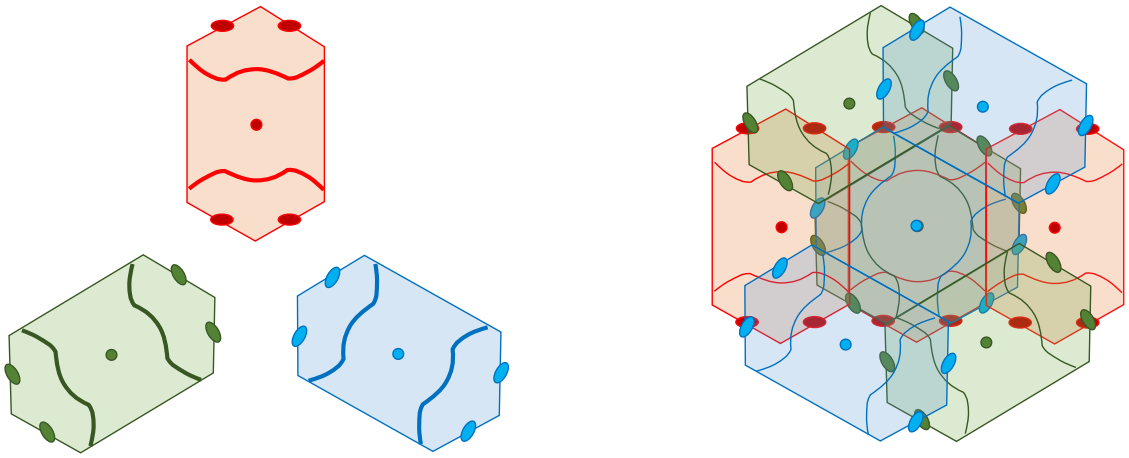

Figure 4.4: **Fermi surface of the $\sqrt{7} \times \sqrt{3}$ phase:** Fermi surfaces in each of the three different isolated domains (left) and combined (right) (adapted from [97]). The Fermi surface associated to the domain presented on fig. 4.3 would correspond to the blue one on the left.

As we did for 2H-$NbSe_2$ we will discuss the pattern of the YSR bound states observed experimentally in relation with the shape of the Fermi surface of the system. In this part we will base our discussion on the ARPES measurements found in [97]. In this paper the authors compared the signal averaged over the three orientations of the domains obtained by ARPES to Fermi surfaces calculated from DFT. Kim et al. found a good agreement between theory and experiment and proposed a Fermi surface with the form presented on fig. 4.4. This Fermi surface is first characterized by two wavy lines crossing the $\sqrt{7} \times \sqrt{3}$ Brillouin zone with little dispersion along the transverse direction. This open Fermi sheet is accompanied by 3 pockets, one at the Γ point and the two others at the frontier with the second Brillouin zones[2].

Another team [98] has proposed another DFT based model for the $\sqrt{3} \times \sqrt{7}$ phase. They obtained slightly different results but the best agreement with ARPES is given by the interpretation of Kim et al. [97] that we described above.

Perpendicular to the Pb lines direction a clear periodicity is observed in the conductance map of fig. 4.3.b that corresponds to twice the lattice parameter ($\simeq$ 3 nm) of the system along the same direction. This double periodicity is better seen on the Fourier transform of the conductance map presented on fig. 4.5. On this figure we represented the first Brillouin zone of the $\sqrt{7} \times \sqrt{3}$ with white lines. Clear spots

[2]These last two pockets are seen as 4 pockets on fig. 4.4 because of their position between two different Brillouin zones but there are actually only two independent ones.

appear at the frontier between the first and second Brillouin zone in the same direction as the interline periodicity (I). These spots are responsible for the doubling of the periodicity in spectroscopy for the YSR bound states. Along the Pb lines we can observe a spatial oscillation that is difficult to precisely quantify (approximately 4 nm). This oscillation corresponds in the Fourier map to the signal observed (II) crossing the first Brillouin zone along the same direction as the previously discussed spots between the Γ point and the apexes of the zone.

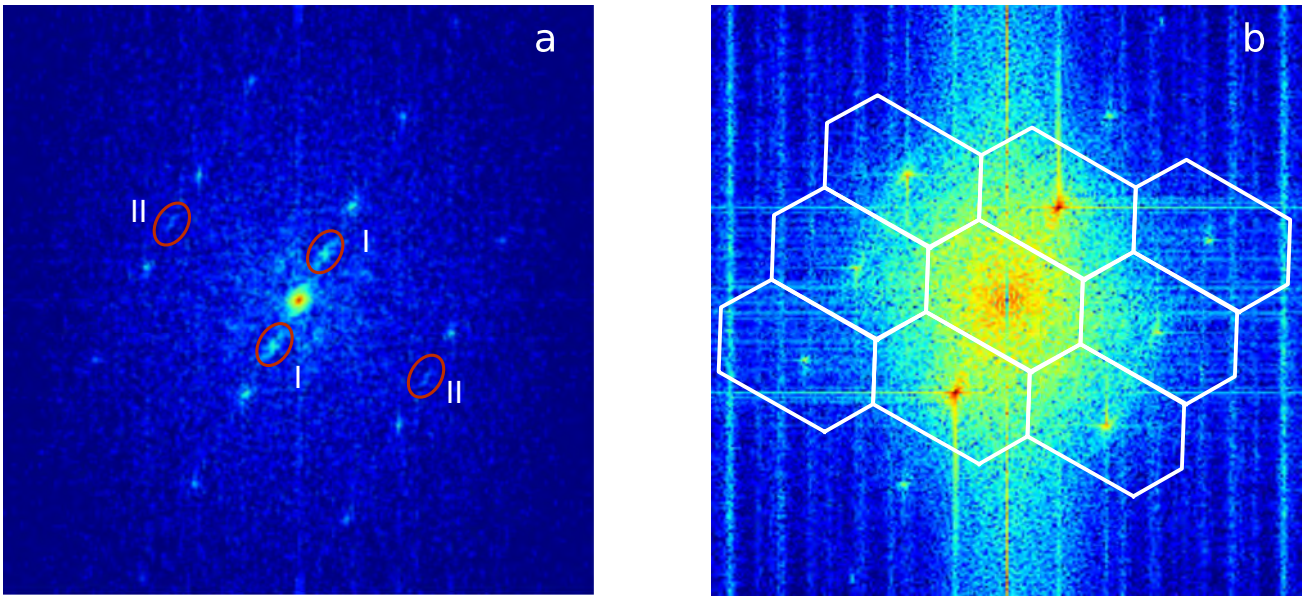

Figure 4.5: **Fourier transform of the LDOS around an impurity in $\sqrt{7} \times \sqrt{3}$ phase:** a. Fourier transform of the signal presented on fig. 4.3.b. b. Fourier transform of the corresponding topography. The white lines represent the different Brillouin zone in the reciprocal space and the red ellipses indicate the position of the scattering wave vectors in reciprocal space.

Unlike 2H-$NbSe_2$ there is no tight binding model describing the full band structure of the Pb/Si(111) $\sqrt{7} \times \sqrt{3}$ system yet. It is therefore not possible to obtain an accurate Fermi surface from which to perform joint-DOS calculation. Our team at the INSP is currently working in collaboration with J. A. Silva-Guillén and L. Chiroli from Madrid university to obtain a DFT model of the $\sqrt{7} \times \sqrt{3}$ phase and perform quasi-particle interference calculations. However, based on the ARPES measurements performed on this system we can try to obtain a qualitative agreement by finding an approximation of the Fermi surface from which we could extract the main features of the YSR pattern.

To simplify the discussion of the different combinations we will use below we start by labeling (following [97]) the parts of the Fermi surface as follows (see fig. 4.6):

- The center pocket will be referred to as the Γ **pocket**
- The four pockets at the limits of the first Brillouin zone will be referred to as S_1 **pockets**
- The two crossing lines will be referred to as S_2 **lines**

From ARPES data we observe that the spectral weight is mostly located on the S_1 pockets. The S_2 lines present a larger spectral weight at the points where the lines abruptly change their direction. Finally the

weight at the Γ pocket is rather small compared to the previously discussed parts of the Fermi surface. Obviously ARPES is subject to matrix elements effects and our simulations do not claim to be a perfect description of the system. Our "model" Fermi surface is presented on fig. 4.6.e.

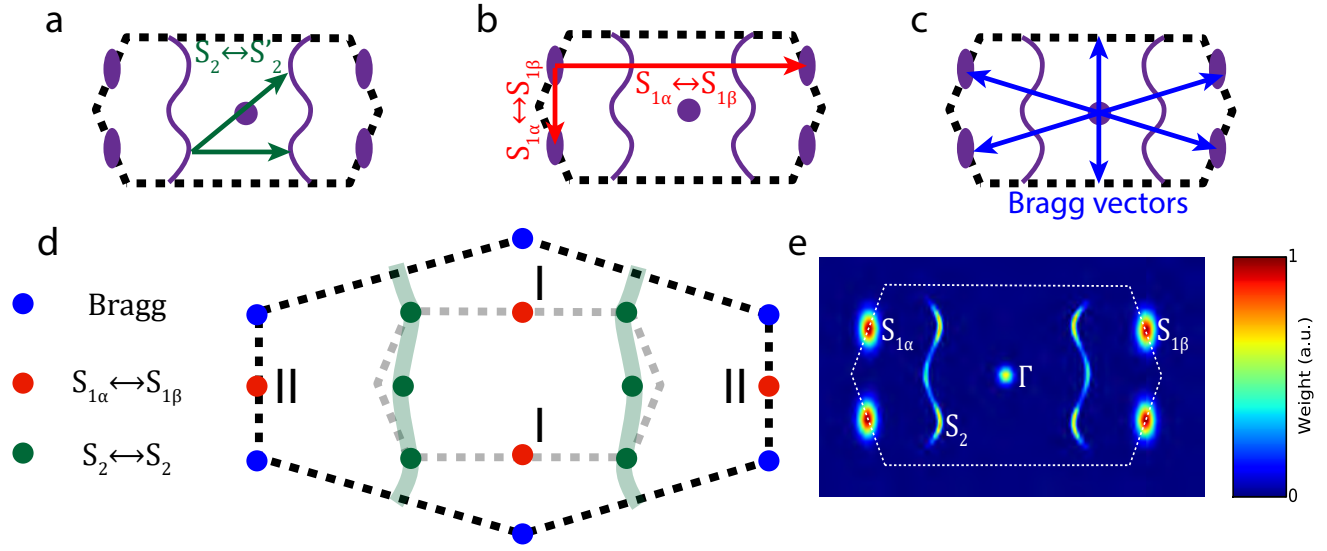

Figure 4.6: **Transitions and Fermi surface for the $\sqrt{7} \times \sqrt{3}$ phase:** a. Schematic representation of high DOS scattering from S_2 pockets onto themselves. b. Schematic representation of transitions from $S_{1\alpha}$ pockets to $S_{1\beta}$ pockets c. Schematic representation of transitions from S_1 pockets of the same type. d. Diffraction spots in reciprocal space related to the transitions described in a., b. and c. The dark dashed line represent the lines joining the first Bragg points. We kept the First Brillouin zone as a guide for the eye in light grey. e. Model Fermi surface based on ARPES data on this system extrapolated for a single domain. The color code refers to the density of states for each point of the F.S.

Using this Fermi surface we can now try several combinations of the different parts of the Fermi surface to compute the joint DOS. We present the result of this calculation on fig. 4.7.a.-f. The analysis of the Fourier transform of the joint DOS makes clear the doubling of the periodicity we observe as we obtain weight at the top and bottom edges of the first Brillouin zone (I), half distance between the Γ point and the vertical Bragg peaks. This periodicity originates from the diffusion of electrons between the different S_1 pockets of the Fermi surface and to a smaller extent from the warped part of the S_2 bands. We also recover the periodicity along the x axis coming from the same type of transitions.

We reiterate that such calculation does not claim to perfectly reproduce the complex physics of the YSR bound states. For instance the spatial extent of these states directly depends on the coherence length of the system, a parameter that joint-DOS calculations do not account for. In the same way we are not capable to extract any information about the phase difference between the positive and negative bias states as such a parameter is governed by the amplitudes of the magnetic and non magnetic diffusion potentials. However the good agreement between our phenomenological calculations and the experimental results in both 2H-$NbSe_2$ and Pb/Si(111) $\sqrt{7} \times \sqrt{3}$ phase show that independently of the restrictions we mentioned, joint DOS calculations are a good way to predict the patterns that the YSR bound states will present around magnetic impurities. This is no real surprise as this technique has been widely used before in cuprates [78, 79] but our results indicate its robustness.

Studying the geometry of the Fermi surface is thus strongly indicative of the final structure of the YSR bound states. Performing such study helps identify what system would be of interest when trying to obtain chains of magnetic impurities for instance as a strongly 1D behavior of the joint DOS would

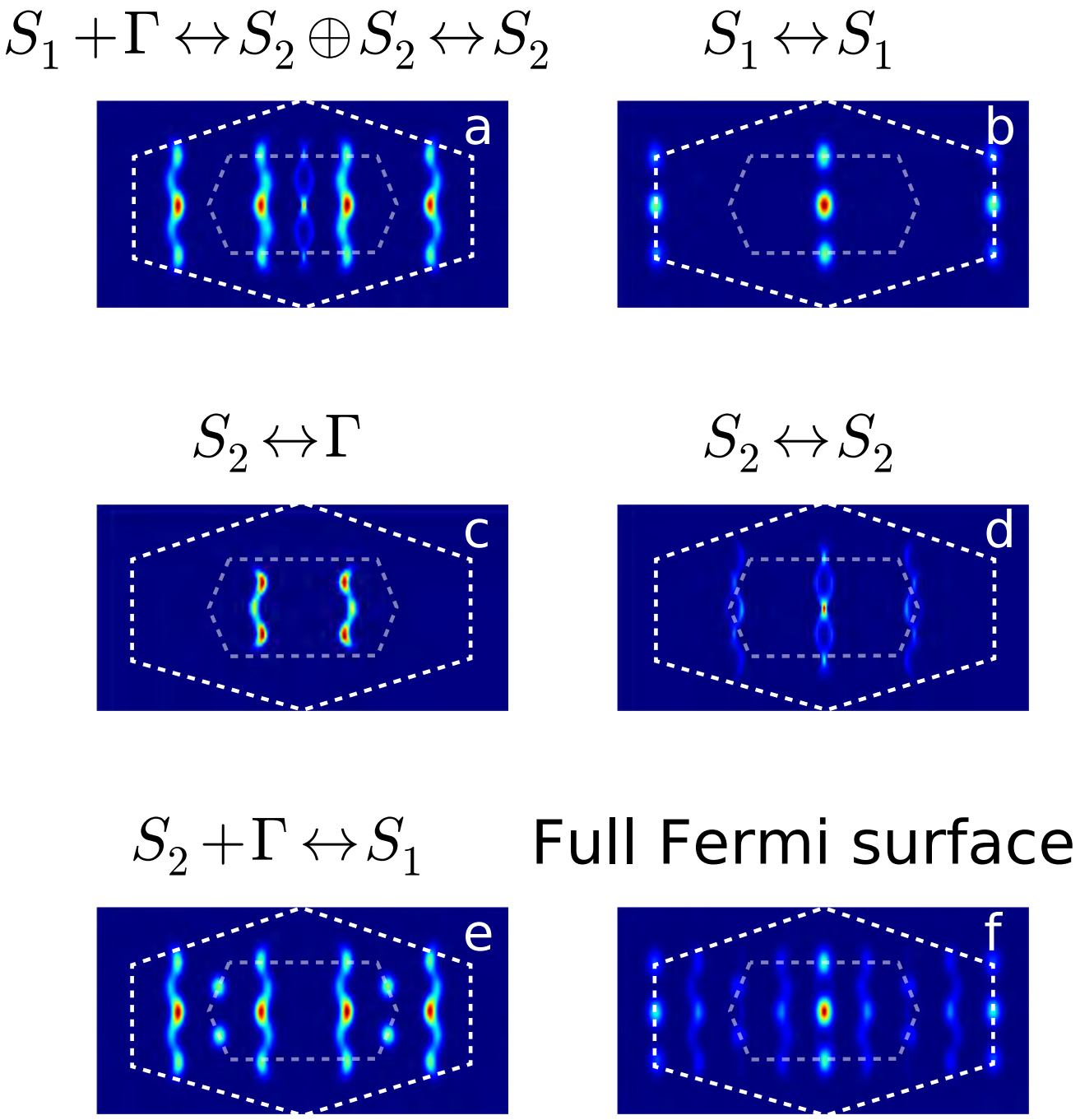

Figure 4.7: **Joint DOS calculation in the $\sqrt{7} \times \sqrt{3}$ structure:** Reciprocal space calculation of the joint DOS for the different possible transitions. The notations refer to those used in fig. 4.6.

indicate a strong preferential direction for the YSR bound states. We would therefore have a possibility to obtain a larger extent of the YSR bound states along said direction that could then be used in order to obtain a wider range of parameters with which to play to couple magnetic impurities.

4.4.2 Non magnetic impurities in $\sqrt{7} \times \sqrt{3}$ phase

We have seen previously that non-magnetic disorder does not induce in-gap states in s-wave superconductors. However, Rashba spin orbit interaction at surfaces is expected to lead to triplet correlations and p-wave superconductivity that becomes sensitive to non-magnetic disorder. In this section we discuss the results obtained in the literature concerning metallic monolayers and present results on the $\sqrt{7} \times \sqrt{3}$ phase in relation to the effect of non-magnetic disorder.

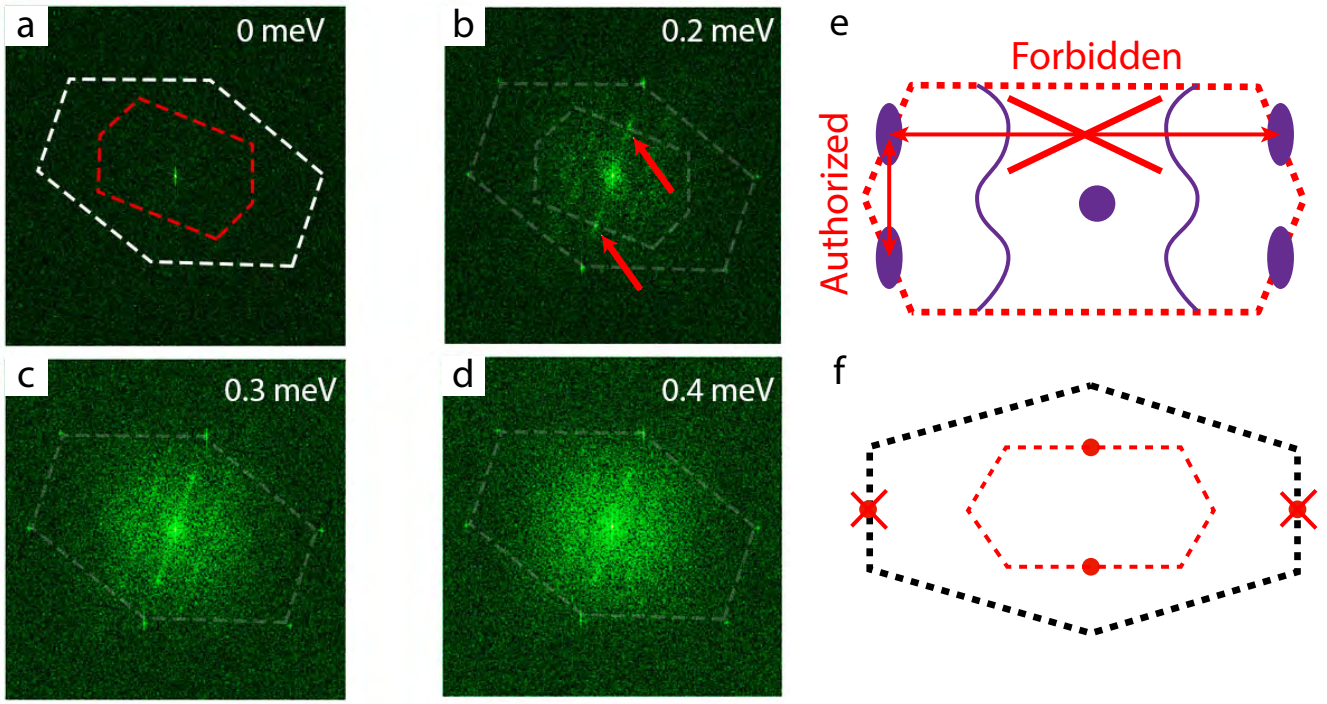

Figure 4.8: **Non-magnetic disorder induced states:** a.-d. Fourier transform of conductance maps obtained from quasiparticle interferences at 4 different in-gap energies. The red dashed lines indicates the first Brillouin zone and the white dashed line its autoconvolution. The red arrows on b. indicate the position of the diffusion spots in the Fourier transform. e. Schematic representation of the authorized and forbidden transition from the different part of the Fermi surface. f. Schematic representation of the expected joint-DOS pattern in the reciprocal space.

Transport measurements in parallel magnetic field show that the monolayer of Pb grown on GaAs(110) shows no difference in a field of 14 T [99] which is one of the effect predicted of Rashba spin-orbit coupling [100]. This effect strongly advocates for a very high spin orbit coupling in the Pb monolayer. Another similar system Tl-Pb/Si(111) was also shown to possess a strong spin-orbit interaction [101].

Another possibility to probe the spin-orbit interaction in the Pb monolayer is to look at the effect of non magnetic disorder. Due to the Anderson theorem, in-gap states are not expected in the case of an s-wave superconductor. However for a p-wave superconductor there is no such fundamental limitation.

We have measured in our team that for the $\sqrt{7} \times \sqrt{3}$ phase we had a gap filling as well as a fluctuation of the height of quasiparticle peaks [96]. These fluctuations are directly related to the existence of a strong spin-orbit coupling in this material and to p-wave superconductivity as only non-magnetic disorder was

present in these experiments.

By measuring conductance maps of the $\sqrt{7} \times \sqrt{3}$ phase far from any YSR bound states we observed fluctuations of the quasiparticle peaks amplitude as well a gap filling at the gap edge. We were able to perform a Fourier transform analysis of these maps and the results are presented on fig. 4.8. On these FFT maps we observe that inside the superconducting gap of the Pb monolayer (i.e. $|V| < 0.3$ meV) we observe a signal associated to electron scattering. We can compare these Fourier transform to what we had obtained for YSR bound states in the case of a single magnetic defect (see fig. 4.5.a). The only spots we observe that also appears on fig. 4.5 are the ones located exactly at the limit of the first Brillouin zone (labeled I) responsible for the doubling of the periodicity in the direction perpendicular to the atomic lines. The two other external points (labelled II) that we expected to appear on the line joining the Bragg spots are not present in the case of states induced by a non magnetic interaction.

The absence of these diffusion spots indicate that the lateral diffusion of electrons ($\Delta k_y = 0$) are only permitted if the spin is included in the interaction. Such link between space and spin is another strong indicator of the presence and the importance of spin-orbit coupling in the Pb/Si(111) monolayer. Calculations are ongoing in order to derive a tight-binding model of the $\sqrt{7} \times \sqrt{3}$ phase from DFT.

4.4.3 Disordered phases

Now that we have seen what happens to the YSR bound states for the ordered $\sqrt{7} \times \sqrt{3}$ phase, we will now study the effect of disorder by looking at the devil's staircase and SIC phases that do not present a long range crystalline order.

On fig. 4.9 we present the topography (a) and spectroscopy (b) of a highly anisotropic phase in the devil's staircase domain. Like for the $\sqrt{7} \times \sqrt{3}$ case it appears in the form of chains with an atomic lattice parameter much longer in one direction than the other. As a consequence we will observe three different orientations of these lines rotated from each other by 60°. The in-gap peaks are well visible and separated inside the superconducting gap as they were before (see fig. 4.9.c). However by looking at the conductance map we see that the YSR bound states manifest themselves in the form of elongated shapes.

We see that the elongation of the YSR bound states follows the orientation of the characteristic lines observed in topography. This anisotropy follows the form of the structure of the lattice in the reciprocal space [102, 97, 98] as we have discussed more in details in the case of the $\sqrt{7} \times \sqrt{3}$ phase.

The SIC phase is more disordered and does not possess a well defined crystalline symmetry. As it can be seen on fig. 4.10.a it is made of small patches arranged in a somewhat triangular pattern but with no long range order. Because the shape of the spectroscopic signature of the YSR bound states observable by STM depends mostly on the shape of the Fermi surface, in order to obtain a clear pattern it is necessary to have a well defined structure in reciprocal space. The absence of a well-defined long-range crystalline order in the case of SIC prevents the establishment of a clear pattern for the Fermi surface and the resulting YSR bound states appear as speckle-like patterns.

However if the disorder only appears at scales larger than the typical extension of the YSR bound states, it becomes once again possible to define locally a clean reciprocal space structure for the Fermi surface. In the case of the devil's staircase phases it is possible to obtain domains large enough to satisfy this condition. In particular when these phases are highly anisotropic (in the form of 1D chains for instance) we can once again observe a specific dispersion of the YSR bound states.

4.5 Towards the Abrikosov-Gorkov limit

We have seen in the previous section how the disorder of the Pb monolayer influenced the YSR bound states. We will now study arrays of randomly distributed impurities with random spin orientation in the same disordered SIC phase. The effect of a disordered array of magnetic impurities in a superconductor was first studied theoretically by Abrikosov and Gor'kov [29]. They showed that two main features were to be observed in this condition. First the superconducting coherence peaks are expected to disappear

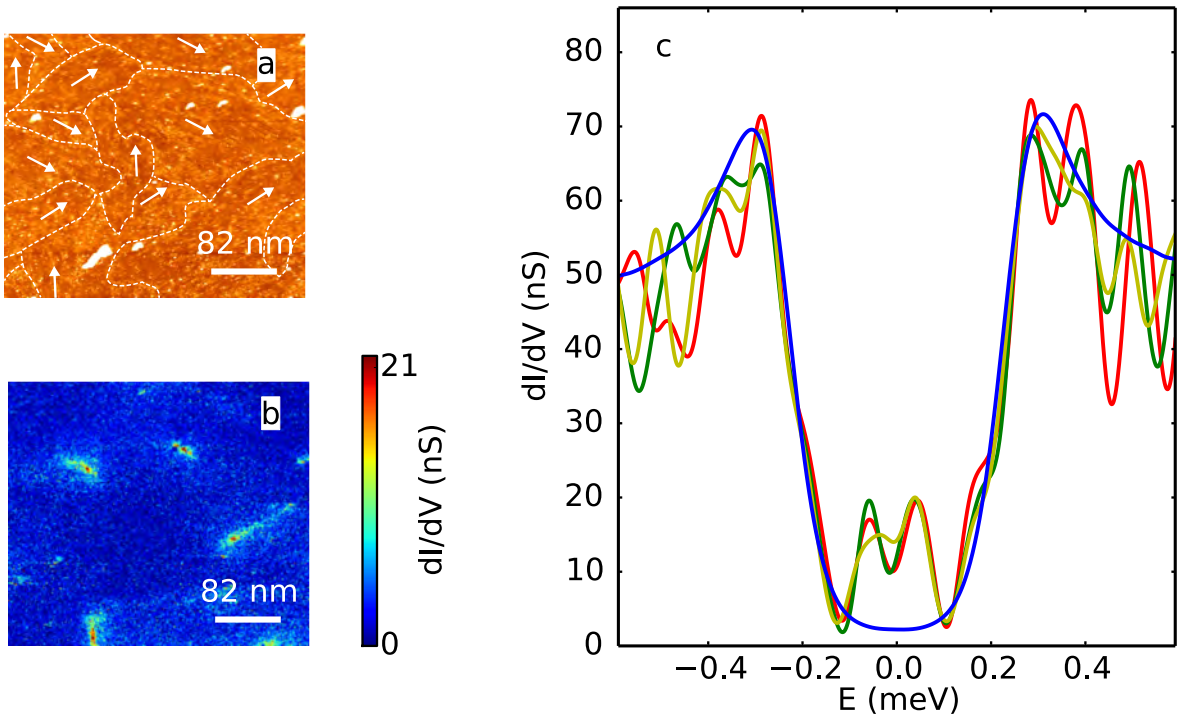

Figure 4.9: **Magnetic impurities in a 1D phase of the devil's staircase phase :** a. Topography of a 413×363 nm^2 area in one of the devil's staircase phase of Pb/Si(111). This 2D phase is highly anisotropic and we can distinguish the three orientations of the domains. The white arrows indicate the orientation of the linear domains delimited by the white dashed lines. b. Conductance map integrated over the superconducting gap showing the YSR bound states in this system. c. Selection of spectra from the spectroscopy shown on fig. b. The blue spectrum is the average spectrum over the whole area.

due to the lost of coherence in the system. Then a gap filling is expected in relation to the appearance of a band of Shiba states. This model is usually well accepted and was very successful in the interpretation of experimental data. We will show here that this is not always the case and that the quasiparticle peaks can be conserved in the presence of magnetic disorder.

4.5.1 Growth conditions

We studied clusters of Co atoms buried below a monolayer of Pb in the SIC phase. We first deposit 10^{-2} ML over the 7×7 reconstructed Si(111) at room temperature. By annealing the Si sample covered with Co atoms by direct current at 375°C, we observe a migration of the magnetic atoms toward the step edges as shown on fig. 4.11.a. This behavior is strongly different from the one observed in [103] for a similar system with a smaller annealing time.

This migration is stopped by step edges and defects in the Si substrate which are mainly the 7×7 twins. On fig. 4.11.b we present a zoom on one of the accumulation area. Those twins appear at places where the steps are in form of wedges and facilitates the accumulation of Co atoms. The disorder we observe seems to indicate that the individual Co atoms do not form any coherent magnetic domain and will behave as individual magnetic scatterers. On the zoomed topography we observe that the Co atoms do not form dimers or trimers as they did in the case of 2H-$NbSe_2$. They rather stay in the form of individual atoms arranged in a very disordered way.

The second step of the preparation is to cover the sample with Pb in the usual proportions before

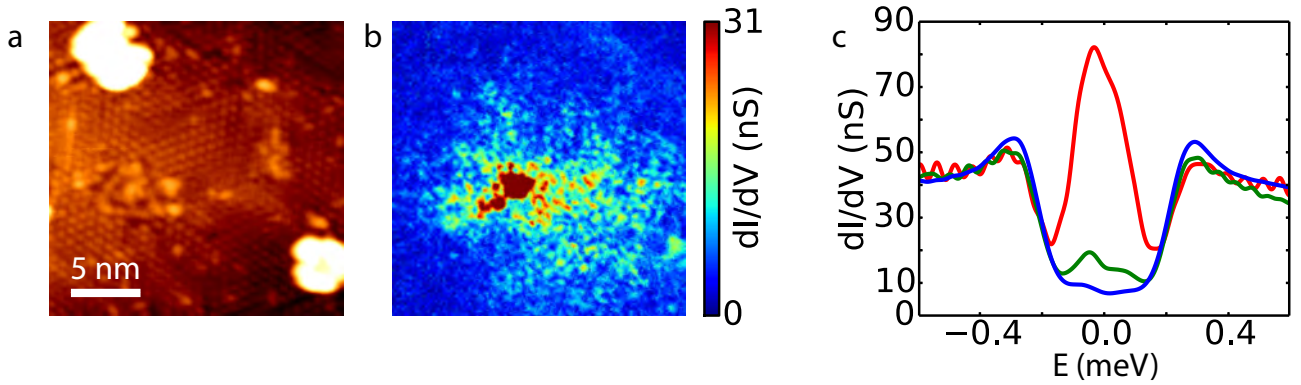

Figure 4.10: **Magnetic impurities in the SIC phase :** a. Topography of a 21×21 nm^2 area in the SIC phase. b. Conductance map integrated over the superconducting gap showing the YSR bound states in this system. c. Spectrum over the impurity (red) far from the impurity (blue) and in between.

annealing the sample at 375°C during 4 min 30 sec. We obtain a sample in the SIC phase with a few dispersed mono-atomically high islands in excess shown on fig. 4.12.a. The phase looks homogeneous at first sight and does not exhibit any clear sign of the buried Co.

In a first approximation we thus expect that once the sample is covered by a monolayer of Pb each impurity will lead to its own YSR bound states. We can then expect these states to overlap due to the lack of phase coherence for the YSR bound states in the SIC phase. Due to the Co clusterisation our sample will still present unaffected superconducting areas with the same properties as in the clean case. In the middle of this unmodified superconductor we will observe areas in which we will have some gap filling induced by these states. This limit can be seen as a pseudo Abrikosov Gorkov regime where we have non interacting classical impurities that form localized clusters rather than a continuous magnetic disorder.

4.5.2 Spectroscopic features

As shown on fig. 4.12.b, when performing spectroscopic measurements we observed a very strong signal on the gap edges presenting a spatial pattern highly similar to the Co clusters visible in topography before the Pb deposition (shown on fig. 4.11). On fig. 4.12.c we show 3 spectra measured over the most visible clusters from the conductance map (in red, orange and green) as well as a reference spectrum measured where we observe the smallest concentration of defects.

The first thing to observe on the spectra of fig. 4.12 is the gap filling effect that originates from the YSR states induced by the buried magnetic impurities. On the perturbed spectra we observe that while we still recognize the characteristic BCS shape, the width of the gap is modulated by the Co. This effect is better seen when one performs a cut through the LDOS as shown on fig. 4.13.c. The direction of the cut is indicated on fig. 4.13.a by a white dashed line.

Due to the gap filling caused by the YSR bound states we cannot fit the spectra with a BCS line shape. Another way to follow spatially the superconducting properties over this type of area is to extract the position of the superconducting coherence peaks. Such analysis is shown on fig. 4.13.b. When compared to the conductance map we observe a clear correlation between the density of states inside the superconducting gap and the energy of the coherence peaks. Therefore a large density of states at the Fermi level will be associated to a lower energy of the quasiparticle peaks. This indicates that unlike what was observed in the case of individual impurities, here the gap undergoes a reduction due to a large density of magnetic clusters.

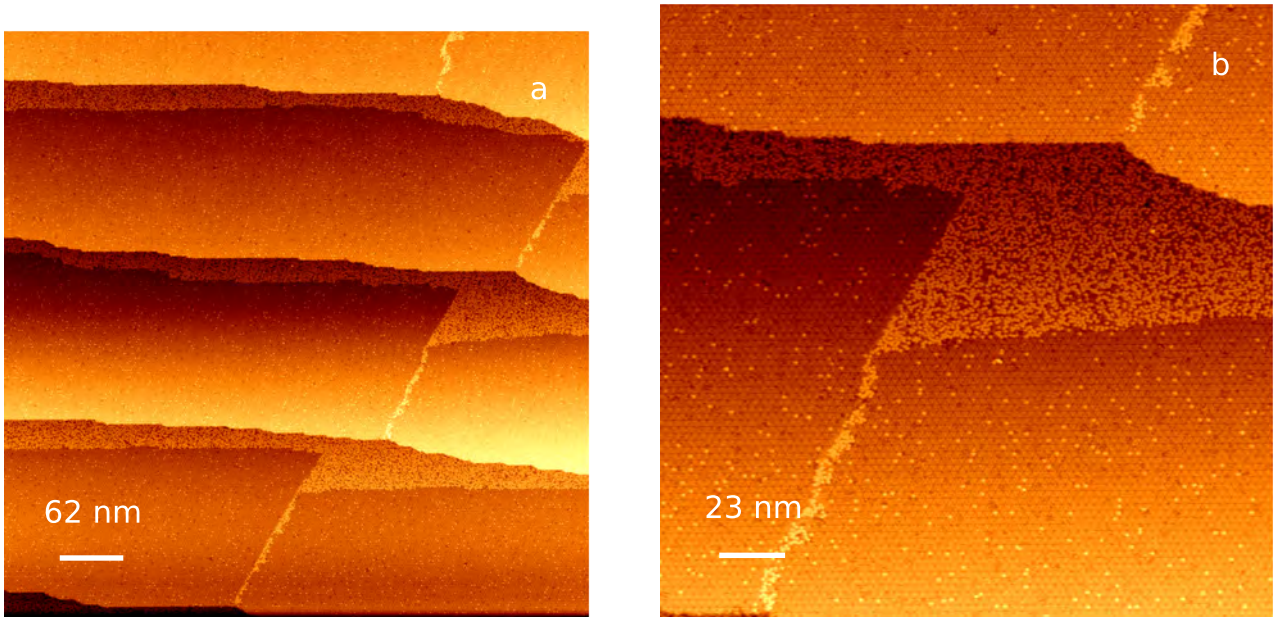

Figure 4.11: **Co on Si annealed at 375°C:** a. Topography of a 622×622 nm^2 area on which were evaporated 10^{-2} ML of Co and then annealed at 375° for 4 min. b. Zoom showing the aggregation of Co atoms along the step edges.

4.5.3 Theoretical analysis and link to Abrikosov-Gorkov theory

In order to interpret the data presented above we will describe our sample by a superposition of Shiba states assuming no interaction between them. This superposition of states will have as a first effect to fill the gap. This gap filling will in return modify the self-consistency equation that will ultimately reduce the superconducting gap Δ.

As we explained in the discussion about the Bogoliubov-de Gennes theory, there exists a self-consistency equation of the superconducting gap (eq. 1.28). This correction to the superconducting gap was previously ignored in the treatment of individual impurities as it was not observed experimentally and only played a secondary role on the phenomenon we were interested in. This simplification does not hold anymore in the case of large clusters. The combined effect of each impurity has a strong effect on the gap as we discussed about fig. 4.12.c.

To describe this system we consider a disc of radius R in which we randomly dispose magnetic scattering centers. As the disorder observed experimentally does not indicate any long range arrangement for the magnetization of the clusters we choose to attribute a random value of the magnetic coupling J comprised between $\pm J_{\max}$. The non magnetic diffusion potential has however no reason to change from one impurity to the other and we therefore choose to take a fixed value for the non magnetic diffusion potential K.

As we consider that each impurity behaves independently from its neighbor we compute for each impurity the associated YSR bound state. In first approximation the YSR wave function is given by the asymptotic formula 2.21 where the terms $\delta^{\pm}$ are determined from the values of J and K. To avoid the divergence at the impurity center we replace the $1/\sqrt{r}$ divergence by a thresholded value $1/\sqrt{\sqrt{r^2+a^2}}$ that behaves as $1/\sqrt{r}$ far from the center and takes a finite value at $r=0$. For the threshold a we took a

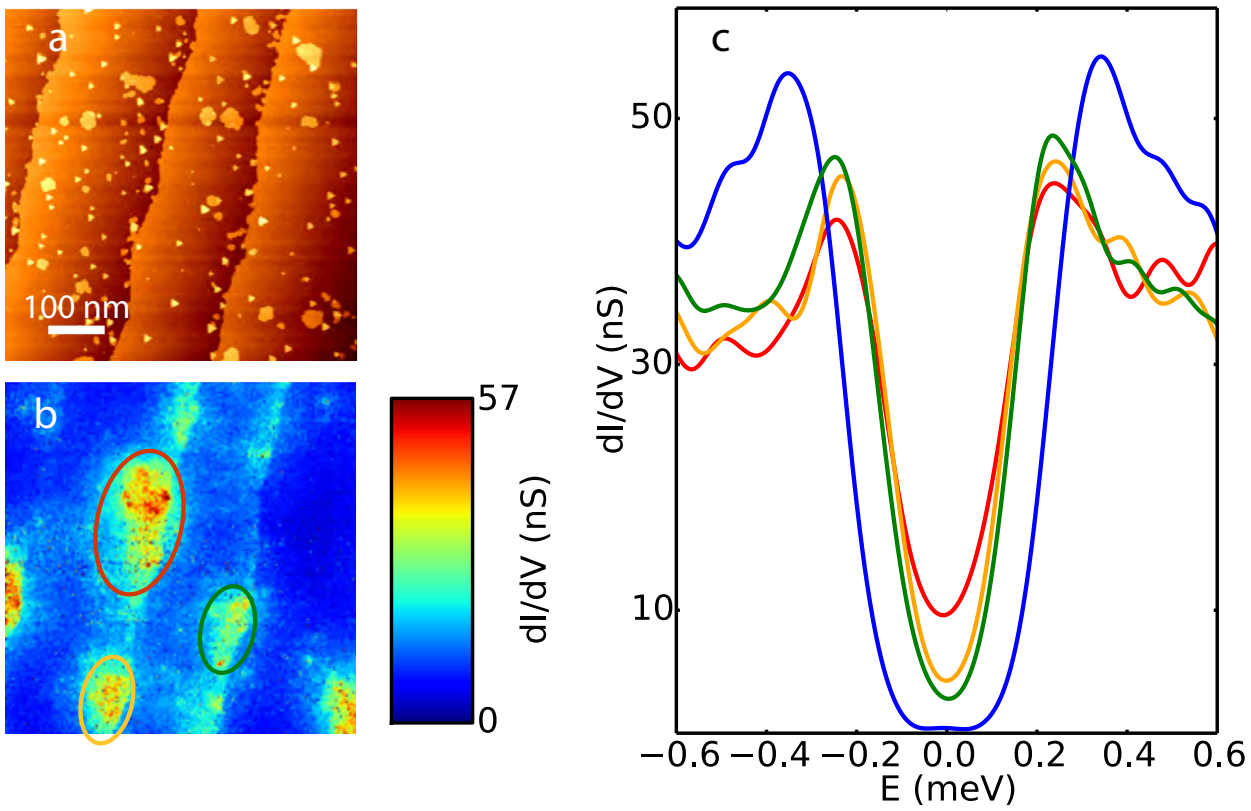

Figure 4.12: **Spectroscopy of the pseudo Abrikosov Gorkov regime:** a. Topography of a 622×622 nm^2 area of Pb/Si(111) in the SIC phase. b. Conductance map of the same area at the gap edge (E = -0.1 meV) revealing the spectroscopic effect of the underlying Co atoms. c. Selected spectra from different impurity patches (red, orange and green from the brightest to the smallest) compared to a spectrum acquired far from any impurity (blue).

small value (0.02 nm) to avoid any normalization issue later on. We take for Δ_0 (the unperturbed gap) a value of 0.35 meV that corresponds to the experimental gap measured at 300 mK

The individual YSR bound states are normalized to 1. We numerically integrate the square modulus of the individual wave functions over the whole area of interest. Because the self-consistent equation of the gap makes use of the terms $u_n(r)$ and $v_n(r)$ obtained from the Bogoliubov-de Gennes equations we see that we can directly use the YSR wave functions calculated before. We thus perform a self-consistent calculation of the gap reduction induced by YSR bound states using eq. 1.28.

The calculation of the gap involves the constant λ linked to the superconducting coupling. We estimate it using the relation [6]

$$k_B T_c = 1,13\hbar\omega_D e^{-\frac{1}{\lambda}} \tag{4.2}$$

and we obtain a value of 0.24 (we take $\hbar\omega_D = 10\ meV$). We checked the convergence of the gap with the iteration and observed that the calculation gives a satisfactory value after 3 to 4 iterations (see fig.4.16.c and d.).

The full Python code written for this calculation is reported in appendix .4.

In order to check the validity of our calculation we first tried to compute the simple case of a single impurity. The gap reduction we obtained is plotted on fig. 4.14.a and the corresponding YSR bound states LDOS on 4.14.b. We then compared to what was obtained by Meng et al. in [104]. In this article the author performed the analytical calculation of the gap variation around a single impurity and found

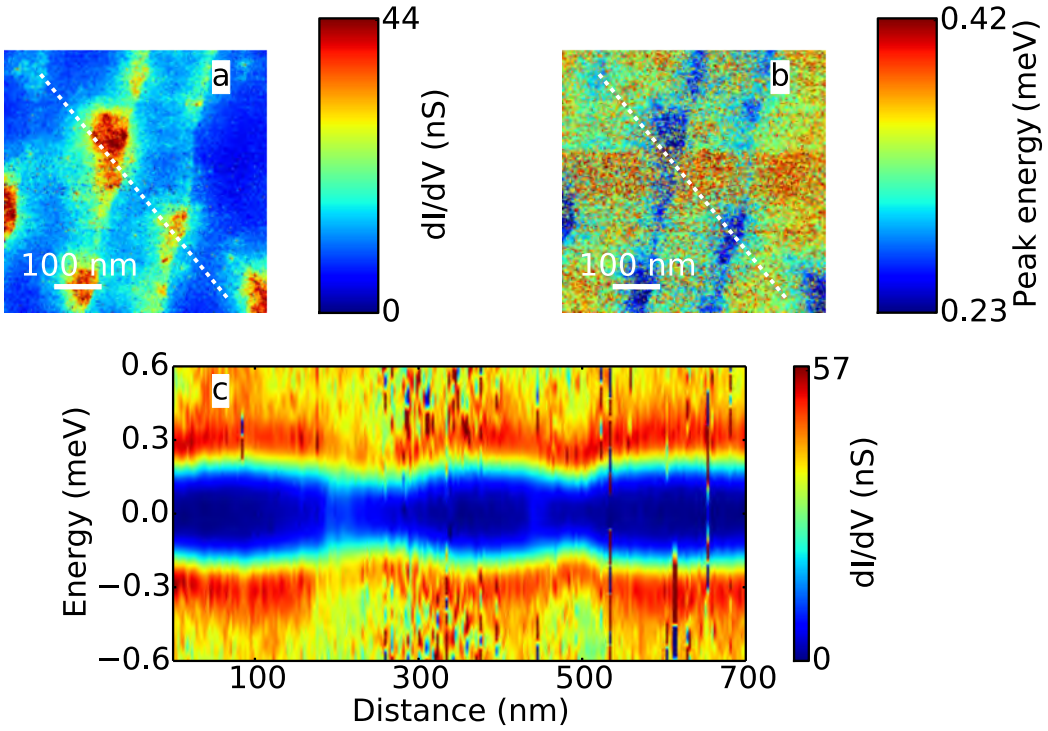

Figure 4.13: **Spectral features of the pseudo Abrikosov-Gorkov regime:** a. Same conductance map as the one of fig. 4.12. b. Map of the coherence peaks energy over the area presented on a. The red area in the middle of the image is due to noise during the spectroscopic measurement. c. Cut through the line indicated on the two top figures showing the spatial variation of the superconducting gap when crossing patches of impurities. 0 nm corresponds to the top left of the conductance map and 700 nm to the bottom right.

that for 3D systems the leading order terms give

$$\delta\Delta(r) \approx \frac{\Delta_0 e^{-r/\xi}}{(k_F r)^2}. \tag{4.3}$$

The power law present in the decay is the same as the one found for the LDOS when performing the Rusinov calculation in 3D. Therefore it seems natural to extend this expression in 2D using the expression

$$\delta\Delta(r)^{2D} \approx \frac{\Delta_0 e^{-r/\xi}}{k_F r}. \tag{4.4}$$

We then fit the results from our own calculation using this expression and we present the result in fig. 4.14.a. We performed this calculation by using a non realistic value of the coherence length $\xi = 5.3$ nm for numerical reasons linked to the discretization of the space. If we want to include the typical scale of the oscillations ($\simeq k_F$) as well as the typical scale of the coherence length (one order of magnitude larger for the Pb monolayer) we need an extremely large amount of numerical points that drastically increase the calculation time.

Once again, in order to avoid some problematic divergence at the origin we perform the substitution $r \to \sqrt{r^2 + a^2}$. The fitting procedure gives us for ξ a value of 5.74 nm and for the maximum gap difference a value of -1.14 μeV. These values are to be compared with what we obtain in our model. Concerning the coherence length we used a value of 5.3 nm and we therefore have a very good agreement with the other model. For the gap difference the final value we obtain is -1.165 μeV on the impurity site and we

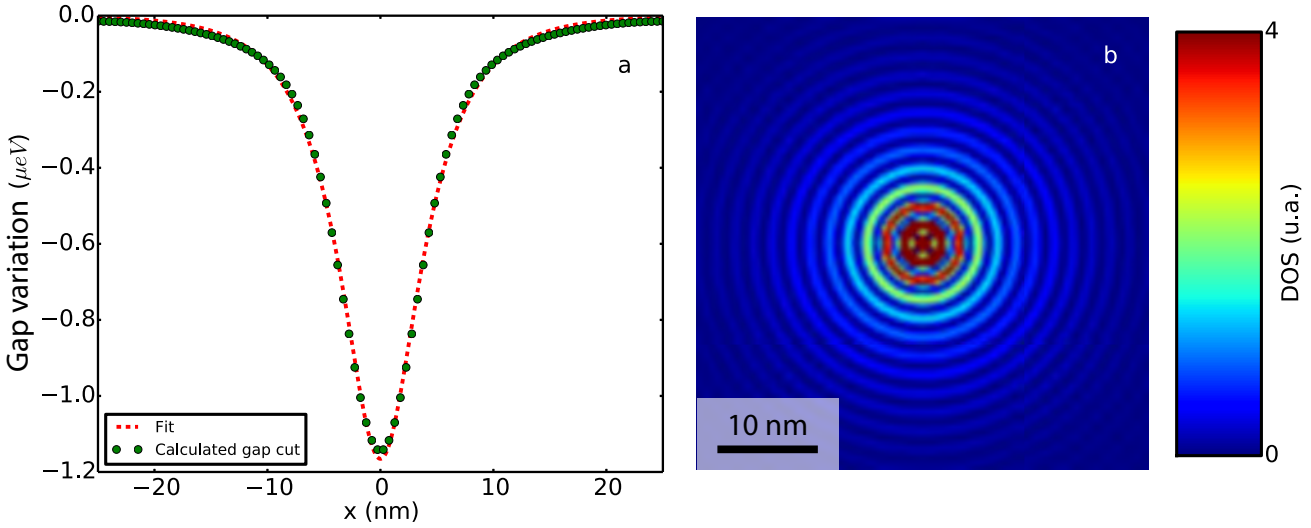

Figure 4.14: **Fit of gap reduction for a single magnetic impurity:** a. Gap profile as a function of the distance from the impurity distance. The dots corresponds to the gap calculated using our semi-analytical method while the dashed lines corresponds to the fit obtained by using the formula from [104] adapted to a 2D case. b. LDOS map of the negative bias YSR bound state for the same impurity.

therefore fall once again very close from the other model. These results seem to confirm the validity of our model in first approximation and allow us to push our investigation forward.

On fig. 4.15 we present in a. the gap map calculated over 500 impurities in a disc of radius 10 nm (2 impurities per nm^2) and in b. the corresponding LDOS map at -0.37 Δ. The positions of individual impurities is represented in fig. 4.15.a by white dots. We see that the gap is strongly modified by the impurity and undergoes in some places a diminution of 30% of its original value. This result is in good agreement with what we obtained by comparing the local value of the energy of the coherence peaks of the superconductor in fig. 4.13.b. Unsurprisingly the larger value of LDOS for in the in-gap states is directly correlated to the smaller value of the gap just as we observed experimentally.

The individual conductance spectra we obtain from this simulation are presented in fig. 4.16.a. The blue spectrum on this figure corresponds to the homogeneous gap from which we started the calculation using the value $\Delta_0 = 0.28$ meV. This spectrum is calculated from the BCS equation for the density of states and in order to reproduce the experiments is convoluted with the derivative of the Fermi-Dirac distribution at 300 mK. The red spectrum on this figure was taken in the center of the cluster and shows the combination of two effects. The first effect we observe here is the gap filling effect that was observed experimentally on fig. 4.12.c, indicating a gapless regime for superconductivity. This gap filling originates from the in-gap YSR bound states. Instead of creating a single peak as we saw in the case of individual impurities, the cluster of randomly oriented impurities leads to a distribution of states inside the gap. This distribution is added to the reduced Δ and increases the zero-bias conductance. The second effect is the gap reduction on the red spectrum: the position of the coherence peaks that are around 0.2 meV.

Fig. 4.16.b. shows a cut through the magnetic cluster. This figure combines both figs. 4.15 as it lets us follow the smooth variation of the superconducting gap as well as the gap filling. When taking a cut through the cluster we also see more defined peaks that correspond to the points where the cut passes right over an impurity. In this case the spectral weight associated to the impurity is strong enough to dominate the other ones and as we did experimentally, we see the in gap pair of YSR bound states.

This whole calculation and observations make the link between the Shiba and the Abrikosov-Gorkov regime. We already discussed the difference with the Shiba case and we will now discuss the link with the Abrikosov-Gorkov theory. In the case described by Abrikosov and Gorkov the impurities are supposed to

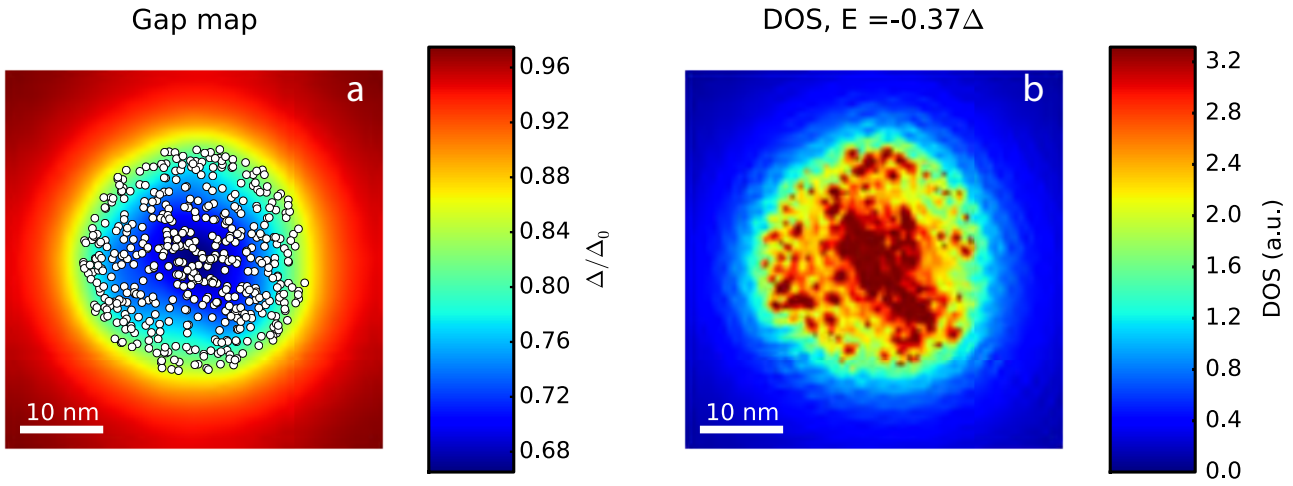

Figure 4.15: **Calculation of the gap and density of states associated to magnetic clusters :** a. Gap map computed in a self-consistent way for 500 impurities in a disc of radius 10 nm for $\Delta_0 = 0.35$ meV. The white dots indicate the random positions of Co atoms. b. LDOS for the in-gap YSR bound states.

be distributed randomly over the full sample while here they are localized in the form of clusters. However inside the clusters the impurity are indeed randomly distributed. The observed and calculated clusters can thus be seen as small 2D Abrikosov-Gorkov superconductors. This comparison can be further extended as we do consider perfectly independent impurities and associated YSR bound states in our model. The same condition is used in the Abrikosov Gorkov theory when the scattering of electrons on different impurities is neglected. This condition corresponds to the lowest order Born approximation.

The main difference between the Abrikosov-Gorkov theory and our results resides in the gap filling effect. As we show on fig. 4.16.d, for increasing values of the effective spin-flip rate the gap filling is only provided from the diminution of the spectral weight of the quasiparticle peaks and leaks from the gap edges continuously toward the Fermi level. Because of this effective spin-flip rate Γ, the role of specific individual impurities is totally neglected in order to favor a statistical approach of the system.

Our phenomenological model does not claim to be a perfectly accurate representation of the physical reality as many second order effects have been neglected. It is however a fast way to perform calculations on magnetic clusters without diagonalizing an Hamiltonian at each iteration loop. Moreover due to its intrinsically continuous nature we are not limited to an on-site calculation as tight-binding is. We think that our model gives a good intuition on the underlying physical phenomena happening and provide a satisfactory explanation for our experimental results.

Our results on this system clearly show the role of magnetic defects in the filling and the reduction of the superconducting gap. Compared to Abrikosov-Gor'kov theory we have shown that the coherence peaks do not necessary disappear before entering a gapless regime for superconductivity. Our results may help interpret some experiments where gap filling was observed without a diminution of the quasiparticle peaks [105, 106]. On a structural point of view our recipe may be used for the patterning of macroscopic samples and the locally weakened order parameter may be useful in the engineering of pinning centers for vortices. The structure of the vortex lattice at low field would be in this case fully determined by the position of the magnetic clusters on the sample.

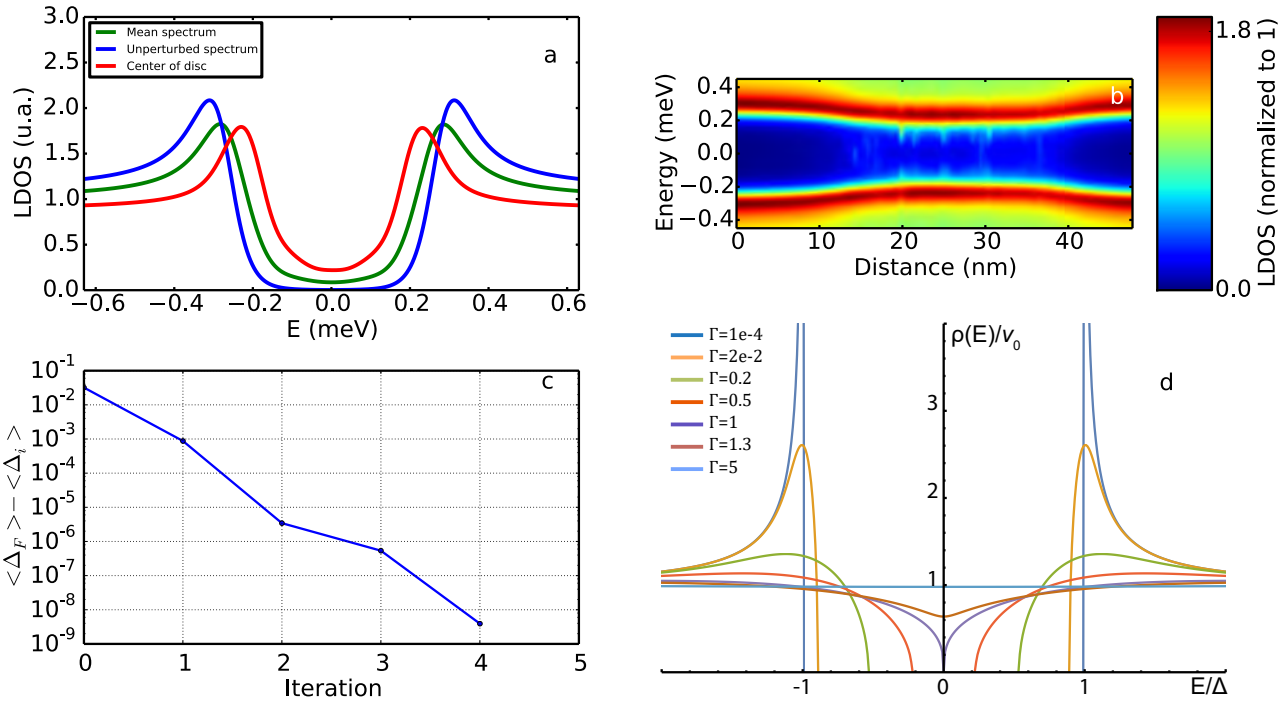

Figure 4.16: **Cut through clusters and gap convergence:** a. Spectra obtained from the self-consistent calculation on magnetic clusters. The blue curve corresponds to the spectrum obtained with an homogeneous gap $\Delta = 0.28$ meV at 300 mK. The red curve corresponds to an average inside a 5 nm radius in the center of the impurity disc. The green curve corresponds to average spectrum over the whole area. b. Cut through the LDOS crossing the center of the disc of impurities. c. Convergence of the gap with iteration of the algorithm. The y axis is in logarithmic scale. d. Abrikosov-Gorkov calculation of the DOS for increase values of the effective spin-flip rate Γ.

4.6 Conclusion

In this chapter we have discussed the influence of nano-magnetism on the Pb/Si(111) system in two different configurations:

- Isolated classical impurities
- Randomly arranged clusters of classical magnetic impurities

We first showed that the results obtained on 2H-$NbSe_2$ about two dimensional superconductors could be extended to the Pb/Si(111) monolayers as we measured the YSR bound states over more that 20 nm from the impurity origin. Due to that enhancement of the bound states range by dimensionality effect we were able to study the Fourier transform of conductance maps for a single impurity. We discussed the role of the atomic structure on the spatial pattern of the highly anisotropic YSR bound states and in the case of the $\sqrt{7} \times \sqrt{3}$ phase how the Fermi surface influences this pattern. We also showed that the disordered monolayer leads to speckle patterns for the YSR bound states. We were able to compared the case of magnetic impurities and non-magnetic impurities and deduce that spin-orbit interaction plays a role in the electronic scattering and thus implies the existence of a triplet component for superconductivity.

We then showed how a large Co concentration could form local accumulations of magnetic impurities and produce a continuum of YSR bound states. These clusters have an effect on the gap-filling and the

gap size that are well reproduced by considering the gap reduction under the influence of the superposition of independent YSR bound states.

In the next chapter we will discuss the intermediate case of ordered Co clusters giving rise to a topological transition and the appearance of topological edge states. We will discuss the role of the different ingredients needed to enter a domain of topological superconductivity and show how we can obtain Majorana bound states by stabilizing a vortex inside of a topological domain.

Chapter 5

Magnetic clusters and topological systems

5.1 Introduction

In this chapter we will present the results obtained in the study of topological superconductivity induced by magnetic Co clusters embedded below Pb/Si(111) monolayers. We will first introduce the theoretical tools needed to discuss topological superconductivity and Majorana quasi-particles. We will then show how one can obtain nanometer sized clusters of Co/Si acting as small ferromagnets on the superconducting Pb overlayer. By analyzing this configuration in terms of field-induced topological transition we will show how the emergence of edge states can be expected. This part was published on arXiv in [107]. Finally we will see how by increasing the size of the Co clusters it becomes possible to create a vortex state that will exhibit a zero-bias state that shows strong similarities with Majorana bound states.

5.2 Topology and Majorana quasi-particles

In an attempt to include special relativity into quantum mechanics Dirac proposed the equation that now bears his name [108, 109]. Dirac's theory first proposed the idea that particles like electrons could be associated to an antiparticle. In 1937 E. Majorana, mostly motivated by esthetic, showed that another equation could be written that would be compatible with both quantum mechanics and special relativity [110]. In his theory, Majorana proposes that there could exist some fermions which are their own antiparticle. While Dirac antiparticles such as positrons were discovered soon after their theoretical prediction, the status of Majorana particles is more uncertain. There are some suspicions that neutrinos might be Majorana particles but no definitive proof has been found yet.

However in the field of condensed matter physics there has been a lot of recent proposals of systems that could exhibit Majorana-like excitations. Superconductivity is involved in most of these proposals due to its build-in electron-hole symmetry which is an essential ingredient for Majorana-Weyl physics. The idea is that from a system described in terms of electronic operators $\hat{c}_{k\sigma}$ it is possible to diagonalize the superconducting Hamiltonian by introducing Majorana operators $\hat{\gamma}$ defined as a combination of electronic operators

$$\begin{aligned} \hat{\gamma}_1 &= \frac{1}{\sqrt{2}}(\hat{c}^\dagger + \hat{c}) \\ \hat{\gamma}_2 &= \frac{i}{\sqrt{2}}(\hat{c}^\dagger - \hat{c}). \end{aligned}$$

These operators have the particularity to be their own adjoined operator as $\hat{\gamma}_i^\dagger = \hat{\gamma}_i$. Because in the framework of superconductivity the Hamiltonian describing the system can be diagonalized using a Bo-

goliubov transformation in which the u_k and v_k factor are respectively the electron and hole weight of the eigenvectors it is natural to expect that under certain conditions these factors will take the same value and we would thus obtain a Bogoliubov operator in the form of a Majorana operator.

Such operators are interesting in condensed matter physics as they are associated to anyonic quasi-particles that obey non-Abelian statistics. When exchanging two fermions the global phase function acquires a $-$ sign, while the exchange of bosons leads to a $+$ sign. Anyons are quasi-particles that acquire a Berry phase $\theta \neq \pm 1$ when exchanging two of them [111]. The non-Abelian statistics on the other hand refers to the fact that the exchange of quasiparticles keeps the trace of the exchange path that was followed through the global phase of the wave-function. This type of statistics allows to perform quantum calculations [112] by braiding of Majorana fermions [113]. These type of calculation are expected to be fault-proof as the topological properties of Majorana bound states should prevent decoherence to occur in the system.

The proposed systems expected to exhibit Majorana fermions are diverse and include vortex cores in topological superconductors [114, 115, 116], superconductor-semiconductor heterostructures [117, 118] as well as chains of magnetic atoms on top of superconductors [119, 120, 121]. In every case one of the key ingredients involved in the emergence of Majorana bound states is spin-orbit coupling [122] and we will discuss this effect more in details below. By combining spin-orbit coupling and magnetism it is expected that one would create a topological superconductor in which a topological index could be defined [123]. The Majorana states would then appear at the interface between a topological and a trivial superconductor.

Signatures of Majorana excitations were claimed to have been observed in two types of experiments. The first type of experiment [124] uses a nanowire made of semi-conducting InAs in contact with an s-wave superconductor (niobium titanium nitride). When applying an external magnetic field in the direction of the nanowire, the authors observed a region of magnetic field in which appeared a zero-energy mode they attributed to Majorana quasiparticles.

The second type of experiment takes the route of magnetic chains on superconductors [125]. In this experiment the authors use a superconducting Pb monocrystal on which they deposit Fe atoms that spontaneously organize in the form of ferromagnetic chains. By using STM they observed zero energy bound states at the end of the ferromagnetic chains. The spin-orbit interaction in this configuration is provided by Pb which is an heavy element.

5.3 Rashba spin-orbit interaction

5.3.1 Origin and effect of the interaction

The Rashba interaction is an effect created by spatial inversion symmetry breaking at surfaces. The coupling of the spin and momentum of electrons is derived from the relativistic Dirac equation (Darwin terms) where the movement of electrons in an electric field creates an artificial magnetic field that will couple to their spin. In crystals this effect is seen when the electrical field experiences a strong spatial variation as it is the case at surfaces. In particular 2D electron gases present a strong variation of the electric field due to the symmetry breaking along the z axis. When expanding the Dirac equation in the low energy limit at the second order in e^2/hc we obtain a term of the form [126]

$$H_{SO} = \frac{\hbar}{4m^2c^2}\hat{\boldsymbol{\sigma}} \cdot (\boldsymbol{\nabla} V \times \hat{\boldsymbol{p}}). \tag{5.1}$$

For a symmetry breaking along the axis $\boldsymbol{u}_r$, the Rashba spin-orbit interaction reads as

$$\hat{H}_{SO} = \alpha(\boldsymbol{k} \times \boldsymbol{\sigma}) \cdot \boldsymbol{u}_r, \tag{5.2}$$

that can be rewritten in two dimensions under the form (for u_r along the z axis)

$$\hat{H}^{2D}_{SO} = \alpha(k_x\sigma_y - k_y\sigma_x). \tag{5.3}$$

The parameter α is therefore mostly a reflect of the asymmetry around the atomic nuclei at which the potential $V(r)$ is localized. For a simple parabolic dispersion the Rashba spin-orbit interaction leads to a splitting of the bands and the new dispersion is written as [127]

$$E_{\pm}(k) = \frac{h^2 k^2}{2m} \pm \alpha k. \tag{5.4}$$

We plot this dispersion on figs. 5.1.a. and b. for one and two dimensions respectively.

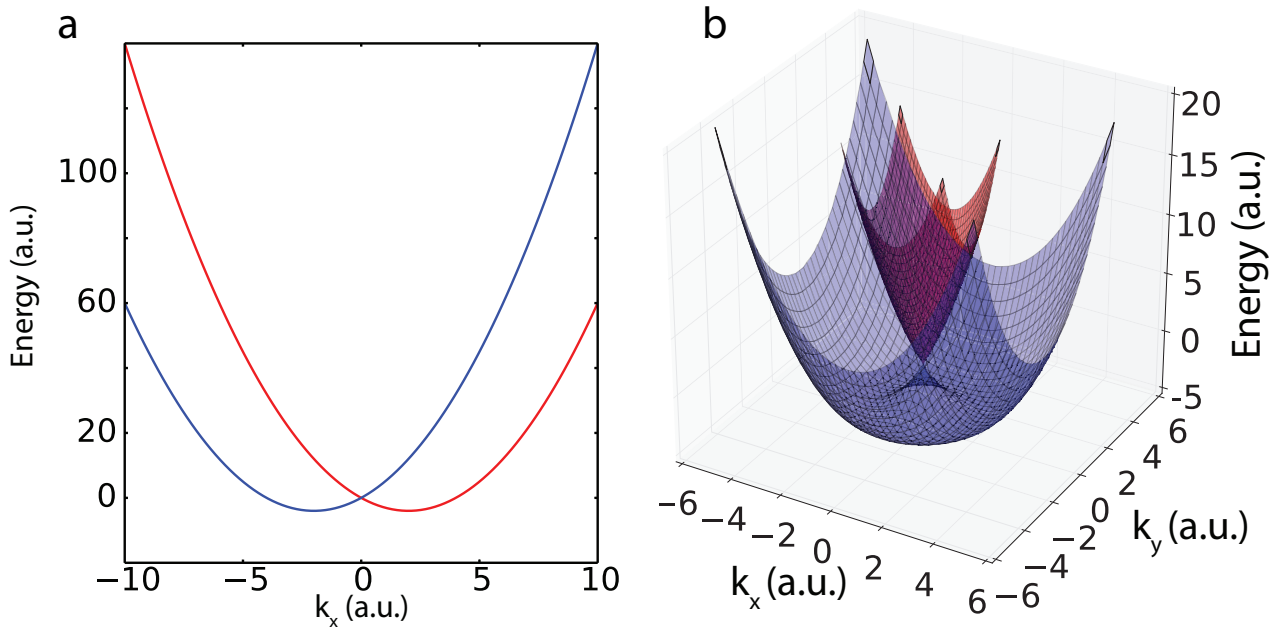

Figure 5.1: **Rashba dispersion:** a. Dispersion relation obtained for a Rashba spin-orbit interaction in 1D. b. Dispersion relation obtained for a Rashba spin-orbit interaction in 2D for a fixed value of k_y.

The projection of the spin along the quantization axis is not a good quantum number in the case of Rashba spin orbit and the eigenbasis of the system will be a chiral basis in which the spin of the electrons is turning with the orientation of the k vector in the reciprocal space (i.e. $\boldsymbol{S} \cdot \boldsymbol{k} = 0$ and $\boldsymbol{S} \cdot \boldsymbol{z} = 0$). The spin thus behaves in Rashba systems in the same fashion as it does in topological insulators around Dirac cones.

Because the eigenstates of a system exhibiting Rashba spin-orbit are a mixture of spins $\uparrow$ and $\downarrow$, a more convenient way to write the eigenbasis of the system will be by introducing an index $\lambda = \pm$ which will correspond to the chirality of the system. The eigenvectors $|\pm\rangle$ can be easily written from the original states $|\uparrow\rangle$ and $|\downarrow\rangle$ as

$$|k, \lambda\rangle = \frac{|k, \uparrow\rangle + i\lambda e^{i\theta_{\boldsymbol{k}}} |k, \downarrow\rangle}{\sqrt{2}}. \tag{5.5}$$

with θ_k the orientation of the $\boldsymbol{k}$ vector. An interesting observation that can be made on the form of this ground state is that it is totally independent of the parameter α that describes the strength of the spin-orbit interaction. This behavior indicates that the interaction deeply modifies the ground state of the system. As we will discuss later, the form of the superconducting interaction is modified in the presence of spin orbit interaction. This will lead to triplet and spinless superconductivity from which topological superconductivity will emerge.

5.3.2 Case of Rashba effect with magnetic field

We now add to the Rashba interaction an external magnetic field whose effect is described by a Zeeman Hamiltonian

$$H_{Zeeman} = \boldsymbol{B} \cdot \hat{\boldsymbol{\sigma}}. \tag{5.6}$$

If we parametrize the orientation of the magnetic field by the angles θ and ϕ (see fig. 5.2.c) and the direction of the in-plane $\boldsymbol{k}$ vector by θ_k it becomes possible to write the Hamiltonian in the Nambu spinor basis $\psi^\dagger = \begin{pmatrix} \hat{c}^\dagger_{k\uparrow} & \hat{c}^\dagger_{k\downarrow} \end{pmatrix}$ as

$$H_{Rashba+Zeeman} = \begin{pmatrix} \xi_k + V\cos\phi & i\alpha k e^{-i\theta_k} + Ve^{-i\theta}\sin\phi \\ -i\alpha k e^{i\theta_k} + Ve^{i\theta}\sin\phi & \xi_k - V\cos\phi, \end{pmatrix} \tag{5.7}$$

where V is the amplitude of the magnetic field ($|\boldsymbol{B}| = V$). It now becomes trivial to obtain the eigenvalues of the system in the form

$$E_\pm = \xi(k) \pm \sqrt{V^2 + k^2\alpha^2 - 2kV\alpha\sin\phi\sin(\theta - \theta_k)}. \tag{5.8}$$

By analyzing this dispersion we observe that for an in-plane field (i.e. $\phi = \pi/2$) the bands possess a degeneracy point at $\boldsymbol{k} = -\frac{V}{\alpha}\begin{pmatrix}\cos\theta \\ \sin\theta\end{pmatrix}$ that is lifted for any finite out-plane magnetic field. For a perfectly normal magnetic field the splitting at the Γ point is exactly of $2V$. We show on fig. 5.2 the effect of an external magnetic field on the electronic dispersion for both in- and out-plane field.

The opening of a gap by means of a magnetic field perpendicular to the surface of the sample will deeply modify the ground state of the superconducting ground state of a Rashba superconductor. The ground state is modified in such a way that if one wants to continuously transform the system to a superconductor with an in-plane magnetic field it would have to be done through a step that would close the gap. This intermediate gap closing will sign a topological transition between a topological superconductor (out of plane field) to a trivial one (in plane field) in the following. When we will include superconductivity inside the problem later on, we will have defined two superconductors with different topological indexes depending on whether superconductivity appears on a system where the bands are already split or not. These topological indexes will also depend on the value of the chemical potential and whether or not the Fermi level falls inside the gap opened by the perpendicular magnetic field.

In the same way as edge states appear at the interface between a trivial and a topological insulator we will see the appearance of states at the edges of the trivial superconductor (with no Zeeman degeneracy lifting) and the topological one (with lifted degeneracy). Here these edge states will be called chiral as they arise from a time-reversal symmetry breaking.

5.3.3 Rashba spin-orbit and form of the superconducting interaction

In 1989 [128] Édel'shtein and in 2001 Gor'kov and Rashba [20] investigated the way spin-orbit interaction influences the superconducting ground state derived from the general Hamiltonian (equivalent to 1.13)

$$H_{int} = \frac{1}{2}\sum_{\lambda\mu\nu\rho}\sum_{\boldsymbol{k}\boldsymbol{k}'\boldsymbol{q}} U_{\lambda\mu\nu\rho}(\boldsymbol{k},\boldsymbol{k}',\boldsymbol{q})\hat{a}^\dagger_{\lambda,\boldsymbol{k}}\hat{a}^\dagger_{\mu,-\boldsymbol{k}-\boldsymbol{q}}\hat{a}_{\nu,-\boldsymbol{k}'-\boldsymbol{q}}\hat{a}_{\rho,\boldsymbol{k}'}. \tag{5.9}$$

where the λ, μ, ν, ρ indexes relate to the spin degrees of freedom. In this case the operators $\hat{\boldsymbol{S}}^2$ and $\hat{S}_z$ do not commute with the Hamiltonian. S and S_z are thus not good quantum numbers anymore. As a consequence, the isotropic s-wave gap used in the absence of spin-orbit interaction does not minimize the energy of the ground state and should therefore be replaced by a momentum dependent gap. Furthermore, the states on which the coupling now applies are the eigenstates of the system in presence of Rashba

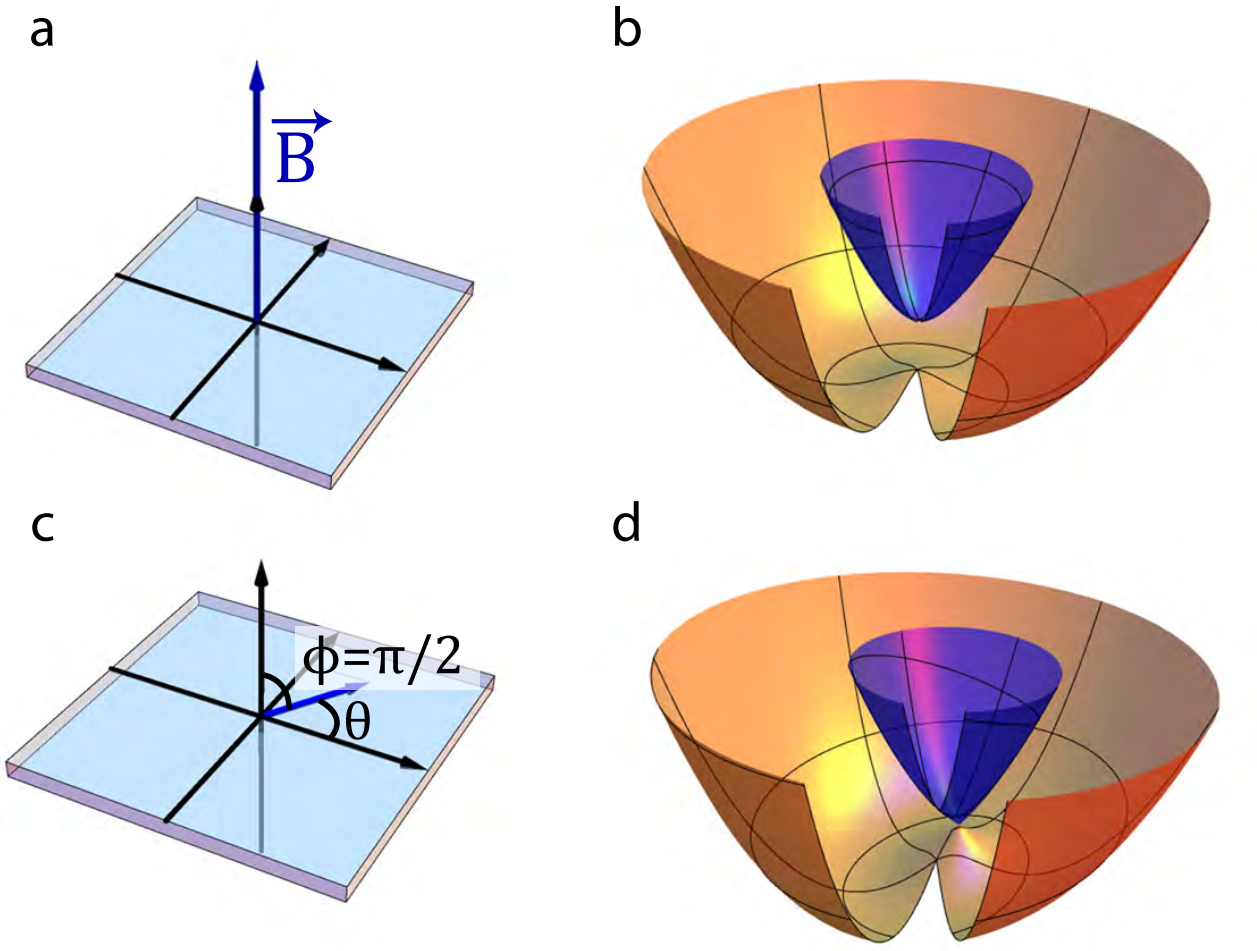

Figure 5.2: **Zeeman effect on Rashba system:** a.-b. Effect of the magnetic field outside of the plane on a Rashba superconductor. Real space configuration versus band dispersion. c.-d. Same thing for a magnetic field inside the plane.

spin-orbit coupling. Under such circumstances the Bogoliubov-de Gennes equations become the Gor'kov equations

$$\begin{aligned}(i\omega_n - \varepsilon_\lambda(\boldsymbol{k}))g_\lambda(\boldsymbol{k},\omega_n) + \Delta(\boldsymbol{k})f^\dagger_\lambda(-\boldsymbol{k},\omega_n) &= 1,\\ \Delta^*(\boldsymbol{k})g_\lambda(\boldsymbol{k},\omega_n) + (i\omega_n - \varepsilon_\lambda(\boldsymbol{k}))f^\dagger_\lambda(-\boldsymbol{k},\omega_n) &= 0\end{aligned}$$

where ω_n are the Matsubara frequencies [19] and g_λ and f_λ are the normal and abnormal Green functions respectively. The index λ refers in these equation to the eigenstate $\pm$ of the system without superconductivity but Rashba spin-orbit coupling (see eq. 5.5).

In the absence of spin-orbit the order parameter Δ is fully described from the abnormal green function $f(\boldsymbol{k})$ as we have for singlet pairing (the α and β indexes refer to the spin degrees of freedom) [129]

$$\Delta_{\alpha\beta} \propto \langle\hat{\psi}_\alpha(\boldsymbol{k})\hat{\psi}_\beta(-\boldsymbol{k})\rangle = f(\boldsymbol{k})(i\hat{\sigma}_y)_{\alpha\beta}. \tag{5.10}$$

Where the proportionality symbol includes the amplitude of the superconducting coupling. The lack of

inversion symmetry redefines the order parameter as a mixture of singlet and triplet pairing in the form

$$\Delta_{\alpha\beta} \propto \langle \hat{\psi}_\alpha(\boldsymbol{k})\hat{\psi}_\beta(-\boldsymbol{k})\rangle = \{if(\boldsymbol{k})\hat{\sigma}_y + (\boldsymbol{d}(\boldsymbol{k})\cdot\hat{\boldsymbol{\sigma}})i\hat{\sigma}_y\}_{\alpha\beta}\,. \tag{5.11}$$

In all generality the type of coupling that one should include inside the Bogoliubov-de Gennes formalism will depend on how the spin-orbit interaction favors either the singlet configuration (corresponding to the term $f(\boldsymbol{k})$) or the triplet configuration (corresponding to the term $\boldsymbol{d}(\boldsymbol{k})\cdot\hat{\boldsymbol{\sigma}}$). As we will discuss later, in order to preserve the time reversal symmetry of the system we have to add some constraint on the two terms. The singlet term must be an even function of $\boldsymbol{k}$ while the $\boldsymbol{d}$ vector must be an odd function of the wave vector $\boldsymbol{k}$. The simplest case one can consider is to write for the singlet term as a constant (as in the usual BCS case)

$$\Delta_{\uparrow\downarrow}(\boldsymbol{k}) = \Delta_S. \tag{5.12}$$

On the other side, the simplest way to write the triplet term is to consider a function of the angle θ_k as

$$\Delta_{\uparrow\uparrow}(\boldsymbol{k}) = \Delta_{\downarrow\downarrow}(\boldsymbol{k}) = \Delta_T|\boldsymbol{k}|e^{i\theta_k}. \tag{5.13}$$

5.3.4 Rashba spin-orbit, Zeeman and superconductivity

Let us now consider a simple singlet superconductor with Rashba spin-orbit coupling on which is applied an external magnetic described by a Zeeman Hamiltonian

$$H = H_0 + H_{Singlet} + H_{Rashba} + H_{Zeeman}. \tag{5.14}$$

This is a crude approximation that neglects the triplet pairing terms discussed previously and will be different from the helical case we will discuss below.

For a magnetic field oriented along the z direction we can obtain the analytical expression for the dispersion of the system.

$$E = \pm\sqrt{V^2 + k^2\alpha^2 + \Delta^2 + \xi^2 \pm 2\sqrt{k^2\alpha^2\xi^2(\boldsymbol{k}) + V^2(\Delta^2 + \xi^2(\boldsymbol{k}))}}. \tag{5.15}$$

By analyzing the dispersion we observe a critical field V_{crit} for which we obtain a gap closure at the Γ point in the reciprocal space

$$V_{crit} = \sqrt{\Delta^2 + \mu^2}. \tag{5.16}$$

The dispersion 5.15 is represented on fig. 5.3 for three different values of V, respectively at zero field (V = 0), at the topological transition induced by the Zeeman field ($V = V_{crit} = \sqrt{\Delta^2 + \mu^2}$) and beyond the topological transition ($V = 2V_{crit}$). For fields larger than V_{crit} the gap reopens as shown on fig. 5.3.c. The reopening of the gap only occurs for a finite Rashba coupling $\alpha \neq 0$. For $\alpha = 0$ the gap still closes at V_{crit} but stays closed at higher field, the superconductor is then in the paramagnetic limit. The topological transition that exists in presence of spin-orbit coupling is thus absent when α is turned down to zero as shown on fig. 5.4.

5.3.5 Symmetries of the Hamiltonian

We have previously discussed the effect of a magnetic field that breaks time reversal symmetry and leads to chiral superconductivity. We will now address triplet superconductivity that preserves time reversal symmetry and leads to helical superconductivity.

A general BCS Hamiltonian respecting the time reversal invariance can be written as

$$H_{BCS-TR} = \sum_{\boldsymbol{k},\boldsymbol{k'},\sigma_1,\sigma_2} V_{\sigma_1,\sigma_2}(\boldsymbol{k},\boldsymbol{k'})\hat{c}^\dagger_{\boldsymbol{k'},\sigma_1}\hat{c}^\dagger_{-\boldsymbol{k'},\sigma_2}\hat{c}_{-\boldsymbol{k},\sigma_2}\hat{c}_{\boldsymbol{k},\sigma_1}. \tag{5.17}$$

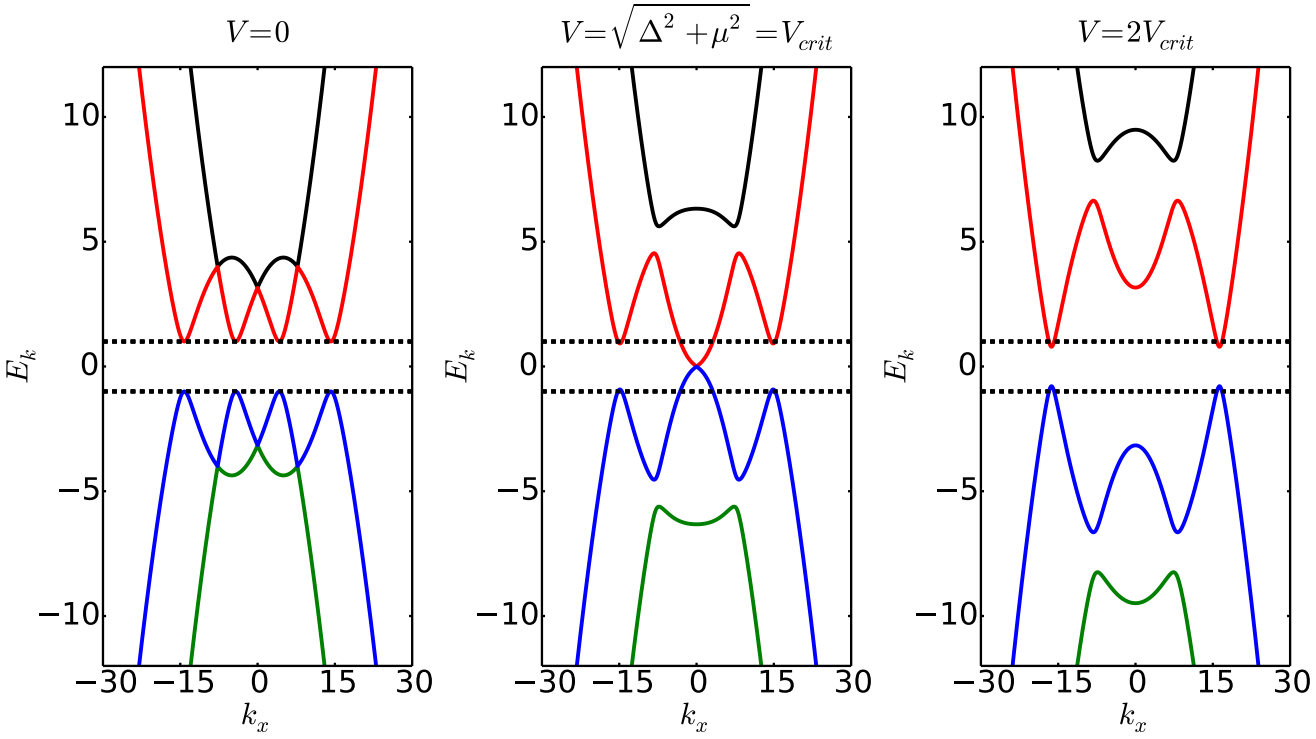

Figure 5.3: **Topological transition in magnetic field of a Rashba superconductor:** Band structure of a Rashba superconductor respectively at zero magnetic field, at the topological critical field and over the topological critical field.

This form leads to three different possibilities for the spin configuration in the mean field case. The first possibility is to have a coupling between opposite spin $(\uparrow,\downarrow)$ leading to a singlet state

$$H^S_{BCS} = \sum_k \left\{ \Delta_S \hat{c}^\dagger_{k,\uparrow} \hat{c}^\dagger_{-k,\downarrow} + h.c. \right\}. \tag{5.18}$$

In this configuration, the spin antisymmetry does not force any symmetry on the order parameter with respect to the spatial inversion $(k \to -k)$ and thus the minimal way to write the s-wave order parameter is to take a constant Δ_S.

The second possibility for the spins to couple in the time-reversal invariant BCS Hamiltonian is the triplet case where the coupling occurs between spins of same orientation $(\uparrow,\uparrow)$ and $(\downarrow,\downarrow)$. The symmetry analysis of this Hamiltonian shows that it is not possible anymore to consider a k invariant order parameter in the mean field limit as $\Delta_T(\boldsymbol{k})$ must transform into $-\Delta_T(-\boldsymbol{k})$ by spatial inversion. The simplest way to do so without introducing any node in the order parameter is to include an angular dependance in the p-wave term such as

$$H^T_{BCS} = \sum_k \left\{ \Delta_T |k| e^{i\theta_k} \hat{c}^\dagger_{k\uparrow} \hat{c}^\dagger_{-k\uparrow} - \Delta_T |k| e^{i\theta_k} \hat{c}^\dagger_{k\downarrow} \hat{c}^\dagger_{-k\downarrow} + h.c. \right\} \tag{5.19}$$

where θ_k refers to the direction of the wave vector $\boldsymbol{k}$ where we write $p_x + ip_y = \hbar |k| e^{i\theta_k}$.

While the triplet component of superconductivity Δ_T is *a priori* authorized in every circumstances, for a system that respects time-reversal invariance it is not necessarily present. The work of Rashba and Gor'kov [20] showed that the presence of Rashba spin-orbit coupling is responsible for the appearance of the triplet correlations. Because the Hamiltonian and the spin operators $\hat{S}^2$ and $\hat{S}_z$ do not commute anymore we will need to take into account both triplet and singlet terms.

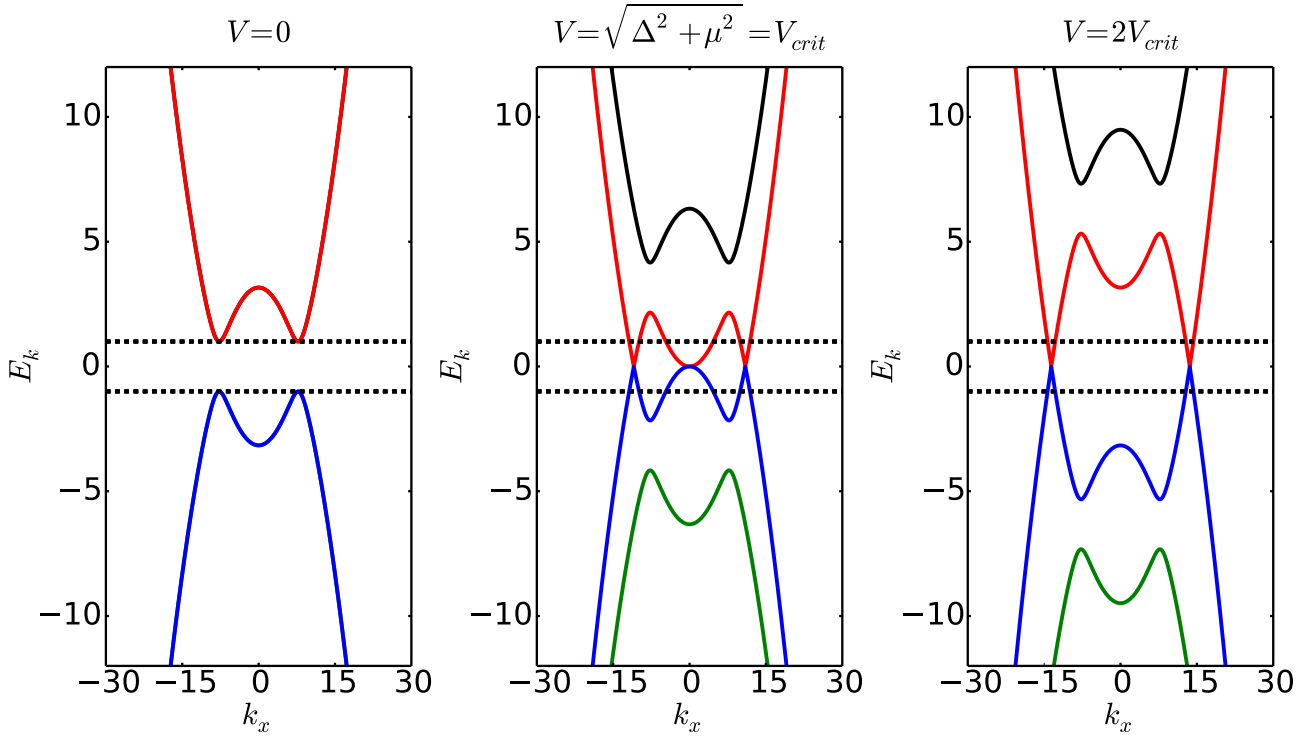

Figure 5.4: **BCS superconductor in magnetic field:** Same figures as in 5.3 in the case where the Rashba interaction has been suppressed ($\alpha = 0$).

If we try to compute the dispersions one should expect in a system with coexisting triplet and singlet order parameters we would obtain the following matrix form for the Hamiltonian[1]

$$H = \begin{pmatrix} V-\mu+\xi_k & \Delta_S & |k|\alpha & -\Delta_T\frac{|k|}{k_F} \\ \Delta_S & V+\mu-\xi_k & \Delta_T\frac{|k|}{k_F} & |k|\alpha \\ |k|\alpha & \Delta_T\frac{|k|}{k_F} & -V-\mu+\xi_k & -\Delta_S \\ -\Delta_T\frac{|k|}{k_F} & |k|\alpha & -\Delta_S & -V+\mu-\xi_k \end{pmatrix} \tag{5.20}$$

With a magnetic field oriented along the z direction and with the inclusion of spin-orbit interaction. This Hamiltonian is written in the basis $\Psi = \begin{pmatrix} \hat{c}_{k\uparrow} & \hat{c}^\dagger_{-k\downarrow} & \hat{c}_{k\downarrow} & \hat{c}^\dagger_{-k\uparrow} \end{pmatrix}$. The positive eigen energies of this Hamiltonian are given by

$$E^{\pm} = \sqrt{V^2 + k^2\alpha^2 + \Delta_S^2 + \frac{|k|^2}{k_F^2}\Delta_T^2 + (\xi_k-\mu)^2 \pm 2\sqrt{V^2(\Delta_S^2+(\xi_k-\mu)^2) + \left(\Delta_S\Delta_T\frac{|k|}{k_F} + |k|\alpha(\xi_k-\mu)\right)^2}}. \tag{5.21}$$

Because spin-orbit is already included in the symmetries of the Hamiltonian *via* the triplet superconductivity term, we can in first approximation ignore the Rashba $k\alpha$ terms in the Hamiltonian. We will also forget about the Zeeman terms as we will only consider a time-reversal invariant system. Then we can show that one can perform a phase transition and change the topology of the ground state by tuning

[1] In order to simplify the notations, the Hamiltonian is written at $\theta_k = 0$. However, the supposed rotational invariance guaranties the independence of the solutions with θ_k and thus diagonalizing the Hamiltonian for this single case is enough to infer the main properties of the dispersion. In order to study the spectrum we redefine the triplet order parameter Δ_T so that it can be expressed in the same unit system as Δ_S. We do so by introducing a term $1/k_F = 1/\sqrt{2m\mu}$ in the expression given in eq. 5.19.

the ratio Δ_T/Δ_S at zero magnetic field. For $\Delta_T/\Delta_S = 1$, the gap closes and for higher values it reopens entering a topological phase. It is thus possible to operate a time-reversal invariant topological transition by playing on the values of the triplet and singlet order parameters. The topological phase obtained in this configuration is called helical as it does not break time-reversal symmetry and leads to a set of two bound states with opposite chiralities.

In the previous section we broke time reversal symmetry by means of a magnetic field normal to the surface. This configuration was called chiral and exhibited one edge state. In the present case of a mixture of triplet and singlet order parameters we preserve time reversal symmetry and instead of one edge state we will obtain a pair of states with opposite chiralities. This configuration is called helical.

This discussion is summarized on fig. 5.5. The top part describes the chiral case (with $\Delta_T = 0$) and the bottom part the helical case (with $V = 0$). Figs. 5.5.a present the band structure of a system with s-wave superconductivity and Rashba spin-orbit interaction for different values of the Zeeman coupling V_Z. One can see that for a critical field $V_Z = \sqrt{\Delta^2 + \mu^2}$, the gap closes at $k = 0$ and then reopens, entering the topological chiral phase. The corresponding μ vs. V_z phase diagram is represented on fig. 5.5.b and the disk in the topological part of the diagram represents the superconducting sample with a single edge state propagating at the interface with the vacuum.

We procede similarly for the helical case where we present on fig. 5.5.b. the evolution of the band structure with Δ_T for a system in which spin-orbit was omitted ($\alpha = 0$) as well as magnetic field ($V_z = 0$) in order to only leave an s-wave superconductivity term Δ_S. Contrary to fig. 5.5.a, the axes here are Δ_S and Δ_T. The topological transition occurs for $\Delta_S = \Delta_T$ and when $\Delta_T > \Delta_S$ the system is in the helical topological phase. The gap closing associated to this transition is presented on fig. 5.5.d with the trivial and topological phases delimited by a black dashed line. When in the helical topological state, there exists two counter-propagating states at the edges of the sample. These edge states are represented by a clock wise and an anti-clockwise arrow of different colors.

What this shows is that there exists many different ways to obtain a topological transition by playing with the different ingredients at our disposal. An analysis of the dispersion 5.21 actually shows that the phase transitions between trivial and helical as well as between chiral and helical respectively appear for the following conditions

$$\sqrt{\Delta_T^2 + V_z^2} = \Delta_S^2, \tag{5.22}$$

$$\sqrt{\Delta_S^2 + \mu^2} = V_z \tag{5.23}$$

We present on fig. 5.6 a summary of the discussion on both helical and chiral cases where we display the Δ_T vs. Δ_S phase diagram of topological superconductivity. On this figure are represented the three possible phases a superconductor can enter by controlling the amplitude of the Zeeman term V_z and the triplet order parameter Δ_T. In all these phases we obtain a fully opened gap that only closes at the transition lines (black dashed lines). The Rashba term is neglected for simplicity as it does not fundamentally modifies the phase diagram. In particular, the transition at $V_z = \sqrt{\Delta_S^2 + \mu^2}$ happens at $k = 0$ and is left unchanged whatever the amplitude of the Rashba term might be.

5.4 Experiment principle

We will now present an experimental realization of topological edge states in Pb/Si. In order to do so we will consider a system in which a small ferromagnet will locally (over the size of a few nanometers) create an area of topological superconductivity by means of a time reversal symmetry breaking interaction (see fig. 5.7). This will define two areas of different topologies (outside and inside the ferromagnet) that will lead to the formation of edge states at the interface between the two areas. In order to realize such system experimentally we need to first obtain the superconductor that will exhibit the necessary triplet correlations and then be able to control the growth of ferromagnets sufficiently coupled to the superconductor in order to trigger the topological transition.

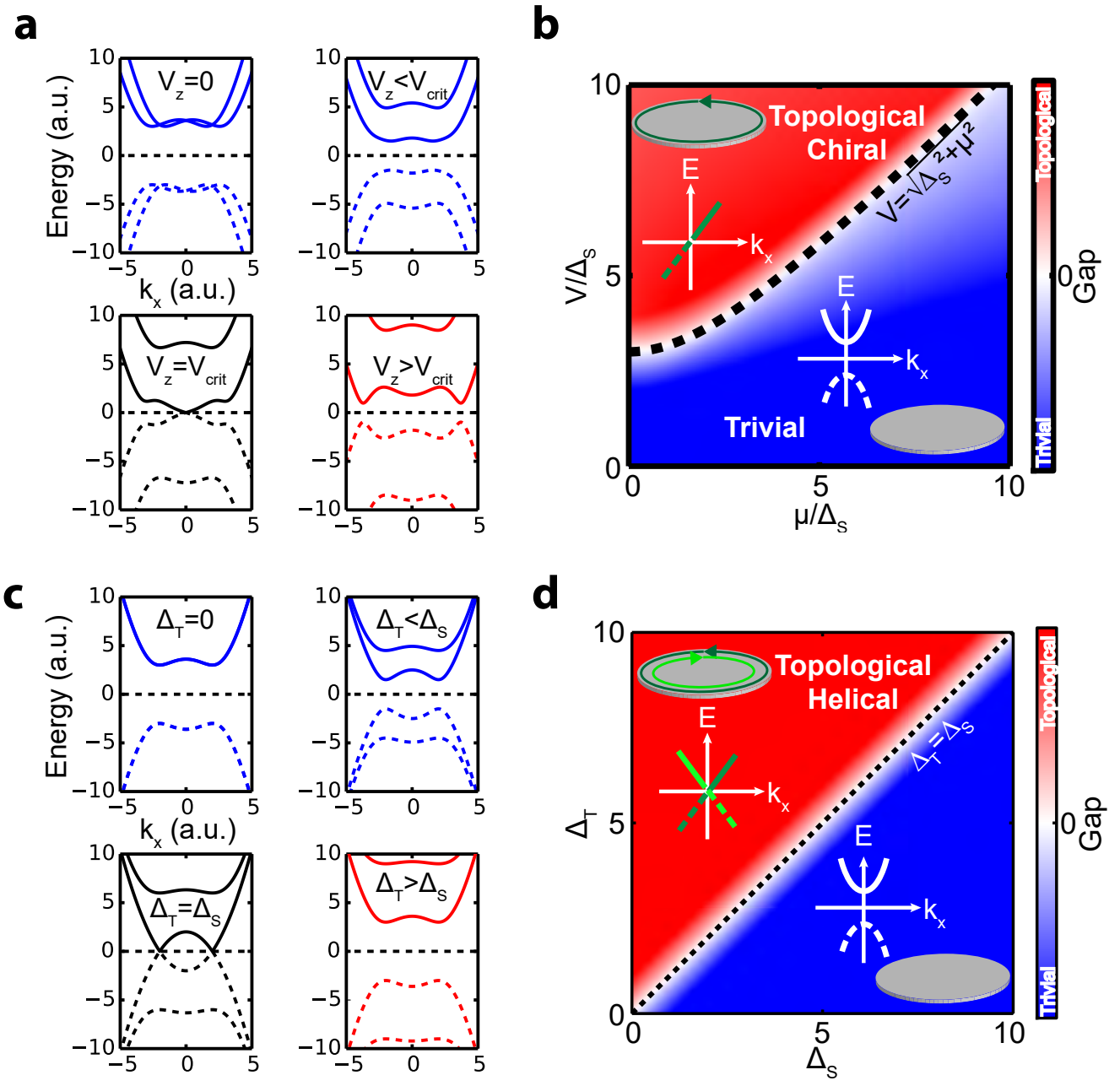

Figure 5.5: **Helical vs. chiral superconductivity:** a. Band structure of a system with Rashba spin-orbit and singlet superconductivity for different values of the magnetic field perpendicular to the surface ($\Delta_T = 0$ here). b. Phase diagram for topological state in this system as a function of the chemical potential μ and the Zeeman coupling V_z. The blacked dashed line represents the topological transition where the gap closes. c. Band structure of a system with a mix of singlet and triplet superconductivity for increasing triplet value. d. Phase diagram for topological state in this system as a function of the amplitude of the singlet pairing Δ_S and the triplet pairing Δ_T ($\alpha = 0$ here).

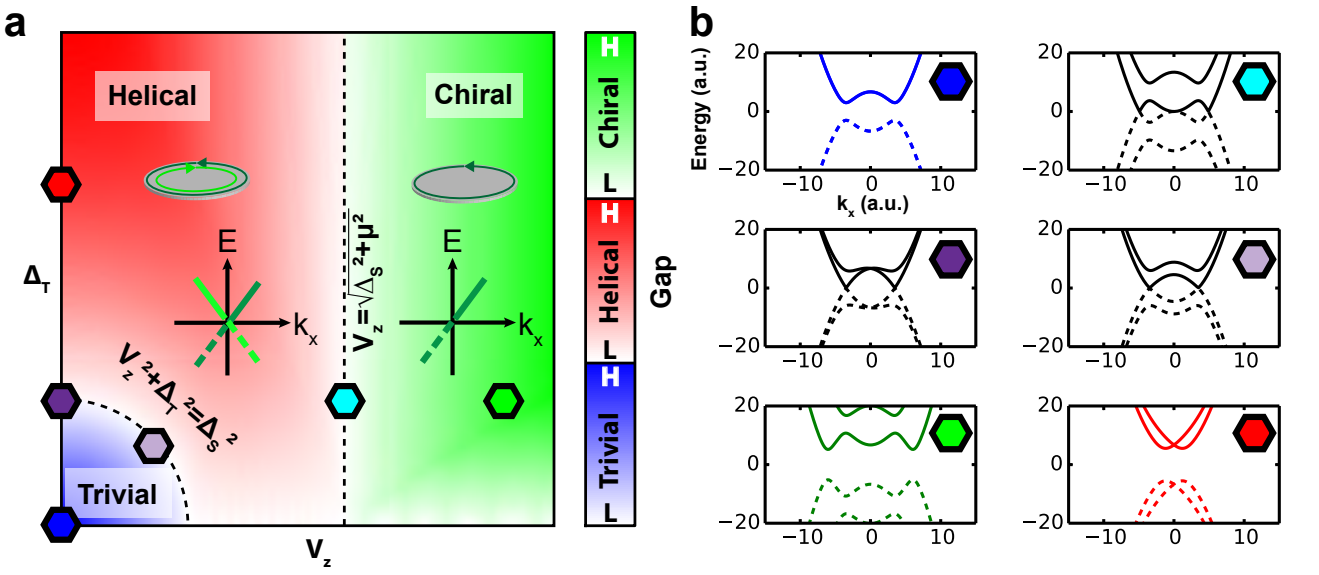

Figure 5.6: **Topological superconductivity phase diagram:** a. Phase diagram presenting the three coexisting phases of superconductivity: trivial (blue), helical (red) and chiral (green). b. Band structure taken at different points of the phase diagram a. at points indicated by the color diamonds.

As we explained before in order to observe topological superconductivity and Majorana fermions spin-orbit coupling is an essential component. It thus becomes necessary to determine what kind of system is the most favorable. Because Rashba spin-orbit coupling arises at surfaces, thin films and monolayer superconductors seem to be good candidates. Strong spin-orbit splitting was indeed reported at the surface of semiconductors covered by a metal layer [130, 131, 132, 133, 134].

The next step is to find a metal with a strong spin-orbit interaction. Because the strength of the interactions varies as Z^3 with Z the atomic number of the element we will privilege heavy elements. The system Pb/Si(111) thus seems to be an interesting one as Pb is known to present strong spin-orbit coupling [135, 136]. Furthermore, as we have shown before (section 4.4.2), the electronic diffusion by non magnetic disorders induces peak height fluctuations as well as a gap filling effect. We showed when discussing fig. 4.8 that the selection rules for the diffusion spots in the Fourier transform were linked to a spin-orbit coupling in the Pb/Si(111) monolayers.

The results we will show in the next session were obtained by combining the Pb monolayer with nanoclusters of Co. We found that the Co arranges in the form of clusters of sizes varying from 5 to a few tenths of nanometers and act as small ferromagnets. We have thus gathered the ingredients necessary to the obtention of topological superconductivity and the observation of edge states.

5.5 Sample preparation

Our samples were prepared under UHV at a maximal pressure of 3.10^{-10} mbar. The first step of the preparation consists into cleaning the Si that will be used for the Pb and Co deposition later on. We used wafers of Si cut along the (111) orientation and doped with phosphorus. We first submitted the Si to a series of "flashes" at 1200°C by direct current heating.

We usually perform about 20 flashes to make sure that we get rid of the biggest defects such as silicon carbides. The Si substrate is then prepared by rapidly changing the temperature from 1200°C to 900°C directly after a flash. If the pressure inside the preparation chamber during this step stays in the range 10^{-10} mbar we then slowly decrease the temperature down to 500°C in order to form the 7×7

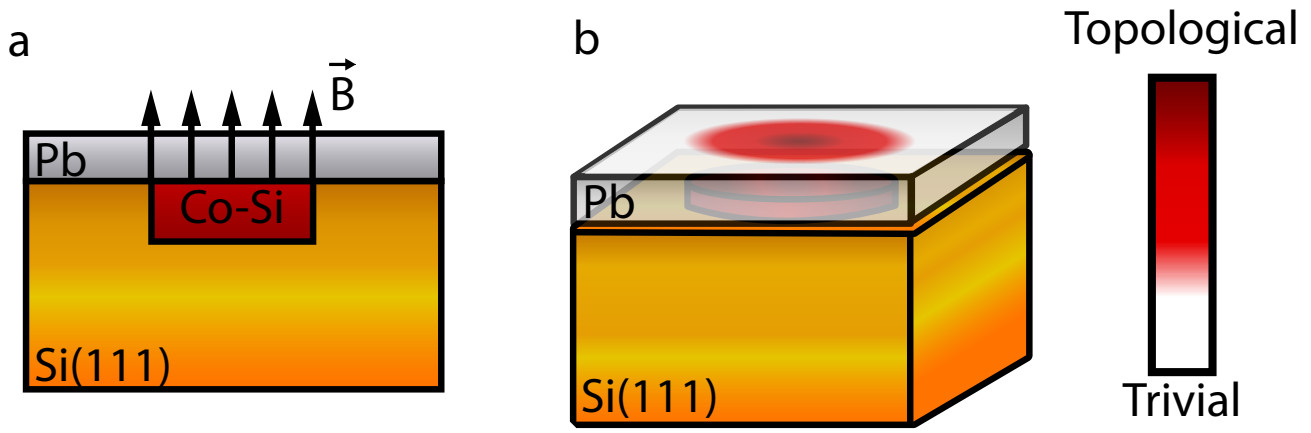

Figure 5.7: **Structure of the sample Pb/Co/Si(111):** a. Side view of the system showing the inclusion of the Co inside the Si substrate. Over this the Pb monolayer remains unmodified but still feels the effect of the magnetic field $\boldsymbol{B}$ created by the underlying Co atoms. b. When in the superconducting state, the superconductivity from the Pb monolayer enters the topological phase under the action of the magnetic field while the rest of the sample remains in the trivial phase.

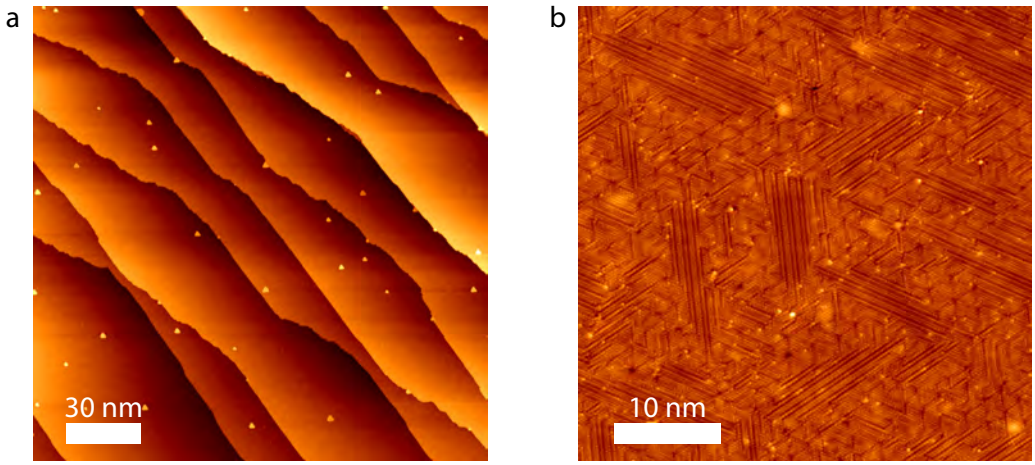

Figure 5.8: **Topography of Pb/Co/Si system:** a. Large scale (181×181 nm^2) topography showing the monoatomic steps from the Si substrate as well as the small islands created by the Pb. b. Zoom of a small area (42×42 nm^2) of the sample showing the atomic structure of the system.

reconstruction (see Fig. 5.9). If the pressure criterion is not satisfied we go back to the previous steps of flashing the sample until we can operate under good conditions of pressure. During all the different preparation stages we cool the cryopot with nitrogen of the preparation chamber allowing for a lower pressure thanks to a cryo-pumping phenomenon on the walls of the chamber.

We then wait for the sample to reach room temperature before proceeding to the Co and Pb deposition. These two depositions were performed one after the other from sources previously calibrated with a quartz microbalance. We evaporate Co onto the sample for 6 sec with a flux of 10^{-2} ML.min^{-1} for a final quantity of 10^{-3} ML. In order to obtain an homogeneous Pb mono-layer we start by depositing 4 ML and then

anneal the whole sample in the structure Pb/Co/Si at 375°C during a time that will depend on the precised structure one wants to obtain (see Fig. 5.9) and can range between 90 sec and 5 min.

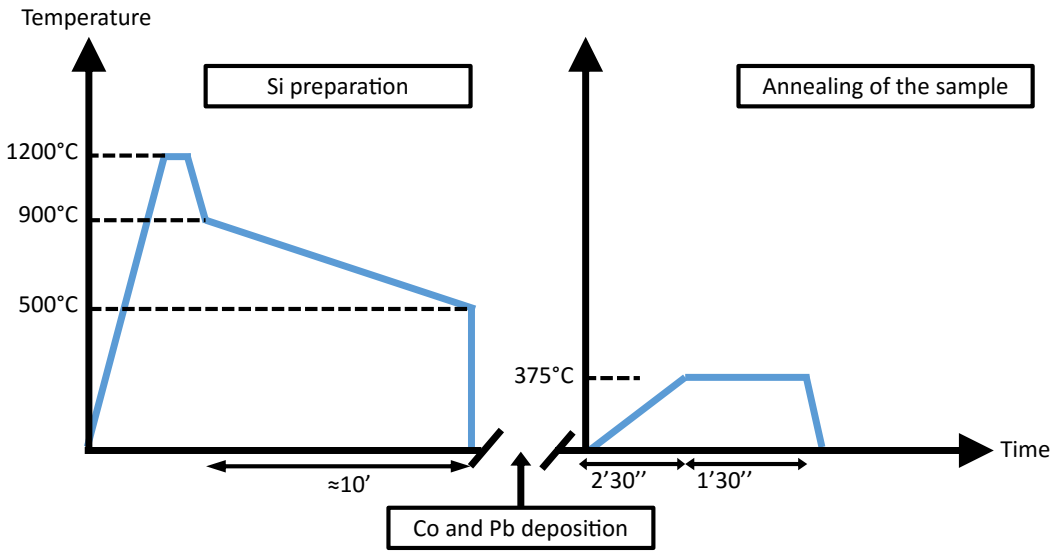

Figure 5.9: **Steps of sample preparation:** The sample is prepared in three separate operations, the Si cleaning, the Pb and Co deposition and the final annealing of the sample.

Using such recipe leaves us with an homogeneous sample with only a few Pb islands as shown on Fig. 5.8.a and the Co is not seen in the topography, leaving a seemingly unperturbed Pb monolayer. We will discuss in the following the Co clusters and the way we can image them. The steps originating from the Si substrate are mono-atomic for the large majority and only a few are double. On the level of the atomic structure we obtain a mixture between a linear and an hexagonal phase (HIC). Both those phases coexist homogeneously in the sample and domain walls are accomodated by $\sqrt{7} \times \sqrt{3}$ boundaries (see Fig. 5.8.b). As usual we observe a few single atomic defects on our samples due to the impurity already present in the Pb source or adsorbed during the sample preparation. As we observed in the case of the individual YSR states, the impurities from the Pb source can give rise to magnetic signatures in the gap. However those impurities are extremely dispersed throughout the sample and their signatures in the LDOS rarely overlap.

5.5.1 Imaging of the Co clusters

One of the question that remains is: why is Co not visible in topography measurements? Our strategy was to anneal a sample containing those clusters up to a point where most of the Pb had evaporated.

We performed an annealing of the sample during 2 hours at 400°C and obtained the structure presented on fig. 5.10.a. The phase we obtained is a mosaic phase and we have only a few island remaining that appear as bright spots on this figure separated by 50 nm in average (some of them are indicated by white arrows on the figure). The step edges have been strongly modified during the annealing and appear shredded indicating that the Si is also moving during this procedure.

The islands left on the sample are actually Co islands capped with Pb that enables for a semi-direct

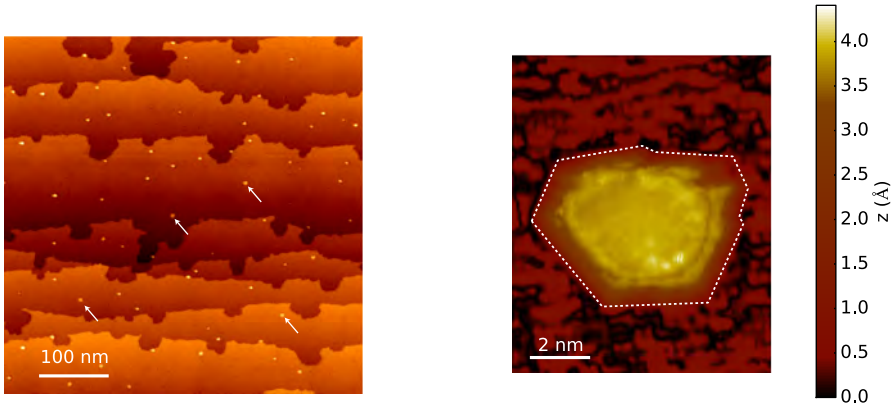

a b

Figure 5.10: **Topography of a Co cluster:** a. 536×536 nm^2 area topography of a Pb/Si sample containing 10^{-3} ML of Co after a 2 hours annealing at 400°C. b. 11×9 nm^2 close-up on a Co cluster capped with bilayer Pb. The white dashed lines delimits the contour of the Pb capping.

observation of the Co clusters. On fig. 5.10.b we present a close-up of such an island where we adapted the color code in order to see both the surface of the sample and the island. While we still have a truncated triangular global shape characteristic of Pb islands we also see on the top of the island a quasi-circular contour that is not seen in the case of Pb islands without Co. The characteristic size of the Co associated features is around 5 nm of lateral size and the measured height is about 4 Å. While the tip tends to induce an artificial broadening the fact that we observe such sharp contour around the Co makes us confident that we do measure the real size of the cluster. However we must be careful with the measurement along z as some electronic effects can play a role.

We also performed, with the help of D. Demaille, transmission electron microscopy (TEM) measurements on our sample and those results are shown on fig. 5.11. These images clearly reveal the existence of nanometer-sized objects in our sample. It was not possible however to obtain a chemical analysis of these objects as they tend to disappear under the electron beam during long exposure measurements.

Most of the previous experimental work on the magnetic and structural properties of Co/Si(111) were done for much larger Co covering [137] and little is known on the magnetism of nano-clusters. In particular it was shown that for coverage of the order of 1 ML, the system did not exhibit magnetic property. However some work showed the dependence of the annealing temperature on the magnetic properties of the Co thin films on Si(111) substrate [138, 139]. In particular it was shown that for annealing temperatures above 600 K, the hysteresis loops essentially disappeared. The difference in size and in temperature with our own samples could help explaining the discrepancy between previous experiments and our own case. In the future it would obviously be necessary to perform complementary magnetic measurement on our own samples in order to confirm the presence of magnetism in our nano-structures and definitively validate our theoretical model.

5.6 Experimental results

5.6.1 Topological edge states

The data presented in this section were obtained by using a superconducting tip in order to increase the resolution. This tip was prepared from Pt-Ir wire that was covered with Pb by crashing the tip into the Pb 3D islands grown over SiC clusters that are sometimes found on the surface. The tip thus exhibits a superconducting gap of 1.3 meV similar to bulk Pb. The samples discussed here were obtained by first

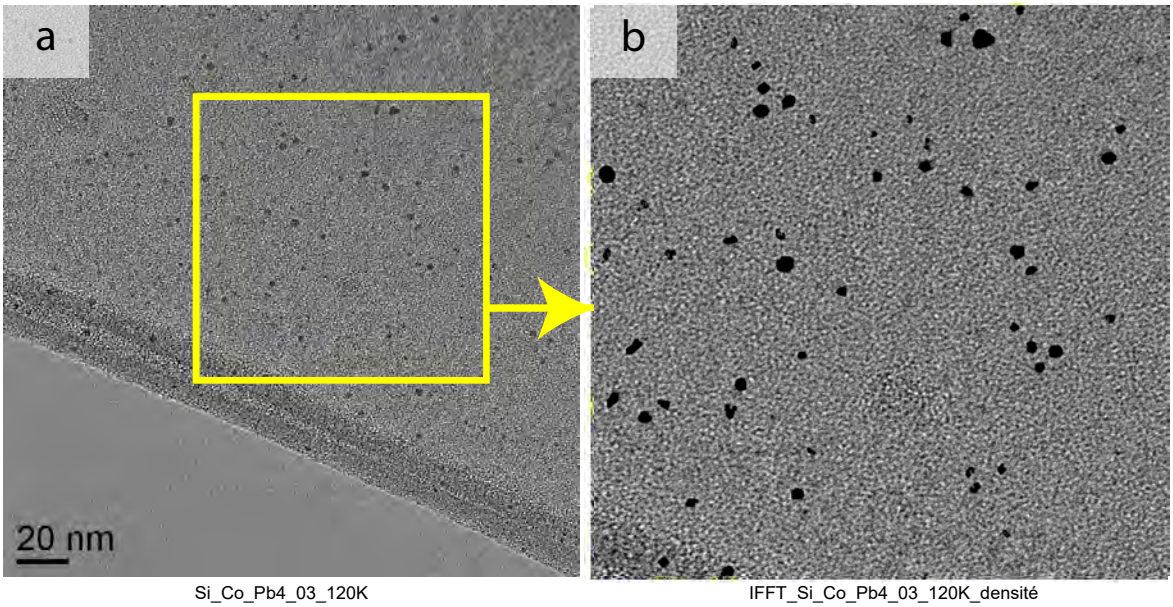

Figure 5.11: **TEM planar view of Pb/Co/Si(111) samples:** a. 213×213 nm^2 area observed by TEM from a planar view of one of our sample revealing the Co clusters as dark spots. b. 105×105 nm^2 zoom of the yellow area.

depositing $0.8.10^{-3}$ ML of Co before Pb deposition and annealing the sample at 365°C for 90 sec. The atomic structure of the Pb monolayer obtained using this set of parameter corresponds to the SIC phase. We show our area of interest on fig. 5.12.a. This part of the sample corresponds to an area where a cluster of Co is buried below the Pb monolayer. This cluster has a radius of approximately 5 nm and is only seen in conductance maps in the gap energy range. The corresponding in-gap spectroscopy is shown on figs. 5.12.b.-d.

At the Fermi level (b.) we observe a perfect circle in the conductance map. This ring corresponds to the edge states at the interface between a trivial superconductor (away from the Co cluster) and a topological one (above the Co cluster). The ring separates for larger biases into an inner and an outer ring (c. and d.). The separation of the zero-bias ring at $E \neq E_F$ thus reveals the helical behavior of the system through its two nonequivalent edge states. If we refer to the phase diagram of fig. 5.6.a we are originally (away from the Co cluster) in the blue area somewhere on the y axis. The magnetic cluster induces the transition as V_z crosses the two phase transitions (along the horizontal direction of the diagram of fig. 5.6.a.). The question is here to know whether we are in the helical configuration or in the chiral configuration.

The separation of the two rings can better be visualized by taking a line cut through the spectroscopic data that crosses the center of the disc. This cut is showed on fig. 5.12.e. On this cut we clearly see the X-shaped crossing of the state at the Fermi level at ±3 nm from the disk center. It should also be noted that the states connect continuously (up to the energy resolution of our measurement) across the full gap thus giving a real dispersion of the states. The existence of a dispersion is clearly in opposition with what we had observed for YSR bound states that only admit a pair of states inside the gap (or a few pairs depending on the potential size) at a given energy.

Because we reach the topological regime by means of a Zeeman field, time-reversal symmetry is broken in our system. Theoretical tight-binding calculation of a spatially variable magnetic field[2] let us think that

[2]We take a Zeeman potential $V_z(r)$ of a gaussian form $V_z(r) = V_{\max} e^{-r^2/\sigma^2}$.

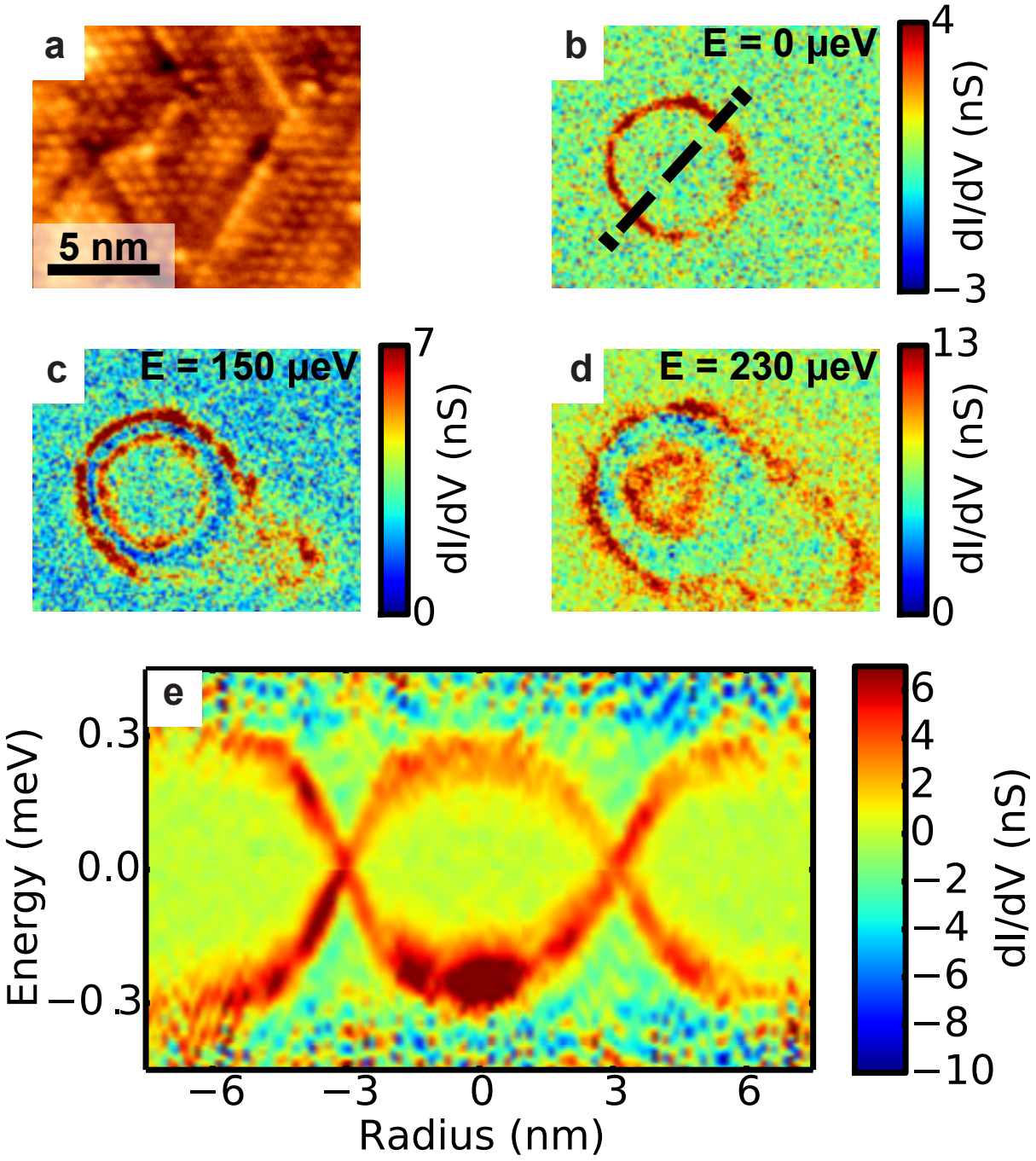

Figure 5.12: **Edge states of a buried ferromagnetic cluster of Co:** a. Topography of a 16×13 nm^2 area of a Pb/Si(111) sample in the devil's staircase phase. b.-d. Conductance maps at 0 meV, 0.1 meV and 0.2 meV respectively showing the edge states induced by the underlying Co cluster. e. 10 nm wide cut passing through the center of the circle showed on b. showing the spatial dispersion of the gap crossing states. On the cut, we suppressed the gap of the tip from the raw data and subtracted the average spectrum measured on the surface far from any defect in order to better adapt the color scale.

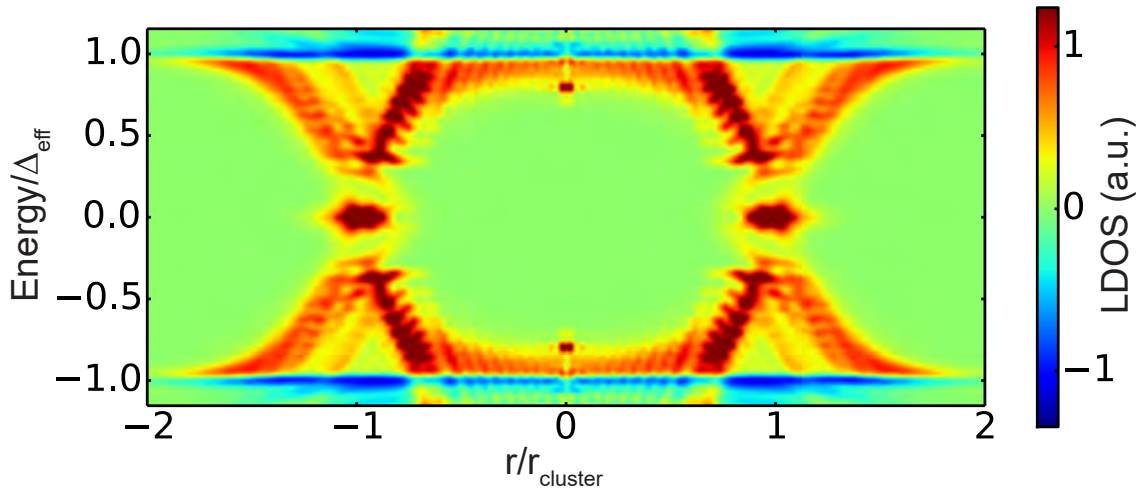

Figure 5.13: **Tight binding calculation of the edge states between an helical and a trivial superconductor:** In this calculation we used the values $\Delta_S = 4$ and $\Delta_T = 1.4$ and the Zeeman energy $V_z = 12$ at $r = 0$. In this configuration the central part of the system is in the chiral phase will the external part not affected by the Zeeman interaction is in the trivial phase. On this figure we subtracted the superconducting spectrum of the trivial phase in order to better show the appearance of the in-gap states.

we are in the chiral configuration. We present in fig. 5.13 the result of the calculation for a topological chiral cluster with a smooth interface with a trivial superconductor. This calculation was performed by projecting the 2D model of our system on a 1D space by supposing a cylindrical symmetry. We were thus able to separate the radial and angular part of our wave-function as

$$\Psi(\boldsymbol{r}) = \sum_{m_J} \psi_{n,m_J}(r) e^{i\hat{J}_z\theta} \tag{5.24}$$

where m_J refer to the eigenvalues of the rotation operator $\hat{J}_z$ commuting with the Hamiltonian describing our system. From the separation of the radial and angular part we are able to only plot the radial part of the LDOS $|\psi(r)|^2$. In that LDOS map (subtracted from the trivial DOS) we recover the typical X shaped crossing of the edge states that we observe experimentally. Calculations performed with other set of parameters show that the crossing of the states can only be obtained if the maximal value of V_z is taken so it satisfies the chiral criterion $V_z > \sqrt{\Delta_S^2 + \mu^2}$.

In our experiment the presence of two gap-crossing states is a reminiscence of the helical phase that is crossed when evolving from chiral to trivial. Our helical edge states are equivalent to those observed for quantum spin Hall effect (which presents two edge states) with an applied magnetic field (that splits the edge states). The spatial splitting of the opposite chiralities is caused by the Zeeman interaction that breaks the time reversal symmetry. The splitting vanishes at the Fermi level as the electron-hole symmetry restores the time reversal equivalence of the two chiralities.

A remark one can make concerning these experimental in-gap signatures is that they do not correlate to any topographic feature. Contrary to what we had previously observed for YSR bound states observed around single magnetic impurities, the in-gap states do not seem to be sensitive to the local disorganization of the Pb monolayer. At 0 bias in particular the width of the ring is approximately 0.7 nm which is comparable to the typical atomic dimensions and Fermi wavelength of the system. This behavior is in direct opposition with the long range extension we observed in the case of YSR bound states where the spatial extent is mostly driven by the coherence length ξ of the superconductor. Here ξ does not seem to

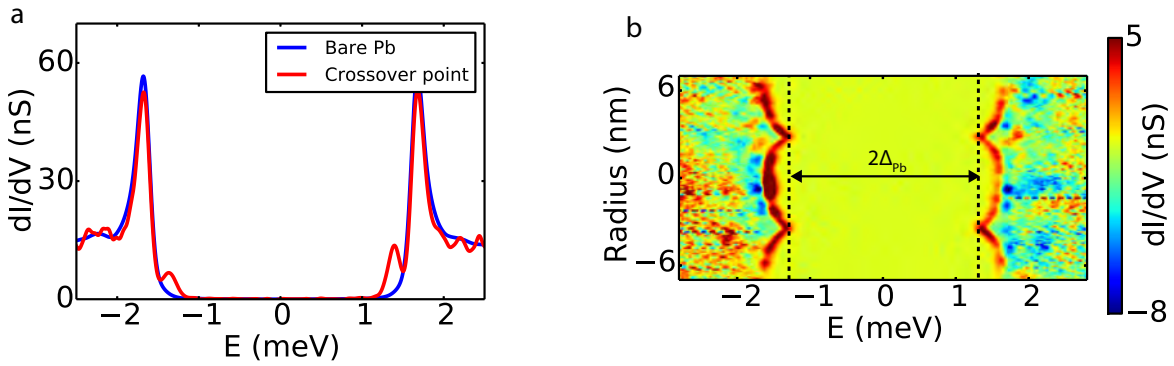

Figure 5.14: **Un-shortened spectrum line cut:** a. Spectra taken on the ring seen at 0 bias in fig. 5.12.b (red) and far from any magnetic perturbation or interface effect (blue). b. Cut through the ring where the removal of the states between $\pm\Delta_{Tip}$ was not performed. The black dashed lines indicate the position of the tip gap and the reference value used to obtain fig. 5.12.e.

play a role and only atomic dimensions are relevant for the zero bias features. However at different biases the spatial extension of the states increase. In particular a nearby defect that is absolutely absent from the zero-bias conductance map starts to become visible at the bottom right corner of the images on figs. 5.12.d and fuses with the previously clean topological edge states. Our explanation for this behavior is that the defect in the bottom is actually a YSR bound state or a small cluster leading to a YSR band that gets included into the edge state at its own characteristic energy. The inclusion of this state to the more global topological edge state is better seen on fig. 5.12.d where we can really follow the outer crown of the helical states that totally surround the YSR state with no discontinuity. Surprisingly the extension of this additional feature is determined by the characteristic length scales of the cluster and not the characteristic length scales of the YSR bound states as one would expect. We do not have an explanation for this fact.

Because these data were acquired using a superconducting tip, there exists a whole area of the spectrum (for $|V| < \Delta_{Tip}$) that does not contain any worthwhile information. Thus in the cut 5.12.e we simply suppressed this area in order to only show the spectroscopic features linked to the sample. This allows us to see the continuation of negative bias states into the positive bias ones and follow the dispersion of the states in the system. On this figure we also subtracted the mean Pb spectrum in order to obtain a better contrast on the in-gap states[3]. In order to compare these results with the original data set, we present on fig. 5.14 the data without the cut. On this figure, as expected, we clearly see that we do not have any spectroscopic signal in the range $|V| < \Delta_{Pb}$.

5.6.2 Majorana bound states in vortex cores

Now that our toolbox contains the necessary ingredients for topological superconductivity, the next challenge is to successfully obtain a zero bias Majorana excitation that can then be manipulated in braiding operations.

Theoretical calculations show us that from the dispersion of chiral edge states we observe at the frontier between a topological and a trivial superconductor, the only way to stabilize a well defined zero bias mode is to introduce a vortex inside the cluster. In cylindrical symmetry we can separate the wave-function in a radial ($\psi_{n,m_j}(r)$) and an angular ($e^{i\theta\hat{J}_z}$) component. For a p-wave superconductor, the vortex allows us

[3]We applied the same gap subtraction procedure on fig. 3.6.

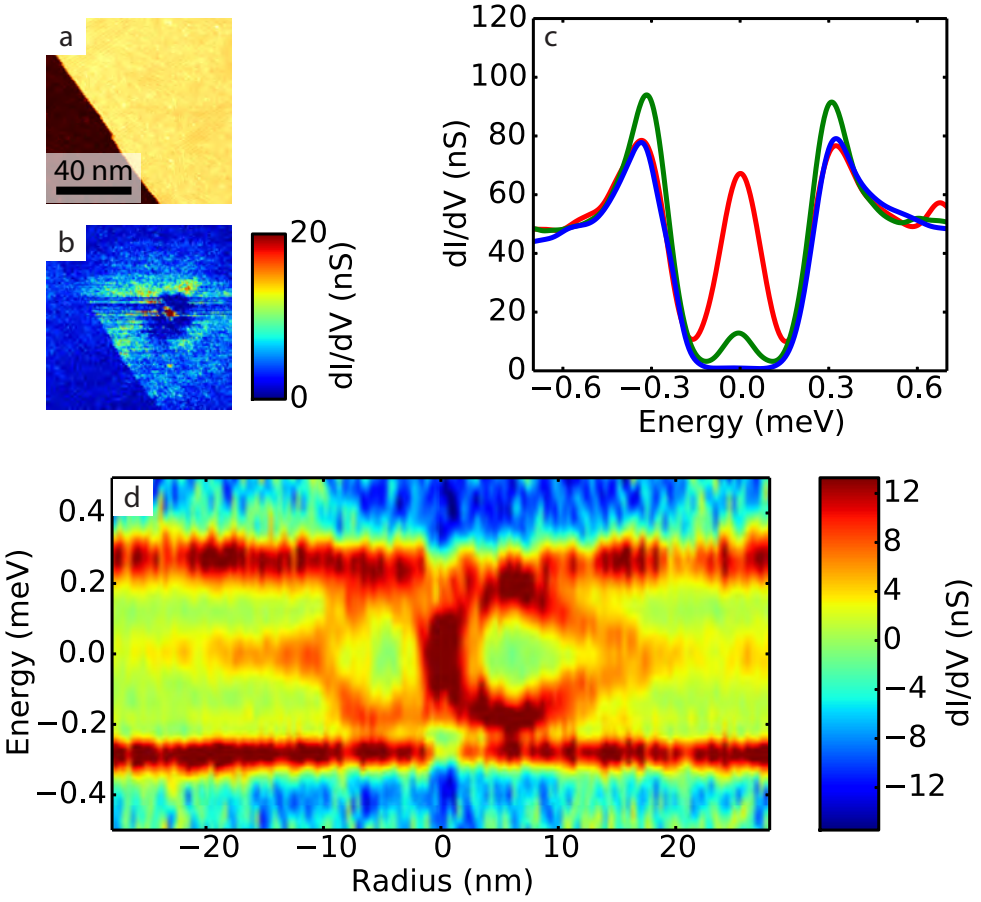

Figure 5.15: **Spectral signature of a disorder proof zero bias spectral signature:** a. Topography of a 100×100 nm^2 area on a Pb/Si(111) sample in a mixture between linear and hexagonal devil staircase phases. b. Zero bias conductance map of the same area. c. Spectra taken at the maximum of the conductance map b. (red), on the ring surrounding this maximum (green) and on the bare monolayer (blue). d. 65 nm long spatial and energy cut through the defect visible on b. along the white line of the same figure.

to write a rotation operator J_z that commutes with the Hamiltonian of the form

$$\hat{J}_z = \hat{L}_z + \frac{1}{2}\hat{\sigma}_z + n\hat{\sigma}_z, \tag{5.25}$$

with L_z the angular momentum and n the vortex winding number. As we look for single solutions at $E = 0$ we want it to be defined by a single quantum number n. For an odd value of n the eigenvalues m_j of J_z will take integer values. On the other hand, the electron-hole symmetry we look for implies that for every positive energy solution $\psi_{m_j,E}$ we have the corresponding negative energy solution $\psi_{-m_j,-E}$. We would thus have for an even value of n a coupling between the positive and negative energies solutions of the states that will prevent the appearance of an isolated zero-bias mode. The only solution is then to have $m_j = 0$ for which $n \in \mathbb{N}$ and the phase of the wave-vector has an even number of winding around the vortex.

We observed experimentally that for larger topological domains with size of the order of 20 nm, a vortex forms in the center of the domain and drastically modifies the structure of the edge states. We reached those experimental conditions by slightly increasing both the amount of Co deposited on the

surface (1.10^{-3} ML instead of $0,8.10^{-3}$ ML in the previous case) as well as the annealing time (4 min 30 sec instead of 1 min 30 sec in the previous case). The objects we obtained in these conditions have a characteristic size of around 20 nm and present drastically different spectral signatures from what was observed and described in the previous section.

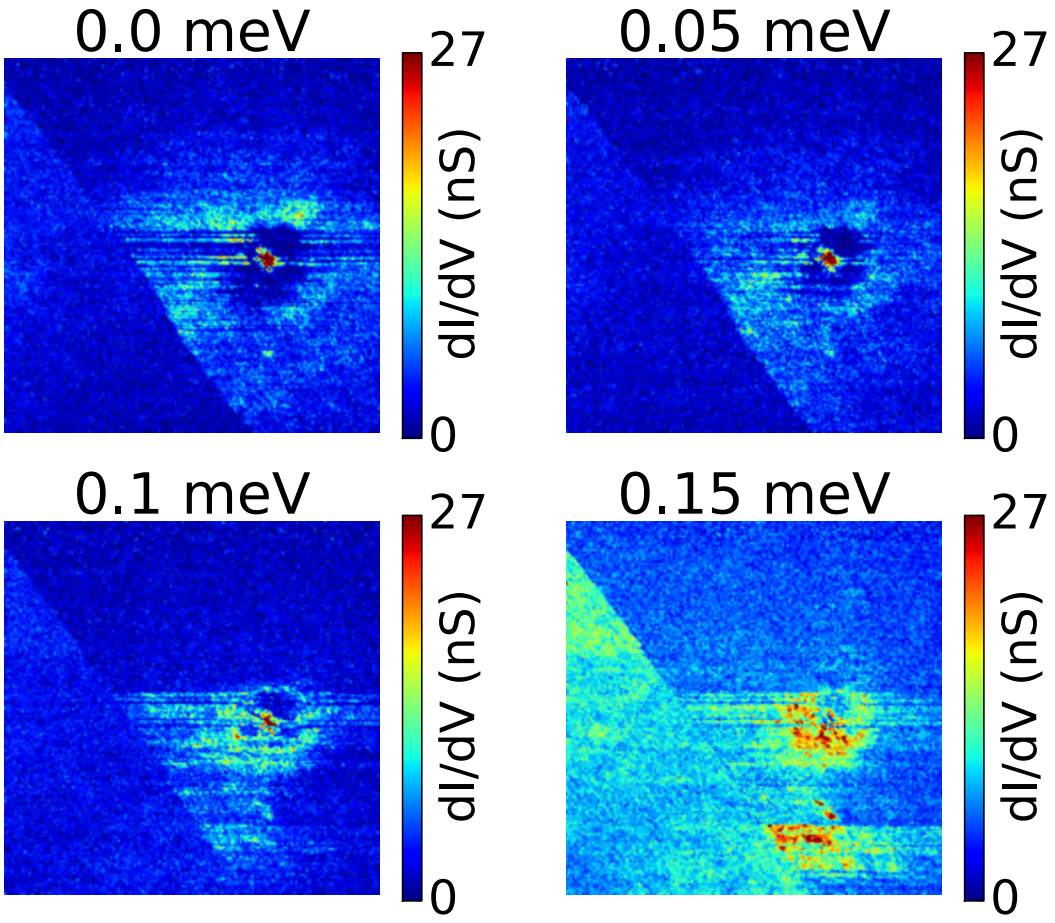

Figure 5.16: **Conductance maps of a Majorana bound state:** Conductance maps at 4 different in-gap energies (0 meV, 0.5 meV, 1 meV and 1.5 meV) showing the energy evolution of the spatial dispersion of Majorana bound states.

We present on Figs. 5.15 and 5.16 the results obtained on a vortex observed inside of a topological area[4]. Despite the different preparation conditions, the Pb phase of the monolayer is the one we had achieved in the previous case and no significant difference can be observed as it can be seen on fig. 5.15.a. When performing spectroscopy of the area presented on fig. 5.15.a we observe two different features at the Fermi level. First we obtain a crown surrounding the topological domain as we had in the previous case, but it is here accompanied with another state localized in the very center of the topological domain characteristic of the presence of a vortex. The spectra taken at these two positions (in the center of the

[4]All of the results of this section were obtained with a normal tip and thus the data manipulations that were used in the previous subsection in order to suppress the tip gap are not necessary here and the data analysis was done using the same procedure as in all the others chapters of this thesis.

cluster and in the outer crown) show clear zero-bias peaks with the center one exhibiting a very strong amplitude as seen in fig. 5.15.c in red. On the outside of the topological domain we observe that the dI/dV peaks collapse at E_F for $r \to \infty$. This evolution of the states is better seen by taking a line cut across the magnetic cluster passing through the center peak. This cut is shown on fig. 5.15.d where the bare superconducting spectrum has been subtracted in order to only leave the contrast of the in-gap states in the LDOS plot. The behavior of the in-gap states is much different from what we had observed in the case of the continuum of interface states. Here, due of the presence of the vortex, a zero energy level is pinned at the high symmetry point of the system which corresponds to the center of the magnetic cluster. This central state is connected with the interface states by a continuum of states that move towards the gap edges before converging back to the Fermi level.

The question arises to explain why such topological effects were not observed in the last chapter for large clusters. The simplest explanation consists in saying that due to the size of the clusters and the growth method used to obtain them we cannot get a well ordered magnetic structure. Ordering is a necessary condition as the Co may form Co silicide having non-ferromagnetic structures, that may not fulfill the necessary condition to enter the topological regime by creating a magnetic field larger than the critical field $V > \sqrt{\Delta_S^2 + \mu^2}$ (for the chiral case) or $\sqrt{\Delta_S^2 + \mu^2} > V > \sqrt{\Delta_S^2 + \Delta_T^2}$ (for the helical case).

5.6.3 Magnetization switches

On Fig. 5.15.b. we can observe a discontinuity in the conductance maps as for some lines we seem to lose the zero bias signatures of the Majorana bound states. By comparing these jumps with the topography we observe that no correlation can be established as the spectroscopic jumps are not visible by any means in the topographic data. This eliminates the possibility of a tip instability that should be observed in topography as well as in spectroscopy. By repeating the measurement from the top of the initial image 5.15.a. to the bottom of the same area we obtained the results presented on fig. 5.17.

On this figure we show that at one point of the spectroscopy measurement, the zero bias signatures suddenly disappear. The transition is marked by a white dashed line in fig. 5.17.a. However we do not lose the in-gap spectroscopic signal totally as shown in fig. 5.17.c. On this figure we show the conductance map obtained at $V = 0.14\ meV$ that exhibit what looks a lot like YSR bound states. The spectra taken in the top part and the bottom part of the scanning area are shown in figs. 5.17.b. and d. respectively. What these spectra reveal is that the sudden disappearance of the zero bias Majorana bound states (on the center and edge of the magnetic cluster) leaves some states at the gap edges (indicated by the two orange arrows on fig. 5.17.d). We attribute the gap edge states to a YSR impurity band due to a domain with in plane magnetization. The crown of the Majoranas is not observed anymore once the shift has occured and the disorder sensitivity typical of YSR bound states is recovered for the gap edges states.

We interpret such drastic differences as a switching of the cluster magnetization from an out of plane field (which leads to the formation of Majorana excitations) to an in plane field which does not satisfy the conditions to enter the topological regime for reasons we evoked when discussing fig. 5.2. The sudden shift of magnetization occurring at the exact point in time when the STM tip passes at the center of the magnetic cluster leads us to attribute this effect to the tip electrical field or inelastic excitation reversing the magnetization. Our explanation is supported by multiple observations of this effect on similar clusters of comparable sizes. The spatial extension of the cluster can easily explain how, compared to the small clusters of the previous section, the anisotropy of the system could make the in and out of plane magnetic configurations almost equivalent. The tip disturbance (by its electric field or a current induced excitation of the magnetization) would become sufficient to overcome the energy barrier between the in and out of plane configuration and induce the switching.

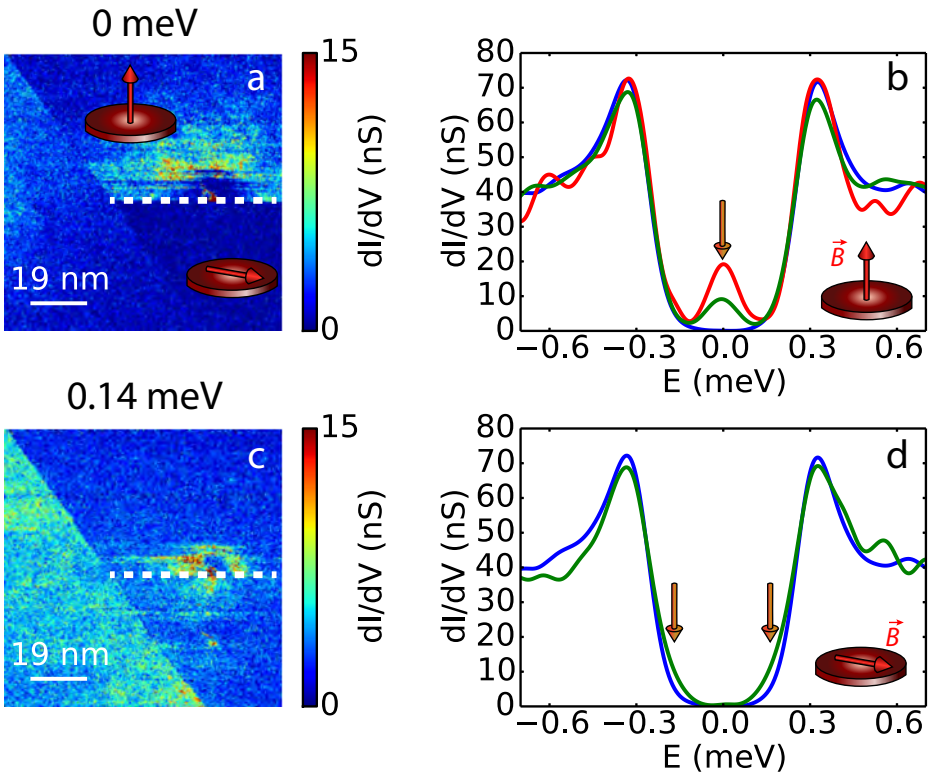

Figure 5.17: **Bi-stability of the system and Majorana switching:** a. Conductance map taken at 0 meV showing the abrupt transition while scanning between the presence and absence of the zero bias peak. b. Spectra taken on the center spot (red) and outer crown (green) on the top part of the conductance map. The arrow shows the position of the Majorana peak at the Fermi level. The blue spectrum is included as a reference for the usual superconducting spectrum of the Pb monolayer c. Conductance map taken at 0.14 meV of the same area showing the Shiba contribution to the Majorana modes (on the top) and the fully Shiba-like states (on the bottom). d. Spectra taken over the disordered YSR states in the bottom part of the scanning area (green) and on the superconducting monolayer far from any magnetic defect (blue). The two arrows indicate the position of the Shiba bound states at the gap edge. The conductance maps were acquired by scanning from the top to the bottom of the scanning area.

5.7 Conclusion

In this chapter we addressed topological superconductivity by first detailing the ingredients necessary to obtain it. We explained the way Rashba spin-orbit interaction modifies the superconducting ground states by introducing triplet correlations. This discussion allowed us to plot the phase diagram of superconductivity as a function of the weight of the triplet order parameter Δ_S and the Zeeman field amplitude V_z. We then presented and discussed the results we obtained by growing magnetic clusters of Co covered by a monolayer of Pb. We showed how the self-organizing Co clusters buried under the Pb monolayer act as small local ferromagnets that induce edge states at the frontier between a topological superconductor and a trivial one. Surprisingly, while we expected a single chiral state due to time reversal symmetry breaking we obtained a pair of chiral states that we interpreted as a signature of the helical phase that is crossed during the transition between the chiral and trivial phases.

When increasing the size of the clusters we showed that we can trap vortices inside the topological and induce zero bias Majorana bound states. The existence of these bound states is determined by the orientation of the Zeeman field that can be switched by using the tip of a STM. We hope to be able in

future studies to better understand the shift mechanism in order to achieve a total control over the state of the system and a full control of the Majorana excitations that could lead to braiding possibilities of said Majoranas.

Chapter 6

The Pb/Si(111) monolayer: A playground for 2D physics

6.1 Introduction

As we have seen in the previous chapter the system Pb/Si(111) presents a large variety of structural phases that depend on the nominal Pb coverage. In this chapter we will discussed results obtained by STM/STS in the system Pb/Si(111) for non superconducting phases not discussed before. Unlike the results presented in the two previous chapters about the $\sqrt{7} \times \sqrt{3}$, HIC and SIC superconducting phases, the results presented here are not yet fully understood or do not benefit from a full and complete theoretical interpretation. Therefore this chapter more than the others will be mostly oriented towards experiments and will be lighter on the theory side.

The first part of this chapter will deal with diluted phases of Pb/Si(111) (namely the 3×3 and $\sqrt{3}\times\sqrt{3}$ phases). We will present the signatures of a quasi-Mott insulator phase and its behavior when placed in proximity to metallic phases. We will conclude by presenting results still not fully understood covering our work on the proximity effect between the $\sqrt{7} \times \sqrt{3}$ and 3×3 phases where one phase is superconducting and the second one is nearly Mott-insulating.

The part concerning the low density monolayer phases in the normal state was performed in collaboration with V. Cherkez and R. Federicci.

6.2 Induced metallicity

6.2.1 Phase coexistence in Pb/Si(111) systems

In this section we focus on the metallic and insulating phases of Pb/Si(111). We will mostly focus on the metallic $\sqrt{7} \times \sqrt{3}$ and 3×3 phases and insulating disordered $\sqrt{3} \times \sqrt{3}$ phase.

When growing monolayer samples it is difficult to obtain homogeneous phases over the whole sample. The most common case is the one where we obtain a mixture of phases over different areas of the sample. This configuration leads to a system globally in the $\sqrt{7}\times\sqrt{3}$ phase with patches of 3×3 at the step edges.

We present on fig. 6.1.a a paradigmatic example of what one should expect for long annealing of a Pb/Si(111) sample. On this figure we see two domains of $\sqrt{7}\times\sqrt{3}$ phase on the bottom and right side of the image. These phases are in contact with a 3×3 domain and are separated from it by a well visible boundary. Inside the 3×3 domain we also observe a disordered $\sqrt{3}\times\sqrt{3}$ part which connects continuously to the 3×3 phase (see for another example fig. 6.1.b on which the unit cells of the $\sqrt{3} \times \sqrt{3}$ and 3×3 are represented using a red losange and a blue hexagon respectively). The difference in the connection between the 3×3 to the $\sqrt{3}\times\sqrt{3}$ and the connection between the 3×3 to the $\sqrt{7}\times\sqrt{3}$ is easily explained by the fact that the 3×3 is derived from the $\sqrt{3}\times\sqrt{3}$ through a temperature dependent phase transition

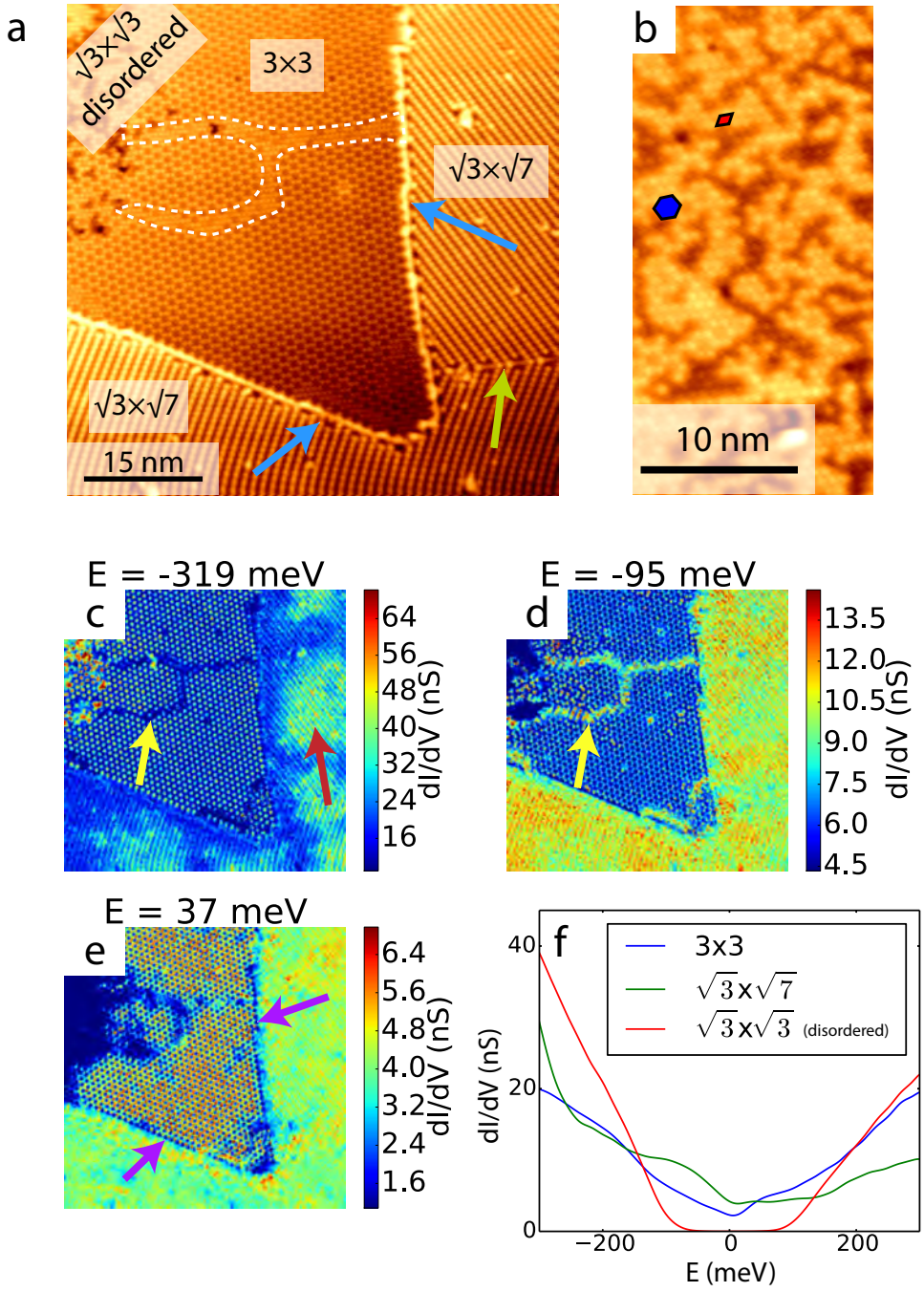

Figure 6.1: **Topography and spectroscopy of Pb/Si(111) phases mixture:** a. Topography of a 62×62 nm^2 area showing the coexistence on the same terrace of $\sqrt{7} \times \sqrt{3}$, 3×3 and disordered $\sqrt{3} \times \sqrt{3}$ phases. b. Topography of a 15× 33 nm^2 area showing the structure of the disordered $\sqrt{3} \times \sqrt{3}$ phase. The red diamond and blue hexagon indicate the primitive cells of the $\sqrt{3} \times \sqrt{3}$ and 3×3 structures respectively. c.-e. Spectroscopic data on the same area for two energies (-319 meV for c., -95 meV for d. and 37 meV for e.) showing the different electronic behaviors in the various phases. f. Typical spectra measured for the $\sqrt{7} \times \sqrt{3}$, 3×3 and disordered 3×3 case.

under 86 K [91]. In these two phases the atomic arrangement is the same in the xy plane and the difference between the two structures comes from a difference in the vertical atomic arrangement. There has been several mechanism proposed to explain this transition [140, 141, 91, 142, 143, 144] that has also been observed in similar systems such as Pb/Ge(111) and Sn/Ge(111) [145]. Recent unpublished calculations by M. Calandra and C. Tresca have shown that this effect is purely structural and also affects the first three top Si layers. They calculated a transition temperature of 90 K, very close to the experimental value of 86 K.

This continuous shift in phases is not observed between the 3×3 and $\sqrt{7} \times \sqrt{3}$ because in this case the primitive cells of both lattices deeply changes its symmetry from hexagonal to rectangular. This difference leads to the appearance of domain walls between the two structures that can be clearly seen in fig. 6.1.a (blue arrows).

Domain walls can also be seen when looking at the connection between two $\sqrt{7} \times \sqrt{3}$ domains with different orientations (green arrows). On the same figure we can clearly observe the specific pattern at the interface of two lines connecting to the interface followed by one seemingly disconnected line (green arrow). The same kind of behavior appears at the connection with the 3×3 at the bottom of the image (blue arrow). We see that depending on the orientation of the $\sqrt{7} \times \sqrt{3}$ lattice the connection of the chains is either continuous (on the vertical interface) or discontinuous (at the horizontal interface).

These boundaries have a direct impact on the electronic properties of the system. We present on figs. 6.1.c. d. and e. three conductance maps at -319 meV and -95 meV and 37 meV. These maps allow us to correlate the topography with the electronic distribution. On the conductance map 6.1.e we can clearly see the boundary state appear in blue at the interface between 3×3 and $\sqrt{7} \times \sqrt{3}$ (purple arrows).

On top of that we also clearly see some defects that are difficult to spot on the topography alone. The most striking one is the fork shaped boundary crossing the 3×3 area signaled by a dashed contour on fig. 6.1.a. This defect is visible in the topography obviously but is extremely contrasted in the conductance map 6.1.c. and d. This defect actually corresponds to a $\sqrt{3} \times \sqrt{3}$ antiphase domain boundary between two 3×3 domains and we can see how it connects to the disordered phase on the left side of the area. This antiphase domain boundary corresponds to an area where two mismatched lattices encounter. A closer look at the 3×3 lattice below and above the antiphase boundary reveals a shift of the dark areas seen in topography by one atomic lattice constant.

If we now look at the disordered $\sqrt{3} \times \sqrt{3}$ part of the scanning area (another example is shown on 6.1.b) on the left side we can observe how the topographic disorder directly influences the electronic distribution. Obviously the disorder on the topography seems to be fixed as dark spots and bright spots are well defined spatially. However this is not the case when looking at the conductance maps. At strong negative bias on fig. 6.1.c. (-320 meV) the topographic defects almost perfectly match the spectroscopy when referring to the position of said defects. By moving towards positive bias we see that the disorder does extend to the well ordered 3×3 part of the scanning area with a clear tendency to be favored inside the twinning "fork". As we will see in the following this behavior corresponds to an induced gap inside the 3×3 phase.

A direct consequence of this phase between the $\sqrt{3} \times \sqrt{7}$ and 3×3 is that a bad connection of the different patches might suppress conductivity on the whole sample. For instance while the $\sqrt{7} \times \sqrt{3}$ becomes superconducting under 1.52 K [83], in the case where a large part of the sample is in the 3×3 phase, the STS signal may not present any gap. It is not clear if this effect is caused by an inverse proximity effect of the normal parts (3×3) on the superconducting parts or if the impossibility to measure a superconducting gap originates from more subtle effects as Coulombic effects induced by the other phases. In this section we are in a case where we were not able to observe any low energy features such as superconducting gaps and we thus focused only on the large energy scale behavior of the coexistence of the different Pb/Si phases.

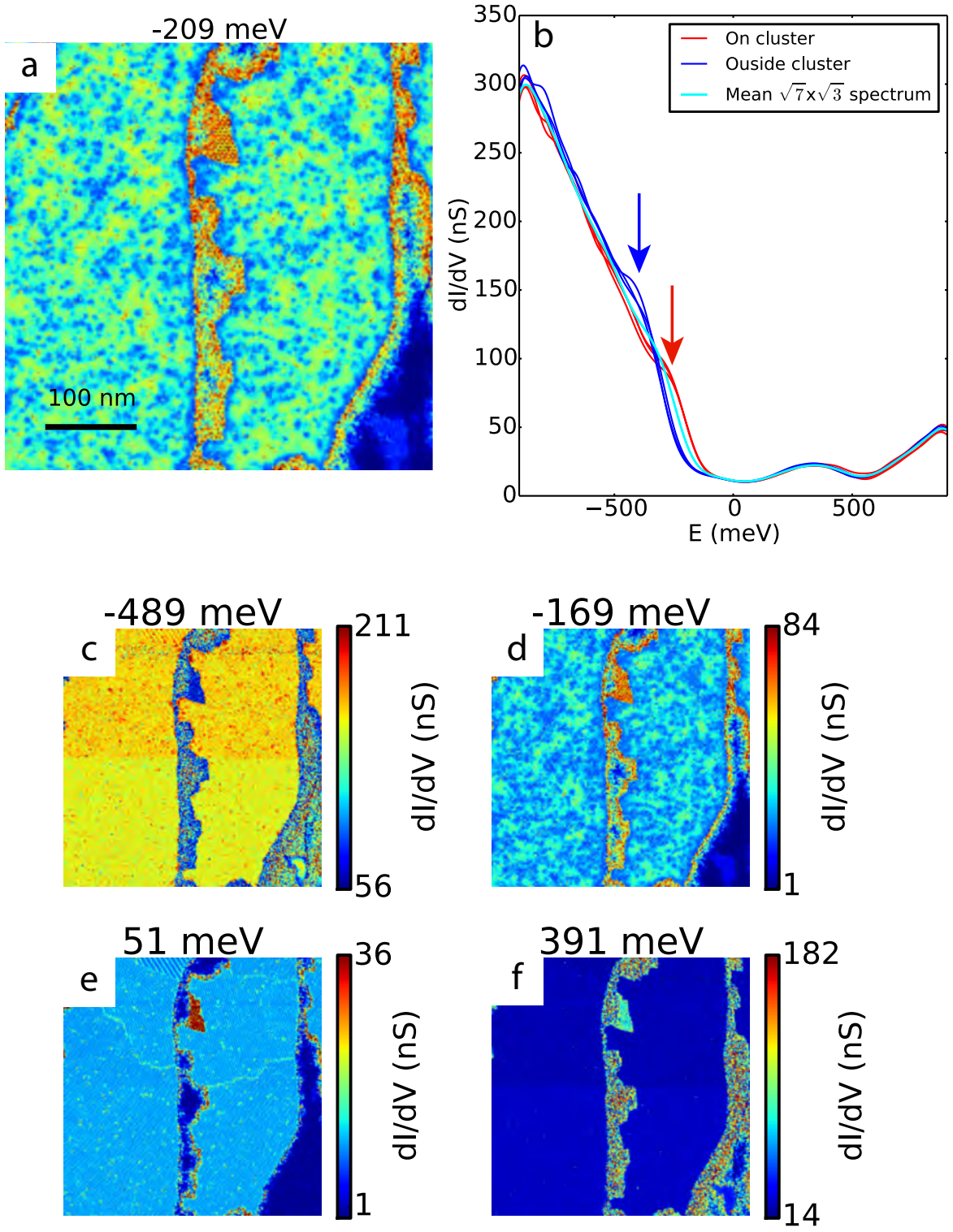

Figure 6.2: **Spectroscopy of defects in metallic Pb/Si monolayer:** a. Conductance map of a 500×500 nm^2 of the system Pb/Si(111) showing a coexistence of phases taken at an energy of -209 meV. b. Spectra taken on the $\sqrt{7} \times \sqrt{3}$ phase either on top of the P defects (red) or on a defect free region (blue) between ± 900 *meV*. The cyan curve is the mean spectrum of the $\sqrt{7} \times \sqrt{3}$ phase averaged over a disc of 40 nm radius. The red and blue arrows indicate the position of the states associated to the dopants. c.-f. Conductance maps of the same area 500×500 nm^2 taken at 4 different energies.

6.2.2 High energy spectroscopy of the Pb/Si(111) phases

A remark that we can make on the data from fig. 6.1 concerns the $\sqrt{7} \times \sqrt{3}$ domains on the right and bottom side of the scanning area. On the conductance map taken at -320 meV areas about a dozen nanometers of size appear over which we observe an increase of the conductance, one of them is indicated by a red arrow. The density of these areas and the fact that we can identify very localized defects inside leads us to link them to dopants from the Si substrate. The associated spectral signature would thus be associated to the phosphorus rather than the Si or the Pb monolayer. This kind of defects can be seen on a larger scale on fig. 6.2.a.

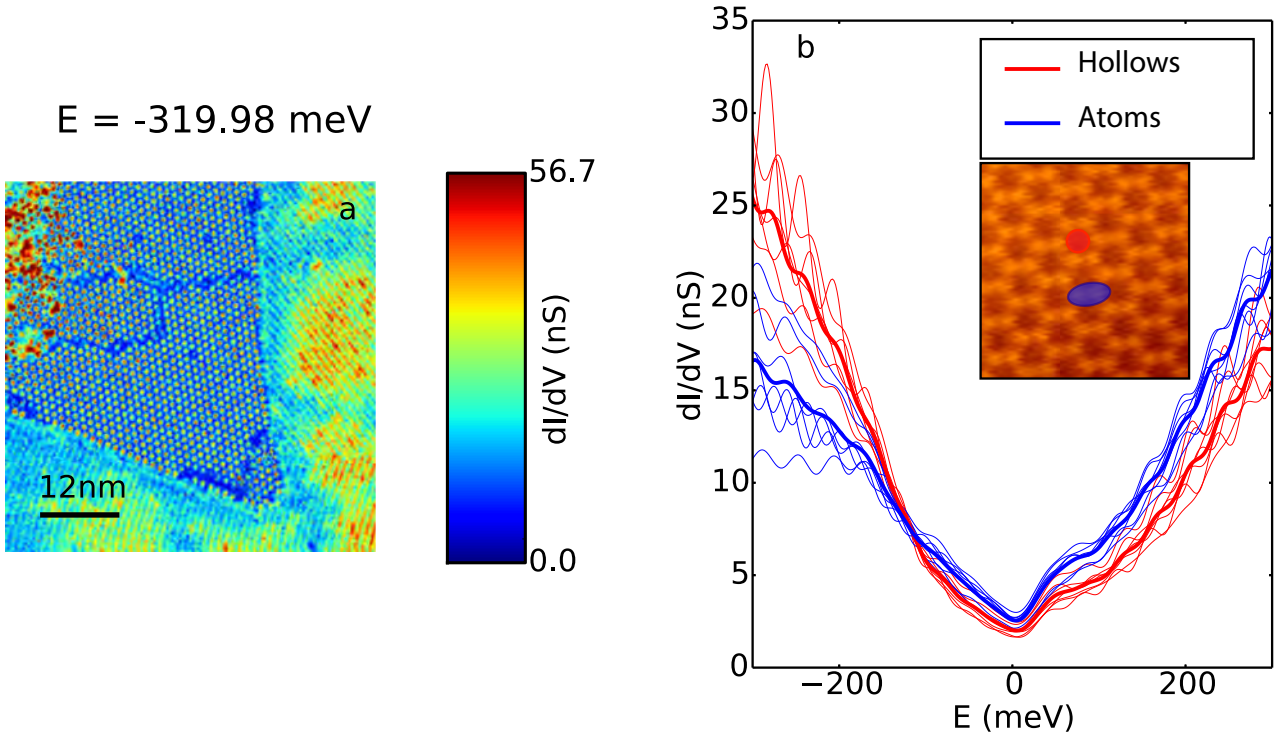

Figure 6.3: **LDOS localization on 3×3 structure:** a. Conductance map at -320 meV (identical to 6.1.c). b. Spectra taken either on the “hollows” on a. (in red) or on the "atoms" (in blue) showing the variation of the atomic distribution at the atomic scale. The two thickest curves correspond to the mean value of the regular size curves of the same color. The inset shows the sites corresponding to atoms and hollows on a topography of the 3×3 phase.

The spectra associated to the P dopants are shown on fig. 6.2.b. On this figure we took a sample of six spectra, three taken on top of the buried defects (in red) and three taken away from these defects (in blue). The main spectroscopic difference between those two sets of spectra is that while without defects a small peaks appears in the conductance around -400 meV, in the presence of defects this peak is shifted towards the Fermi level around -270 meV. As a consequence the P can be seen in the conductance maps at all energies between -478 meV and -95 meV. We do not observe any spectroscopic difference at positive biases and therefore the clusters are not seen at any positive energy (see fig. 6.2). Strangely enough the P is seen only on the $\sqrt{7} \times \sqrt{3}$ and does not seem to leave any kind of signature on the 3×3 phase.

In the 3×3 phase we observe a strong localization effect that can be seen on fig. 6.1.c., d. and e. On these figures we observe a strong localization of the electronic states. For convenience we will refer to the high conductance sites on fig. 6.1.c as *atoms* and the lower conductance sites as *hollows* as they respectively relate to the bright and dark spots seen on the topographic map 6.1.a.

The spectra associated to the *atoms* and the *hollows* are shown on fig. 6.3.b together with a conductance map identical to 6.1.b. These spectra show that even if the two configurations share the same global shape, the spectral weight of *atoms* is larger than the one of *hollows* above -117 meV. For any other bias within the investigated range the ratio is inverted.

If we enlarge the spectroscopic window and look at the 3×3 phase globally, we observe that around ± 300 meV the spectra exhibit two peaks (see blue curve on fig. 6.4.c). These two peaks are also present in the disordered $\sqrt{3} \times \sqrt{3}$ phase but are shifted around ± 400 meV and surround a 300 meV gap symmetrical around the Fermi level (yellow curve). Such a gap opening in the presence of disorder hints toward an Anderson localization effect [146] in the $\sqrt{3} \times \sqrt{3}$ phase. On the other hand, the sharp localization of the electronic states of the 3×3 phases as well as the energy symmetrical peaks (potentially Hubbard bands according to DFT + U calculations) are strong indicator that this phase is actually close to be a Mott insulator [147] or that it at least exhibits strong electronic correlations. The Mott picture is consistent with what was observed for the analogous system Sn/Si(111) in the $(\sqrt{3} \times \sqrt{3})$ phase [148] which is closely related to Pb/Si.

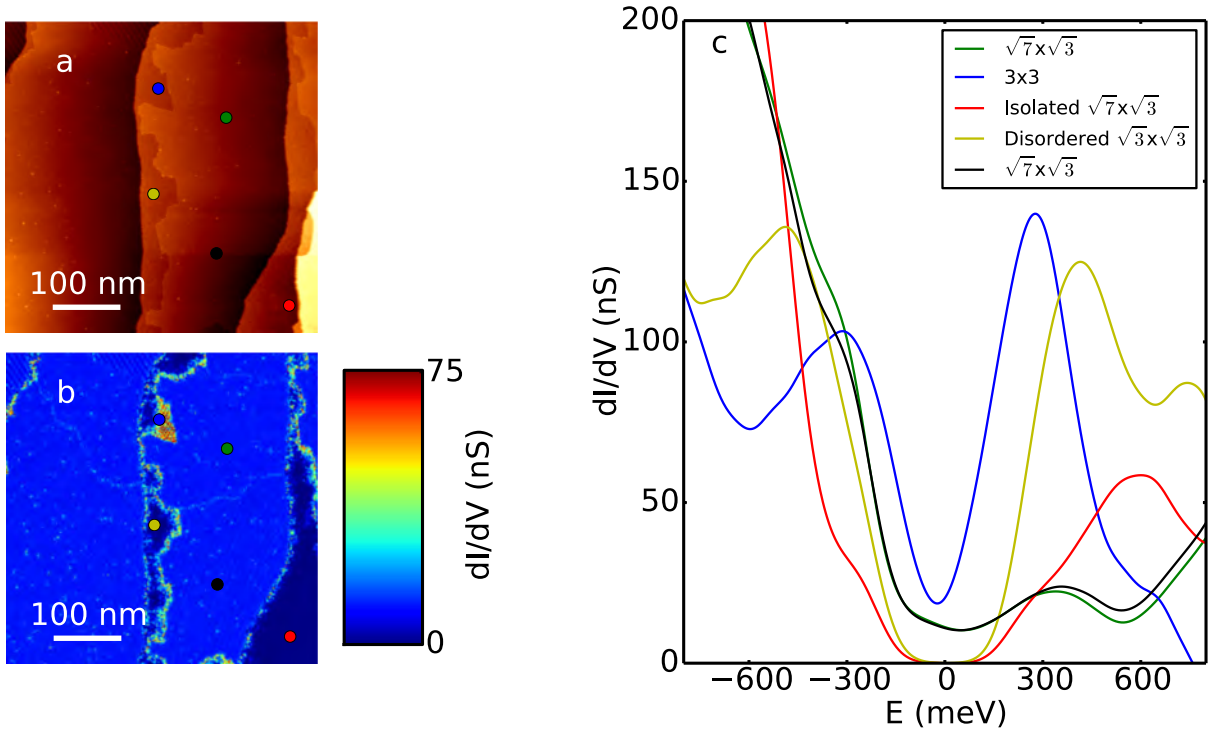

Figure 6.4: **Effect of the interaction between different phases:** a. Topography of an area 500×500 nm^2 showing the usual appearance of a sample with coexistence of phases 3×3, $\sqrt{7} \times \sqrt{3}$ and disordered $\sqrt{3} \times \sqrt{3}$. b. Conductance map of the same area at the energy of 71 meV. c. Spectra selected over the different phases seen on a. and b. The spectra are measured at the positions indicated on figures a. and .b by the points of the same color.

6.2.3 Modified behavior of the $\sqrt{7} \times \sqrt{3}$ by proximity with disordered $\sqrt{3} \times \sqrt{3}$ regions

An interesting feature observable on fig. 6.4 is the inclusion of a small patch of $\sqrt{7} \times \sqrt{3}$ surrounded by disordered $\sqrt{3} \times \sqrt{3}$. This part of the scanning area is located at the position of the red dot on figs. 6.4.a. and b. The corresponding characteristic spectra is shown in red on fig. 6.4 c. This inclusion of the $\sqrt{7} \times \sqrt{3}$ patch strongly modifies its characteristic density of states compared to the usual $\sqrt{7} \times \sqrt{3}$

case (green curve) as we observe that a full gap (red curve), of the same size as the one of the disordered $\sqrt{3} \times \sqrt{3}$ phase, is induced.

Around -300 meV, at the energy where we were previously able to image the underlying dopants, we observe a strong diminution of the density of states that is counterbalanced by the appearance of a large "bump" at 600 meV. This bump hides a small features around 320 meV that corresponds to the states observed in the green and black spectra of the homogeneous $\sqrt{7} \times \sqrt{3}$ phase and that are an intrinsic feature of this phase.

On fig. 6.5 we observe a similar situation where we have a triangular island of $\sqrt{7} \times \sqrt{3}$ surrounded by both ordered 3×3 and disordered $\sqrt{3} \times \sqrt{3}$. In this configuration, the LDOS measured inside the island more closely resembles the usual $\sqrt{7} \times \sqrt{3}$ density of states. However, we do observe a diminution of the LDOS around the Fermi level that in this case is closer to the behavior of the 3×3 phase. Unlike the case of a fully insulating disordered $\sqrt{3} \times \sqrt{3}$ surrounding neighborhood we do not measure any dramatic variation around -300 meV.

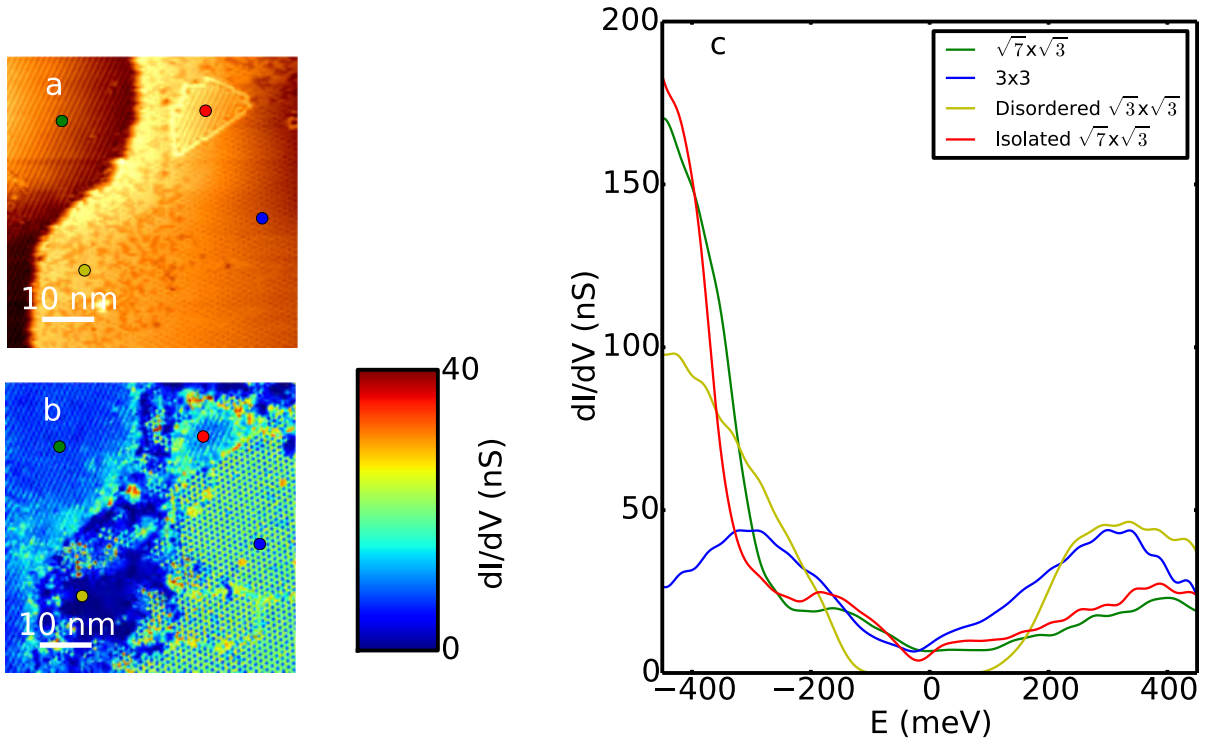

Figure 6.5: **Effect of the interaction between different phases:** a. Topography of an area 80×80 nm^2 showing the coexistence of the phases $\sqrt{7} \times \sqrt{3}$, 3×3 and disordered $\sqrt{3} \times \sqrt{3}$. b. Conductance map of the same area selected at the energy of 94 meV. c. Spectra selected over the different phases seen on b. and c. The spectra are taken from the positions indicated on figures a. and .b by the points of the same color.

We have seen in this section that the 3×3 phase possesses a well reconstructed structure and is quasi-Mott insulator as our spectroscopic measurements and DFT calculations show. On the other hand, the $\sqrt{3} \times \sqrt{3}$ behaves as a fully gapped Anderson insulator. Complementary measurements and DFT+U calculations are being performed in order to model our experimental results. In the following section we will discuss the precise way these two structure 3×3 and disordered$\sqrt{3} \times \sqrt{3}$ coexist and study the spatial evolution of the localization gap.

6.2.4 Proximity between disordered $\sqrt{3} \times \sqrt{3}$ and 3×3 ordered regions

Because the two phases ordered 3×3 and disordered $\sqrt{3} \times \sqrt{3}$ derive from one another, this kind of system in which we observe the coexistence of both phases might be an interesting playground for studying the interplay between Mott and Anderson localization. We present on fig. 6.6 the measurements performed over a 50×46 nm^2 area in which we go continuously from a disordered $\sqrt{3} \times \sqrt{3}$ region to a well ordered 3×3 phase. On fig. 6.6.e we show the individual spectra measured continuously from the $\sqrt{3} \times \sqrt{3}$ part of the system (blue spectra) to the 3×3 crystalline part (red spectra). On this figure we can follow the localization gap (≃200 meV) that we already discussed above as it induced a smaller gap (≃ 100 meV) in the 3×3. This small gap of the 3×3 is not present in cases where the $\sqrt{3} \times \sqrt{3}$ is not in close contact.

Because the 3×3 is not insulating on its own, the continuity with the fully gapped $\sqrt{3} \times \sqrt{3}$ can be seen as a crossover from low to high disorder for Anderson localization [149, 146, 150] in a Mott system.

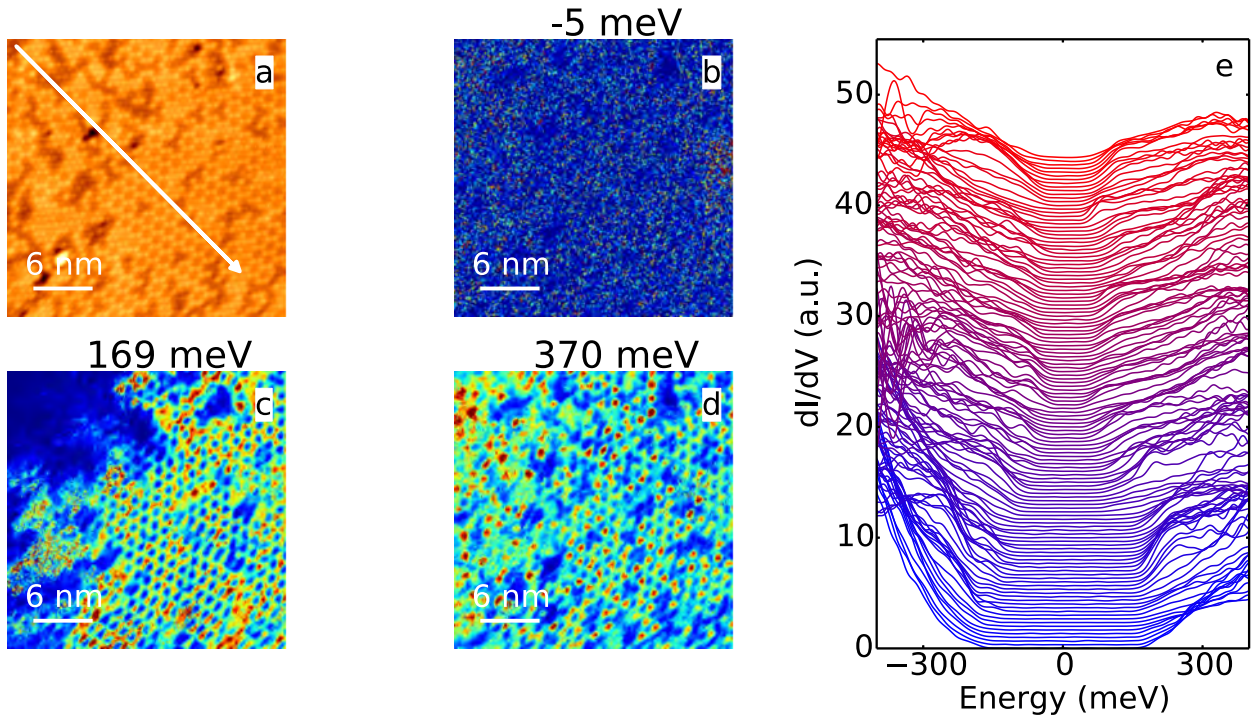

Figure 6.6: **Proximity effect between a metal and an insulator:** a. Topography of a 50×46 nm^2 area showing the coexistence of the 3×3 phase (on the right) and the disordered $\sqrt{3} \times \sqrt{3}$ phase (on the left). b.-d. Conductance maps taken at -5 meV, 169 meV and 370 meV of the same area. e. Cut along the line indicated on a. showing the spatial evolution of the insulating gap transmitted by proximity into the 3×3 area.

The coexistence of the two phases can also be seen on fig. 6.5 which corresponds to the same sample as the one presented on fig. 6.1, where we can recognize the characteristic fork in the bottom of the topography and spectroscopy that can be seen in both images. As we showed on fig. 6.4, we observe the ±300 meV bands of the 3×3 structure as well as the gapped $\sqrt{3} \times \sqrt{3}$ phase surrounded by its own two sidebands at larger energies.

6.3 Superconducting proximity effect between $\sqrt{7}\times\sqrt{3}$ and 3×3

The superconducting proximity effect describes how the properties of a superconductor can be induced to either another superconductor with different characteristic parameters, a normal metal or an insulator. If a normal metal (that we will call N) is in good electrical contact with a superconductor (that we will call S), the Cooper pairs from the superconductor can "leak" to the normal metal and as a consequence modify the electronic properties of the normal metal. This effect has been widely studied during the 1960's [151, 152] and was recently revitalized by the possibilities to study this effect at much smaller length and energy scales [153]. This physical effect originates from the fact that only Cooper pairs can penetrate a superconductor below the gap energy $|E|<\Delta$. It is however possible for an incoming electron from the normal part to create an electron-hole pair with opposite spins, where the hole is reflected and a second electron is transmitted and forms with the original incoming electron a Cooper pair. This process thus conserves the spin and charge of the system.

Another way to see this process is to have a Cooper pair that passes from the superconducting part to the normal part and progressively looses its coherence due to the absence of a "glue" for the electrons. This pair becomes a pair of time-reversed electron states that propagate coherently over a distance L_C that is given in diffusive metals by $L_C=\min\{\sqrt{\hbar D/E},L_\phi\}$ with D the diffusion constant of the system, E the electron state energy and L_ϕ the phase-coherence length in N. This diffusive case is the one we are working in as we have $\xi\simeq50$ nm for the superconducting coherence length and $\ell_e\simeq4$ nm for the elastic mean free path in the monolayer systems.

Such Cooper pair leakage modifies the local density of states of the normal metal over a distance L_C from the $S-N$ interface. This modification has been spatially resolved in recent years by means of tunneling probes [154, 155] as well as STM/STS techniques applied to mesoscopic systems [156, 157, 158, 159, 160]. Very recently, the considerable progress in the controlled growth of atomically clean materials under ultrahigh vacuum conditions has made it possible to probe the proximity effect with high spatial and energy resolution in *in situ* STM/STS experiments [161, 162].

We will describe here the coexistence between small non-superconducting quasi-Hubbard 3×3 patches and the superconducting $\sqrt{7}\times\sqrt{3}$ phase.

We discussed in the previous sections how the 3×3 phase presented a quasi-Hubbard behavior and the disordered $\sqrt{3}\times\sqrt{3}$ an Anderson localization effect. In such a configuration of the sample we were not able to probe the superconducting gap of the adjacent $\sqrt{7}\times\sqrt{3}$ phase due to a transport gap induced by the disordered $\sqrt{3}\times\sqrt{3}$ phase in the whole sample. It thus became necessary to slightly change our recipe in order to decrease the disorder and get rid of the transport gap by being closer to the clean $\sqrt{7}\times\sqrt{3}$ coverage.

The sample was prepared by depositing 1.7 ML of Pb at ambient temperature before being annealed at 375°C for 3 minutes (plus two minutes during which we slowly increased the temperature from 0°C to 375°C. Compared to the recipe used to obtain a full superconducting system in a dense phase like SIC or HIC), the Pb covering from which we start is very low, thus the annealing will lead to a large depletion of Pb at the step edges of the substrate and the appearance of many 3×3 flakes along them. More rarely we also observe these flakes appearing in the middle of the terraces. The typical size of the flakes can vary between 10 nm and more than 100 nm[1]. Despite the appearance of these 3×3 flakes, the system is globally superconducting and in the $\sqrt{7}\times\sqrt{3}$ phase with domains of a typical size of about 500 nm.

On fig. 6.7.a we show the topography of a 102×89 nm^2 area in such configuration. We see on this figure a triangular patch of 3×3 surrounded by $\sqrt{7}\times\sqrt{3}$ domains (lower left of the image) and a step edge (top right of the image). Even if the 3×3 part is well reconstructed, it still contains local defects like missing or adatoms clearly visible on the topography. In this configuration, the $\sqrt{7}\times\sqrt{3}$ reconstruction is superconducting and the 3×3 is a strongly correlated metal and presents two side bands centered around ±300 meV (see fig. 6.4.c) due to the proximity to a Mott transition.

[1]The 3×3 flakes tend to be elongated along the steps edges and in this direction we have observed continuous domains of more than 500 nm while in the perpendicular direction the typical extension of these flakes is about 50 nm

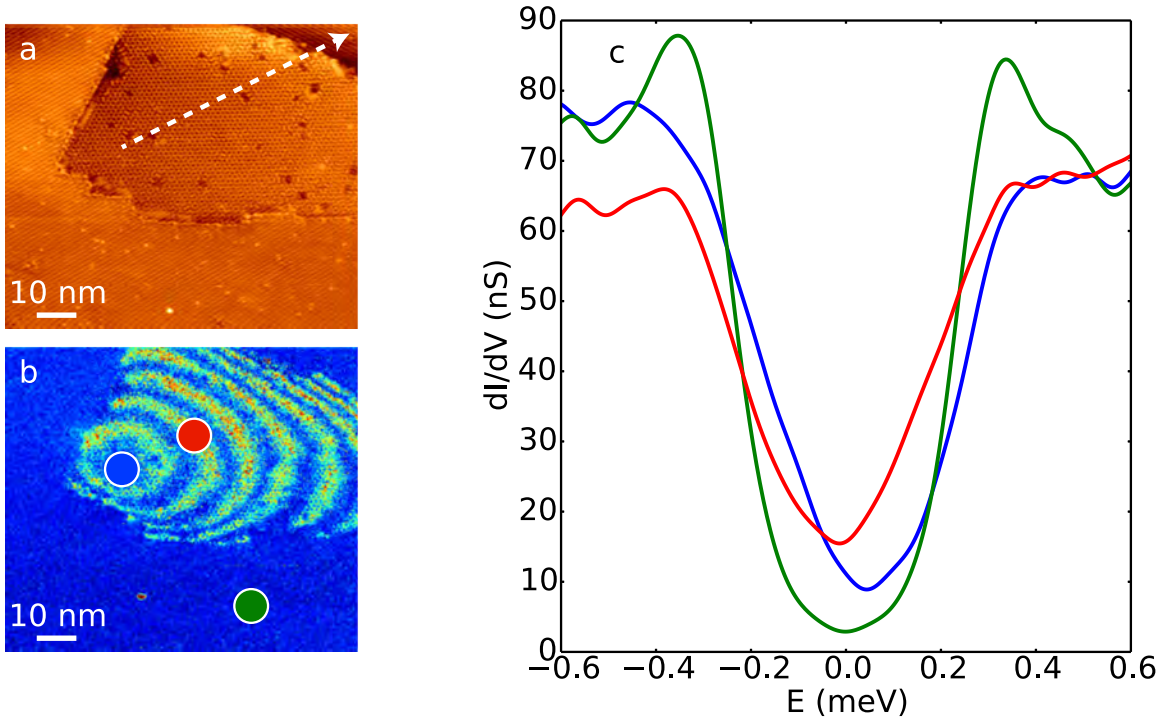

Figure 6.7: **Proximity effect between $\sqrt{7} \times \sqrt{3}$ and 3×3 phases:** a. Topography of an area 102×89 nm^2 showing the coexistence between a $\sqrt{7} \times \sqrt{3}$ domain and a 3×3 domain. b. Conductance map of the corresponding area at 0.1 meV. c. Selected spectra over the $\sqrt{7} \times \sqrt{3}$ phase (green), at the center of the ring in the 3×3 phase (blue) and at a point of maximum intensity of the ring (red). The color dots on the conductance map refer to the color of the spectra on c.

By performing STS on this system, we observe the appearance of an induced gap in the 3×3 flake of the same size as the superconducting gap (see fig. 6.7.c). Inside this gap, two spatially fluctuating peaks are measured as presented on the conductance map acquired at 0.1 meV on fig. 6.7.b. These in-gap states appear in the form of rings centered around the bottom left corner of the 3×3 flake, with a pseudo periodicity depending on the direction and the distance from the flake edges.

On the conductance map at the Fermi level we observe that these states are also present in the $\sqrt{7} \times \sqrt{3}$ phase very close from the interface with the 3×3 flake.

Due to the size of the superconducting gap and therefore the size of the induced gap, the in-gap states we observe are very close from each other. Because of the thermal broadening of the spectra they seem at first to overlap in one single band. On fig. 6.8 we show a line cut through the oscillating pattern starting from the center of the oscillations (left) and going on the other atomic terrace (right). On this figure we subtracted the bare superconducting $\sqrt{7} \times \sqrt{3}$ mean spectrum in order to have a better contrast on the in-gap states. Doing so seems to show that there are two separated in-gap states that overlap due to thermal broadening. However we cannot exclude that these states correspond to a continuum of in-gap states. Another example of this kind of proximity is presented on fig 6.9.

We tried many different approaches to interpret these in-gap states but unfortunately none of them were able to reproduce the observed pattern. We will describe below these different approaches and the results obtained.

The first model we tried to implement in order to reproduce the spectroscopic features was to consider Andreev states in ballistic regime (in a quantum billiard configuration) induced by the inclusion of a normal metal between superconducting electrodes. Andreev states have been widely studied in the context

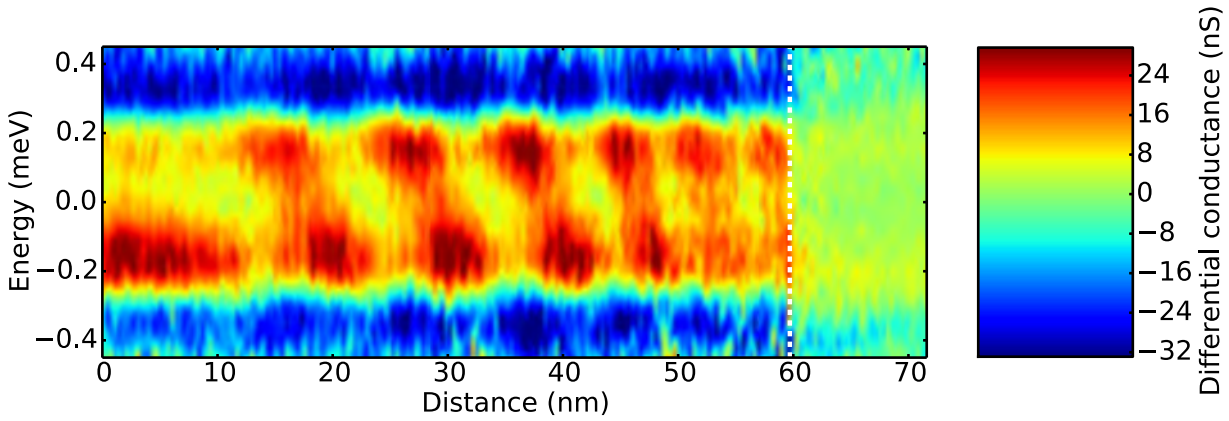

Figure 6.8: **Cut through the oscillation pattern of Fig. 6.7:** Spectral line cut over a distance of 70 nm through the 3×3 proximity area subtracted from the mean spectrum of the $\sqrt{7} \times \sqrt{3}$ phase. The direction of the cut is indicated by a white dashed arrow on the topography 6.7.a. The dashed white line represents the position of the step seen in topography in the top right corner.

of nanowires for SN [163] or SNS junctions [164, 165] or atomic contacts [166, 167]. The principle of these Andreev states stems from the fact that electrons at energies below the superconducting gap, incoming from a normal electrode cannot penetrate a superconductor without reflecting a hole inside the normal electrode in order to create a Cooper pair that is allowed to enter the superconductor at energies below the energy of the superconducting gap. Then, when multiple reflections occur from both superconducting electrodes in an SNS system, a gap appears inside the normal part accompanied with in-gap states whose energy will depend on the size of the N part and the phase difference between the two superconducting electrodes.

In the context of our enclosed 3×3 patch, we expect a superconducting gap to be induced by the $\sqrt{7} \times \sqrt{3}$ and to observe these in-gap Andreev bound states. These states can easily be obtained in 1D by using a Bogoliubov de Gennes tight binding calculation. We tried to perform the same calculation in 2D by considering diverse simple geometrical shapes for the normal zone (square, circle, triangle) in order to understand how the form of the flake would modify the shape of the Andreev eigen-modes. Unsurprisingly these type of calculations did not reproduce the circular shape of the experimentally observed in-gap states. Instead we found the eigen-modes of the shape of the normal area (see figs. 6.10.a). Another issue of this type of calculation is that it relies on the diagonalization of the full band and thus necessitates very large arrays in order to obtain the sufficient energetic resolution. Indeed generally the superconducting gap is much smaller than the band energy. For instance for a gap of the order of 1/100 of the band size, if we want about a hundred points in the gap we would need a total of 10.000 points for the full band and thus the same number of atoms. In a 4×4 formalism we would have to diagonalize matrices of size 40.000×40.000. This kind of calculation thus rapidly becomes unmanageable as the size of the matrix we wish to diagonalize increases.

The second approach we followed was based on an optical analogy. We imagined that inside a triangular area a particle would reflect on the edges multiple times. Because in our system the three sides of the flake are not equivalent[2], we can consider that the reflectivity of the three sides of the triangle could have different physical properties. For instance the electronic connection at the edges is far less efficient than it is on the terrace and particles arriving at the top side of the flake would be more reflected than the ones arriving at the sides. By summing the contribution for different initial angles and positions over the

[2]As two are directly connected to the $\sqrt{7} \times \sqrt{3}$ and one consists of the step edge.

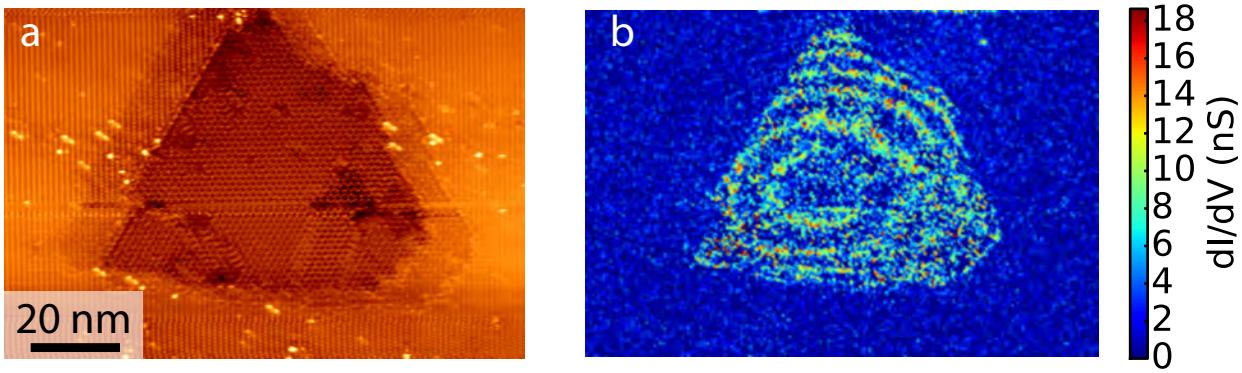

Figure 6.9: **Another example of proximity effect between $\sqrt{7}\times\sqrt{3}$ and 3×3 phases:** a. Topography of a 116×73 nm^2 area showing the inclusion of a triangular patch of 3×3 in the middle of an homogeneous $\sqrt{7}\times\sqrt{3}$ domain. b. Spectroscopy of the same area showing the characteristic rings.

whole system we should be able to reproduce the interference pattern produced by the multiple reflections on the edges. Like in the previous case (see for instance fig. 6.10.b), we did not obtain satisfying results and the eigenmodes of the triangles were the one we observed in the end.

Finally the last model we tried to apply to this system is a resistance model. By considering the STM tip as one electrode and the $\sqrt{7}\times\sqrt{3}$ as another one we tried to calculate what would be the resistance seen by an electron injected inside the 3×3 flake. The idea behind this model is that the observed spectroscopic signature might come not from real electronic states inherent to our system but rather to an electric field induced by our STM tip. When injecting an electron at a point M of the 3×3 flake it would try to return to the electrodes by finding the closest path to the $\sqrt{7}\times\sqrt{3}$ reservoir. By calculating the equivalent resistance at each point of a triangle we did observe a smooth evolution from the center of the triangle to the edges with a rapid divergence at the edges as expected. However in this case we did not reproduce the oscillating pattern we observe. A step we did not have the time to execute would consist into solving the Schrödinger equation for an electric potential following the equivalent resistance map calculated by this model. One could expect to observe eigenmodes that might eventually give both the oscillating pattern and the circular shape we observe experimentally.

The conclusion we draw from these theoretical failures is that the correlations in this system should probably be incorporated in the model and not neglected. The main issue with this conclusion is that the easy to use Bogoliubov de Gennes formalism cannot be applied anymore as Hubbard term in the Hamiltonian makes use of 4 different operators and therefore the spinors and the matrix form of the Hamiltonian cannot be used.

6.4 Conclusion

In this chapter we discussed the versatility of the Pb/Si(111) monolayer in the way the different phases could be combined in order to study interesting proximity effects based on their own spectral characteristics. We first presented these spectral characteristics and showed that the 3×3 and $\sqrt{3}\times3$ phases present strong electronic correlation effects (Mottness) and that the disorder of the $\sqrt{3}\times\sqrt{3}$ opens an Anderson localization gap. We showed how contacting these two phases modifies continuously the localization gap by proximity.

Finally we discussed the case of the superconducting proximity between a superconductor and a correlated metal where we have observed an induced superconducting gap as well as in-gap Andreev bound states appearing spatially in the form of rings. The calculation we did were not able to reproduce

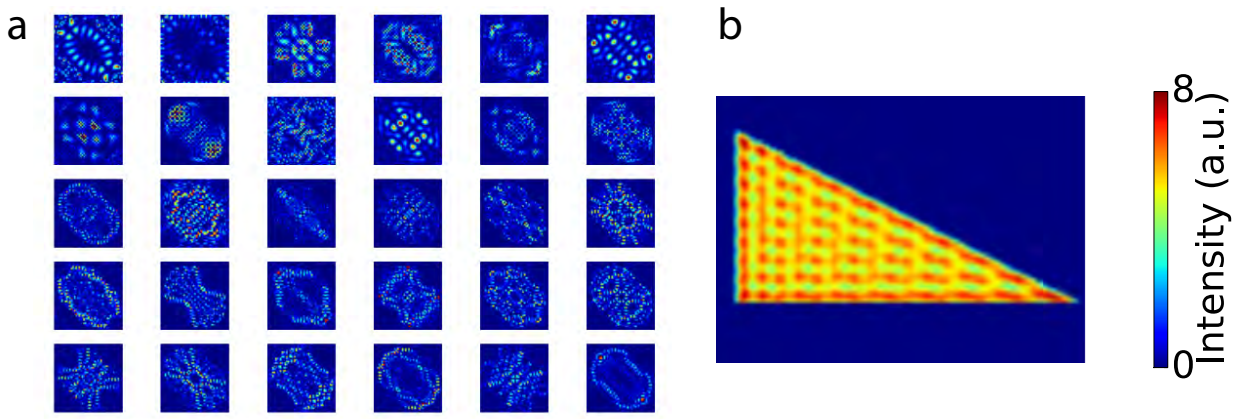

Figure 6.10: **Attempts to reproduce the effect of the proximity effect between a superconductor and a quasi-Hubbard system:** a. Bogoliubov-de Gennes calculation for a billiard shaped normal area surrounded by a superconducting area showing some of the eigenmodes of the system. b. Reflexions model in a triangular domain.

the experimental data and more theoretical work will be needed in the future in order to understand the geometry of these states probably caused by the Coulombic interaction in the 3×3 phase.

Chapter 7

Superconducting proximity effect

7.1 Introduction

The proximity effect is obviously not exclusive to $S-N$ systems. For instance if a superconductor S_1 described by its critical temperature T_{c1} and its energy gap Δ_1 is brought into contact with another superconductor S_2 with its own critical temperature $T_{c2} < T_{c1}$ and energy gap $\Delta_2 < \Delta_1$, the LDOS of both superconductors near the interface will feel the effect of the other side and be modified accordingly. At low enough temperatures ($T < T_{c2}$) the modification of the LDOS will be significant within the energy interval $|E| \in [\Delta_1, \Delta_2]$ and may be observable over a distance L_{C_i} from the interface. In the intermediate case where $T_{c2} < T < T_{c1}$ one expects the proximity effect to induce a finite local order parameter in a formally non-superconducting S_2 by means of a nonzero attractive pairing interaction λ_2 existing in S_2. Such mechanism should result in a proximity-induced interface superconductivity. A subtlety emerges as we should make clear that order parameter and superconducting correlations are two different things. On one side the order parameter $\Delta(\boldsymbol{r})$ emerges from the pairing interaction $V(\boldsymbol{r})$ that is strictly equal to 0 in a normal metal. On the other side the superconducting correlations $F(\boldsymbol{r})$ are related to $\langle\hat{\psi}_\uparrow(\boldsymbol{r})\hat{\psi}_\downarrow(\boldsymbol{r})\rangle$. Both quantities are related by $\Delta(\boldsymbol{r}) = V(\boldsymbol{r})F(\boldsymbol{r})$. Therefore for a normal metal with $V = 0$ we would obtain $\Delta = 0$ but in no case forces F to get suppressed. The superconducting correlations stay finite close to the interface between a superconductor and a normal metal due to the propagation of Cooper pairs in the normal area.

To our best knowledge, except from the theoretical and qualitative discussion from the 1960's [151, 152], no experiment has ever been reported in which this effect has been spatially resolved before our work.

7.2 System

We study the case of two superconductors S_1 and S_2 in close contact, a study that was published in [168]. The two superconductors are respectively the SIC monolayer that covers most of our sample and a 7 ML high Pb nano-island. This sample was obtained following the same basic recipe as previously discussed; only vary the initial quantity of Pb deposited on the surface and the time and temperature of the annealing. In this case, after preparing the Si by heating it at 1200°C in order to obtain the 7×7 reconstruction, we deposited 1.65 ML of Pb at room temperature before annealing the sample at 230°C [169]. This procedure leads to a $\sqrt{7} \times \sqrt{3}$ that can be continuously transformed into a denser SIC phase by adding 0.2 ML at room temperature onto the sample. As a result of a Stransky Krastanow growth [170] once the SIC monolayer is completed, the system grows islands from the excess of Pb. The Pb islands are mostly nanometer sized 1 ML high and a few are 5 to 7 ML high with size typically larger than 100 nm with a distribution of one every μm^2. The 3D topography of the system is presented in false colors spectroscopy on fig. 7.1.a. The superconducting characteristics of these islands are slightly under the bulk

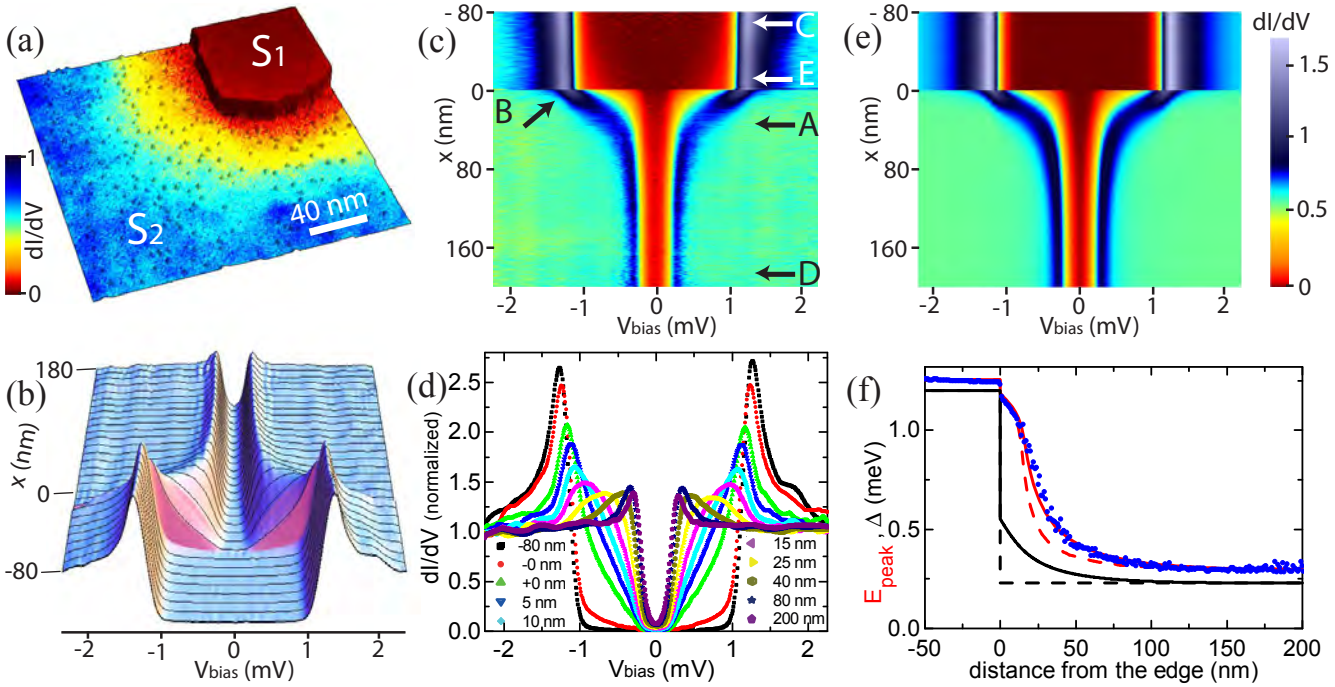

Figure 7.1: **Proximity effect between two superconductors at 0.3 K:** (a) Topographic STM image of the sample showing the Pb nano-island S_1 connected to the striped incommensurate Pb monolayer S_2. The superposed color-coded spectroscopy map at $E = -0.3\ meV$ allows to visualize the proximity effect. 256×256 spectra were measured in the STS map. (b) Spatial and energy evolution of the experimental tunneling conductance spectra $dI/dV(V,x)$ across the junction (3D view). One spectrum is plotted every 1 nm and highlighted by a black line every 10 nm. (c) Color-coded experimental $dI/dV(V,x)$ spectra across the interface. One spectrum is plotted every nanometer. (d) Selected local tunneling spectra (dots). The last spectrum measured on the top flat part of the island before the edge is denoted by -0 nm. The first spectrum measured on the SIC monolayer is denoted by +0 nm. The distance between the +0 nm and -0 nm spectra is about 1 nm. (e) Color-coded computed $dI/dV(V,x)$ across the interface. (f) Spatial evolution of the energy of the peak maximum $E_{\rm peak}(x)$ across the interface. The experimental results (symbols) are nicely reproduced by self-consistent calculation of the order parameter (red solid line), while the red dashed line corresponds to the non-self-consistent results. The evolution of the order parameter is shown by black lines: self-consistent (solid) and non-self-consistent (dashed).

Pb but much larger than the monolayer SIC phase as we have $T_{C1} \simeq 6.2$ K and $\Delta_1 \simeq 1.2$ meV. On the other hand, the monolayer characteristic superconducting parameters are $T_{C2} \simeq 1.8$ K and $\Delta_2 \simeq 0.3$ meV [83, 171].

7.3 Results at 300 mK

The results obtained at 300 mK (for $T < T_{c2} < T_{c1}$)on this system are summarized on fig. 7.1 (a) to (f). At this temperature the two electrodes S_1 and S_2 are superconducting and the "stronger" superconductor S_1 will inject Cooper pairs into the "weaker" S_2. On fig. 7.1.a the superimposed color code is the conductance map obtained at -0.3 meV. This bias value corresponds to the small gap S_2. On this figure the non perturbed S_2 appears in blue (outside the small gap) while S_1 appears in red (inside the gap). The yellow color allows to visualize in real space the proximity effect. Another way to visualize this effect is by averaging the different spectra at a given distance from the interface as shown on fig. 7.1.(b), (c)

and (d). A striking feature observed on this data is the sharp discontinuity at the interface (occurring over less than 1 nm) that is followed by a smooth spatial evolution in both S_1 and S_2 toward their bulk form. In S_2 the evolution from the interface spectrum (B) to the reservoir spectrum (D, far from the interface) is soft and can be followed over more than 100 nm.

Because S_1 acts as the "stronger" superconductor, the inverse proximity effect where a superconductor with a smaller gap tends to diminish the superconducting correlation in the larger gap system, is extremely small. This inverse proximity effect is better seen on fig. 7.2.c. at -1.06 meV. For the inverse proximity effect in S_1 this evolution can be seen over approximately 60 nm.

Before describing how the proximity effect is modified at 2 K where S_2 is in its normal states we will discuss the theoretical framework of the Usadel equations to better understand our observations. Most theoretical studies of the proximity effect between two superconducting systems have focused on the analysis of the critical temperature using either the Ginzburg-Landau theory or the linearized Gorkov equations [152] which are only valid close to the critical temperature of the whole system. Here we want to be able to describe the local spectra at arbitrary temperatures and we will use the Usadel approach [172]. This approach summarizes the quasiclassical theory of superconductivity in the diffusive limit, where the mean free path is smaller that the superconducting coherence length $\xi = \sqrt{\hbar D/\Delta}$. The quasiclassical theory describes all the equilibrium properties in terms of a momentum-averaged retarded Green's function $\hat{G}(\boldsymbol{R}, E)$ which depends on position $\boldsymbol{R}$ and energy E (see appendix .1 for a discussion of the Green's function formalism). This Green's function is a 2×2 matrix in the electron-hole (Nambu) from whose components we will be able to extract the values of the LDOS and the superconducting order parameter.

$$\hat{G} = \begin{pmatrix} g & f \\ \tilde{f} & \tilde{g} \end{pmatrix}. \tag{7.1}$$

In the case where the inelastic and phase-breaking interactions are neglected, the propagator $\hat{G}(\boldsymbol{R}, E)$ satisfies the following equation [172]

$$\frac{\hbar D}{\pi} \nabla(\hat{G} \nabla \hat{G}) + [E\tau_z + \hat{\Delta}, \hat{G}] = 0, \tag{7.2}$$

where τ_z is the Pauli matrix in electron-hole space and

$$\hat{\Delta} = \begin{pmatrix} 0 & \Delta(\boldsymbol{R}) \\ \Delta^*(\boldsymbol{R}) & 0 \end{pmatrix}, \tag{7.3}$$

where $\Delta(\boldsymbol{R})$ is the space dependent order parameter that needs to be determined self-consistently *via* the following equation (equivalent to eq.1.28)

$$\Delta(\boldsymbol{R}) = V \int_{-\varepsilon_c}^{\varepsilon_c} \frac{dE}{2\pi} \Im\{f(\boldsymbol{R}, E)\} \tanh\left(\frac{\beta E}{2}\right). \tag{7.4}$$

In this equation $\beta = 1/k_B T$, V is the superconducting coupling constant and ε_c is the cutoff energy. These two parameters can be eliminated in favor of the critical temperature of the system (in absence of proximity effect) in the usual manner. In our case, as the two reservoirs S_1 and S_2 will not present any phase difference, the order parameter Δ can be chosen to be real, as it was implicitly done in 7.4.

To solve the Usadel equations we will model our system as two superconducting reservoirs R_1 and R_2 connected by a proximity zone in 1D. Due to the thickness difference between S_1 and S_2, we will consider that S_1 is a perfect reservoir R_1 in which the order parameter Δ_1 remains constant and unmodified at the interface. The inverse proximity effect will thus not be taken into account. S_2 on the other side will be approximated as a semi-infinite wire with a constant pairing interaction $\lambda(\boldsymbol{R}) = \lambda_2$ with a critical temperature T_{C2}.

The 1D Usadel equations were solved by J. C. Cuevas following [173] using the Ricatti parametrization [174] by describing the junction interface using Nazarov's boundary conditions, valid for arbitrary

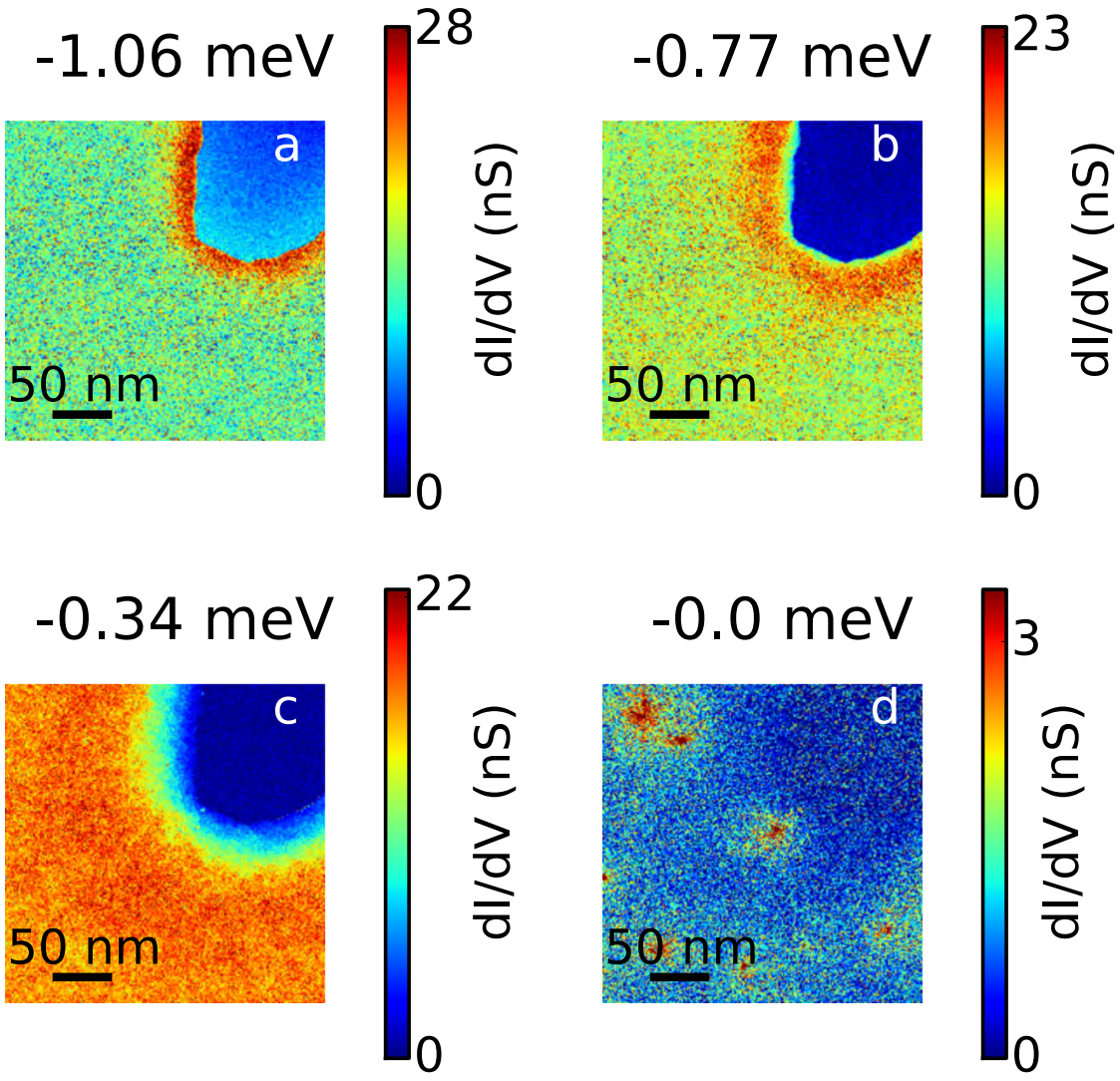

Figure 7.2: **Conductance maps of a 311×311 nm^2 area at 300 mK:** a.-d. Conductance maps taken at the energies of -1.06 meV, -0.77 meV, -0.34 meV and 0 meV respectively.

transparency [175]. In order to well describe the boundary conditions, a key parameter is the effective transparency coefficient r that can be roughly defined as the ratio between the resistances of the $S_1 - S_2$ barrier and of the monolayer[1]. Within this model, the LDOS $\rho(x, E)$ can be computed as a function of the distance from the interface x as $\rho(x, E) = -\Im\{g(x, E)\}/\pi$, while the normalized tunneling spectrum is obtained by making use of eq. 1.37.

In order to obtain the parameters of this model we first fixed the bulk gaps in S_1 and S_2 by performing a BCS fit of their local tunneling spectra obtained far from the interface. The best fits we obtained were for $\Delta_1 = 1.20$ meV and $\Delta_2 = 0.23$ meV for an effective electron temperature of 0.55 K (slightly higher than the base temperature of our STM). Then, we determined the value of the reflectivity coefficient r by adjusting the discontinuity in the spectra observed at the interface leading to a value $r = 0.02$ corresponding to a highly transparent yet non perfect interface. Finally, the value of the diffusion constant D_2 is fixed in order to reproduce the spatial dependence of the energy of the spectral maximum E_{peak} ($x > 0$) (see fig. 7.1. f). We obtained a value of $D_2 \simeq 7.3$ cm^2.s^{-1}, which corresponds to a coherence length $\xi_2 \simeq 45.7$ nm, in good agreement with the ξ_2 value extracted from the analysis of the vortex core profile in the SIC phase ([83] and in our own analysis in fig. 4.2.c). Moreover, the value of D_2 suggests that the mean free path in the monolayer is of the order of 4 nm and is therefore much smaller than ξ_2, which justifies the Usadel approach in this problem[2].

Fig. 7.1.f shows the spatial evolution of the peak height both as experimentally measured (blue dots) and numerically calculated with (solid red line) and without (dashed red line) self-consistency on the order parameter, i.e. $\Delta = cte$ or $\Delta(\boldsymbol{r})$ as given from equation 7.4. In the case where self-consistency is not implemented, the calculated spatial dependence $E_{\text{peak}}(x)$ does not follow the experimental data. The jump at the interface is also well captured and fits the experimental data nicely. On the same figure we show the self-consistent order parameter $\Delta(x)$ (in black) in the monolayer. This parameter exhibits a jump at the island edge and decays gradually to the S_2 bulk value within $80 - 100$ nm. These results underline the importance of fully self-consistent calculations which is in any case required based on fundamental principles. In fig. 7.1.e we show the full $dI/dV(V, x)$ spectra obtained from the solution of the Usadel equations using the parameter values determined above. The theory clearly reproduces all the salient features of the experimental results shown on figs. 7.1.(c) and 7.1.(d).

7.4 Results at 2 K

We now turn to the 2 K case. At such temperature, the monolayer is not in the superconducting state anymore. The experimental results are presented on fig. 7.3. The spectra acquired on the monolayer do not show a superconducting gap anymore far from the Pb island. Only close to the interface is present a smooth induced gap that gradually disappears over a typical distance of 60 nm away from the island edge. The behavior of the spatial evolution of the spectra closely resembles the case described in [162] for a S-N system where instead of a crystalline Pb monolayer, an amorphous Pb wetting layer plays the role of the normal metal. There are some differences however: (i) here, the Atshuler-Aronov reduction of the low bias tunneling density of states, characteristic of electronic correlations, is absent and (ii) the crystalline monolayer is superconducting at low temperatures which is not the case of the disordered Pb wetting layer.

We can now compare the experimental proximity spectra with the results given by our model, using the values determined at 0.3 K. The temperature used for the calculation is the one measured experimentally from the thermometer placed close to the sample. The results of this calculations are presented on fig. 7.3.e. In this case also, the theoretical results qualitatively reproduce the experimental spectra on fig. 7.3.c

[1] We have $r = G_N/G_B$ where G_N is equal to $\sigma_2 S/L$ with σ_2 the normal state conductivity of the monolayer, S the section of the barrier and L its length. G_B on the other side is equal to $G_0 M\tau$ with G_0 the quantum of conductance $2e^2/h$, τ the transmission coefficient of the interface and M the number of interface open channels.

[2] The diffusion coefficient is given by $D = \frac{1}{2} v_F l$ in two dimensions. For $v_F \simeq 10^6$ m.s^{-1} we obtain a mean free path $\ell \simeq 4$ nm.

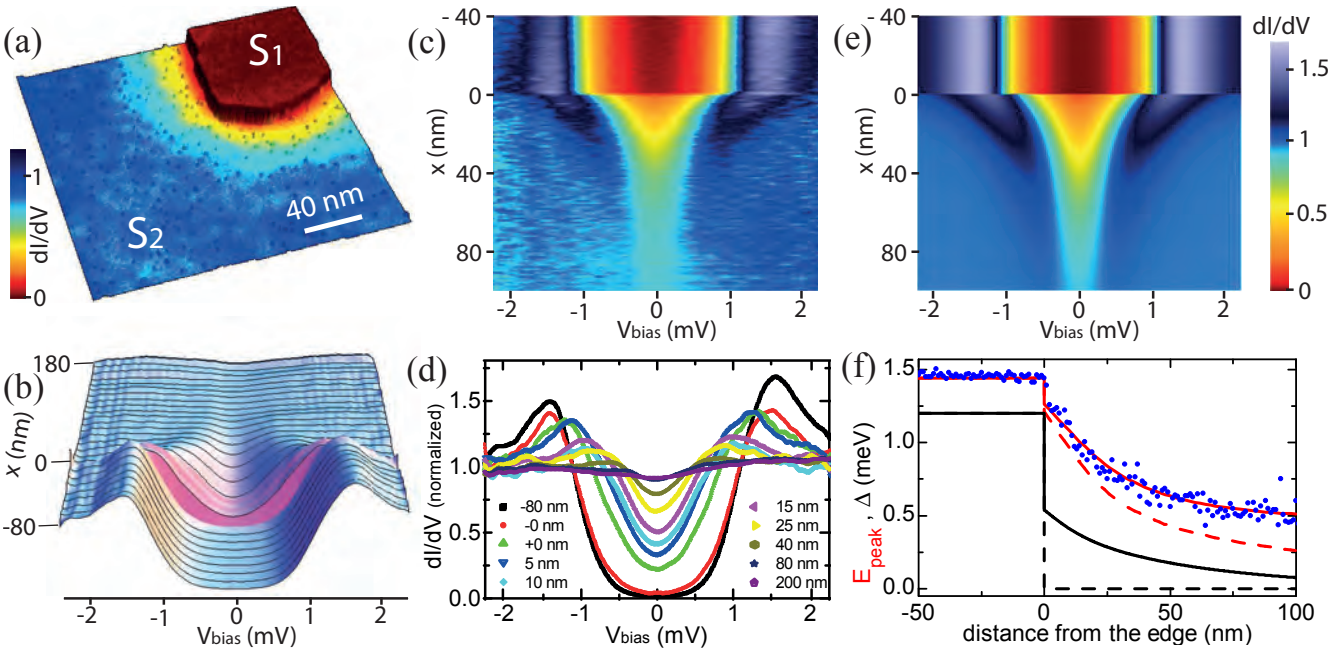

Figure 7.3: **Proximity effect between two superconductors at 2 K:** The same as in Fig. 7.1, but for T=2.05 K. At this temperature, the striped incommensurate Pb monolayer S_2 is in its normal state. Notice that the order parameter determined self-consistently exhibits a finite value close to the $S_1 - S_2$ interface.

without any adjustable parameter. More importantly, as we show in fig. 7.3.f, the Pb monolayer locally develops, in the vicinity of the interface, a finite order parameter that survives over a distance larger than 100 nm. The impact of this proximity-induced order parameter can be appreciated by comparing these results with a non-self-consistent calculation where the order parameter is assumed to vanish at this temperature, which would correspond to the case where S_2 is a non superconducting metal. Such calculations show that the induced gap extends over a much shorter distance inside the Pb monolayer as compared to the experimental dependence. This fact is illustrated on fig. 7.3.f where we show that the experimental data for $E_{\rm peak}(x)$ are much better fitted by the self-consistent calculation. Our results thus provide clear evidence for the existence of the proximity-induced superconductivity in the interface region.

We present on fig. 7.4 four different conductance maps showing the energy dependence of the proximity effect. These maps can be compared to what was measured at 300 mK (fig. 7.2) where we could observe the inverse proximity effect. This effect is not seen at 2 K on the conductance maps but due to the nature of the calculations we performed, we cannot provide any theoretical calculation to support this observation.

The inverse proximity effect observed at 300 mK is much weaker that the direct proximity effect. This difference is due to the difference in electron densities of the two systems as the density of electrons in much larger in the three dimensional islands than it is in the two-dimensional monolayer. In principle, the inverse proximity effect can be described within a natural extension of our 1D model. However, such a description is not quite satisfactory and this limitation calls for an extension of our model that is presently in progress.

Shortly after the publication of our work, similar experiments were performed by Kim et al. [176] confirming our observations.

7.5 Conclusion

To summarize, in this chapter we have presented our results on proximity effect at 300 mK when both Pb islands and the SIC monolayer are superconducting and at 2 K when Pb islands are superconducting and the monolayer is metallic. We explained our results by using a 1D Usadel model based on solving the self-consistent gap equation. Our results show the appearance of proximity-induced interface superconductivity in S_2 in the vicinity of the $S_1 - S_2$ interface for temperatures above T_{c2} thus confirming the theoretical prediction by de Gennes and co-workers [151].

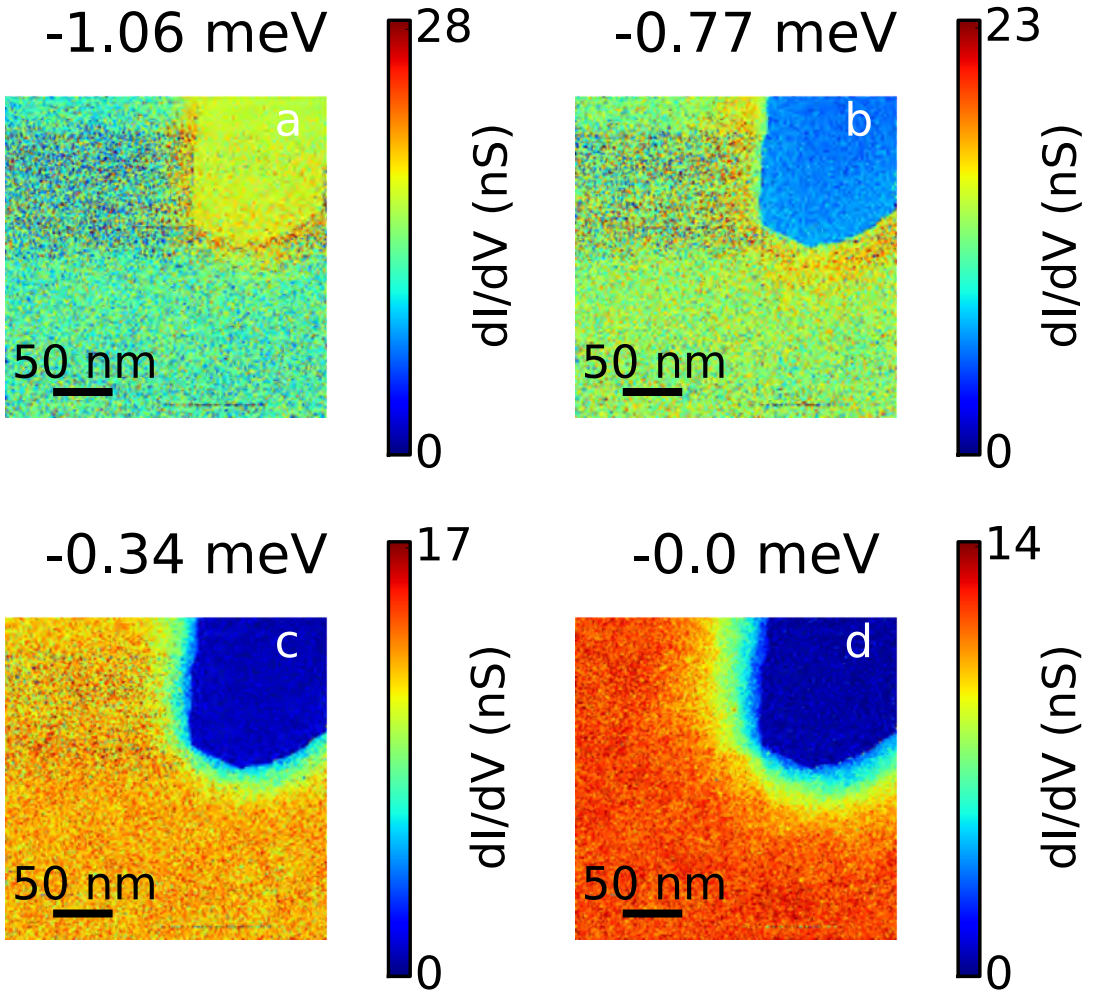

Figure 7.4: **Conductance maps of a 311×311 nm^2 area at 2 K:** a.-d. Conductance maps taken at the energies of -1.06 meV, -0.77 meV, -0.34 meV and 0 meV respectively.

Conclusion

In this thesis we have discussed and presented results related to the interaction between superconductivity and local magnetism. We particularly explored three limiting case :

- Individual impurities
- Ferromagnetic clusters
- Disordered clusters of magnetic impurities

From the first case we identified a direct connection between the dimensionality of the superconductor and the spatial extent of the YSR bound states induced by the local magnetic moments. The increase of the spatial extent of YSR bound states in two dimensional systems allowed us to further explore the role of the Fermi surface of the superconductor in the spatial pattern seen around magnetic impurities in conductance maps. We showed in two systems, 2H-$NbSe_2$ and Pb/Si(111) that the structure and symmetry of the Fermi surface is directly responsible for the diffraction patterns of the YSR bound states. In particular we evidenced the $2k_F$ periodic oscillations in those patterns and linked them to the relevant parts of the Fermi surface. By comparing the Fourier transform of these conductance maps we were able to show the disappearance of some electronic transition in the absence of magnetic interaction thus highlighting the spin-orbit coupling present in the Pb/Si(111) monolayer. The work on $NbSe_2$ in relation to individual magnetic impurities was done with the assistance of M. Leclerc who was working on his M2 internship at the time while the work on the Pb/Si(111) system was done partially during the internship of R. Leriche.

By studying ferromagnetic clusters of Co buried below the Pb/Si(111) monolayer we showed that we could locally induce a topological transition. The transition between trivial and topological is triggered by the magnetic moments of the Co clusters and we explored the phase diagram of such system. We measured the dispersion associated to edge states at the interface between a topological and trivial superconductor and discussed them in terms of chiral and helical edge states. We then showed that by increasing the size of the magnetic clusters we were able to trap vortices in the topological patches leading to zero bias anomalies characteristic of Majorana bound states. We finally demonstrated that due to size effects and magnetic anisotropy we were able to shift the magnetization of the Co clusters from an out of plane configuration to an in-plane configuration. This shifting was associated to a transition from topological to trivial for the clusters and a disappearance of the zero bias Majorana bound states. We would like to mention here the participation of D. Demaille and L. Largeau who performed TEM measurements on our samples at the INSP and LPN. This work will be continued by R. Leriche who will start his PhD in 2016 and will aim at reproduce and extend the results we obtained on the Pb/Si(111) monolayer for other systems.

The last configuration studied for the interaction between magnetic moments and superconductivity corresponds to clusters of randomly arranged impurities. At this point we showed the limitations of the Abrikosov-Gor'kov theory as the predicted attenuation of the quasiparticle peaks was not observed. We showed however that the gap gets locally reduced by the magnetic clusters and we were able to reproduce these results by considering the combination of YSR bound states with the gap auto-coherence equation.

The results we presented hint at exciting future developments in the use of superconductors in the elaboration of nano-patterned quantum electronic systems. In particular the possibility to manipulate the magnetization of magnetic clusters by using the STM tip and thus the topological state of a system is very promising. Future work could consist in the elaboration of full magnetic layers below a two dimensional superconductor that could be made locally topological by electrical stimulation from the tip. Then for large enough topological regions it should be theoretically possible to continuously move those trapped vortices by designing the adequate topological regions. Such proposition would thus allow the braiding of vortices and could lead to applications in the field of quantum nano-electronics.

Abrikosov Gor'kov theory

.1 Self-energy

In the following, we will base our calculations on a BCS Hamiltonian submitted to the perturbation $\hat{H}_{imp}$ as written section 2.2. In a fully general way, the self-energy for a superconducting material can be written in Nambu space as

$$M(k) = \omega\tau_0 - \Delta\tau_1 = \begin{pmatrix} \omega & -\Delta \\ -\Delta & \omega \end{pmatrix},$$

where $\tau_{1,2,3}$ refers to the Pauli matrices and τ_0 to identity. When put in presence of an impurity, a supplementary contribution M^i must be added to the self-energy leading to the following expression for the Green function

$$\mathcal{G}^{-1} = \varepsilon_k\tau_3 - \omega\tau_0 - M^i + \Delta\tau_1.$$

This Green function can be written by introducing $\tilde{\Delta}$ and $\tilde{\omega}$ without any lost of generality and we then obtain

$$\mathcal{G}^{-1} = \varepsilon_k\tau_3 + \tilde{\Delta}\tau_1 - \tilde{\omega}\tau_0.$$

This function can be easily inverted leading to the following expression for the Green function

$$\mathcal{G} = \frac{1}{\tilde{\omega}^2 - \varepsilon_k^2 - \tilde{\Delta}^2}\begin{pmatrix} -\varepsilon_k - \tilde{\omega} & \tilde{\Delta} \\ \tilde{\Delta} & \varepsilon_k - \tilde{\omega} \end{pmatrix}$$

We suppose an isotropic dispersion relation ε_k for simplicity and we can then write

$$\begin{aligned}
M^i_{diff} &= n_i \int \frac{d^2\Omega}{4\pi} v_1(\vec{k},\vec{k}') v_1(\vec{k}',\vec{k}) \int \frac{dk'}{2\pi^2}\tau_3\mathcal{G}(k')\tau_3 \\
&= n_i \int \frac{d^2\Omega}{4\pi} |v_1(\vec{k},\vec{k}')|^2 \int \frac{dk}{2\pi^2}\frac{1}{\tilde{\omega}^2 - \varepsilon_k^2 - \tilde{\Delta}^2}\begin{pmatrix} -\varepsilon_k - \tilde{\omega} & -\tilde{\Delta} \\ -\tilde{\Delta} & \varepsilon_k - \tilde{\omega} \end{pmatrix} \\
&= n_i \langle |v_1(\vec{k},\vec{k}')|^2 \rangle \int \frac{dk}{2\pi^2}\frac{1}{\tilde{\omega}^2 - \varepsilon_k^2 - \tilde{\Delta}^2}\begin{pmatrix} -\varepsilon_k - \tilde{\omega} & -\tilde{\Delta} \\ -\tilde{\Delta} & \varepsilon_k - \tilde{\omega} \end{pmatrix} \\
&= n_i \langle |v_1(\vec{k},\vec{k}')|^2 \rangle \int \frac{d\varepsilon_k}{2\pi^2}\frac{N(\varepsilon_k)}{\tilde{\omega}^2 - \varepsilon_k^2 - \tilde{\Delta}^2}\begin{pmatrix} -\varepsilon_k - \tilde{\omega} & -\tilde{\Delta} \\ -\tilde{\Delta} & \varepsilon_k - \tilde{\omega} \end{pmatrix}
\end{aligned}$$

We now make the hypothesis that over the considered integration domain, the density of states can be considered to be constant and we thus have for the density of states by spin $N(\varepsilon_k) = N_0$. Then, if we observe that the integrals containing ε_k on the numerator are integrations of odd functions in a symmetrical way around 0, we can then forget about these contributions and we only have to consider

$$M^i_{diff} = \frac{n_i}{2} N_0 \langle |v_i(\vec{k},\vec{k}')|^2 \rangle \int \frac{d\varepsilon}{\pi^2}\frac{1}{\tilde{\omega}^2 - \varepsilon^2 - \tilde{\Delta}^2}\begin{pmatrix} -\tilde{\omega} & \tilde{\Delta} \\ \tilde{\Delta} & -\tilde{\omega} \end{pmatrix}.$$

This integral can be easily calculated and gives

$$\begin{aligned}
\int \frac{d\varepsilon}{\pi^2} \frac{1}{\tilde{\omega}^2 - \varepsilon^2 - \tilde{\Delta}^2} \begin{pmatrix} -\tilde{\omega} & \tilde{\Delta} \\ \tilde{\Delta} & -\tilde{\omega} \end{pmatrix} &= \frac{1}{\tilde{\omega}^2 - \tilde{\Delta}^2} \int \frac{d\varepsilon}{\pi^2} \frac{1}{1 + \frac{\varepsilon^2}{\tilde{\Delta}^2 - \tilde{\omega}^2}} \begin{pmatrix} -\tilde{\omega} & \tilde{\Delta} \\ \tilde{\Delta} & -\tilde{\omega} \end{pmatrix} \\
&= \frac{1}{\tilde{\omega}^2 - \tilde{\Delta}^2} \int \frac{d\varepsilon}{\pi^2} \frac{1}{1 + \frac{\varepsilon^2}{\tilde{\Delta}^2 - \tilde{\omega}^2}} \begin{pmatrix} -\tilde{\omega} & \tilde{\Delta} \\ \tilde{\Delta} & -\tilde{\omega} \end{pmatrix} \\
&= -\frac{1}{\sqrt{\tilde{\omega}^2 - \tilde{\Delta}^2}} \begin{pmatrix} -\tilde{\omega} & \tilde{\Delta} \\ \tilde{\Delta} & -\tilde{\omega} \end{pmatrix} \int \frac{dx}{\pi^2} \frac{1}{1 + x^2} \\
&= -\frac{1}{\pi} \frac{1}{\sqrt{-\tilde{\omega}^2 + \tilde{\Delta}^2}} \begin{pmatrix} \tilde{\omega} & \tilde{\Delta} \\ \tilde{\Delta} & -\tilde{\omega} \end{pmatrix} \\
&= -\frac{i}{\pi} \frac{1}{\sqrt{\tilde{\omega}^2 - \tilde{\Delta}^2}} \begin{pmatrix} -\tilde{\omega} & \tilde{\Delta} \\ \tilde{\Delta} & -\tilde{\omega} \end{pmatrix}
\end{aligned}$$

Finally the self-energy is given by

$$M^i_{diff}(1) = -i \frac{n_i}{2\pi} N_0 \langle |v_1|^2 \rangle \frac{1}{\sqrt{\tilde{\omega}^2 - \tilde{\Delta}^2}} \begin{pmatrix} -\tilde{\omega} & \tilde{\Delta} \\ \tilde{\Delta} & -\tilde{\omega} \end{pmatrix},$$

that we can rewrite in the more convenient form

$$M^i_{diff} = \frac{1}{2} i(\Gamma_1 + \Gamma_2) \frac{\tilde{\omega}\tau_0 - \tilde{\Delta}\tau_1}{\sqrt{\tilde{\omega}^2 - \tilde{\Delta}^2}}$$

where

$$\frac{1}{2}(\Gamma_1 + \Gamma_2) = n^i \pi N_0 \langle |v_1|^2 \rangle .$$

Now that we are done with the diffusive part of the self-energy we are left with the calculation of the part containing the spin interaction. The lowest order term will make the following term appear

$$\langle k | v_2 \hat{\vec{S}}_i \cdot \hat{\vec{s}} | k' \rangle \langle k' | v_2 \hat{\vec{S}}_i \cdot \hat{\vec{s}} | k \rangle$$

for the diagonal part of the self-energy and

$$\langle Tk | v_2 \hat{\vec{S}}_i \cdot \hat{\vec{s}} | Tk' \rangle \langle k' | v_2 \hat{\vec{S}}_i \cdot \hat{\vec{s}} | k \rangle = - \langle k | v_2 \hat{\vec{S}}_i \cdot \hat{\vec{s}} | k' \rangle \langle k' | v_2 \hat{\vec{S}}_i \cdot \hat{\vec{s}} | k \rangle$$

for the non diagonal part. By averaging over the impurity spin we simply obtain a factor $\frac{1}{3} S(S+1)$ due to the work hypothesis concerning the absence of correlation of individual impurity spins. Finally the rest of the calculation is identical to the purely diffusive case and we obtain

$$M^i_{spin} = i \frac{n_i}{2\pi} N_0 \langle |v_2|^2 \rangle \frac{1}{4} S(S+1) \frac{1}{\sqrt{\tilde{\omega}^2 - \tilde{\Delta}^2}} \begin{pmatrix} \tilde{\omega} & \tilde{\Delta} \\ \tilde{\Delta} & \tilde{\omega} \end{pmatrix}$$

By defining

$$\frac{1}{2}(\Gamma_1 - \Gamma_2) = n^i \pi N_0 \langle |v_2|^2 \rangle \frac{1}{4} S(S+1),$$

the full self-energy can be written as

$$M^i = \frac{i}{\sqrt{\tilde{\omega}^2 - \tilde{\Delta}^2}} (\Gamma_1 \tilde{\omega}\tau_0 - \Gamma_2 \tilde{\Delta}\tau_1).$$

Another equation must be taken into account for our study to be coherent. This equation is the auto-coherence equation for the superconducting order parameter. This equation must be modified compared to its usual form in the following way

$$\Delta = \frac{N_0 V}{2} \int_{-\omega_{D'}}^{\omega_{D'}} \Re\left\{ \frac{\tilde{\Delta}}{\sqrt{\tilde{\omega}^2 - \tilde{\Delta}^2}} \right\} d\omega,$$

where the cutoff energy $\omega_{D'}$ for the superconducting interaction has been introduced. The link between this cutoff and the BCS cutoff is given by $\omega_{D'} = \sqrt{\omega_D^2 + \Delta^2}$.

The structure of the Green function calculated previously allows us to write

$$\begin{aligned} \tilde{\omega} &= \omega + i\Gamma_1 \frac{\tilde{\omega}}{\sqrt{\tilde{\omega}^2 - \tilde{\Delta}^2}} \\ \tilde{\Delta} &= \Delta + i\Gamma_2 \frac{\tilde{\Delta}}{\sqrt{\tilde{\omega}^2 - \tilde{\Delta}^2}}. \end{aligned}$$

If we define Γ as $\Gamma = \Gamma_1 - \Gamma_2$ and u as $u = \tilde{\omega}/\tilde{\Delta}$, the previous equations can be simplified as

$$\begin{aligned} u\Delta &= \omega + i\Gamma \frac{u}{\sqrt{u^2 - 1}}, \\ \Delta(0, \Gamma) &= \frac{N_0 V}{2} \int_{\omega_{D'}}^{\omega_{D'}} d\omega \Re\left\{ \frac{1}{\sqrt{u^2 - 1}} \right\}. \end{aligned}$$

We do indeed have

$$\omega = \tilde{\omega} - i\Gamma_1 \frac{\tilde{\omega}}{\sqrt{\tilde{\omega}^2 - \tilde{\Delta}^2}} = u\tilde{\Delta} - i\Gamma_1 \frac{u}{\sqrt{u^2 - 1}},$$

as well as

$$u\tilde{\Delta} = \omega + i\Gamma_1 \frac{u}{\sqrt{u^2 - 1}}.$$

If we introduce inside this relation the expression of $\tilde{\Delta}$, we obtain

$$u\Delta + ui\Gamma_2 \frac{\tilde{\Delta}}{\sqrt{\tilde{\omega}^2 - \tilde{\Delta}^2}} = \omega + i\Gamma_1 \frac{u}{\sqrt{u^2 - 1}},$$

i.e.

$$u\Delta = -ui\Gamma_2 \frac{1}{\sqrt{u^2 - 1}} + \omega + i\Gamma_1 \frac{u}{u^2 - 1} = \omega + \frac{i\Gamma u}{\sqrt{u^2 - 1}}.$$

At non-zero temperature, the auto-coherence equation integrates a temperature dependance for Δ in the form of a factor $\tanh \frac{1}{2}\beta\omega$ (where $\beta = \frac{1}{k_B T}$) leading to the following equation

$$\Delta(T, \Gamma) = N_0 V \int_0^{\omega_{D'}} d\omega \Re\left\{ \frac{1}{\sqrt{u^2 - 1}} \right\} \tanh \frac{\beta\omega}{2}.$$

One should note here the modification of the integration limits that leads to the disappearance of the $1/2$ factor. This new form must therefore be introduced inside the equation for $u\Delta$ where $\Delta(0, \Gamma)$ now becomes $\Delta(T, \Gamma)$.

.2 Critical temperature and concentration

The value of the critical temperature is obtained by the cancellation of the order parameter as a function of the tempereature, i.e. for $\Delta(T_c, \Gamma) = 0$. An equivalent way is to look at the limit $\Delta \to 0$ in which we have

$$u = \frac{\tilde{\omega}}{\tilde{\Delta}} \gg 1.$$

The term $\frac{u}{\sqrt{u^2-1}}$ approaches 1 and in $u\Delta$, the final result is

$$\lim_{T\to T_c} u\Delta = \omega + i\Gamma.$$

The auto-coherence equation for Δ can then be written as

$$\begin{aligned} 1 &= N_0 V \int_0^{\omega_D} \Re\left\{\frac{1}{\Delta\sqrt{u^2-1}}\right\} \tanh\frac{1}{2}\beta\omega d\omega \\ &\simeq N_0 V \int_0^{\omega_D} \Re\left\{\frac{1}{\Delta u}\right\} \tanh\frac{1}{2}\beta_c\omega d\omega \\ &= N_0 V \int_0^{\omega_D} \Re\{\frac{1}{\omega+i\Gamma}\} \tanh\frac{1}{2}\beta_c\omega d\omega. \end{aligned}$$

This equation can be simply written as (one should note that $\omega_{D'}$ has became ω_D due to the fact that $\Delta \to 0$)

$$1 = N_0 V \int_0^{\omega_D} d\omega \frac{\omega}{\omega^2+\Gamma^2} \tanh\frac{1}{2}\beta_c\omega.$$

This result is identical to the one in the absence of spin diffusion for $\Gamma \to 0$. The presence of the impurity thus induces a broadening of the function $\frac{\omega}{\omega^2+\Gamma^2}$ linked to a finite life time effect.

We can now calculate the critical concentration for which the critical temperature falls to zero. For $\beta_c \to +\infty$, the hyperbolic tangent behaves as $2\left[\theta(x)-\frac{1}{2}\right]$ (where $\theta(x)$ refers to the Heaviside function) and in the considered integration interval we are in the case where $\tanh\frac{1}{2}\beta_c\omega \simeq 1$. The consequence of this is that

$$1 = N_0 V \int_0^{\omega_D} \frac{\omega}{\omega^2+\Gamma^2} d\omega = N_0 V \int_0^{\frac{\omega_D}{\Gamma}} \frac{x}{x^2+1} dx,$$

where we used the variable change $x = \frac{\omega}{\Gamma}$. The previous integration gives us the following result

$$1 = \frac{N_0 V}{2}\left(\ln\left[\left(\frac{\omega_D}{\Gamma_{cr}}\right)^2 + 1\right] - \ln 1\right),$$

that can be simplified as

$$\frac{2}{N_0 V} = \ln\left(\frac{\omega_D^2}{\Gamma_{cr}^2} + 1\right).$$

By remembering that in the BCS theory

$$\frac{1}{N_0 V} = \ln\left(\frac{2\omega_D}{\Delta^P(0)}\right),$$

where $\Delta^P(0)$ is the value of the gap at $T = 0$ for a pure material, we obtain

$$\frac{\sqrt{\omega_D^2+\Gamma_{cr}^2}}{\Gamma_{cr}} = \frac{2\omega_D}{\Delta^P(0)}.$$

In the limit $\omega_D^2 \gg \Gamma_c^2$, we simply find

$$\Gamma_{cr} = \frac{\Delta^P(0)}{2},$$

which allows us to determine the critical concentration from which superconductivity is destroyed in the material.

Computation of the Shiba wave function in 2D and 3D

In the continuum limit, eq. 2.19 transforms into

$$\psi(\boldsymbol{r}) = \int \frac{d\boldsymbol{k}^d}{(2\pi)^d} e^{i\boldsymbol{k}\cdot\boldsymbol{r}} \frac{-JS/2 + K\tau_z}{E^2 - \xi_k^2 - \Delta^2} [E + \xi_k\tau_z + \Delta\tau_x]\psi(\boldsymbol{r}_{imp}), \tag{5}$$

where d is the dimensionality of the system. Assuming a constant density of states on the range of the superconducting gap, we can solve [177, 31] Eq. (5) with $r = r_{imp}$ as :

$$\{\mathbb{1} - \frac{\alpha + \beta\tau_z}{\sqrt{\Delta^2 - E^2}}[E + \Delta\tau_x]\}\psi(\boldsymbol{r}_{imp}) = 0 \tag{6}$$

where $\alpha = \frac{\pi\nu_0 JS}{2}$ and $\beta = \pi\nu_0 K$ and ν_0 is the density of states at the Fermi energy. The Shiba energy and the amplitude ratio of the wavefunctions on the impurity site therefore read as :

$$E = \Delta \frac{1 - \alpha^2 + \beta^2}{\sqrt{4\alpha^2 + (1 - \alpha^2 + \beta^2)^2}} \quad ; \quad \frac{\psi_+(0)}{\psi_-(0)} = \frac{1 + (\alpha - \beta)^2}{\sqrt{4\alpha^2 + (1 - \alpha^2 + \beta^2)^2}} \tag{7}$$

To solve completely Eq. (5) we follow Ref. [177, 31]. We need to compute these two integrals:

$$f_0(\boldsymbol{r}) = \int \frac{d\boldsymbol{k}^d}{(2\pi)^d} \frac{e^{i\boldsymbol{k}\cdot\boldsymbol{r}}}{E^2 - \xi_k^2 - \Delta^2}, \tag{8}$$

and

$$f_1(\boldsymbol{r}) = \int \frac{d\boldsymbol{k}^d}{(2\pi)^d} \frac{\xi_{\boldsymbol{k}} e^{i\boldsymbol{k}\cdot\boldsymbol{r}}}{E^2 - \xi_k^2 - \Delta^2}. \tag{9}$$

In order to obtain an analytical expression for the spatial evolution of the Shiba states, we make the assumption of an isotropic energy dispersion $\xi_k = k^2/2m + \mu$ where μ is the chemical potential. The result depends of the dimensionality d. Let us detail both the 3D and 2D cases for completeness.

.3 Shiba state in a 3D system

We change the integration variable to ξ_k and $x = \cos\theta_k$ with the polar angle θ measured relative to $\boldsymbol{r}$.

$$f_0(r) = \frac{\nu_0}{2} \int d\xi_k \int_{-1}^{1} dx \frac{e^{ikrx}}{E^2 - \xi_k^2 - \Delta^2}, \tag{10}$$

We first perform the integral on ξ_k by linearizing k with $k(\xi) = k_F + \xi/\hbar v_F$,

$$f_0(r) = -\frac{\nu_0\pi}{2\sqrt{\Delta^2 - E^2}} \int_{-1}^{1} dx e^{ik_F rx} e^{-k_S r|x|}, \tag{11}$$

where $k_S = \sqrt{\Delta^2 - E^2}/\hbar v_F$. This gives

$$f_0(r) = -\frac{\nu_0 \pi}{\sqrt{\Delta^2 - E^2}} \frac{e^{-k_S r}(k_F r \sin k_F r - k_S r \cos k_S r) - k_S r}{(k_F r)^2 + (k_S r)^2}. \tag{12}$$

Finally by the assumption $k_F >> k_S$ we find:

$$f_0(r) = -\frac{\nu_0 \pi}{\sqrt{\Delta^2 - E^2}} \frac{e^{-k_S r} \sin k_F r}{k_F r}. \tag{13}$$

The second integral reads:

$$f_1(r) = \frac{\nu_0}{2} \int d\xi_k \int_{-1}^{1} dx \frac{\xi_{\boldsymbol{k}} e^{ikrx}}{E^2 - \xi_k^2 - \Delta^2} \frac{\omega_D^2}{\omega_D^2 + \xi_k^2}. \tag{14}$$

We have incorporated the Debye frequency ω_D as a UV cut-off, to ensure the convergence of the integral [177]. In the same way we first perform the integral on ξ_k,

$$f_1(r) = i\frac{\pi \nu_0}{2} \frac{\omega_D^2}{\Delta^2 - E^2 - \omega_D^2} \int_{-1}^{1} dx \frac{x}{|x|} e^{ik_F r x}(e^{-k_S r|x|} - e^{r|x|\omega_D/\hbar v_F}), \tag{15}$$

and then on x

$$f_1(r) = \pi \nu_0 \Re[\frac{e^{ik_F r} e^{-k_S r}(-ik_F r + \frac{\omega_D r}{\hbar v_F}) + ie^{ik_F r} e^{-\omega_D r/\hbar v_F}(k_F r + ik_S r) + (k_S - \frac{\omega_D r}{\hbar v_F})}{(k_F r + i\frac{\omega_D r}{\hbar v_F})(-ik_F r + k_S r)}]. \tag{16}$$

Now we compute the asymptotic limit and suppose $k_F r >> \frac{\omega_D r}{\hbar v_F} >> 1$ and $k_F >> k_S$. This gives:

$$f_1(r) \approx \pi \nu_0 e^{-k_S r} \frac{\cos k_F r}{k_F r}. \tag{17}$$

.4 Shiba state in a 2D system

We proceed in the same way for the 2D case:

$$f_0(r) = \frac{\nu_0}{2\pi} \int d\xi_k \int_0^{2\pi} d\theta \frac{e^{ikr\cos\theta}}{E^2 - \xi_k^2 - \Delta^2}, \tag{18}$$

$$f_1(r) = \frac{\nu_0}{2\pi} \int d\xi_k \int_0^{2\pi} d\theta \frac{\xi_k e^{ikr\cos\theta}}{E^2 - \xi_k^2 - \Delta^2}, \tag{19}$$

We first perform the integral on ξ_k and then on θ:

$$f_0(r) = -\frac{\pi \nu_0}{\sqrt{\Delta^2 - E^2}} \Re[J_0(k_F r + ik_S r) + iH_0(k_F r + ik_S r)], \tag{20}$$

$$f_1(r) = \pi \nu_0 \Im[J_0(k_F r + ik_S r) + iH_0(k_F r + ik_S r)], \tag{21}$$

where $J_0(r)$ and $H_0(r)$ are the Bessel and the Struve function of order 0. These results are in agrement with [178]. Here again we compute the asymptotic limit assuming $k_F >> k_S$, which provides

$$f_0(r) \approx -\frac{\pi \nu_0}{\sqrt{\Delta^2 - E^2}} \sqrt{\frac{2}{\pi k_F r}} \cos(k_F r - \frac{\pi}{4}) e^{-k_S r}, \tag{22}$$

$$f_1(r) \approx \pi \nu_0 \sqrt{\frac{2}{\pi k_F r}} \sin(k_F r - \frac{\pi}{4}) e^{-k_S r} + \frac{2\nu_0}{k_F r}. \tag{23}$$

In the regime where we can neglect the last term of $f_1(r)$, $f_1(r) \approx \sqrt{\frac{2}{\pi k_F r}} \sin(k_F r - \frac{\pi}{4}) e^{-k_S r}$.

Derivation of the Bogoliubov-de Gennes equations

Let us consider the following Hamiltonian

$$H = \sum_{k,\sigma} \varepsilon_k \hat{c}^\dagger_{k,\sigma} \hat{c}_{k,\sigma} + \sum_k \left(\Delta \hat{c}^\dagger_{k\uparrow} \hat{c}^\dagger_{-k\downarrow} + \Delta^* \hat{c}_{-k\downarrow} \hat{c}_{k\uparrow} \right). \tag{24}$$

We will look for a way to diagonalize this Hamiltonian under the form [17]

$$H = E_g + \sum_{n,\sigma} \varepsilon_n \hat{\gamma}^\dagger_n \hat{\gamma}_n. \tag{25}$$

The simplest way to do so is to rewrite the creation operators as a linear combination of the γ operators in real space. We then define

$$\hat{\psi}_{\mathbf{r},\uparrow} = \sum_n \left(\hat{\gamma}_{n,\uparrow} u_n(\mathbf{r}) - \hat{\gamma}^\dagger_{n\downarrow} v^*_n(\mathbf{r}) \right) \tag{26}$$

$$\hat{\psi}_{\mathbf{r},\downarrow} = \sum_n \left(\hat{\gamma}_{n,\downarrow} u_n(\mathbf{r}) + \hat{\gamma}^\dagger_{n\uparrow} v^*_n(\mathbf{r}) \right) \tag{27}$$

where the operators $\hat{\psi}$ are linked to the operators $\hat{c}_k$ in the reciprocal space by

$$\hat{\psi}(r,\sigma) = \sum_k e^{ik\cdot r} \hat{c}_{k,\sigma}. \tag{28}$$

The eigenvalues equation can also be rewritten in the form of commutation relations

$$\begin{aligned} [H, \hat{\gamma}_{n,\sigma}] &= -\varepsilon_n \hat{\gamma}_{n,\sigma} \\ \left[H, \hat{\gamma}^\dagger_{n,\sigma}\right] &= \varepsilon_n \hat{\gamma}^\dagger_{n,\sigma} \end{aligned}$$

Obtaining the eigenstates of our systems is achieved through the equations for v_n and u_n. This equation is obtained by computing the commutation relations between $\hat{H}$ and $\hat{\psi}$.

$$[H, \hat{\psi}_{r,\sigma}] = H_e \sum_{r',\sigma'} [\hat{\psi}^\dagger_{r',\sigma'} \hat{\psi}_{r',\sigma'}, \hat{\psi}_{r',\sigma'}] + \sum_{r',\sigma'} \left\{ \Delta [\hat{\psi}^\dagger_{r',\sigma'} \hat{\psi}^\dagger_{r',-\sigma'}, \hat{\psi}_{r,\sigma}] + \Delta^* [\hat{\psi}_{r',-\sigma'} \hat{\psi}_{r',\sigma'}, \hat{\psi}_{r,\sigma}] \right\} \tag{29}$$

The last of these terms is equal to zero and we are simply left with the first two. The first term gives the following commutator

$$\begin{aligned} [\hat{\psi}^\dagger_{\sigma'} \hat{\psi}_{\sigma'}, \hat{\psi}_\sigma] &= \hat{\psi}^\dagger_{\sigma'} \hat{\psi}_{\sigma'} \hat{\psi}_\sigma - \hat{\psi}_\sigma \hat{\psi}^\dagger_{\sigma'} \hat{\psi}_{\sigma'} \\ &= -\hat{\psi}^\dagger_{\sigma'} \hat{\psi}_\sigma \hat{\psi}_{\sigma'} - \hat{\psi}_\sigma \hat{\psi}^\dagger_{\sigma'} \hat{\psi}_{\sigma'} \\ &= (\hat{\psi}_{\sigma'} \hat{\psi}^\dagger_{\sigma'} - \delta_{\sigma,\sigma'}) \hat{\psi}_{\sigma'} - \hat{\psi}_\sigma \hat{\psi}^\dagger_{\sigma'} \hat{\psi}_{\sigma'} \\ &= -\hat{\psi}_\sigma \delta_{\sigma,\sigma'}, \end{aligned}$$

while the superconducting coupling gives the commutator

$$\begin{aligned}
[\hat{\psi}^\dagger_{\sigma'}\hat{\psi}^\dagger_{-\sigma'},\hat{\psi}_\sigma] &= \hat{\psi}^\dagger_{\sigma'}\hat{\psi}^\dagger_{-\sigma'}\hat{\psi}_\sigma - \hat{\psi}_\sigma\hat{\psi}^\dagger_{\sigma'}\hat{\psi}^\dagger \\
&= \hat{\psi}^\dagger_{\sigma'}(\delta_{\sigma,\sigma'} - \hat{\psi}_\sigma\hat{\psi}^\dagger_{-\sigma'}) - \hat{\psi}_\sigma\hat{\psi}^\dagger_{\sigma'}\hat{\psi}^\dagger_{-\sigma'} \\
&= \hat{\psi}^\dagger_{\sigma'}\delta_{\sigma,-\sigma'} - (\delta_{\sigma,\sigma'} - \hat{\psi}_\sigma\hat{\psi}^\dagger_{\sigma'})\hat{\psi}^\dagger_{-\sigma'} - \hat{\psi}_\sigma\hat{\psi}^\dagger_{\sigma'}\hat{\psi}^\dagger_{-\sigma'} \\
&= \delta_{\sigma,-\sigma'}\hat{\psi}^\dagger_{\sigma'} - \delta_{\sigma,\sigma'}\hat{\psi}^\dagger_{-\sigma'} \\
&= -\sigma\delta_{\sigma,-\sigma'}\hat{\psi}^\dagger_{-\sigma'}
\end{aligned}$$

The general commutator from which we started can therefore be rewritten under the following form

$$[H,\hat{\psi}_\sigma] = -H_e\hat{\psi}_\sigma - \sigma\Delta\hat{\psi}^\dagger_{-\sigma}. \tag{30}$$

Finally we only have to do the same with the commutator $[H,\hat{\psi}^\dagger_\sigma]$ and we obtain

$$[H,\hat{\psi}^\dagger_\sigma] = -H_e\hat{\psi}^\dagger_\sigma - \sigma\Delta^*\hat{\psi}_{-\sigma} \tag{31}$$

Note that the difficulty of the commutation with the kinetic term H_e has been left aside as this terms trivially commutes with the field operators that form its eigenvectors by a simple Fourier transform.

We can now rewrite the previous commutators with the help of the γ operators by replacing the ψ by the corresponding expressions. We then obtain

$$\begin{aligned}
[H,\hat{\psi}_\sigma] &= [H,\sum_n \left\{\hat{\gamma}_\sigma u_n - \sigma\hat{\gamma}^\dagger_{-\sigma}v^*_n\right\}] \\
&= \sum_n \left\{u_n[H,\hat{\gamma}_\sigma] - \sigma v^*_n[H,\hat{\gamma}^\dagger_{-\sigma}]\right\} \\
&= \sum_n \left\{-u_n\varepsilon_n\hat{\gamma}_\sigma - \sigma v^*_n\varepsilon_n\hat{\gamma}^\dagger_{n,-\sigma}\right\},
\end{aligned}$$

while the counterpart of this previously computed commutator reads

$$\begin{aligned}
[H,\hat{\psi}_\sigma] &= -H_e\hat{\psi}_\sigma - \sigma\Delta\hat{\psi}^\dagger_{-\sigma} \\
&= -\sum_n \left\{H_e\left(\hat{\gamma}_\sigma u_n - \sigma\hat{\gamma}^\dagger_{-\sigma}v^*_n\right) + \sigma\Delta\left(\hat{\gamma}^\dagger_{-\sigma}u^*_n + \sigma\hat{\gamma}_\sigma v_n\right)\right\}
\end{aligned}$$

By doing the same for the conjugated terms of the field operators we finally obtain the two equations

$$\begin{aligned}
\sum_n \left\{u_n\varepsilon_n\hat{\gamma}_\sigma + \sigma v^*_n\varepsilon_n\hat{\gamma}^\dagger_{-\sigma}\right\} &= \sum_n \left\{H_e(\hat{\gamma}_\sigma u_n - \sigma\hat{\gamma}^\dagger_{-\sigma}v^*_n) + \sigma\Delta(\hat{\gamma}^\dagger_\sigma u^*_n + \sigma\hat{\gamma}_{-\sigma}v_n)\right\} \\
\sum_n \left\{u^*_n\varepsilon_n\hat{\gamma}^\dagger_\sigma + \sigma v_n\varepsilon_n\hat{\gamma}_{-\sigma}\right\} &= \sum_n \left\{-H_e(\hat{\gamma}^\dagger_\sigma u^*_n - \sigma\hat{\gamma}_{-\sigma}v_n) + \sigma\Delta^*(\hat{\gamma}_{-\sigma}u_n + \sigma\hat{\gamma}^\dagger_\sigma v^*_n)\right\}
\end{aligned}$$

By identifying the left and right terms of the equations the terms multiplied by γ_σ and $\gamma^\dagger_{-\sigma}$ we obtain the Bogoliubov-de Gennes equations for the terms u_n and v_n

$$u_n\varepsilon_n = H_e u_n + \Delta v_n \tag{32}$$

$$v_n\varepsilon_n = -H_e v_n + \Delta^* u_n \tag{33}$$

This equation can then be written in a matrix form using the spinor $\Psi_n = \begin{pmatrix} u_n & v_n \end{pmatrix}$ and we obtain

$$\epsilon_n\Psi = M\Psi \tag{34}$$

where the matrix M is written

$$M = \begin{pmatrix} H_e & \Delta \\ \Delta^* & H_e \end{pmatrix}. \tag{35}$$

Fano resonance

We consider the general problem of the coupling of a single electronic state to an electron gas. The form of the obtained peak is called Fano form from U. Fano who first found this expression in the context of an He resonance probed by mean of inelastic electron scattering [61].

We take the following Hamiltonian

$$\hat{H}_0 = \sum_k \varepsilon_k \hat{c}_k^\dagger \hat{c}_k + \varepsilon_d \hat{d}^\dagger \hat{d}, \tag{36}$$

describing two non-interacting systems. The first system is described by the operators $\hat{c}_k$ and $\hat{c}_k^\dagger$ and corresponds to a continuum of states $|k\rangle$ following the energy dispersion ε_k. The second system is a single electronic level $|d\rangle$ described by the operators $\hat{d}$ and $\hat{d}^\dagger$. This isolated level is at the energy ε_d.

We now add an Anderson like coupling between these two states described by the following Hamiltonian

$$\hat{H}_{int} = V \sum_k \hat{c}_k \hat{d}^\dagger + h.c. \tag{37}$$

The discrete level $|d\rangle$ without the interaction from eq. 37 is described by the Green function

$$G_d^{(0)} = \frac{1}{\omega + i0^+ - \varepsilon_d}. \tag{38}$$

When taking into account the interaction Hamiltonian, one creates an hybridization of the discrete level to the continuum *via* the introduction of a self-energy of the type $|V|^2 G_c^0$. The Green function now reads as

$$G_d^{(1)} = \frac{1}{\omega + i0^+ - \varepsilon_d - |V|^2 \sum_k \frac{1}{\omega + i0^+ - \varepsilon_k}}. \tag{39}$$

The $|k\rangle$ state being a continuum of states we can go from a discrete sum to a continuous integral over band of width D. We then obtain

$$\sum_k \frac{1}{\omega - \varepsilon_k} \to \int_{-D}^{D} \frac{1}{\omega + i0^+ - \varepsilon_k} = N_0 \ln \left| \frac{\omega + D}{\omega - D} \right| - i\pi N_0, \tag{40}$$

where N_0 is the density of states at the Fermi level of our electronic bath. By taking D to infinity, we only keep the second term of eq.40 and the Green function fro eq.39 can be written as

$$G_d^{(1)} = \frac{1}{\omega + i0^+ - \varepsilon_d + i\pi N_0 |V|^2}. \tag{41}$$

We are interested in the density of states which given by the imaginary part (up to a term $1/\pi$) of the Green function and therefore

$$\rho(\omega) = \frac{1}{\pi} \frac{\Gamma^2}{(\omega - \varepsilon_d)^2 + \Gamma^2} \tag{42}$$

with $\Gamma = \pi N_0 |V|^2$. The effect of coupling a discrete level to a continuum of states is thus shown to be a Lorentzian broadening of the density of states of this level and equivalently the introduction of finite life time of the quasi-particles excitations.

If we now want to perform an STM experiment in which the tip of our microscope exchanges electrons with the surface of our sample a new coupling must be introduced and will lead to a further modification of density of states of the discrete level *via* the possibility of new virtual electronic transitions contributing to the self-energy. The lowest order corrections to the continuum density of states is given by

$$\delta G_c(\omega) = |V|^2 G_c^0 G_d G_c^0. \tag{43}$$

As we want the associated density of states we must take the imaginary value of this quantity. Given that for two complex numbers z and z' we have $\Im\{z \times z'\} = \Im z \Re z' + \Re z \Im z'$, the correction to the density of states can be written

$$\delta\rho_c = \frac{|V|^2}{\pi}\left[\Im\{Gd\}\,\Re\left\{G_c^0 G_c^0\right\} + \Re\{G_d\}\,\Im\left\{G_c^0 G_c^0\right\}\right]. \tag{44}$$

By writing $q_c = -\frac{\Re\{G_c^0\}}{\Im\{G_c^0\}}$, the real and imaginary parts of G_c^0 can be written as

$$\begin{aligned}
\Im\left\{G_c^0 G_c^0\right\} &= (\Im\{G_c^0\})^2(q_c^2 - 1), \\
\Re\left\{G_c^0 G_c^0\right\} &= -2q_c(\Im\{G_c^0\})^2.
\end{aligned}$$

The correction to the density of states now becomes

$$\begin{aligned}
\delta\rho_c(\omega) &= -\frac{|V|^2}{\pi}\Im\{G_c^0(\omega)\}^2[(q_c^2-1)\Im G_d(\omega) - 2q_c\Re G_d(\omega)] \\
&= -\frac{|V|^2}{\pi}\pi^2\rho_0^2[(q_c^2-1)\Im G_d(\omega) - 2q_c\Re G_d(\omega)] \\
&= -\Gamma\rho_0[(q_c^2-1)\Im G_d(\omega) - 2q_c\Re G_d(\omega)].
\end{aligned}$$

If we now suppose that our discrete level is already hybridized by the electronic bath, the Green function $G_d(\omega)$ to use is the one obtained previously in eq.41. Defining $x = \frac{\omega-\varepsilon_d}{\Gamma}$ we have for $\delta\rho_c(\omega)$

$$\delta\rho_c(\omega) = \frac{\rho_0}{x^2+1}[(q_c^2-1) - 2q_c x] \tag{45}$$

and for the total density of states obtained from the summation $\rho_c(\omega) = \rho_0 + \delta\rho_c(\omega)$

$$\rho_c(\omega) = \rho_0\frac{(q_c+x)^2}{x^2+1}. \tag{46}$$

This expression for the density of states leads to the resonance called the Fano form (Cf. Figure 2.8).

Gap reduction calculation

```
from math import *
from pylab import *
from numpy import *
from numpy import random as rand
from functools import partial
from scipy.sparse import csr_matrix as spmat
from scipy.sparse import kron as kr
from scipy.sparse.linalg import eigsh
from scipy import special
from scipy import interpolate
from myfunctions import *
from scipy.interpolate import interp1d
from scipy.ndimage.filters import median_filter
from scipy.ndimage.filters import gaussian_filter
from mpl_toolkits.mplot3d import Axes3D
from matplotlib import cm


from matplotlib import *

def psip(kF, r, deltplus, deltminus, vF, Delta):
        #Computes the wavefunction Psi+ taking as arguments the fermi wave vector,
        #the distance from the center, delta+, delta-, the fermi velocity and the SC Gap
    a = 0.02
    return 1/sqrt(pi*kF*sqrt(r**2+a**2))*
                sin(kF*r - pi/4 + deltminus)*exp( -Delta*abs(sin(deltplus - deltminus))*r/vF )

def psim(kF, r, deltplus, deltminus, vF, Delta):
        #Computes the wavefunction Psi- taking as arguments the fermi wave vector,
        #the distance from the center, delta+, delta-, the fermi velocity and the SC Gap
    a = 0.02
    return 1/sqrt(pi*kF*sqrt(r**2+a**2))
                *sin(kF*r - pi/4 + deltplus)*exp( -Delta*abs(sin(deltplus - deltminus))*r/vF )


def spectre(energies, Delta, temp):
    energies = energies.astype('complex') #Converting the energy values to complex format
    bcs = real(abs(energies)/sqrt((energies)**2 + 1j*0.002 - Delta**2))
        #0 Temperature BCS density of states computed over the values of energies
    const_list = zeros(len(energies)) + 1.
        #Const list to suppress the edge effects due to the convolution procedure
    temperature_list = thermal_broad(energies, 0, temp)
        #Convolution function
    output = convolve(bcs, temperature_list, 'same')/convolve(const_list, temperature_list, 'same')
        #Normalized convolution
    return output.astype('float')


def wavefunc(dist_max, Delta, J, K):
        #Function computing and normalizing correctly the Shiba wave function
    kF = 1.5
    N0 = 1.
    vF = 5.
    S = 1.

    deltplus = atan(K*N0+N0*J*S/2.)
    deltminus = atan(K*N0-N0*J*S/2.)
```

```
    E_shiba = Delta*cos(deltplus-deltminus)

    r_space = linspace(0, dist_max, dist_max*kF*2)
    dr = 1/(kF*2)

    psi_plus = psip(kF, r_space, deltplus, deltminus, vF, Delta)
    psi_minus = psim(kF, r_space, deltplus, deltminus, vF, Delta)
    #psi_plus[0] = psi_plus[1]
    #psi_minus[0] = psi_minus[1]

    normplus = 2*pi*sum( r_space*abs(psi_plus)**2 )*dr
    normminus = 2*pi*sum( r_space*abs(psi_plus)**2 )*dr

    normalization = normplus + normminus # N = I1 + I2

    f1 = interp1d(r_space, psi_plus/sqrt(normalization))
    f2 = interp1d(r_space, psi_minus/sqrt(normalization))

    return f1, f2, E_shiba, normalization

def wavefunc3D(dist_max, Delta, J, K):
        #Function computing and normalizing correctly the Shiba wave function
        #energ = ener_r_space[0]
    kF = 1.5
    N0 = 1.
    vF = 5.
    S = 1.

    deltplus = atan(K*N0+N0*J*S/2.)
    deltminus = atan(K*N0-N0*J*S/2.)
    E_shiba = Delta*cos(deltplus-deltminus)

    r_space = linspace(0, dist_max, dist_max*kF*2)
    dr = 1/(kF*2)

    psi_plus = psip3D(kF, r_space, deltplus, deltminus, vF, Delta)
    psi_minus = psim3D(kF, r_space, deltplus, deltminus, vF, Delta)
    #psi_plus[0] = psi_plus[1]
    #psi_minus[0] = psi_minus[1]

    normplus = 4*pi*sum( r_space**2*abs(psi_plus)**2 )*dr
    normminus = 4*pi*sum( r_space**2*abs(psi_plus)**2 )*dr

    normalization = normplus + normminus # N = I1 + I2

    f1 = interp1d(r_space, psi_plus/sqrt(normalization))
    f2 = interp1d(r_space, psi_minus/sqrt(normalization))

    return f1, f2, E_shiba, normalization

def thermal_broad(E, E0, T):
        #Returns the derivative of the Fermi Dirac distribution over the energies E centered
        #around E0 at temperature T
    if T ==0:
        return 1.
    else:
        Fermi_dirac = exp((E-E0)/T)/((1. + exp((E-E0)/T))**2)
        return Fermi_dirac

#Calculation parameters

lat_size = 100 #Lateral size of the system in pixels
area_size = 50. #Size of the system in nm

pixel_size = area_size/float(lat_size)

Delta0 = 0.3
print 'Delta0 =', Delta0, 'meV'
Tc = Delta0*1.13/2.#Critical temperature in meV
kB = 1.38e-23 #Boltzman constant
```

```
Mag_coupl = 8. #Value of the magnetic potential in meV
Diff_coupl = 3. #Value of the diffusion potential in meV
num_ener = 800 #Number of energy points considered
T = 0.3 #Temperature in Kelvin
temperature = T*kB/1.6e-19*1e3 #Temperature in meV
num_iterations = 6 #Number of iterations for auto coherence
num_impurities = 500 #Number of impurities in our system


pos = []
#empty list that will contain the positions and values of the magnetic potential for each impurity

for i in range(num_impurities):
        #Initializing the positions of the impurities and the strength of the magnetic coupling
    incircle = False
    while incircle == False:
        x0 = random()*50-25
        y0 = random()*50-25
        incircle = sqrt(x0**2+y0**2)<15
        if incircle == True:
            theta = (random()-0.5)*2+5
            pos.append([x0, y0, theta])


if temperature<Tc:
    Gap = Delta0*sqrt(1. - temperature/Tc) #Value of the gap in meV
else:
    Gap = 0


vF = 5.
xi = vF/(pi*Delta0)
SC_coupling = 1./log(1.764*1.13*100./(Delta0*1e-3*1.6e-19/1.38e-23))
        #Evaluating the superconducting coulping of electrons using the formula
        # N0*V =1/ln(1.764*1.13*hbar*omega_D/Delta) estimating omega_D as around 100 K.

print 'Temperature = ', round(temperature, 4), 'meV --------- ', T, 'K'
print 'Delta = ', round(Gap, 2), 'meV'
print 'J = ', Mag_coupl, 'meV'
print 'K = ', Diff_coupl, 'meV'
print 'xi = ', xi, 'nm'
print 'Tc = ', Tc, 'meV --------- ', Tc*1e-3*1.6e-19/kB, 'K'



print 'Estimated superconducting coupling = ', SC_coupling, 'meV'

const = transpose(zeros(num_ener*lat_size*lat_size).reshape(num_ener, lat_size, lat_size))+1.
#Array on which to construct the broadening of the Shiba BS
DOS = zeros(num_ener*lat_size*lat_size).reshape(num_ener, lat_size, lat_size)
#Will contain the DOS once calculation and normalization of SBS made
gap_map = (zeros(lat_size**2*(num_iterations+1)).reshape(num_iterations + 1, lat_size, lat_size) +1)*Gap
#2D array containing the local values of the gap (initialized as Delta constant)


print 'Number of impurities = ', num_impurities
print '_____________________________\n'

print 'position ok'

gap_history = []
#empty list to keep track of the gap evolution with the iterations

x = linspace(-area_size/2., area_size/2., lat_size) #Space in x direction
y = linspace(-area_size/2., area_size/2., lat_size) #Space in y direction
energy_range = linspace(-3*Delta0, 3*Delta0, num_ener) #Values of the energies
x, y = meshgrid(x, y) #Grid x and y

for j in range(num_iterations):#_____________________________________________________________________________
    print 'iteration #', j+1
    shiba_ener = [] #empty list that will contain the position of the energies of every impurity
```

```
    amp = [] #empty list that will contain the normalization values of each wave function
    gap_history.append(gap_map[j].flatten())

    #coupl = linspace(0, 50, num_impurities)

    gap_list = gap_map.flatten()




    for i in range(num_impurities):#Calculating the DOS associated to each impurity
        index_x = int(pos[i][1]/pixel_size + area_size/2.) #!!!!!!!!!!!!!!!
        index_y = int(pos[i][0]/pixel_size + area_size/2.) #!!!!!!!!!!!!!!!
        gap_imp = gap_map[j][index_y][index_x]

        r = sqrt((x-pos[i][0])**2 + (y-pos[i][1])**2)
                                #Array of the distance from the center of impurity i

        r = r.flatten()

        interp_wf1, interp_wf2, Shiba_energy, amplitude =
                                wavefunc(max(r), gap_imp, cos(pos[i][2])*Mag_coupl, Diff_coupl)
        #Computation of the radial wave function
        #of impurity i as a function of r, returns psi+, psi-, Es and normalization of the state

        shiba_ener.append(Shiba_energy)
        amp.append(amplitude)

        wf1 = (interp_wf1(r)).reshape(lat_size, lat_size)
                                #Calculation of the Psi+ over the values of r
        wf2 = (interp_wf2(r)).reshape(lat_size, lat_size)
                                #Calculation of the Psi- over the values of r

        #Fermi Dirac broadening of the wave functions for wf1 and wf2
        broad1 = (const*thermal_broad(energy_range, Shiba_energy, temperature))
                                .transpose().reshape(num_ener, lat_size, lat_size)
        broad2 = (const*thermal_broad(energy_range, -Shiba_energy, temperature))
                                .transpose().reshape(num_ener, lat_size, lat_size)

        if j == num_iterations - 1:
            DOS += wf1**2*broad1 + wf2**2*broad2
        #Adding the convoluted wave function to the global DOS

        gap_map[j+1] += -SC_coupling*abs(wf1*wf2)*(1 - thermal_broad(Shiba_energy, 0, temperature))
                                #Gap difference induced by impurity i
        gap_map[j+1] += -SC_coupling*abs(wf2*wf1)*(1 - thermal_broad(-Shiba_energy, 0, temperature))
                                #Gap difference induced by impurity i



        if i%10 == 0:#Indicator for the impurity index
            print '    impurity #', i
    gap_map[j+1] = gaussian_filter(abs(gap_map[j+1]), xi, mode = 'wrap')
                #Eliminating the effect of the SBS divergence
    print min(gap_map[j+1].flatten())
DOS = array(map(partial(median_filter, size = 1), DOS))
#Median filter to suppress divergences in the DOS

gap_vals = gap_map[j+1].flatten()

#spectre_renormalization = array(map(mean, DOS.transpose().reshape(lat_size*lat_size, num_ener)))

evaluation_gaps = zeros(len(energy_range)*lat_size**2).reshape(lat_size**2, len(energy_range))
        #Array of 0 that will contain the
  #modified spectra after having taken into account the renormalization by the impurities
for i in range(len(gap_vals)):
        #Calculation of the final BCS spectra (without the impurities)
    evaluation_gaps[i] = spectre(energy_range, gap_vals[i], temperature) #-spectre_renormalization[i]
```

```
evaluation_gaps = evaluation_gaps.transpose().reshape(len(energy_range), lat_size, lat_size)
#Reshaping the array evaluation_gaps to correspond to
#the form of the DOS array

DOS = DOS*max(energy_range)*2

total_DOS = DOS + evaluation_gaps #Total DOS with both BCS spectra (thermally broaden) and Shiba states
```

Bibliography

[1] H. K. Onnes. The resistance of pure mercury at helium temperatures. *Commun. Phys. Lab. Univ. Leiden*, **12**:120, 1911.

[2] The Nobel prize in physics 1913. http://www.nobelprize.org/nobel_prizes/physics/laureates/1913.

[3] W. Meissner and R. Ochsenfeld. Ein neuer effekt bei eintritt der supraleitfähigkeit. *Naturwissenschaften*, **21**:787–788, 1933.

[4] F. London and H. London. The electromagnetic equations of the supraconductor. *Proceedings of the Royal Society of London A*, **149**:71–88, 1935.

[5] A. B. Pippard. An experimental and theoretical study of the relation between magnetic field and current in a superconductor. *Proc. Roy. Soc. (London)*, **A216**:547, 1953.

[6] M. Tinkham. *Introduction to Superconductivity, second edition*. Dover, 2004.

[7] V. L. Ginzburg and L. D. Landau. Contribution to the theory of superconductivity. *Zh. Eksp. Teor. Fiz.*, **20**:1064, 1950.

[8] E. P. Gross. Structure of a quantized vortex in boson systems. *Il Nuovo Cimento*, **20**:454–477, 1961.

[9] L. P. Pitaevskii. Vortex lines in an imperfect Bose gas. *Soviet Phys. JETP*, **13**:451–454, 1961.

[10] A. A. Abrikosov. The magnetic properties of superconducting alloys. *J. Phys. Chem. Solids*, **2**:199–208, 1957.

[11] D. Roditchev, C. Brun, L. Serrier-Garcia, J. C. Cuevas, V. H. Loiola Bessa, Milosević, F. Debontridder, V. Stolyarov, and T. Cren. Direct observation of Josephson vortex cores. *Nature Physics*, **11**:332–337, 2015.

[12] J. Bardeen, L. N. Cooper, and J. R. Schrieffer. Theory of superconductivity. *Phys. Rev.*, **108**:1175–1204, 1957.

[13] H. Frölich. Theory of the superconducting state. I. the ground state at the absolute zero temperature. *Phys. Rev.*, **79**:845–856, 1950.

[14] E. Maxwell. Isotope effect in the superconductivity of mercury. *Phys. Rev.*, **78**:487, 1950.

[15] C. A. Reynolds, B. Serin, W. H. Wright, and L. B. Nesbitt. Superconductivity of isotopes of mercury. *Phys. Rev.*, **78**:487, 1950.

[16] L. N. Cooper. Bound electron pairs in a degenerate Fermi gas. *Phys. Rev.*, **15**:1189–1190, 1956.

[17] P.-G. de Gennes. *Superconductivity of metals and alloys*. ABP, 1966.

[18] Y. Nambu. Quasi-particles and gauge invariance in the theory of superconductivity. *Phys. Rev.*, **117**:648–663, 1960.

[19] A. A. Abrivosov, L. P. Gorkov, and Dzyaloshinski I. E. *Methods of quantum field theory in statistical physics*. Prentice-Hall, Inc., 1963.

[20] L. P. Gor'kov and E. I. Rashba. Superconducting 2D system with lifted spin degeneracy: mixed singlet-triplet state. *Phys. Rev. Lett.*, **87**:037004, 2001.

[21] G. Binnig and H. Rohrer. Scanning tunneling microscopy. *IBM journal of research and development*, **30**:355–369, 1986.

[22] H. F. Hess, R. B. Robinson, R. C. Dynes, J. M. Valles Jr., and J. V. Waszczak. Scanning-tunneling-microscope observation of the Abrikosov flux lattice and the density of states near and inside a fluxoid. *Phys. Rev. Lett.*, **62**:214–216, 1989.

[23] H. Bruus and K. Flensberg. *Many-Body quantum theory in condensed matter physics*. Oxford university press, 2004.

[24] J. R. Schrieffer. *Theory of Superconductivity*. W. A. Benjamin, Inc., 1964.

[25] J. Bardeen. Tunneling into superconductors. *Phys. Rev. Lett.*, **9**:147–149, 1962.

[26] A. Savitzky and M. J. E. Golay. Smoothing and differentiation of data by simplified least squares procedures. *Analytical Chemistry*, **8**:1627–1639, 1964.

[27] R. D. Parks. *Superconductivity, Volume 1*. Marcel Dekker, Inc., 1969.

[28] P. W. Anderson. Localized magnetic states in metals. *Physical Review*, **124**:41, 1961.

[29] A. A. Abrikosov and L. P. Gor'kov. Contribution to the theory of superconducting alloys with paramagnetic impurities. *Soviet Physics JETP*, **12**:1243–1253, 1961.

[30] H. Shiba. Classical spins in superconductors. *Progress of Theoretical Physics*, **40**:435–451, 1968.

[31] A. I. Rusinov. Superconductivity near a paramagnetic impurity. *JETP Lett.*, **85**:85, 1969.

[32] L. Yu. Bound state in superconductors with paramagnetic impurities. *Acta Phys. Sin*, **21**:75–91, 1965.

[33] J. Kondo. Resistance minimum in dilute magnetic alloys. *Progress of theoretical physics*, **32**:31, 1964.

[34] A. V. Balatsky, I. Vekhter, and J.-X. Zhu. Impurity-induced states in conventional and unconventional superconductors. *Review of Modern Physics*, **78**:373–433, 2006.

[35] S. Skalski, O. Betbeder-Matibet, and P. R. Weiss. Properties of superconducting alloys containing paramagnetic impurities. *Physical review*, **136**:A 1500, 1964.

[36] H. Shiba. A Hartree-Fock theory of transition-metal impurities in a superconductor. *Progress of theoretical physics*, **50**:50, 1973.

[37] J. Zittartz and A. Bringer. Impurity bands in superconductors with magnetic impurities. *Solid State Communications*, **10**:513–516, 1972.

[38] E. Schachinger, J. M. Daams, and J. P. Carbotte. Paramagnetic impuritites in strong coupling superconductors. *Phys. Rev. B*, **22**:3194–3199, 1980.

[39] U. Sun and K. Maki. Comparison between d-wave superconductor with nonmagnetic impurities and s-wave superconductor with magnetic impurities. *Physica B*, **230-232**:942–944, 1997.

[40] M. A. Woolf and F. Reif. Effect of magnetic impurities on the density of states of superconductors. *Physical Review*, **137**:A557–A564, 1965.

[41] T. Sugawara and H. Eguchi. Paramagnetic impurity effect in dilute superconducting La-alloys. *Journal of the physical society of Japan*, **23**:965–974, 1967.

[42] A. S. Edelstein. Anomalous gapless superconductivity due to scattering from localized noninteracting spins. *Phys. Rev. Lett.*, **19**:1184–1186, 1967.

[43] D. M. Ginsberg. Tunneling conductance for superconducting alloys with $3d$ magnetic impurities. *Phys. Rev. B*, **13**:2895–2897, 1976.

[44] V. Ambegaokar and A. Griffin. Theory of the thermal conductivity of superconducting alloys with paramagnetic impurities. *Phys. Rev.*, **137**:A1151–A1167, 1965.

[45] N. Hatter, B. W. Heinrich, M. Ruby, J. I. Pascual, and K. J. Franke. Magnetic anisotropy in Shiba bound states across a quantum phase transition. *Nature Communications*, **6**:8988, 2015.

[46] J. Bauer, A. Oguri, and A. C. Hewson. Spectral properties of locally correlated electrons in a Bardeen-Cooper-Schrieffer superconcuctor. *Journal of physics: condensed matter*, **19**:486211, 2007.

[47] G. C. Ménard, S. Guissart, C. Brun, S. Pons, V.S. Stolyarov, F. Debontridder, M.V. Leclerc, E. Janod, L. Cario, D. Roditchev, P. Simon, and T. Cren. Coherent long-range magnetic bound states in a superconductor. *Nature Physics*, **11**:1013–1016, 2015.

[48] W. Bauriedl, P. Ziemann, and W. Buckel. Electron-tunneling observation of impurity bands in superconducting manganese-implanted lead. *Phys. Rev. Lett.*, **47**:1163–1165, 1981.

[49] A. Yazdani and al. Probing the local effects of magnetic impurities on superconductivity. *Science*, **275**:1767–1770, 1997.

[50] Michael E. Flatté and David E. Reynolds. Local spectrum of a superconductor as a probe of interactions between magnetic impurities. *Physical Review B*, **61**:14810–14814, 2000.

[51] Michael E. Flatté and Jeff M. Byers. Local electronic structure of defects in superconductors. *Physical Review B*, **56**:11213–11231, 1997.

[52] M. I. Salkola, A. V. Balatsky, and J. R. Schrieffer. Spectral properties of quasiparticle excitations induced by magnetic moments in superconductors. *Phys. Rev. B*, **55**:12648, 1997.

[53] Shuai-Hua Ji, Tong Zhang, Ying-Shuang Fu, Xi Chen, Xu-Cun Ma, Jia Li, Wen-Hui Duan, Jin-Feng Jia, and Qi-Kun Xue. High-resolution scanning tunneling spectroscopy of magnetic impurity induced bound states in the superconducting gap of Pb thin films. *Physical Review Letters*, **100**:226801, 2008.

[54] K. J. Franke, G. Schulze, and J. I. Pascual. Competition of superconducting phenomena and Kondo screening at the nanoscale. *Science*, **332**:940, 2011.

[55] J. R. Schrieffer and P. A. Wolff. Relation between the Anderson and Kondo hamiltonian. *Physical review*, **149**:491, 1966.

[56] E. Müller-Hartmann and J. Zittartz. Kondo effect in superconductors. *Physical review letters*, **26**:428, 1971.

[57] T. Matsuura. The effect of impurities on superconductors with Kondo effect. *Progress of theoretical physics*, **57**:1823, 1977.

[58] J. Shuai-Hua, F. Ying-Shuang, Tong Z., C. Xi, J. Jin-Feng, X. Qi-Kunn, and M. Xu-Cun. Kondo effect in self-assembled manganese phtalocyanine monolayer on Pb islands. *Chinese physical letters*, **27**:087202, 2010.

[59] P. Wahl, P. Simon, Diekhöner, V. S. Stepanyuk, P. Bruno, M. A. Schneider, and K. Kern. Exchange interaction between single magnetic adatoms. *Physical review letters*, **98**:056601, 2007.

[60] P. Wahl, L. Diekhöner, M. A. Schneider, L. Vitali, G. Wittich, and K. Kern. Kondo temperature of magnetic impurities at surfaces. *Physical review letters*, **93**:176603, 2004.

[61] U. Fano. Effects of configuration interaction on intensities and phase shifts. *Physical review*, **124**:1866, 1961.

[62] D.-J. Choi, S. Guissart, P. Simon, and L. Limot. Spin-current induced Kondo-resonance splitting of a single cobalt atom. *Arxiv:1305.5903*, 2013.

[63] Y. Noat, J. A. Silva-Guillén, T. Cren, V. Cherkez, C. Brun, S. Pons, F. Debontridder, D. Roditchev, W. Sacks, L. Cario, P. Ordejón, A. García, and E. Canadell. Quasiparticle spectra of 2H-$NbSe_2$: Two-band superconductivity and the role of tunneling selectivity. *Phys. Rev. B*, **92**:134510, 2015.

[64] T. Straub, T. Finteis, R. Claessen, P. Steiner, S. Hüfner, P. Blaha, C. S. Oglesby, and E. Bucher. Charge-density-wave mechanism in 2H-$NbSe_2$: Photoemission results. *Phys. Rev. Lett.*, **82**:4504–4507, 1999.

[65] J. C. Tsang and J. E. Smith Jr. Raman spectroscopy of soft modes at the charge-density-wave phase transition in 2H-$NbSe_2$. *Phys. Rev. Lett*, **37**:1407–1410, 1976.

[66] Y. Noat, T. Cren, F. Debontridder, D. Roditchev, W. Sacks, P. Toulemonde, and A. San Miguel. Signatures of multigap superconductivity in tunneling spectroscopy. *Phys. Rev. B*, **82**:014531, 2010.

[67] H. Suhl, B. T. Matthias, and L. R. Walker. Bardeen-Cooper-Schrieffer theory of superconductivity in the case of overlapping bands. *Phys. Rev. Lett.*, **3**:552–554, 1959.

[68] N. Schopohl and K. Scharnberg. Tunneling density of states for the two-band model of superconductivity. *Solid State Comm.*, **22**:371–374, 1977.

[69] T. Kiss, T. Yokoya, A. Chainani, S. Shin, M. Nohara, and H. Takagi. Fermi surface and superconducting gap of 2H-$NbSe_2$ using low-temperature ultrahigh-resolution angle-resolved photoemission spectroscopy. *Physica B: Condensed Matter*, **312**:666, 2002.

[70] K. Selte and A. Kjekshus. On the structural properties of the $Nb_{1+x}Sse_2$ phase. *Acta Chemica Scandinavica*, **18**:697–706, 1964.

[71] K. Rossnagel, O. Seifarth, L. Kipp, M. Skibowski, D. Voß, P. Krüger, A. Mazur, and J. Pollmann. Fermi surface of 2H-$NbSe_2$ and its implications on the charge-density-wave mechanism. *Phys. Rev. B*, **64**:235119, 2001.

[72] M. Ruby, F. Pientka, Y. Peng, F. von Oppen, B. W. Heinrich, and K. J. Franke. Tunneling processes into localized subgap states in superconductors. *Phys. Rev. Lett.*, **115**:087001, 2015.

[73] D. J. Rahn, S. Hellmann, M. Kalläne, C. Sohrt, T. K. Kim, L. Kipp, and K. Rossnagel. Gaps and kinks in the electronic structure of the superconductor 2H-$NbSe_2$ from angle-resolved photoemission at 1 K. *Phys. Rev. B*, **85**:224532, 2012.

[74] N. V. Smith, S. D. Kevan, and F. J. DiSalvo. Band structures of the layer compounds 1T-TaS_2 and 2H-$TaSe_2$ in the presence of commensurate charge-density waves. *J. Phys. C*, **18**:3157, 1985.

[75] K. Rossnagel, E.H. Rotenberg, Koh, N. V. Smith, and L. Kipp. Fermi surface, charge-density-wave gap, and kinks in 2H-$TaSe_2$. *Phys. Rev. B*, **72**:121103 (R), 2005.

[76] D. S. Inosov, V. B. Zabolotnyy, D. V. Evtushinsky, A. A. Kordyuk, B. B. Ìuchner, R. Follath, H. Berger, and S. V. Borisenko. Fermi surface nesting in several transition metal dichalcogenides. *New J. Phys.*, **10**:125027, 2008.

[77] D. S. Inosov, D. V. Evtushinsky, V. B. Zabolotnyy, A. A. Kordyuk, B. B. Ìuchner, R. Follath, H. Berger, and S. V. Borisenko. Temperature-dependent Fermi surface of 2H-$TaSe_2$ driven by competing density wave order fluctuations. *Phys. Rev. B*, **79**:125112, 2009.

[78] K. McElroy, R. W. Simmonds, J. E. Hoffman, D.-H. Lee, J. Orenstein, H. Eisaki, S. Uchida, and J. C. Davis. Relating atomic-scale electronic phenomena to wave-like quasiparticle states in superconducting $Bi_2Sr_2CaCu_2O_{8+\delta}$. *Nature*, **422**:592–596, 2003.

[79] J. Lee, M. P. Allan, M. A. Wang, J. Farrell, S. A. Grigera, F. Baumberger, J.C. Davis, and A. P. Mackenzie. Heavy *d*-electron quasiparticle interference and real-space electronic structure of $Sr_3Ru_2O_7$. *Nature Physics*, **5**:800–804, 2009.

[80] J. Tersoff and D. R. Hamann. Theory of the scanning tunneling microscope. *Phys. Rev. B*, **31**:805–813, 1985.

[81] W. A. Hofer, K. Palotás, S. Rusponi, T. Cren, and H. Brune. Role of hydrogen in giant spin polarization observed on magnetic nanostructures. *Phys. Rev. Lett.*, **100**:026806, 2008.

[82] Q. Dubout, F. Donati, C. Wäckerlin, F. Calleja, M. Etzkorn, A. Lehnert, L. Claude, P. Gambardella, and H. Brune. Controlling the spin of Co atoms on Pt(111) by hydrogen adsorption. *Phys. Rev. Lett.*, **114**:106807, 2015.

[83] T. Zhang, P. Cheng, W.-J. Li, Y.-J. Sun, G. Wang, X.-G. Zhu, K. He, L. Wang, X. Ma, X. Chen, Y. Wang, Y. Liu, H.-Q. Lin, J.-F. Jia, and Q.-K. Xue. Superconductivity in one-atomic-layer metal films grown on Si(111). *Nature Physics*, **6**:104–108, 2010.

[84] J. Noffsinger and M. L. Cohen. Superconductivity in monolayer Pb on Si(111) from first principles. *Solid state Communications*, **151**:421–424, 2011.

[85] A. Linscheid, A. Sanna, and E. K. U. Gross. Ab initio calculation of a Pb single layer on a Si substrate: two-dimensionnality and superconductivity. *arxiv: 1503.00977v1*, 2015.

[86] J. Noffsinger and M. L. Cohen. First-principles calculation of the electron-phonon coupling in ultrathin pb superconductors: Suppression of the transition temperature by surface phonons. *Phys. Rev. B*, **81**:214519, 2010.

[87] Tzu-Liang Chan, C. Z. Wang, M. Hupalo, M. C. Tringides, Zhong-Yi Lu, and K. M. Ho. First-principles studies of structures and stabilities of Pb/Si(111). *Physical Review B*, **68**:045410, 2003.

[88] V. Yeh, M. Yakes, M. Hupalo, and M.C. Tringides. Low temperature formation of numerous phases in Pb/Si(111). *Surf. Science Lett.*, **532**:L238–L244, 2004.

[89] S. Stepanovsky, M. Yakes, V. Yeh, M. Hupalo, and M. C. Tringides. The dense $\alpha - \sqrt{3} \times \sqrt{3}$ Pb/Si(111) phase: A comprehensive STM and SPA-LEED study of ordering, phase transitions and interactions. *Surface science*, **600**:1417–1430, 2006.

[90] M. Hupalo, T. L. Chan, C. Z. Wang, K. M. Ho, and M. C. Tringides. Atomic models, domain-wall arrangement, and electronic structure of the dense Pb/Si(111)-$\sqrt{3} \times \sqrt{3}$ phase. *Phys. Rev. B*, **66**:161410(R), 2002.

[91] I. Brihuega, O. Custance, R. Pérez, and J. M. Gómez-Rodríguez. Intrinsic character of the (3×3) to $(\sqrt{3} \times \sqrt{3})$ phase transition in Pb/Si(111). *Phys. Rev. Lett.*, **94**:046101, 2005.

[92] M. Yakes, V. Yeh, ML Hupalo, and M. C. Tringides. Self-organization at finite temperatures of the devil's staricase in Pb/Si(111). *Phys. Rev. B*, **69**:224103, 2004.

[93] M. R. Eskildsen, M. Kugler, S. Tanaka, J. Jun, S. M. Kazakov, J. Karpinski, and Ø. Fischer. Vortex imaging in the π band of magnesium diboride. *Phys. Rev. Lett.*, **89**:187003, 2002.

[94] N. Bergeal, V. Dubost, Y. Noat, W. Sacks, D. Roditchev, N. Emery, C. Hérold, J.-F. Marêché, P. Lagrange, and G. Loupias. Scanning tunneling spectroscopy on the novel superconductor CaC_6. *Phys. Rev. Lett.*, **97**:077003, 2006.

[95] Y. X. Ning, C. L. Song, Y. L. Wang, X. Chen, J. F. Jia, Q. K. Xue, and X. C. Ma. Vortex properties of two-dimensional superconducting Pb films. *J. Phys.: Condens. Matter*, **22**:065701, 2010.

[96] C. Brun, T. Cren, V. Cherkez, F. Debontridder, S. Pons, L. B. Ioffe, B. L. Altshuler, D. Fokin, M. Tringides, S. Bozhko, and D. Roditchev. Remarkable effects of disorder on superconductivity of single atomic layers of lead on silicon. *Nat. Phys.*, **10**:444–450, 2014.

[97] K. S. Kim, S. C. Jung, M. H. Kang, and H. W. Yeom. Nearly massless electrons in the silicon interface with a metal film. *Phys. Rev. Lett.*, **104**:246803, 2010.

[98] S. C. Jung and M. H. Kang. Triple-domain effects on the electronic structure of Pb/Si(111)-$(\sqrt{7} \times \sqrt{3})$: density-functional calculations. *Surf. Science*, **605**:551–554, 2010.

[99] T. Sekihara, R. Masutomi, and T. Okamoto. Two-dimensional superconducting state of monolayer Pb films grown on GaAs(110) in a strong parallel magnetic field. *Phys. Rev. Lett.*, **111**:057005, 2013.

[100] V. Barzykin and P. Gor'kov. Inhomogeneous stripe phase revisited for surface superconductivity. *Phys. Rev. Lett.*, **89**:227002, 2002.

[101] A. V. Matetskiy, S. Ichinokura, L. V. Bondarenko, A. Y. Tupchaya, D. V. Gruznev, A. V. Zotov, A. A. Saranin, R. Hobara, A. Takayama, and S. Hasegawa. Two-dimensional superconductor with a giant Rashba effect: One-atom-layer Tl-Pb compound on Si(111). *Phys. Rev. Lett.*, **115**:147003, 2015.

[102] W. H. Choi, H. Koh, Rotenberg, and H. W. Yeom. Electronic structure of dense Pb overlayers on Si(111) investigated using angle-resolved photoemission. *Phys. Rev. B*, **75**:075329, 2007.

[103] A. Fleurence, G. Agnus, T. Maroutian, B. Bartenlian, and P. Beauvillain. Au-assisted Co island growth on Si(111). *Applied Surface Science*, **258**:9675–9679, 2012.

[104] T. Meng, J. Klinovaja, S. Hoffman, P. Simon, and D. Loss. Superconducting gap renormalization around two magnetic impurities: From Shiba to Andreev bound states. *Phys. Rev. B*, **92**:064503, 2015.

[105] P. C. J. J. Coumou, E. F. C. Driessen, J. Bueno, C. Chapelier, and T. M. Klapwijk. Electrodynamic response and local tunneling spectroscopy of strongly disordered superconducting TiN films. *Phys. Rev. B*, **88**:180505 (R), 2013.

[106] M. Chand, G. Saraswat, A. Kamlapure, M. Mondal, S. Kumar, J. Jesudasan, V. Bagwe, L. Benfatto, V. Tripathi, and P. Raychaudhurri. Phase diagram of the strongly disordered s-wave superconductor NbN close to the metal-insulator transition. *Phys. Rev. B*, **85**:014508, 2012.

[107] G. M. Ménard, S. Guissart, C. Brun, M. Trif, F. Debontridder, R. T. Leriche, D. Demaille, D. Roditchev, P. Simon, and T. Cren. Two-dimensional topological superconductivity in Pb/-Co/Si(111). *Arxiv:1607.06353*.

[108] P. A. M. Dirac. The quantum theory of the electron. *Proceedings of the Royal society of London*, **117**:610–624, 1928.

[109] P. A. M. Dirac. A theory of electrons and protons. *Proceedings of the Royal society of London*, **126**:360–365, 1929.

[110] E. Majorana. Teoria simmetrica dell'elettrone e del positrone. *Il Nuovo Cimento*, **14**:171–184, 1937.

[111] J. M. Leinaas and J. Myrheim. On the theory of identical particles. *Il Nuovo Cimento B.*, **37**:1–23, 1976.

[112] M. Sato and S. Fujimoto. Majorana fermions and topology in superconductors. *Arxiv: 1601.02726*, 2016.

[113] D. A. Ivanov. Non-Abelian statistics of half-quantum vortices in p-wave superconductors. *Phys. Rev. Lett.*, **86**:268–271, 2001.

[114] A. Stern, F. von Oppen, and E. Mariani. Geometric phases and quantum entanglement as building blocks for non-Abelian quasiparticle statistics. *Phys. Rev. B*, **70**:205338, 2004.

[115] K Björnson and A. M. Black-Schaffer. Vortex states and Majorana fermions in spin-orbit coupled semiconductor-superconductor hybrid structures. *Phys. Rev. B*, **88**:0245013, 2013.

[116] K Björnson and A. M. Black-Schaffer. Probing vortex Majorana fermions and topology in semiconductor/superconductor heterostructures. *Phys. Rev. B*, **91**:214514, 2015.

[117] K. Björnson, S. S. Pershoguba, A. V. Balatsky, and A. M. Black-Schaffer. Spin-polarized edge currents and majorana fermions in one- and two-dimensional topological superconductors. *Phys. Rev. B*, **92**:214501, 2015.

[118] S. B. Chung, C. Chan, and H. Yao. Dislocation majorana zero modes in perovskite oxide 2DEG. *Arxiv:1505.00790*, 2016.

[119] S. Nadj-Perge, I. K. Drozdov, B. A. Bernevig, and A. Yazdani. Proposal for realizing Majorana fermions in chains of magnetic atoms on a superconductor. *Physical review B.*, **88**:020407, 2013.

[120] M. M. Vazifeh and M. Franz. Self-organized topological state with Majorana fermions. *Phys. Rev. Lett.*, **111**:206802, 2013.

[121] B. Braunecker and P. Simon. Interplay between classical magnetic moments and superconductivity in quantum one-dimensional conductors: toward a self-sustained topological Majorana phase. *Phys. Rev. Lett.*, **111**:147202, 2013.

[122] A. Manchon, H. C. Koo, J. Nitta, S. M. Frolov, and R. A. Duine. New perspectives for Rashba spin-orbit coupling. *Nature Materials*, **14**:871–882, 2015.

[123] B. A. Bernevig and T. L. Hughes. *Topological insulators and topological superconductors*. Princeton university press, 2013.

[124] V. Mourik, K. Zuo, S. M. Frolov, S. R. Plissard, E. P. A. M. Bakkers, and L. P. Kouwenhoven. Signatures of Majorana fermions in hybrid superconductor-semiconductor nanowire devices. *Science*, **336**:1003–1007, 2012.

[125] S. Nadj-Perge, I. K. Drozdov, J. Li, H. Chen, S. Jeon, J. Seo, A. H. MacDonald, B. A. Bernevig, and A. Yazdani. Observation of Majorana fermions in ferromagnetic atomic chains on a superconductor. *Science*, **346**:602–607, 2014.

[126] V. B. Berestetskii, E. M. Lifshitz, and L. P. Pitaevskii. *Quantum electrodynamics, second edition.* Pergamon Press, 1982.

[127] Y. A. Bychkov and É. I. Rashba. Properties of a 2D electron gas with lifted spectral degeneracy. *P. Zh. Eksp. Teor. Fiz.*, **39**:66–69, 1984.

[128] V. M. Édel'shtein. Characteristics of the Cooper pairing in two-dimensional noncentrosymmetric electron systems. *Zh. Eksp. Teor. Fiz.*, **95**:2151–2162, 1989.

[129] L. P. Gor'kov. Surface and superconductivity. *International Journal of Modern Physics B*, **20**:2569–2573, 2006.

[130] I. Gierz, T. Suzuki, E. Frantzeskakis, S. Pons, S. Ostanin, A. Ernst, M. Grioni, K. Kern, and C. R. Ast. Silicon surface with giant spin splitting. *Phys. Rev. Lett.*, **103**:046803, 2009.

[131] K. Yaji, Y. Ohtsubo, S. Hatta, H. Okuyama, K. Miyamoto, T. Okuda, A. Kimura, H. Namatame, M. Taniguchi, and T. Aruga. Large Rashba spin splitting of a metallic surface-state band on a semiconductor surface. *Nature Commun.*, **1**:17, 2010.

[132] C. R. Ast, J. Henk, A. Ernst, L. Moreschini, M. C. Falub, Pacilé D., P. Bruno, K. Kern, and M. Grioni. Giant spin splitting through surface alloying. *Phys. Rev. Lett.*, **98**:186807, 2007.

[133] E. Frantzeskakis, S. Pons, and M. Grioni. Giant spin-orbit splitting in a surface alloy grown on a Si substrate: $BiAg_2$/Ag/Si(111). *Physica B*, **404**:419–421, 2009.

[134] E. Frantzeskakis, L. Moreschini, M. C. Falub, M. Grioni, S. Pons, C. R. Ast, D. Pacilé, and M. Papagno. New mechanism for spin-orbit splitting of conduction states in surface alloys. *Journal of Surf. Science and Nanotech.*, **7**:264–268, 2009.

[135] J. H. Dil, F. Meier, J. Lobo-Checa, L. Patthey, G. Bihlmayer, and J. Osterwalder. Rashba-type spin-orbit splitting of quantum well states in ultrathin Pb films. *Phys. Rev. Lett.*, **101**:266802, 2008.

[136] B. Slomski, G. Landolt, G. Bihlmayer, J. Osterwalder, and J. H. Dil. Tuning of the Rashba effect in Pb quantum well states via a variable Schottky barrier. *Sci. Rep.*, **3**, 2013.

[137] P. Luches, A. Rota, S. Valeri, I. I. Pronin, D. A. Valdaitsev, N. S. Faradzhev, and M. V. Gomoyunova. The Co/Si(111) interface formation: a temperature dependent reaction. *Surface science*, **511**:303–311, 2002.

[138] H. W. Chang, J. S. Tsay, Y. C. Hung, F. T. Yuan, W. Y. Chan, W. B Su, C. S. Chang, and Y. D. Yao. Magnetic properties and microstructures of ultrathin Co/Si(111) films. *Journal of applied Physics*, **101**:09D124, 2007.

[139] J. S. Tsay, T. Y. Fu, M. H. Lin, C. S. Yang, and Y. D. Yao. Microscopic interfacial structures and magnetic properties of ultrathin Co/Si(111) films. *Applied Physics Letters*, **88**:102506, 2006.

[140] J. Avila, A. Mascaraque, E. G. Michel, M. C. Asensio, G. LeLay, J. Ortega, R. Pérez, and F. Flores. Dynamical fluctuations as the origin of a surface phase transition in Sn/Ge(111). *Phys. Rev. Lett*, **82**:442–445, 1999.

[141] J. Ortega, R. Pérez, and F. Flores. Dynamical fluctuations and the $\sqrt{3} \times \sqrt{3} \leftrightarrow 3 \times 3$ transition in α-Sn/Ge(111) and Sn/Si(111). *Journ. of Phys.: Cond. Mat.*, **14**:5979–6004, 2002.

[142] A. V. Melechko, J. Braun, H. H. Weitering, and E. W. Plummer. Role of defects in two-dimensional phase transitions: an STM study of the Sn/Ge(111) system. *Phys. Rev. B*, **61**:2235–2245, 2000.

[143] A. V. Melechko, J. Braun, H. H. Weitering, and E. W. Plummer. Two-dimensional phase transition mediated by extrinsic defects. *Phys. Rev. Lett.*, **83**:999–1002, 1999.

[144] J. Shi, B. Wu, X. C. Xie, E. W. Plummer, and Z. Zhang. Surface phase transitions induced by electron mediated adatom-adatom interaction. *Phys. Rev. Lett.*, **91**:076103, 2003.

[145] J. M. Carpinelli, H. H. Weitering, E. W. Plummer, and R. Stumpf. Direct observation of a surface charge density wave. *Nature*, **381**:398–400, 1996.

[146] P. W. Anderson. Absence of diffusion in certain random lattices. *Phys. Rev.*, **109**:1492–1505, 1958.

[147] N. F. Mott. Metal-insulator transition. *Review of modern physics*, **40**:677, 1968.

[148] S. Modesti, L. Petaccia, G. Ceballos, I. Vobornik, G. Panaccione, G. Rossi, L. Ottaviano, R. Larciprete, S. Lizzit, and A. Goldoni. Insulating ground state of Sn/Si(111)-($\sqrt{3} \times \sqrt{3}$)r30°. *Phys. Rev. Lett.*, **98**:126401, 2007.

[149] B. Kramer and A. MacKinnon. Localization: theory and experiment. *Rep. Prog. Phys.*, **56**:1469, 1993.

[150] P. A. Lee and T. V. Ramakrishnan. Disordered electronic systems. *Rev. Mod. Phys.*, **57**:287, 1985.

[151] P.-G. de Gennes. Boundary effects in superconductors. *Review of Modern Physics*, **36**:225, 1964.

[152] Deutscher G. and P. G. de Gennes. *Superconductivity: Proximity effects*, volume **2**. R. D. Parks (Marcel Dekker, New York), 1969.

[153] B. Pannetier and H. Courtois. Andreev reflection and proximity effect. *J. Low temp. phys.*, **118**:599, 2000.

[154] S. Guéron, H. Pothier, N. O. Birge, D. Esteve, and M. H. Devoret. Superconducting proximity effect probed on a mesoscopic length scale. *Phys. Rev. Lett.*, **77**:3025, 1996.

[155] M. Meschke, J. T. Peltonen, J. K. Pekola, and F. Giazotto. Tunnel spectroscopy of a proximity Josephson junction. *Phys. Rev. B*, **84**:214514, 2011.

[156] M. Vinet, C. Chapelier, and F. Lefloch. Spatially resolved spectroscopy on superconducting proximity nanostructures. *Phys. Rev. B*, **63**:165420, 2001.

[157] N. Moussy, H. Courtois, and B. Pannetier. Local spectroscopy of a proximity superconductor at very low temperature. *Europhys. Lett.*, **55**:861, 2001.

[158] W. Escoffier, C. Chapelier, N. Hadacek, and Villégier J.-C. Anomalous proximity effect in an inhomogeneous disordered superconductor. *Phys. Rev. Lett.*, **93**:217005, 2004.

[159] H. le Sueur, P. Joyez, H. Pothier, C. Urbina, and D. Esteve. Phase controlled superconducting proximity effect probed by tunneling spectroscopy. *Phys. Rev. Lett.*, **100**:197002, 2008.

[160] M. Wolz, C. Debuschewitz, W. Belzig, and E. Scheer. Evidence for attractive pair interaction in diffusive gold films deduced from studies of the superconducting proximity effect with aluminum. *Phys. Rev. B*, **84**:104516, 2011.

[161] J. Kim, V. Chua, G. A. Fiete, H. Nam, A. H. MacDonald, and C.-K. Shih. Visualization of geometric influences on proximity effects in heterogeneous superconductor thin films. *Nat. Phys.*, **8**:464, 2012.

[162] L. Serrier-Garcia, J. C. Cuevas, T. Cren, C. Brun, V. Cherkez, F. Debontridder, D. Fokin, Bergeret F. S., and D. Roditchev. Scanning tunneling spectroscopy study of the proximity effect in a disorderd two-dimensional metal. *Phys. Rev. Lett.*, **110**:157003, 2013.

[163] E. J. H. Lee, X. Jiang, M. Houzer, R. Aguado, C. M. Lieber, and S. De Franceschi. Spin-resolved Andreev levels and parity crossings in hybrid superconductor-semiconductor nanostructures. *Nature Nanotech.*, **9**:79–84, 2014.

[164] J.-D. Pillet, C. H. L. Quay, P. Morfin, C. Bena, A. Levy Yeyati, and P. Joyez. Andreev bound states in supercurrent-carrying carbon nanotubes revealed. *Nature physics*, **6**:965, 2010.

[165] L. C. Bretheau, Ç. Ö. Girit, C. Urbina, D. Esteve, and H. Pothier. Exciting andreev pairs in a superconducting atomic contact. *Nature*, **499**:312–315, 2013.

[166] T. Dirks, T. L. Hugues, S. Lal, B. Uchoa, Y.-F. Chen, C. Chialvo, P. M. Goldbart, and N. Mason. transport through andreev bound states in a graphene quantum dot. *Nature Phys.*, **7**:386–390, 2011.

[167] L. C. Bretheau, Ç. Ö. Girit, C. Urbina, D. Esteve, and H. Pothier. Supercurrent spectroscopy of andreev states. *Phys. Rev. X*, **3**:041034, 2013.

[168] V. Cherkez, J. C. Cuevas, C. Brun, T. Cren, G. Ménard, F. Debontridder, V. S. Stolyarov, and D. Roditchev. Proximity effect between two superconductors spatially resolved by scanning tunneling spectroscopy. *Physical Review X*, **4**:011033, 2014.

[169] C. Kumpf, O. Bunk, J. H. Zeysing, M. M. Nielsen, M. Nielsen, R. L. Johnson, and R. Reidenhans. Structural study of the commensurate-incommensurate low-temperature phase transition of Pb on Si(111). *Surf. Sci.*, **448**:L213, 2000.

[170] I. N. Stranski and L. Krastanow. Zur theorie der orientierten ausscheidung von ionenkristallen aufeinander. *Akademie der Wissenschaften Wien*, **146**:797–810, 1938.

[171] M. Yamada, T. Hirahara, and S. Hasegawa. Magnetoresistance measurements of a superconducting surface state of In-induced and Pb-induced structures on Si(111). *Phys. Rev. Lett.*, **110**:237001, 2013.

[172] K. D. Usadel. Generalized diffusion equation for superconducting alloys. *Phys. Rev. Lett.*, **25**:507, 1970.

[173] K. C. Hammer, J. C. Cuevas, F. S. Bergeret, and W. Belzig. Density of states and supercurrent in diffusive SNS junctions: role of nonideal interfaces and spin-flip scattering. *Phys. Rev. B*, **76**:064514, 2007.

[174] M. Eschrig, J. Kopu, A. Konstandin, J. C. Cuevas, M Fogelström, and G. Schön. Singlet-triplet mixing in superconductor-ferromagnet hybrid devices. *Adv. Solid State Phys.*, **44**:533, 2004.

[175] Y. V. Nazarov. Novel circuit theory of Andreev reflection. *Superlattices Microstruct.*, **25**:1221, 1999.

[176] H. Kim, S.Z. Lin, M. J. Graf, T. Kato, and Y. Hasegawa. Enhancement and termination of the superconducting proximity effect due to atomic-scale defects visualized by scanning tunneling microscopy. *arXiv:14012602*, 2014.

[177] F. Pientka, L. I. Glazman, and F. von Oppen. Topological superconducting phase in helical Shiba chain. *Phys. Rev. B*, **88**:155420, 2013.

[178] P. M. R Brydon, S. Das Sarma, H.-Y. Hui, and J. D. Sau. Topological Yu-Shiba-Rusinov chain from spin-orbit coupling. *Phys. Rev. B*, **91**:064505, 2015.

Supraconducteurs 2D perturbés par un magnétisme local: des états de Yu-Shiba-Rusinov aux quasiparticles de Majorana

Gerbold Ménard

July 6, 2016

1 Introduction

Dans ce résumé nous aborderons les points principaux détaillés dans le manuscrit "2D superconductors perturbed by local magnetism; from Yu-Shiba-Rusinov bound states to Majorana quasiparticles" en langue anglaise.

Cette thèse couvre l'étude de l'effet de perturbations magnétiques à l'échelle nanométrique dans des supraconducteurs bidimensionnels. La motivation de cette étude était d'obtenir un type de supraconductivité particulier dit topologique en manipulant des moments magnétiques dans des supraconducteurs possédant une forte interaction spin-orbite.

Deux systèmes en particuliers y sont discutés. Tout d'abord nous avons étudié l'effet d'impuretés magnétiques dans des monocristaux de $NbSe_2$ qui sont des matériaux tri-dimensionnels du point de vue de la supraconductivité mais dont la structure électronique est bidimensionnelle. En insérant des impuretés de Fe dans ces cristaux il nous a alors été possible d'étudier les états de Yu-Shiba-Rusinov produits et d'observer leur structure spatiale en parfait accord avec les prédictions théoriques pour un supraconducteur bidimensionnel.

Le deuxième système étudié est la monocouche de Pb/Si(111), les résultats lui étant dédiés sont ici séparés en deux parties. La première partie traite de l'effet d'impuretés magnétiques dans ce système bidimensionnel. Nous avons étudié des impuretés magnétiques dans différentes phases de la reconstruction du Pb en monocouche et mis en évidence le rôle de la surface de Fermi dans les structures spatiales résultantes ainsi que confirmé le rôle de la dimensionnalité dans l'extension spatiale des états de Yu-Shiba-Rusinov. En combinant ensuite les impuretés magnétiques sous la forme de clusters enterrés sous la monocouche nous avons étudié le comportement du gap et développé un modèle permettant de comparer nos résultats à la théorie d'Abrikosov et Gor'kov généralement admise dans cette configuration.

La deuxième partie portant sur la monocouche de Pb/Si(111) supraconductrice traite de la manière d'induire de la supracondutivité topologique en tirant profit de l'organisation d'impuretés magnétiques sous la forme de clusters ordonnés. Nous commençons par mettre en évidence les états de bords à la frontière d'une zone définie par un cluster nanométrique enfoui sous la couche de Pb. Nous avons mesuré la dispersion spatiale associée à ces états et interprété les résultats en termes de dispersion de Majorana à la frontière entre un supraconducteur trivial et un supraconducteur topologique hélical. En augmentant la taille de ces clusters nous montrons qu'il est possible

d'admettre des vortex ayant pour effet de piéger un mode électronique au niveau de Fermi, réalisant ainsi une quasiparticule de Majorana. Nous montrons de plus que la magnétisation des clusters peut être influencée par la pointe du STM, ce qui permet une manipulation des excitations de Majorana, un pré-requis essentiel à l'élaboration d'une électronique quantique basée sur les propriétés de statistique non anyonique desdites excitations [1, 2].

Enfin dans une dernière partie nous explorons la structure électronique des différentes phases de la monocouche de Pb/Si(111). Nous discutons entre autre dans cette section le comportement d'isolant de Mott de la phase 3×3 présentant deux bandes de Hubbard symétrique en énergie dans la spectroscopie. Cette section s'achève par l'étude de l'effet de proximité supraconducteur dans deux configurations. La première configuration concerne la proximité d'un supraconducteur avec un domaine métallique corrélé tandis que la seconde concerne la proximité entre deux supraconducteurs possédant des caractéristiques différentes.

2 Supraconductivité et microscopie à effet tunnel

La supraconductivité est un phénomène découvert en 1911 par H. Kamerlingh Onnes [3] caractérisé par une résistivité nulle des matériaux de certains matériaux en dessous d'une température critique. Ces propriétés de conductivité parfaite vont de paire avec un phénomène de diamagnétisme appelé effet Meissner-Ochsenfeld [4]. La compréhension théorique de ce phénomène fut apportée par Bardeen, Cooper et Schrieffer [5] et fait intervenir le concept de paires de Cooper [6] dans lequel deux électrons s'apparient avec des vecteurs d'onde et des spins de singe opposés. Nous détaillons ici le développement théorique amenant à la densité d'état BCS 1.

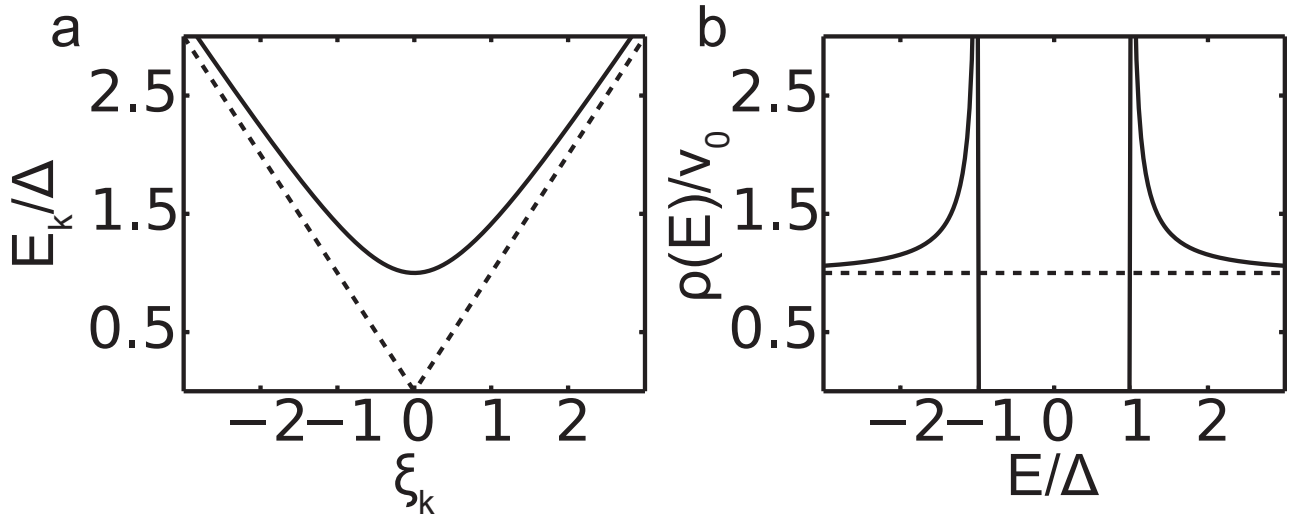

Figure 1: **Densité d'état BCS:** a. Relation de dispersion pour un supraconducteur BCS avec un gap Δ. b. Densité d'état d'excitations pour un supraconducteur BCS avec un gap Δ. Les lignes poitillées dans les deux figures rappellent le cas normal pour la dispersion et la densité d'états.

Nous rentrons dans ce chapitre dans les détails du formalisme des équations de Bogoliubov-de Gennes. Ce formalisme permet de résoudre sous une forme matricielle les équations pour les excitations d'un supraconducteur et dans la suite du manuscrit sera abondamment employé pour étudier les états de Yu-Shiba-Rusinov ainsi que la supraconductivité topologique.

Il est possible de sonder les propriétés des supraconducteurs par l'intermédiaire de la microscopie et de la spectroscopie à effet tunnel. Le gap d'énergie dans la densité d'état des supraconducteurs est en particulier directement accessible en effectuant une mesure dI/dV du courant tunnel. La mesure de cette conductance permet en effet d'accéder à la densité d'état locale convoluée par la dérivée de la fonction de Fermi-Dirac dans le cas d'une pointe métallique. Il est également possible de s'affranchir des limitations liées à l'élargissement thermique en utilisant des pointes supraconductrices. La résolution énergétique est ainsi limitée par la largeur des pics de quasiparticules, indépendante de la température de la mesure. Nous utilisons dans le corps du manuscrit principal ces deux méthodes pour venir sonder la supraconductivité et en particulier les signatures d'impuretés magnétiques au sein du gap.

3 États de Yu-Shiba-Rusinov

Pour un supraconducteur s-wave, le couplage des électrons en paires de Cooper se fait entre deux électrons de spin et de vecteur d'onde opposé [5]. Une conséquence directe de cette forme d'appariement est que sous l'application d'un champ magnétique l'un des électrons verra son énergie augmenter tandis que le second verra son énergie diminuer par effet Zeeman. De cette manière les paires pourront se retrouver brisées lorsque l'énergie Zeeman se trouve en compétition avec l'énergie d'appariement des électrons supraconducteurs. Ce fait, d'abord révélé par les travaux d'Abrikosov et Gor'kov [7] trouve un écho particulier dans le travail indépendant des physiciens Yu, Shiba et Rusinov. Dans le cas où l'interaction magnétique est générée par un atome isolé il est théoriquement anticipé l'apparition d'états liés dans le gap du supraconducteur appelés états liées de Yu-Shiba-Rusinov (YSR) [8, 9, 10]. Ces états se manifestent dans une mesure spectroscopique par l'intermédiaire de pics dans le gap à des énergies symétriques par rapport au niveau de Fermi. Le nombre de ces pics est contraint par la portée de l'interaction magnétique et pour une interaction de la forme $\delta(\boldsymbol{r}_{imp})$ se limite a une seule paire de pics.

Ces états ont été pour la première fois révélés en STM par Yazdani *et al.* [11]. Néanmoins la structure interne de ces états prédites par la théorie n'a jamais pu être observée jusqu'à présent. Une des raisons pour laquelle cette structure de la fonction d'onde associée à ces états magnétiques n'a jamais été observée vient de la décroissance rapide de celle-ci dans un matériau tri-dimensionnel dans lequel la fonction d'onde suit une loi de puissance en $1/k_F r$. En revanche pour un matériau bidimensionnel cette loi de puissance devient de la forme $1/\sqrt{k_F r}$. La faible amplitude de ces états se retrouve alors compensée par la décroissance plus lente du signal spectroscopique pour un matériau bidimensionnel et permet la mesure des oscillations de la densité d'état locale attendue théoriquement.

4 Impuretés individuelles dans 2H-$NbSe_2$

Les résultats présentés dans cette partie reprennent majoritairement le travail publié dans [12]. 2H-$NbSe_2$ est un cristal constitué de plans faiblement liés entre eux par des interactions de type Van de Waals. Ce matériau devient supraconducteur en dessous de la température critique de 33.5 K. Ce matériau bien que tridimensionnel possède une structure électronique bidimensionnelle, idéale pour les effets que nous cherchons à mettre en évidence. Les cristaux utilisés pour nos expériences contiennent un faible pourcentage d'impuretés magnétiques (principalement du Fe ainsi qu'une faible quantité de Cr et de Mn) ayant été introduit lors de la préparation. Comme nous le montrons sur la figure 2.a, lorsque l'on effectue une mesure de carte de conductance à la

surface de l'échantillon, nous observons sur une échelle de l'ordre de la dizaine de nanomètres, des structures de forme étoilée pour des énergies à l'intérieur du gap supraconducteur. Ces étoiles correspondent dans la spectroscopie à une paire de pics (voir fig. 2.b) et les énergies de ces pics peuvent varier en fonction du type d'impureté magnétique ainsi que la possibilité pour celles-ci de former des clusters de deux ou trois atomes.

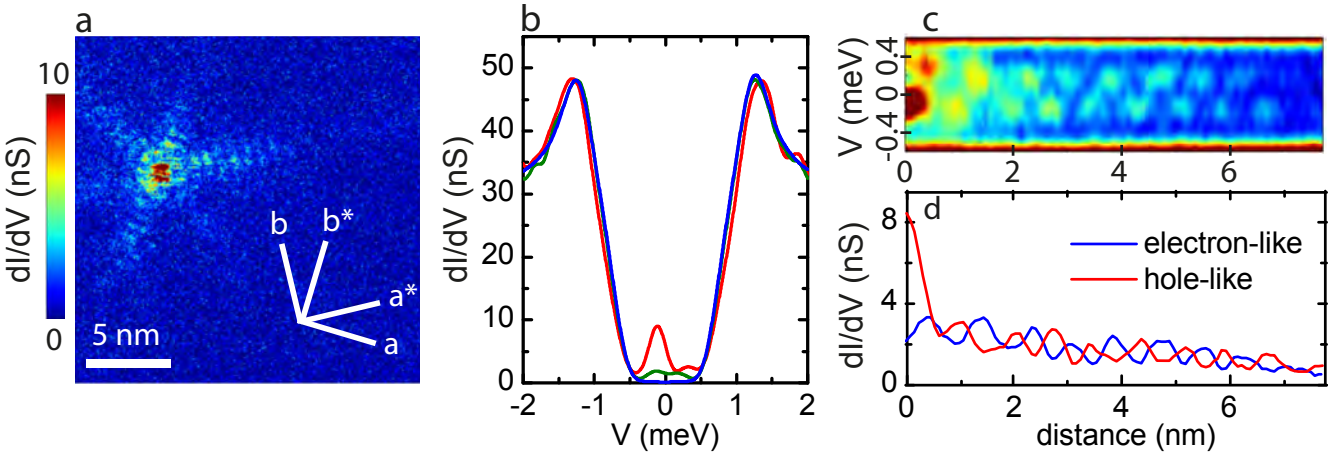

Figure 2: **Propriétés spatiales et spectrales d'un états lié étendu de Yu-Shiba-Rusinov dans 2H-$NbSe_2$** a. Carte de conductance expérimentale acquise à -0.13 meV. Deux lignes a et b indiquent la direction des axes cristallographiques tandis que a* et b* indiquent les directions dans l'espace réciproque. b. Spectres expérimental caractéristique pris au dessus de l'impureté (rouge), sur la branche de droite, à 4 nm du centre de l'impureté (vert) et loin de l'impureté (bleu). c. Évolution spatiale et énergétique des spectres de conductance tunnel expérimentaux, $dI/dV(x, V)$ le long d'une branche de l'étoile. La partie de droite de la figure correspond au centre de l'étoile et la partie droite haute de la zone de mesure. L'échelle de conductance en couleur est la même que celle utilisée en a. d. Profiles de conductance des états de YSR de type électron et trou en fonction de la distance à l'impureté le long de la même ligne que dans le cas de c.

En raison de l'étendue spatiale supérieure à la dizaine de nanomètres de ces états magnétiques, il est possible d'étudier la structure interne de ces états. En particulier, il est possible d'accéder aux oscillations de cette densité d'état qui sont visibles dans les branches de l'étoile et représentées en coupe sur les figures 2.c et d. Ces oscillations présentent un décalage de phase entre les états de type trou et les états de type électron directement lié à l'énergie des états par rapport au gap supraconducteur. Ainsi la différence de phase $\delta^+ - \delta^-$ entre ces états pour la fonction d'onde obéit à la relation $E_S = \Delta \cos(\delta^+ - \delta^-)$. Dans la mesure où le STM sonde la densité d'états et non la fonction d'onde, le déphasage mesuré correspond en réalité au double du déphasage de la fonction d'onde. Une conséquence directe de cette relation est que des états au sein du gap se trouvent en opposition de phase tandis que des états en bord de gap se trouvent en phase l'un avec l'autre. Cet aspect correspond parfaitement à nos mesures expérimentales dans le cas présenté dans la figure 2 ainsi que dans d'autres exemples sur différents types d'impuretés.

La compréhension de la forme étoilée des états de Shiba se fait par l'intermédiaire de la surface de Fermi de $NbSe_2$. Nous montrons dans le manuscrit principal qu'un calcul liaison forte permet de prendre en compte cet aspect de la structure électronique et reproduit de manière fidèle les résultats expérimentaux. Un autre moyen de prendre en compte les effets de structure de bande, sans pour autant être limité par la résolution sur site intrinsèque au modèle de liaison forte est de

passer par l'intermédiaire d'un calcul de joint-DOS. Cette deuxième manière de procéder permet d'obtenir des informations qualitatives sur les parties de la surface de Fermi jouant un rôle dans les diffusions électroniques par comparaison aux résultats expérimentaux. Nous avons ainsi mis en évidence le rôle prédominant de l'une des surface de Fermi et au sein de celle-ci le rôle centrale de la poche entourant le point Γ en raison de l'existence d'un point col dans la dispersion qui conduit à une augmentation substantielle de la densité d'états aux coins de cette surface.

Cette partie s'achève par un bref commentaire concernant les signatures d'impuretés non magnétiques de Ta. Celles-ci ont en effet un rôle à jouer sur les éléments de matrice tunnel déterminant le poids respectif de chacun des gap de 2H-$NbSe_2$. Nous avons ainsi observé que le petit gap de $NbSe_2$ voit son poids spectral augmenter au dessus d'impuretés magnétiques. Il est ainsi possible d'observer ces impuretés spectroscopiquement, cependant la nature de cet effet est purement lié à la technique expérimentale utilisée. Ainsi l'extension spatiale caractéristique des états de Shiba n'est pas retrouvée pour les impuretés non magnétiques et nous n'observons pas non plus de structure spatiale liée à la structure électronique du matériau.

5 Impuretés dans Pb/Si(111)

Cette section traite de l'effet d'impuretés magnétiques dans le système Pb/Si(111) en monocouche. La supraconductivité dans ces systèmes a pour la première fois été mise en évidence par Zhang *et al.* [13] en 2010. L'intérêt de ces systèmes par comparaison avec 2H-$NbSe_2$ est qu'il s'agit d'un système purement 2D où la supraconductivité est limitée à un gaz d'électron couvrant la couche supérieure de Pb ainsi que les trois premières couches de Si. Il s'agit par conséquent de la limite ultime dans la réduction de la dimensionnalité pour la supraconductivité. Le fait que ce système exhibe ses propriétés majoritairement à la surface du matériau rentre également en compétition avec un autre effet qu'est l'interaction Rashba spin-orbite provenant de la brisure de symétrie spatiale aux interfaces. Comme nous le verrons dans la partie suivante, la coexistence des phénomènes de supraconductivité et d'interaction spin-orbite donne naissance à une supraconductivité de type triplet, élément essentiel pour l'émergence de propriétés de supraconductivité topologique.

Il existe différentes phases supraconductrices de la monocouche de Pb/Si(111). Nous commençons par considérer la structure $\sqrt{7} \times \sqrt{3}$ présentant une forte anisotropie et apparaissant dans les mesures topographiques sous la forme de lignes atomiques (fig. 3.a). Cette anisotropie se retrouve dans les mesures spectroscopiques comme cela est présenté sur la fig. 3.b.

Sur cette figure il apparaît clairement que l'élongation des états YSR se fait dans la direction des chaînes atomiques visibles en topographie et l'étendue spatiale caractéristique d'un système 2D est observée. De plus la périodicité perpendiculairement à la direction de ces lignes se fait avec exactement le double de la périodicité atomique. Une autre périodicité peut être observée dans la direction des lignes mais est plus difficile à saisir dans l'espace réel. En prenant la transformée de Fourier d'une telle carte de conductance il apparaît alors clairement un signal correspondant à chacune de ces périodicités. Il est alors possible en partant de la structure de la surface de Fermi de cette phase [14] d'interpréter les diffusions électroniques à partir des deux différentes poches se trouvant à la limite de la première zone de Brillouin. Nous reprenons alors le principe des calculs de joint-DOS utilisés dans le cas de 2H-$NbSe_2$ en paramétrant une surface de Fermi *ad-hoc* se basant sur les résultats de photoémission.

Bien que ce type de calcul ne prenne pas en compte des effets liés directement à la supraconductivité (e.g. la longueur de cohérence n'intervient pas dans le calcul), il est tout de même possible d'en tirer des informations qualitatives. Ainsi nous montrons que les interférences de quasipar-

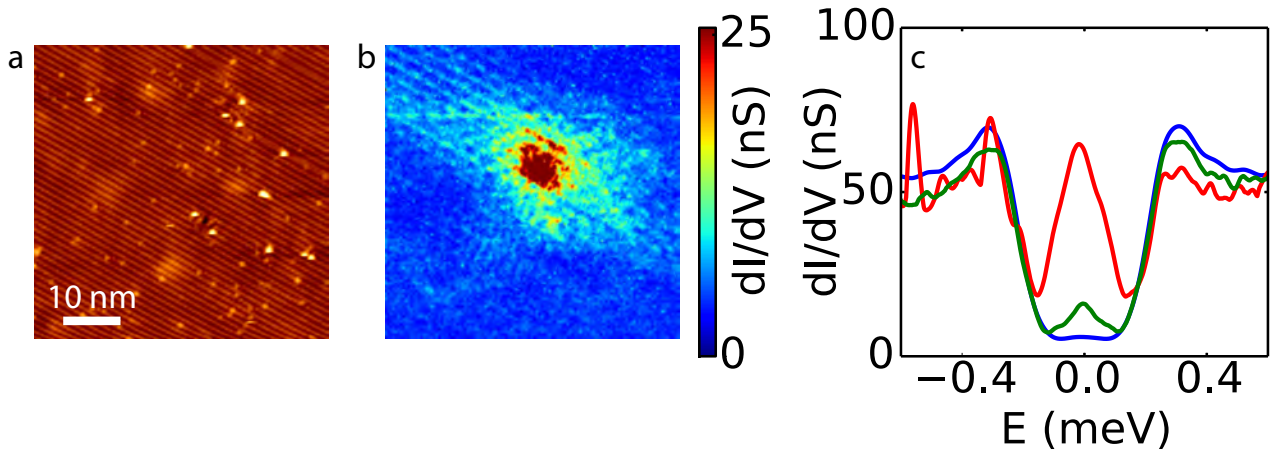

Figure 3: **États de Shiba dans la structure $\sqrt{7} \times \sqrt{3}$:** a. Topographie résolue atomiquement d'une zone 51×51 nm^2. b. Spectroscopie de la même zone autour du niveau de Fermi. c. Spectres selectionnés sur le site d'intensité maximum (rouge), à 3 nm (vert) et à 15 nm (bleu) du centre de l'impureté.

ticules dans cette même phase ne montrent pas de signal dans le sens des lignes en transformée de Fourier. Ce fait indique l'interdiction de certaines diffusions dans le cas d'une interaction non magnétiques et illustre par conséquent l'existence d'un fort effet spin-orbite dans ce système. Ces constatations sont cohérentes avec l'effet Rashba spin-orbit qui est attendu dans ce système de supraconductivité de surface.

Dans la suite de cette section nous présentons les résultats obtenus dans la phase HIC de la monocouche de Pb/Si(111). Cette structure possède un taux couverture de Pb supérieure à la phase $\sqrt{7}\times\sqrt{3}$ et une température critique légèrement supérieure. Néanmoins les valeurs de gap et de longueur de cohérence restent du même ordre de grandeur (respectivement $\Delta \simeq 0.3$ meV et $\xi \simeq 50$ nm). Une particularité de la structure HIC est qu'il s'agit d'une phase incommensurable avec le substrat de Si et apparaît par conséquent extrêmement désordonnée dans les images topographiques (voir fig. 4.a). Il n'est pas possible dans le cas d'une structure incommensurable de définir une surface de Fermi et la conséquence directe en est que les états de YSR apparaîtront dans les cartes de conductance sous une structure de type tavelure (voir fig. 4.b). Cet effet lié à la structure électronique n'empêche pas l'existence d'une portée étendue des états de YSR de l'ordre de la longueur de cohérence.

Dans la dernière partie de ce chapitre nous présentons les résultats acquis dans l'étude de clusters d'impuretés de Co enterrées sous la monocouche de Pb dans la phase HIC. Dans cette configuration, les impuretés vont se comporter comme des diffuseurs individuels et la structure incommensurable et désordonnée de la monocouche de Pb permet de supprimer les effet de phase des états de YSR. Il est ainsi possible de considérer que les états magnétiques générés par chacune de ces impuretés vit indépendamment de son voisinage et le signal mesuré en spectroscopie se réduit à la sommation d'états de Shiba produit par des impuretés distribuées avec des moments magnétiques aléatoires dans une certaine zone de l'espace. Nous mettons ainsi en évidence le remplissage du gap supraconducteur accompagné par une diminution locale de la distance pic-à-pic du gap supraconducteur. Cet effet est en net décalage avec ce qui est attendu dans le cadre de la théorie d'Abrikosov-Gor'kov. En effet dans cette théorie généralement admise comme rendant

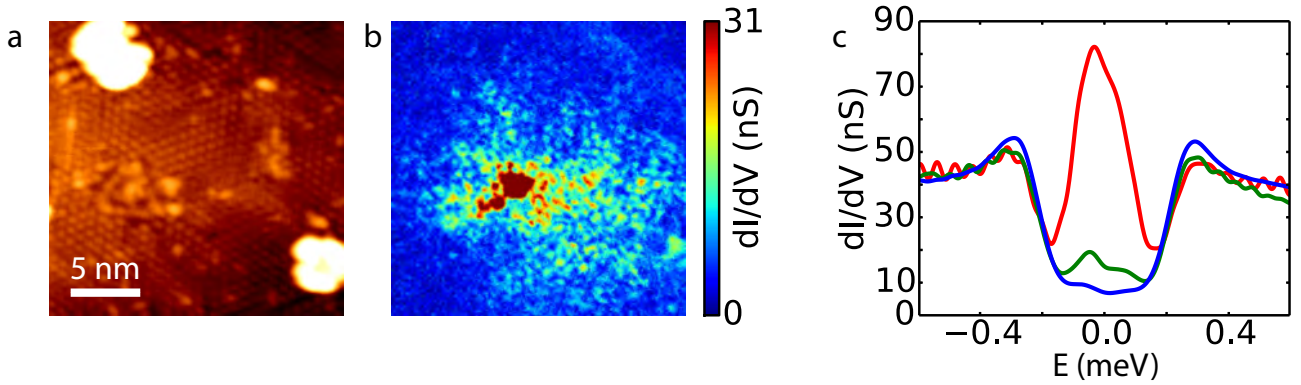

Figure 4: **Impuretés magnétique dans la phase HIC :** a. Topographie d'une zone 21×21 nm^2 dans la phase HIC. b. Carte de conductance intégrée sur la gamme d'énergie du gap montrant la structure spatiale des états YSR dans ce système. c. Spectre pris au niveau de l'impureté (rouge), loin de l'impureté (bleu) et à une distance intermédiaire (vert).

compte de cet effet d'impuretés aléatoirement réparties, le premier effet attendu est la disparition des pics de quasi-particules au bénéfice d'une densité d'états régulière. La conservation de nos pics de quasiparticules dans nos mesures expérimentales indique que la théorie d'Abrikosov-Gor'kov n'est pas adapté à ce type de configuration, tandis qu'un simple modèle numérique de sommation d'impuretés couplé à un calcul auto-cohérent spatial du gap supraconducteur permet de reproduire nos résultats.

6 Clusters topologiques dans Pb/Si(111)

Comme nous l'avons montré dans la section précédente, la monocouche de Pb/Si(111) possède une interaction spin-orbite liée à la structure bidimensionnelle de surface de ce système. Rashba et Gor'kov [15] précédés d'Edelstein [16] ont montré que l'état fondamental d'un système supraconducteur en présence d'une interaction Rashba spin-orbite acquérait une composante triplet. L'existence d'une telle composante triplet permet l'apparition d'une supraconductivité dite topologique. À l'instar des isolants topologiques, les supraconducteurs topologiques peuvent être décrit par un indice dit topologique décrivant la classe dans laquelle ils se trouvent. Deux matériaux d'indices différents correspondent à des structures de bandes fondamentalement différentes. Tout comme deux isolants topologiques possédant des invariants différents donnent naissance à des états de bords à l'interface entre eux, deux supraconducteurs d'indices topologiques différents donneront naissance à des états de bords topologiques. Ces états de bords topologiques sont particulièrement intéressant dans le cas de supraconducteurs topologiques dans la mesure où la symétrie électron-trou inhérente aux supraconducteurs conduit à une dispersion dite de Majorana.

Sur la figure 5 nous présentons le diagramme de phase d'un supraconducteur en fonction de l'intensité de la partie triplet ainsi que celle du champ Zeeman appliqué perpendiculairement au plan décrit par un système 2D. Dans la description théorique que nous avons adoptée, nous observons l'apparition de deux phases particulières appelées chirale et hélicale. En contact avec un système non topologique (tel que le vide, système trivial par excellence) ces deux phases feront apparaître des états de bords de nature différente. Les systèmes hélicaux, invariants par renversement

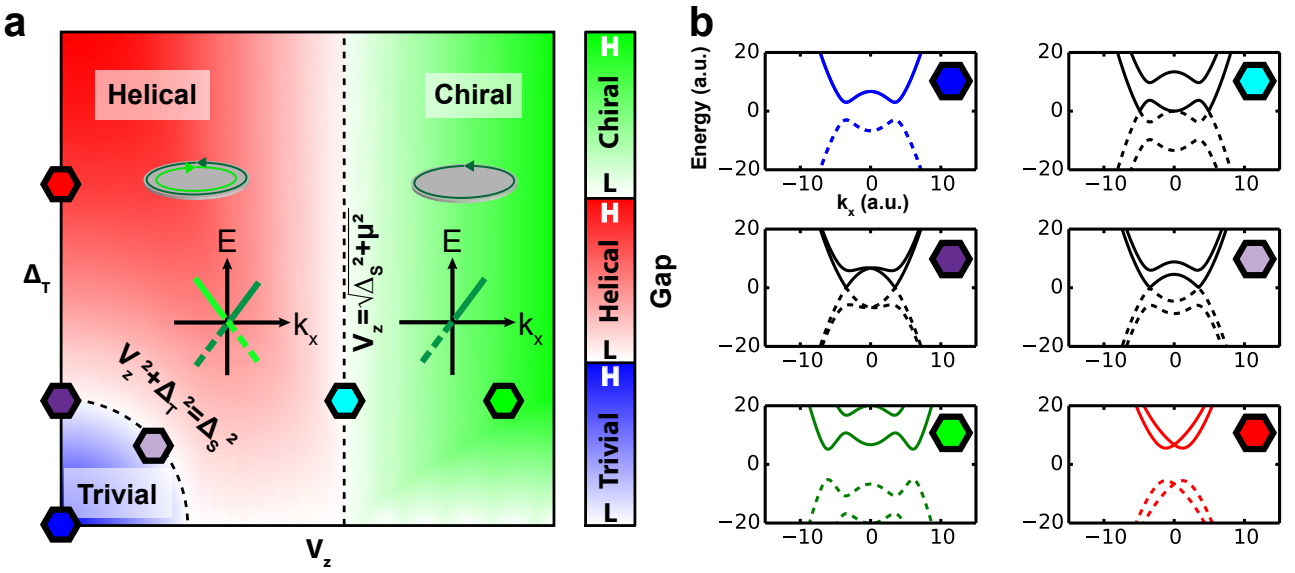

Figure 5: **Phases de la supraconductivité topologique:** a. Diagramme de phase de la supraconductivité topologique en fonction du couplage Zeeman et de l'amplitude du paramètre d'ordre triplet. Les couleurs correspondent aux différentes phases et les lignes pointillées les séparant font référence aux lignes de fermeture du gap pour lesquelles les transitions topologiques apparaissent. b. Structures de bandes correspondants aux différentes phases ainsi qu'aux transitions topologiques. Les symboles colorés correspondent aux points du diagramme de phase indiqués en a.

du temps, posséderont une paire d'états de bord contrapropagatifs, tandis que les systèmes chiraux, brisant la symétrie par renversement du temps posséderont un seul état de bord se propageant dans une direction déterminée par l'orientation du champ magnétique.

Pour obtenir ce type de système topologique nous avons fait croître sous la monocouche de Pb supraconductrice des clusters ferromagnétiques de Co d'une taille caractéristique comprise entre 5 et 10 nm. La structure schématique de ce système est présentée sur la figure 6.a. La spectroscopie tunnel de ce système révèle au niveau de Fermi l'existence d'un état de bord à la frontière des clusters de Co (voir fig. 6.b).

Il est important de noter que la structure de la couche de Pb n'est pas modifiée par la présence du cluster de Co comme en atteste la topographie 6.c. Une étude plus précise de ces états de bord montre qu'ils sont associés à une dispersion spatiale comme montré sur les figures 6.d.-f. De l'anneau unique observé au niveau de Fermi, les états se séparent pour une énergie finie. En prenant une coupe passant au centre de la zone topologique (voir fig. 6.g.) nous pouvons suivre l'évolution dans l'espace et en énergie de ces états de manière plus précise. On observe ainsi l'apparition d'un croisement des états au niveau de Fermi caractéristique d'états dispersifs de Majorana.

Dans le cas de systèmes unidimensionnels comme des fils [17] ou des chaînes d'atomes magnétiques [18], l'interface est unidimensionnelle et ne donne pas naissance à une dispersion mais à des états liés à zéro énergie. Dans le cas qui nous intéresse, des supraconducteurs bidimensionnels possèdent une interface unidimensionnelle responsable du caractère dispersif des états de bords.

Les objets d'intérêt pour l'électronique quantique ne sont néanmoins pas les dispersions de Majorana, mais bien les excitations de Majorana. Celles-ci peuvent être stabilisées à partir de

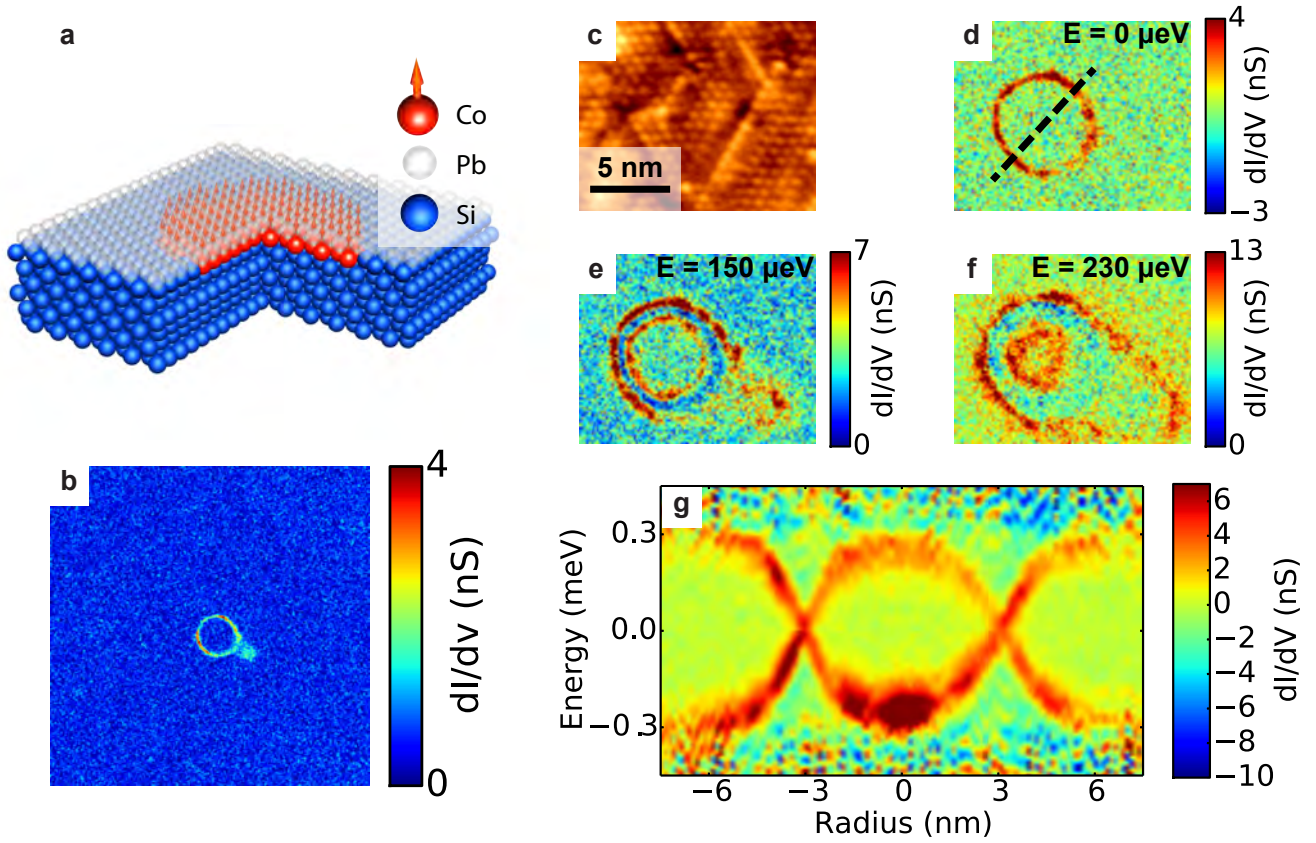

Figure 6: **États de bords d'un supraconducteur topologique:** a. Structure schématique du système considéré de clusters ferromagnétiques de Co enterrés sous la monocouche de Pb. b. Spectroscopie à grande échelle au niveau de Fermi des états de bords générés. c. Topographie d'une zone de taille 16×13 nm^2 montrant la structure atomique de la monocouche recouvrant un cluster ferromagnétique de Co. d.-f. Spectroscopie de la zone considérée à des énergies comprises dans le gap supraconducteur. g. Coupe dI/dV en fonction de la distance au centre du disque topologique et de l'énergie.

systèmes tels que celui présenté ci-dessus en introduisant un vortex dans la partie topologique. De cette manière il est possible de montrer théoriquement qu'un état se trouve piégé au niveau de Fermi correspondant à ces fameuses excitations de Majorana. Nous sommes parvenus à réaliser de tels objets en augmentant la taille des clusters magnétiques de Co (voir fig. 7).

Cependant en augmentant la taille caractéristique de ces objets, ils acquièrent un comportement instable responsable d'un renversement de la magnétisation de hors-plan vers une magnétisation dans le plan du supraconducteur. Cette transition fait perdre au systèmes ses propriétés topologiques et fait disparaître les excitations de Majorana. En conséquence en utilisant le champ électrique généré par la pointe du STM il nous est possible de modifier cette aimantation et par là de manipuler l'apparition ou l'extinction de quasiparticules de Majorana. Cet effet nous permet à long terme d'envisager un contrôle fin des fermions de Majorana pour une éventuelle application au "tressage" de ceux-ci tel que décrit dans la littérature pour l'élaboration de qubits.

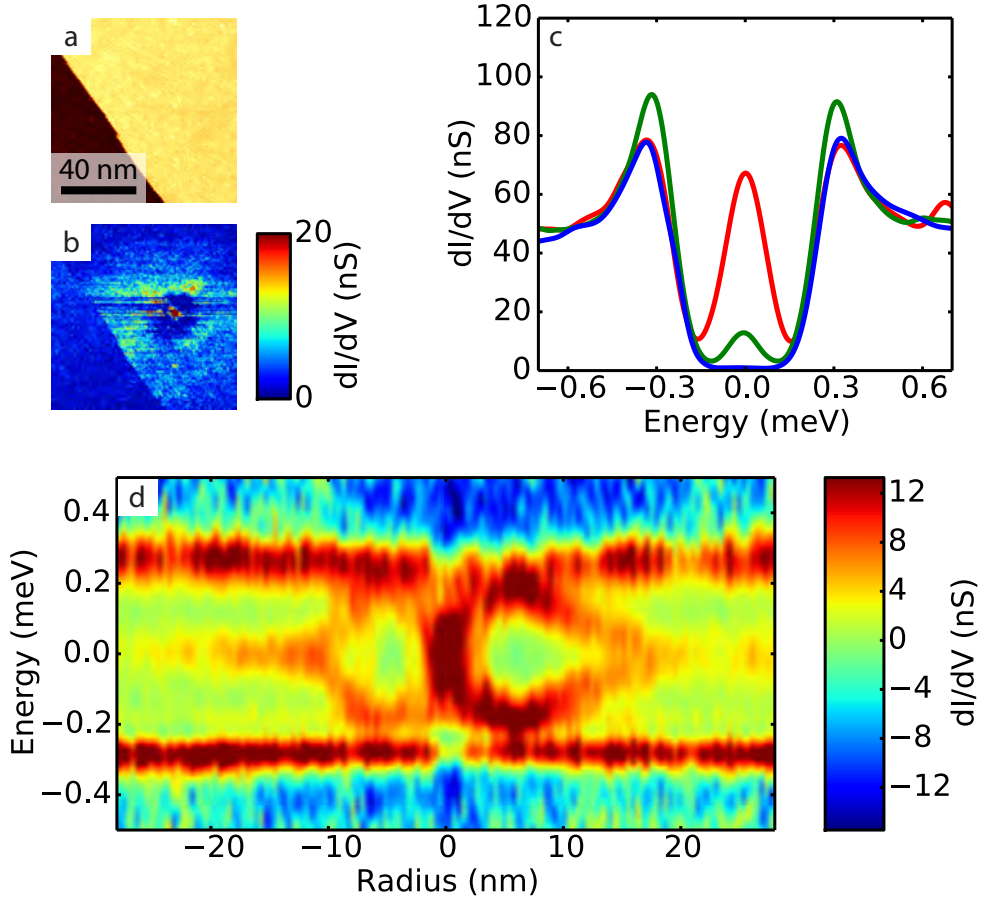

Figure 7: **Signature spectrale d'un pic au niveau de Fermi insensible au désordre local:** a. Topographie d'une zone 100×100 nm^2 d'un échantillon de Pb/Si(111) dans une phase HIC. b. Carte de conductance au niveau de Fermi de la même zone. c. Spectres pris au maximum de la carte de conductance b. (rouge), sur l'anneau d'interface entourant ce maximum (vert) et sur la couche de Pb loin de tout désordre magnétique (bleu). d. Coupe de 65 nm montrant la dépendance en énergie et spatiale au travers du vortex montré en b.

7 Phases peu denses des monocouches de Pb/Si(111)

Ce chapitre est séparé en deux parties. La première partie traite des propriétés électroniques générales de ces phases à des énergies bien supérieures au gap supraconducteur typique de $\sqrt{7}\times\sqrt{3}$. La deuxième partie quant à elle présente les résultats obtenus relatifs à l'effet de proximité des monocouches avec des patchs isolants de monocouche dans la structure 3×3.

Les monocouches de Pb/Si(111) présentent un grand nombre de phases qui diffèrent par la quantité nominale de Pb constituant la couche [**?**] (see fig. 8). Dans cette partie nous décrivons les propriétés électroniques de ces différentes phases en mettant particulièrement l'accent sur deux phases non supraconductrices appelées 3×3 et $\sqrt{3}\times\sqrt{3}$. Ces deux phases correspondent à la même quantité de Pb et sont obtenues l'une depuis l'autre par une transition de phase à une température de 86 K [19]. La phase haute température est la phase $\sqrt{3} \times \sqrt{3}$ et la phase basse température la phase 3×3. Il est néanmoins possible à basse température (300 mK) de conserver localement des

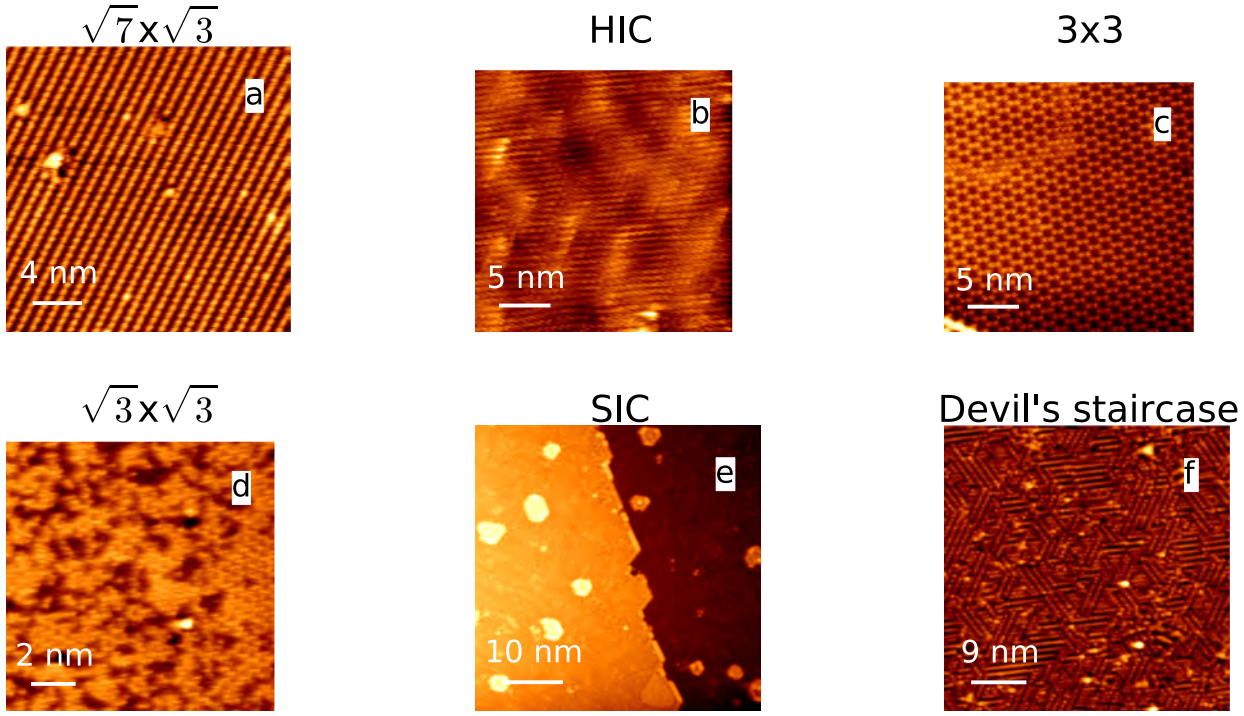

Figure 8: **Différentes phases de monocouches de Pb/Si(111):** Le nom des différentes pahses est indiqué au dessus des images topographiques.

parties $\sqrt{3} \times \sqrt{3}$ hautement désordonnées coexistant avec la phase 3×3.

Nos mesures spectroscopiques montrent que la phase 3×3 est métallique et présente deux bandes symétriques par rapport au niveau de Fermi associées à une forte interaction électronique dans le système. Ces bandes de Mott-Hubbard sont également présentent dans la phase $\sqrt{3} \times \sqrt{3}$ désordonnée mais se retrouvent déplacées à des énergies plus élevées. De plus le désordre dans la phase $\sqrt{3} \times \sqrt{3}$ ouvre un gap de plusieurs centaines de meV en raison d'un phénomène de localisation d'Anderson.

Nous mettons également en évidence dans cette partie les signatures des dopants du Si dans la spectroscopie et leur comportement percolatif dans la densité d'état tunnel à haute énergie.

Nous achevons notre discussion de l'effet de proximité en traitant le cas du contact entre la phase $\sqrt{7} \times \sqrt{3}$ et la phase 3×3. La première de ces phases est supraconductrice tandis que la seconde est isolante à basse température et présente des fortes corrélations. La structure de telles échantillons est montrée sur la figure 9.a.

Nous observons en spectroscopie l'apparition d'états dans le gap dont la nature précise nous échappe encore malgré le grand nombre de modèles utilisés. Ces états apparaissent sous la forme de paires d'états à des énergies symétriques par rapport au niveau de Fermi (fig. 9.b). Ils forment spatialement des anneaux dans la partie 3×3 de nos échantillons se déplaçant à partir d'un centre commun en fonction du potentiel appliqué (fig. 9.c). L'un des aspects les plus important réside dans l'apparition d'un gap réminiscent du gap supraconducteur dans l'intégralité des patch 3×3. Ce gap de proximité laisse suggérer que les états observés correspondent à des états liés d'Andreev, néanmoins des calculs tight-binding ainsi que des calculs de reflections multiples menées n'aboutissent pas à des résultats compatibles avec les observations expérimentales. Il est

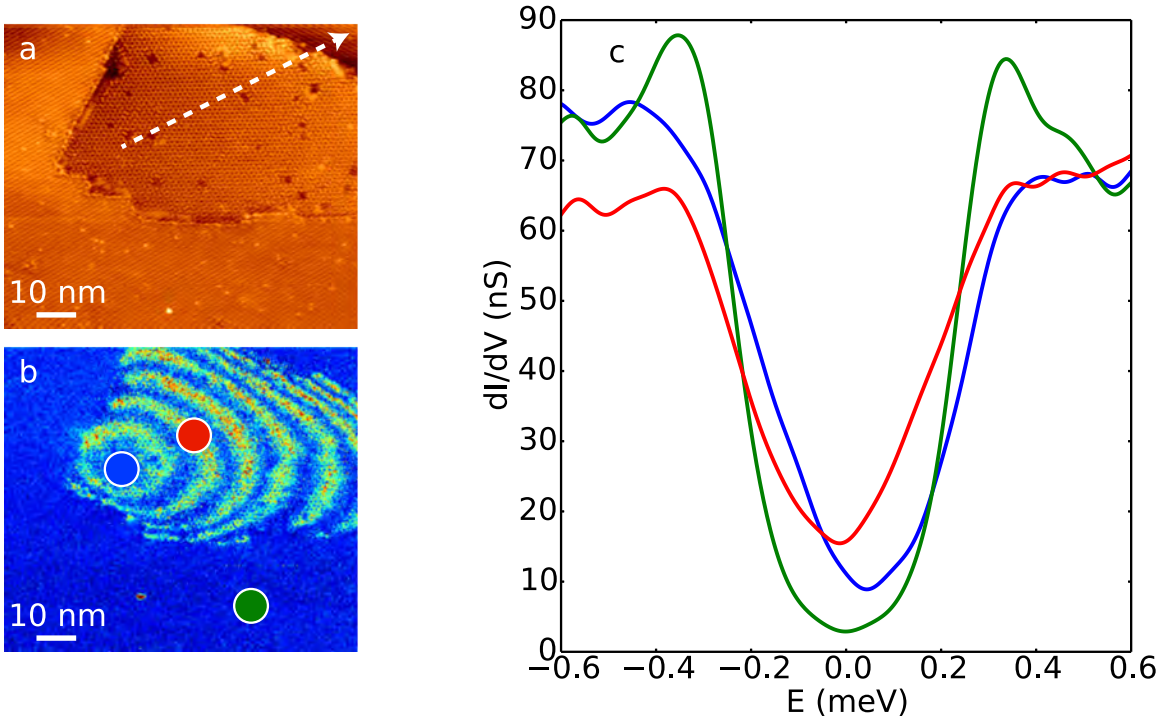

Figure 9: **Effet de proximité entre les phases** 3×3 **et** $\sqrt{7} \times \sqrt{3}$**:** Topographie d'une zone 102×89 nm^2 montrant la frontière entre un domaine $\sqrt{7} \times \sqrt{3}$. b. Carte de conductance de la même zone à 0.1 meV. c. Spectres sélectionnés dans la zone $\sqrt{7} \times \sqrt{3}$ (vert), au centre de l'anneau dans la partie 3×3 (bleu) et un point d'intensité maximum de l'un des anneaux (rouge).

fort probable que les différences avec la théorie proviennent des forts effets de corrélation électronique existant dans ces matériaux qui ne sont pas pris en compte dans les simples calculs de type Bogoliubov-de Gennes que nous avons mis en place.

8 Effet de proximité

En tirant profit de la possibilité de faire croître de nombreuses variétés de phases en contact dans un même échantillon nous avons réalisé des îlots de Pb d'une épaisseur d'une dizaine de couches atomiques [20]. Ces îlots possèdent les caractéristiques supraconductrices du Pb volumique et présentent en particulier un gap très supérieur à celui de la monocouche ($\simeq$ 1.3 meV). En conséquence la mise en contact de tels îlots avec une phase HIC donne lieu à un "écoulement" des paires de Cooper dans la monocouche sur une échelle de ξ, validant ainsi les prédictions théoriques de de Gennes [21]. Nous présentons les résultats spectroscopiques à deux températures, 300 mK et 2.05 K. Dans le premier cas les deux systèmes, îlot et monocouche se trouvent dans l'état supraconducteur, tandis que dans le deuxième, seul l'îlot conserve ses propriétés de supraconductivité. Nous mettons ainsi en évidence la susceptibilité de la monocouche à rentrer dans l'état supraconducteur au dessus de sa température critique. Ces résultats sont appuyés par des calculs réalisés par J. C. Cuevas utilisant les équations d'Usadel décrivant un supraconducteur dans la limite diffusive.

9 Conclusion

En conclusion, dans cette thèse nous avons exploré l'interaction entre supraconducteur bidimensionnel et magnétisme local en allant de l'atome individuel aux clusters d'impuretés magnétiques, qu'ils soient ordonnés ou non.

Dans le cas d'impuretés individuelles nous avons montré que la dimensionnalité du supraconducteur donnait lieu à une extension spatiale exceptionnelle des états liés de YSR. Cette extension nous a permis d'étudier plus précisément la structure spatiale de ces états et de mettre en évidence le lien entre la phase de ces états et leur énergie.

Nous avons également discuté le rôle de la structure électronique du matériau dans la structuration spatiale de ces états. En appliquant une méthode de joint-DOS dans le cas de 2H-$NbSe_2$ et de la phase $\sqrt{7}\times\sqrt{3}$ de la monocouche de Pb/Si(111) nous avons ainsi pu mettre en évidence les parties de la surface de Fermi dominant les diffusions électroniques par les impuretés individuelles.

Notre compréhension de la structure spatiale des états de YSR nous a permis de comprendre les effets en jeu dans des clusters d'impuretés magnétiques désordonné et d'interpréter la réduction locale du gap supraconducteur et le remplissage du niveau de Fermi comme un effet combiné des différentes impuretés enfouies.

En parvenant à organiser de manière cohérente nos clusters d'impuretés magnétiques nous avons montré qu'il était possible d'établir des domaines topologiques dans les monocouches de Pb/Si(111) par l'application d'un champ magnétique étendu sur une échelle de quelques nanomètres. La mise en évidence des états de bords résultant et de la dispersion les accompagnant constitue une mise en évidence directe de la supraconductivité topologique.

La suite de ce travail a constitué à générer des vortex dans la partie topologiques piégeant ainsi des excitations électroniques au niveau de Fermi qui correspondent à des états liés de Majorana. Nous avons alors montré que ces états liés pouvaient être manipulés en basculant l'aimantation des clusters magnétiques par l'intermédiaire de la pointe du STM.

Nous avons enfin décrit les différentes structures électroniques des phases monocouches de Pb/Si(111) sur de larges gammes d'énergie. Ce faisant nous avons pu réaliser des structures de proximité mettant en évidence le comportement fortement corrélé de la phase 3×3.

Ce travail apporte ainsi une vision d'ensemble de l'interaction entre supraconducteur et impuretés magnétiques allant de l'impureté individuelle aux clusters d'impuretés. Les résultats présentés sur la supraconductivité topologique laisse espérer un développement ultérieur de l'étude des propriétés topologiques des monocouches supraconductrices et de la manipulation d'excitations de Majorana dans ces systèmes. Une des pistes les plus prometteuses réside dans la possibilité de manipuler les excitations de Majorana par l'intermédiaire d'une pointe de STM ouvrant ainsi la voie à des possibilités de tressage de ces excitations.

References

[1] D. A. Ivanov. Non-Abelian statistics of half-quantum vortices in p-wave superconductors. *Phys. Rev. Lett.*, **86**:268–271, 2001.

[2] M. Sato and S. Fujimoto. Majorana fermions and topology in superconductors. *Arxiv: 1601.02726*, 2016.

[3] H. K. Onnes. The resistance of pure mercury at helium temperatures. *Commun. Phys. Lab. Univ. Leiden*, **12**:120, 1911.

[4] W. Meissner and R. Ochsenfeld. Ein neuer effekt bei eintritt der supraleitfähigkeit. *Naturwissenschaften*, **21**:787–788, 1933.

[5] J. Bardeen, L. N. Cooper, and J. R. Schrieffer. Theory of superconductivity. *Phys. Rev.*, **108**:1175–1204, 1957.

[6] L. N. Cooper. Bound electron pairs in a degenerate Fermi gas. *Phys. Rev.*, **15**:1189–1190, 1956.

[7] A. A. Abrikosov and L. P. Gor'kov. Contribution to the theory of superconducting alloys with paramagnetic impurities. *Soviet Physics JETP*, **12**:1243–1253, 1961.

[8] L. Yu. Bound state in superconductors with paramagnetic impurities. *Acta Phys. Sin*, **21**:75–91, 1965.

[9] H. Shiba. Classical spins in superconductors. *Progress of Theoretical Physics*, **40**:435–451, 1968.

[10] A. I. Rusinov. Superconductivity near a paramagnetic impurity. *JETP Lett.*, **85**:85, 1969.

[11] A. Yazdani and al. Probing the local effects of magnetic impurities on superconductivity. *Science*, **275**:1767–1770, 1997.

[12] G. C. Ménard, S. Guissart, C. Brun, S. Pons, V.S. Stolyarov, F. Debontridder, M.V. Leclerc, E. Janod, L. Cario, D. Roditchev, P. Simon, and T. Cren. Coherent long-range magnetic bound states in a superconductor. *Nature Physics*, **11**:1013–1016, 2015.

[13] T. Zhang, P. Cheng, W.-J. Li, Y.-J. Sun, G. Wang, X.-G. Zhu, K. He, L. Wang, X. Ma, X. Chen, Y. Wang, Y. Liu, H.-Q. Lin, J.-F. Jia, and Q.-K. Xue. Superconductivity in one-atomic-layer metal films grown on Si(111). *Nature Physics*, **6**:104–108, 2010.

[14] K. S. Kim, S. C. Jung, M. H. Kang, and H. W. Yeom. Nearly massless electrons in the silicon interface with a metal film. *Phys. Rev. Lett.*, **104**:246803, 2010.

[15] L. P. Gor'kov and E. I. Rashba. Superconducting 2D system with lifted spin degeneracy: mixed singlet-triplet state. *Phys. Rev. Lett.*, **87**:037004, 2001.

[16] V. M. Édel'shtein. Characteristics of the Cooper pairing in two-dimensional noncentrosymmetric electron systems. *Zh. Eksp. Teor. Fiz.*, **95**:2151–2162, 1989.

[17] V. Mourik, K. Zuo, S. M. Frolov, S. R. Plissard, E. P. A. M. Bakkers, and L. P. Kouwenhoven. Signatures of Majorana fermions in hybrid superconductor-semiconductor nanowire devices. *Science*, **336**:1003–1007, 2012.

[18] S. Nadj-Perge, I. K. Drozdov, J. Li, H. Chen, S. Jeon, J. Seo, A. H. MacDonald, B. A. Bernevig, and A. Yazdani. Observation of Majorana fermions in ferromagnetic atomic chains on a superconductor. *Science*, **346**:602–607, 2014.

[19] V. Yeh, M. Yakes, M. Hupalo, and M.C. Tringides. Low temperature formation of numerous phases in Pb/Si(111). *Surf. Science Lett.*, **532**:L238–L244, 2004.

[20] I. Brihuega, O. Custance, R. Pérez, and J. M. Gómez-Rodríguez. Intrinsic character of the (3×3) to $(\sqrt{3} \times \sqrt{3})$ phase transition in Pb/Si(111). *Phys. Rev. Lett.*, **94**:046101, 2005.

[21] V. Cherkez, J. C. Cuevas, C. Brun, T. Cren, G. Ménard, F. Debontridder, V. S. Stolyarov, and D. Roditchev. Proximity effect between two superconductors spatially resolved by scanning tunneling spectroscopy. *Physical Review X*, **4**:011033, 2014.

[22] P.-G. de Gennes. Boundary effects in superconductors. *Review of Modern Physics*, **36**:225, 1964.